University of California
Santa Barbara

Linking crystal structure and magnetism in intermetallics

A dissertation submitted in partial satisfaction
of the requirements for the degree
Doctor of Philosophy
in
Materials
by

Joshua David Bocarsly

Committee in charge:

Professor Ram Seshadri, Chair
Professor Stephen D. Wilson
Professor Anton Van der Ven
Professor Ania C. Bleszynski Jayich

June 2020

The Dissertation of Joshua David Bocarsly is approved.

Professor Stephen D. Wilson

Professor Anton Van der Ven

Professor Ania C. Bleszynski Jayich

Professor Ram Seshadri, Committee Chair

February 2020

Linking crystal structure and magnetism in intermetallics

by

Joshua David Bocarsly

To my parents, who were my first science teachers,

and to my wife Aliisa

Acknowledgements

I am deeply grateful for the support of a great number of people in completing this dissertation and my degree. Without the help and support of so many mentors, colleagues, friends, and family members this journey would not have been possible.

Firstly, I would like to thank my advisors, Ram Seshadri and Stephen Wilson. I have benefitted tremendously from being able to be a part of two different groups with two exemplary advisors. To Ram: Thank you for welcoming me into your group and supporting my scientific and personal development for these past four and a half years. So much of what I have learned in graduate school has come from unstructured conversations with you, or from simply observing how you function as a scientist, a teacher, and an advisor. Thank you for working so hard to make the Materials Research Laboratory a vibrant, diverse, well-outfitted research center and community; I cannot imagine a better place to go through graduate school. I especially appreciate how you challenged me to think independently and allowed me flexibility in my research directions, while also being extremely generous with your time, guidance, knowledge, and resources.

To Stephen: Thank you for welcoming me into your group, taking a chance on me as your first co-advised student. I especially appreciate how you are always willing to take the time to give thoughtful feedback and support, and to patiently explain physics concepts to me. I have learned so much from talking to you, and from being in your group. Coming from a chemistry background, I am particularly grateful for the opportunity I had in your group to learn new perspectives and ways of approaching materials science.

I would also like to thank Anton Van der Ven and Ania Jayich, my other dissertation

committee members for supporting my development throughout my time at UC Santa Barbara. I feel especially fortunate to have had the opportunity to work with you two in IRG-1 for these last two years. Your perspectives have challenged me and enriched my research. In this area, I would also like to thank Dan Gianola.

My favorite experiences during graduate school have been in collaborating with a fantastic group of researchers from a variety of backgrounds. I would like to thank Michelle Johannes at NRL for our long and enlightening conversations about manganese arsenide and the nature of magnetic interactions. At TU Darmstadt, I would like to thank Barbara Albert, Christina Birkel, Anne-Marie Zieschang, Christin Hamm, Wolfgang Donner, and Tom Faske for very fruitful collaborations. I would especially like to thank Barbara Albert for inviting me to TU Darmstadt, and Christina Birkel for generously hosting me in her home on two occasions. I would further like to thank Claudia Felser for inviting me to spend time at the Max Planck Institute for Chemical Physics of Solids in Dresden. I also thank Luis Echegoyen at UTEP for an excellent collaboration and many valuable conversations, as well as Ben Bales and Linda Petzold, and Trevor Hayton, Andrew Cook, and Alex Touchton here at UC Santa Barbara.

I am deeply grateful for all of my groupmates past and present in both the Seshadri and Wilson groups. You have all made campus a wonderful place to work and have taught me so much. I would like to especially mention those I have had the opportunity to work more closely with: Emily Levin, Jason Grebenkemper, Joya Cooley, Linus Kautzsch, Molleigh Preefer, Emily Schueller, Ryan Need, Yuzki Oey, Jason Douglas, Doug Fabini, Hayden Evans, Tom Hogan, Rebecca Dally, Eli Zoghlin, Zach Porter, Mitchell Bordelon, Julia Zuo, Jayden Plumb and Justin Mayer. I am also grateful to my IRG-1 collaborators Eric Yao, Simon Meynell, Yolita Eggeler, Daniil Kitchaev, Daipeng Yang, and Wenbo Wang. I would also like to thank Christina Garcia, Sam Humphrey,

and Weiheng Fu, each of whom I had the opportunity to work with as undergraduates.

I would further like to thank Fuzzy Rogers, Youli Li, Rachel Behrens, and, especially, Amanda Strom for keeping the MRL research facilities running. I'd also like to thank you, along with the rest of the MRL staff for making the MRL such a fun and welcoming community. I'd like to thank Dotti Pak, Mary McGuan, Julie Standish, Frank Kinnaman, and Claudia Gutierrez-Mazzotti for running an excellent education outreach program and for providing me with lots of opportunities to get involved.

Much of the work in this dissertation would not have been possible without the help of dedicated collaborators at synchrotron and neutron sources. I would especially like to thank Saul Lapidus, Lynn Ribaud, and Leighanne Gallington at APS, Craig Brown, Colin Heikes, Julie Borchers and Dustin Gilbert at NCNR, and Simon Kimber, Ashfia Huq, Lisa Debeer-Schmitt and Melanie Kirkham at ORNL.

Finally, I would like to acknowledge the vital role that my friends and family have played in my life throughout graduate school and beyond. To my parents: I would never be the scientist, or the person, I am today without your love, teaching and guidance. You are my role models, and and I always look to your example of selflessness, integrity, creativity, and perseverance both in and out of the lab. To my sisters and brothers-in-law (and niblings!): Thank you for always being there for me and looking out for me. To all my friends in Santa Barbara and afar: Thank you for the laughs, games, and advice. Lastly, I would like to thank the most important person in my life, my wonderful wife Aliisa. Your support and love have been a guiding light during graduate school.

Curriculum Vitæ

Joshua David Bocarsly

Education

Sep 2014 – Mar 2020 Ph.D. in Materials (expected), University of California, Santa Barbara.
Co-advisors: Professor Ram Seshadri and Professor Stephen D. Wilson

Sep 2011 – Jun 2015 *A.B.* in Chemistry *summa cum laude*, Princeton University
Senior thesis advisor: Professor Robert J. Cava

Publications

22. **J. D. Bocarsly**, M. Johannes, S. D. Wilson, R. Seshadri, Magnetostructural coupling from competing magnetic and chemical bonding effects, *manuscript in preparation (working title)*.
21. E. C. Schueller, D. A. Kitchaev, J. L. Zuo, **J. D. Bocarsly**, J. A. Cooley, A. Van der Ven, S. D. Wilson, R. Seshadri, Structural evolution and skyrmionic phase diagram of the lacunar spinel $GaMo_4Se_8$, *in press at Phys. Rev. Mater.*
20. Y. M. Oey, **J. D. Bocarsly**, D. Mann, E. E. Levin, M. Shatruk, and R. Seshadri, Structural changes upon magnetic ordering in magnetocaloric $AlFe_2B_2$, *in press at Appl. Phys. Lett.*
19. M. B. Preefer, M. Saber, Q. Wei, N.H. Bashian, **J.D. Bocarsly**, W. Zhang, G. Lee, J. Milam-Guerrero, E. S. Howard, R.C. Vincent, B.C. Melot, A. Van der Ven, R. Seshadri, B. Dunn, Multielectron redox and insulator-to-metal transition upon lithium insertion in the fast-charging, Wadsley-Roth phase PNb_9O_{25}, *in press at Chem. Mater.* doi:10.1021/acs.chemmater.0c00560
18. A. W. Cook, **J. D. Bocarsly**, R. A. Lewis, A. J. Touchton, S. Morochnik, and T. W. Hayton. An iron ketimide single-molecule magnet $[Fe_4(N{=}CPh_2)_6]$ with sup- pressed through-barrier relaxation. *Chem. Sci.* **11** (2020) 4753–4757. doi:10.1103/PhysRevMaterials.4.044405
17. J. A. Cooley, **J. D. Bocarsly**, E. C. Schueller, E. E. Levin, E. E. Rodriguez, A. Huq, S. H. Lapidus, S. D. Wilson, and R. Seshadri, Evolution of non-collinear magnetism in magnetocaloric MnPtGa, *Phys. Rev. Mater.* **4** (2020) 044405. doi:10.1103/PhysRevMaterials.4.044405
16. E. E. Levin, **J. D. Bocarsly**, J. H. Grebenkemper, R. Issa, S. D. Wilson, T. M. Pollock, and R. Seshadri. Structural coupling and magnetic tuning in $Mn_{2-x}Co_xP$ magnetocalorics for thermomagnetic power generation. *APL Mater.* **8** (2020) 041106. doi:10.1063/1.5142000

15. L. Kautzsch, **J. D. Bocarsly**, C. Felser, S. D. Wilson, and R. Seshadri. Controlling Dzyaloshinskii-Moriya interactions in the skyrmion host candidates $FePd_{1-x}Pt_xMo_3N$. *Phys. Rev. Mater.* **4** (2020) 024412. doi:10.1103/PhysRevMaterials.4.024412

14. C. A. C. Garcia, **J. D. Bocarsly**, and R. Seshadri. Computational screening of magnetocaloric alloys. *Phys. Rev. Mater.* **4** (2020) 024402. doi:10.1103/PhysRevMaterials.4.024402

13. A.-M. Zieschang, **J. D. Bocarsly**, J. Schuch, C. V. Reichel, B. Kaiser, W. Jaegermann, R. Seshadri, and B. Albert. Magnetic and electrocatalytic properties of nanoscale cobalt boride, Co_3B. *Inorg. Chem.* **58** (2019) 16609–16617. doi:10.1021/acs.inorgchem.9b02617

12. M. B. Preefer, J. H. Grebenkemper, F. Schroeder, J. D. Bocarsly, K. Pilar, J. A. Cooley, W. Zhang, J. Hu, S. Misra, F. Seeler, K. Schierle-Arndt, and R. Seshadri. Rapid and tunable assisted-microwave preparation of glass and glass-ceramic thiophosphate "$Li_7P_3S_{11}$" Li-ion conductors. *ACS Appl. Mater. Interfaces* **11** (2019) 42280–42287. doi:10.1021/acsami.9b15688

11. E. C. Schueller, J. L. Zuo, **J. D. Bocarsly**, D. A. Kitchaev, S. D. Wilson, and R. Seshadri. Modeling the structural distortion and magnetic ground state of the polar lacunar spinel GaV_4Se_8. *Phys. Rev. B* **100** (2019) 1–6. doi:10.1103/PhysRevB.100.045131

10. **J. D. Bocarsly**, E. E. Levin, S. A. Humphrey, T. Faske, W. Donner, S. D. Wilson, and R. Seshadri. Magnetostructural coupling drives magnetocaloric behavior: The case of MnB versus FeB. *Chem. Mater.* **31** (2019) 4873–4881. doi:10.1021/acs.chemmater.9b01476

9. **J. D. Bocarsly**, C. Heikes, C. M. Brown, S. D. Wilson, and R. Seshadri. Deciphering structural and magnetic disorder in the chiral skyrmion host materials $Co_xZn_yMn_z$ ($x + y + z = 20$). *Phys. Rev. Mater.* **3** (2019) 014402. doi:10.1103/PhysRevMaterials.3.014402

8. **J. D. Bocarsly**, R. F. Need, R. Seshadri, and S. D. Wilson. Magnetoentropic signatures of skyrmionic phase behavior in FeGe. *Phys. Rev. B* **97** (2018) 100404(R). doi:10.1103/PhysRevB.97.100404

7. A.-M. Zieschang, **J. D. Bocarsly**, M. Dürrschnabel, H.-J. Kleebe, R. Seshadri, and B. Albert. Low-temperature synthesis and magnetostructural transition in antiferromagnetic, refractory nanoparticles: chromium nitride, CrN. *Chem. Mater.* **30** (2018) 1610–1616. doi:10.1021/acs.chemmater.7b04815

6. J. H. Grebenkemper, **J. D. Bocarsly**, E. E. Levin, G. Seward, C. Heikes, C. Brown, S. Misra, F. Seeler, K. Schierle-Arndt, S. D. Wilson, and R. Seshadri. Rapid microwave preparation and composition tuning of the high-performance magnetocalorics $(Mn,Fe)_2(P,Si)$. *ACS Appl. Mater. Interfaces* **10** (2018) 7208–7213. doi:10.1021/acsami.9b15688

5. E. E. Levin, **J. D. Bocarsly**, K. E. Wyckoff, T. M. Pollock, and R. Seshadri. Tuning the magnetocaloric response in half-Heusler/Heusler $MnNi_{1+x}Sb$ solid solutions. *Phys. Rev. Mater.* **1** (2017) 075003. doi:10.1103/PhysRevMaterials.1.075003

4. C. M. Hamm, **J. D. Bocarsly**, G. Seward, U. I. Kramm, and C. S. Birkel. Non-conventional synthesis and magnetic properties of MAX phases $(Cr/Mn)_2AlC$ and $(Cr/Fe)_2AlC$. *J. Mater. Chem. C* **5** (2017) 5700–5708. doi:10.1039/C7TC00112F

3. **J. D. Bocarsly**, E. E. Levin, C. A. C. Garcia, K. Schwennicke, S. D. Wilson, and R. Seshadri. A simple computational proxy for screening magnetocaloric compounds. *Chem. Mater.* **29** (2017) 1613–1622. doi:10.1021/acs.chemmater.6b04729

2. A.-M. Zieschang, **J. D. Bocarsly**, M. Dürrschnabel, L. Molina-Luna, H.-J. Kleebe, R. Seshadri, and B. Albert. Nanoscale iron nitride, ϵ-Fe_3N: Preparation from liquid ammonia and magnetic properties. *Chem. Mater.* **29** (2017) 621–628. doi:10.1021/acs.chemmater.6b04088

1. **J. D. Bocarsly**, D. Hirai, M. N. Ali, and R. J. Cava. Superconducting phase diagram of In_xWO_3 synthesized by indium deintercalation. *Europhys. Lett.* **103** (2013) 17001. doi:10.1209/0295-5075/103/17001

Abstract

Linking crystal structure and magnetism in intermetallics

by

Joshua David Bocarsly

Intermetallic materials, which are compounds of two or more metals and metalloids, host a diversity of magnetic phenomena that promise to enable next-generation technologies. For example, several families of intermetallics can undergo large changes in temperature when placed into a magnetic field. This phenomenon, known as the magnetocaloric effect, can be used to build heat pumps that can replace traditional vapor compression refrigerators and air conditioners. Such "magnetic refrigeration" can operate with high efficiencies and without the harmful chlorofluorocarbon or hydrofluorocarbon refrigerants that traditional vapor compression devices rely on. As another example, magnetic intermetallics with non-centrosymmetric crystal structures can host skyrmions: nanoscale vortices of the magnetic moments that behave like stable particles. Skyrmions can be manipulated using small electrical currents or magnetic fields, potentially allowing for ultra-high-density magnetic memory that is more energy-efficient than present alternatives.

The interesting properties of intermetallics can be attributed to their ability to simultaneously host several different types of structural and magnetic interactions, including a mix of covalent, metallic and ionic bonding and magnetic interactions that are a combination of itinerant and local-moment-like. Furthermore, these structural and magnetic interactions often couple. This flexibility presents tremendous opportunities for the realization of desirable functionality in intermetallics; however, it also means

that the behavior of these systems is often difficult to understand. In order to harness the potential of magnetic intermetallics, an improved understanding of the interplay between crystal structure and magnetism is required. In this dissertation, I investigate several key magnetocalorics and skyrmion hosts in order to uncover the mechanisms by which magnetism and crystal structure couple in highly functional intermetallics.

The first portion of the dissertation aims to establish a general understanding of the physical origins of large magnetocaloric effects. Chapters 2 and 3 present strategies for rapid computational screening of potential magnetocalorics using high-throughput density functional theory calculations. These studies provide evidence that magnetostructural coupling, generically, is the primary driver of strong magnetocaloric effects across a very broad range of ferromagnetic materials. This connection is made concrete in Chapters 4 and 5, which provide detailed computational and experimental studies of two specific magnetocalorics: MnAs and MnB. In each case, it is found that competition between magnetism and chemical bonding leads to coupling between magnetic and structural degrees of freedom. This competition-driven coupling results in systems that are delicately balanced between magnetic and structural stability and can easily be "tipped" in one direction by the application of a small field, resulting in a large magnetic entropy changes. The results and ideas included in this section of the dissertation are pulled together in a perspective review on magnetostructural coupling in magnetocalorics, which is included in the introductory chapter of this dissertation (Chapter 1).

The latter portion of the dissertation focuses on skyrmionic magnetic phases in noncentrosymmetric intermetallics. Chapter 6 presents an experimental method to study subtle magnetic phase diagrams using magnetic entropy measurements and applies this method to understand the magnetic behavior of the near-room-temperature skyrmion

host FeGe. Chapter 7 uses this technique, along with synchrotron and neutron scattering and electronic structure calculations, in an in-depth study of the $Co_xZn_yMn_z$ family of high-temperature skyrmion hosts. The experimentally observed crystal structures are found to arise from competing magnetic and bonding effects, and these structures are found to host frustrated magnetic interactions. This results in an interesting magnetic state involving the coexistence of ordered and disordered magnetism on the Co and Mn atoms, respectively. This unique phenomenon is proposed to enable the formation of remarkable disorder-driven skyrmionic phases that have been observed in $Co_xZn_yMn_z$.

Contents

List of Figures

Chapter 1

Introduction

1.1 The study of magnetic intermetallics

Magnetic materials, and especially ferromagnets, have been studied since the ancient world, with scientific investigation arising in Greece, India, and China at least as early as 500-700 BC. [1] In each case, these original discoveries were of "lodestones," which are pieces of the mineral magnetite (Fe_3O_4) that can be found naturally magnetized in nature, perhaps as a result of fortuitous lightning strikes. [2, 3] Ferromagnetism was later found in the elements iron, cobalt, and nickel and their alloys, as well as the rare earth element gadolinium. In 1901, however, a landmark discovery vastly opened up the study of magnetic materials: Fritz Heusler observed that the combination of the non-ferromagnetic elements manganese, copper, and aluminum remarkably resulted in a compound that was strongly ferromagnetic at room temperature. [4] $MnCu_2Al$ now known as a "Heusler compound," was perhaps the first clear example of a magnetic "intermetallic," an ordered compound of two or more metals and metalloids. Soon thereafter, many new Heusler compounds and other magnetic

intermetallics were discovered. [5–9]

Nowadays, the properties of magnetic intermetallics with diverse properties are exploited for a variety of technological applications. For example, the strongest permanent magnets available are rare-earth-based intermetallics like $Nd_2Fe_{14}B$ and $SmCo_5$. [10] The large remnant magnetization of these materials allows them to be used to power electric motors, wind turbine generators, and hard drives. On the other hand, soft magnets like permalloy can be used as inductor cores or shielding, and magnetostrictive Terfenol-D and ferromagnetic shape memory compounds are used in sensors, actuators, and transducers. [11] In coming years, intermetallic magnets promise to enable next-generation technologies including energy-efficient and environmentally friendly magnetic refrigeration, [12] spintronics, [13] and quantum computers. [14, 15]

Despite this long history of investigation, intermetallic magnets are still poorly understood. Much of the remarkable magnetic behavior of intermetallics can be attributed to the fact that they have properties that are intermediate between those of the magnetic elements and ceramic compounds. Intermetallics are typically highly electronically conductive like metals, and yet brittle like ceramics. They typically show a combination of metallic, covalent, and ionic bonding and may simultaneously host electrons that are localized, dispersive, or somewhere in between. Figure 1.1 shows a "family tree" made up of some related intermetallic crystal structures that feature in this dissertation. For each structure type, the strongest covalent bonding interactions are drawn, and it can be seen that a diversity of bonding schemes (and therefore electronic structures) are possible even in closely related intermetallic crystal structures. This ability to host multiple types of coupled structural, magnetic, and electronic interactions can breed fantastic functionality. However, this flexibility also entails considerable com-

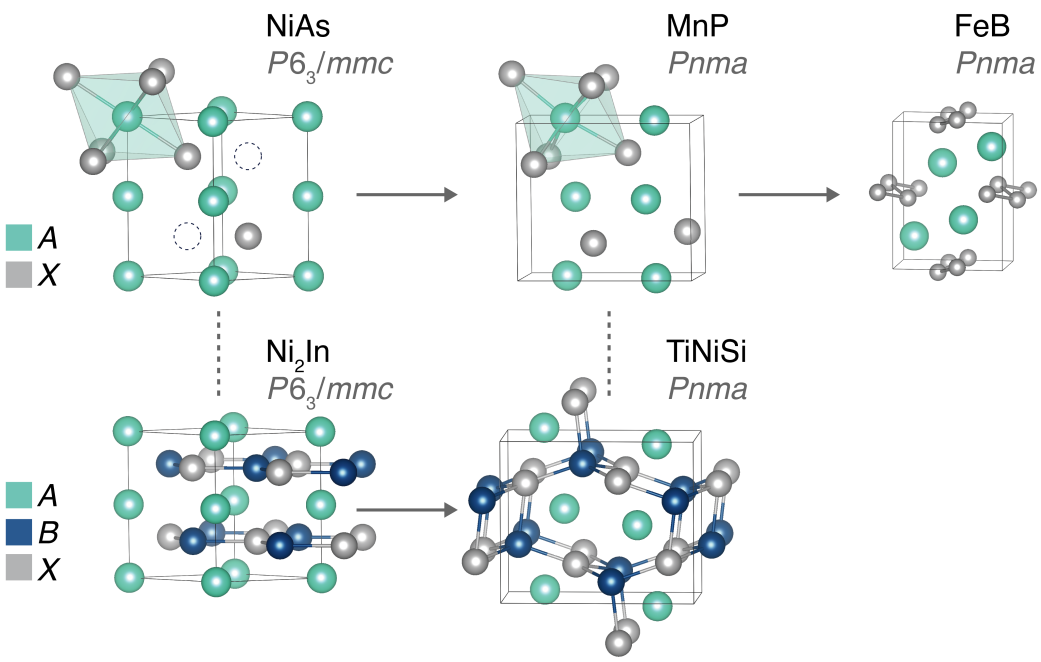

Figure 1.1: Some intermetallic structure types discussed in this dissertation. The drawn structure types have chemical stoichiometry AX and ABX, where A and B are transition metals and X is a metalloid. The grey solid arrows indicate that a distortion transforms one structure into another. The grey dotted lines indicate that the NiAs and MnP structures may be derived from the Ni_2In and TiNiSi structure types by replacing the B atom with a vacancy. In each case, the strongest covalent bonds are drawn, illustrating the diversity of bonding schemes possible even in closely-related intermetallic structure types.

plexity, and understanding, predicting, and manipulating the properties of magnetic intermetallics is a major research challenge.

In studying magnetic intermetallics, there is always a tension between which fundamental models of magnetic interactions should be applied. Insulating magnets with well-localized moments, as may be found in some oxides, can often be well-explained by local moment approaches such as Weiss's mean field model, or the models of Heisenberg, Mott, and Hubbard. On the other end of the spectrum, a small number of materials show ferromagnetism arising almost exclusively from spin-polarization of delo-

calized bands of electrons, behaving as ideal itinerant magnets. These compounds typically show weak moments relative to local-moment magnets and are well-described by the electronic-structure-based method of Stoner and Wolfarth, [16] and Moriya's spin-wave based theory [17]. Each of these models provides quantitative tools and predictions that can be used reliably for the analysis and control of magnetic systems that are either highly-localized or highly-itinerant.

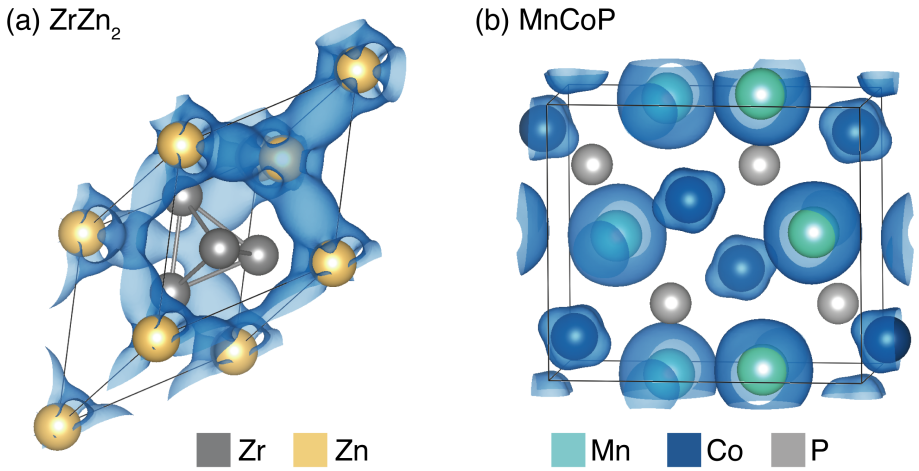

Figure 1.2: Magnetization density from DFT calculations for two intermetallics, (a) $ZrZn_2$ and (b) MnCoP. (a) $ZrZn_2$ is considered a rare example of a purely itinerant magnet where the magnetism arises entirely from spin-polarization of the metallic conductive electrons. (b) Nearly all other magnetic intermetallics, on the other hand, have substantial local character to the magnetic moments, as shown for the material MnCoP. Calculations are from Ref. 18.

However, the vast majority of metallic ferromagnetics, and particularly intermetallics, lie somewhere in between the pictures of localized and itinerant magnetism. In these cases, the moments behave as a combination of local moment and itinerant. This point is illustrated in Figure 1.2, which shows the magnetization density for two intermetallics, $ZrZn_2$ and MnCoP. $ZrZn_2$ is a rare example of a material that shows ferromagnetism that is truly itinerant: the magnetism arises from spin-polarization of the conduction electron bands. On the other hand, most intermetallics have magneti-

zation densities that look like that of MnCoP, with substantial local character despite the fact that the material is a good metal and has dispersive electrons. There are a number of strategies to handle such systems: in many cases, the itinerant or localized models may function reasonably well in systems that are close enough to one or the other end of the spectrum. For example, the Stoner criterion for magnetism appears to work quite well for many materials, including the elemental magnets Fe, Co, and Ni and other materials with substantially local moment character. On the other hand, it is well established that Mn often behaves as a highly-localized moment even when it is in a strongly metallic compound, [19, 20] and therefore local pictures such as the Curie-Weiss and Heisenberg models are frequently employed (perhaps with enhanced coupling of those moments *via* itinerant electrons [21]). Alternately, empirical models and observations, such as the Slater-Bethe curve [22–24] and the Rhodes-Wolfarth ratio, [25] or models that mix itinerant and localized moments [26] can also be used. In general, a single theoretical framework that captures the magnetic interactions of every magnetic intermetallic well does not exist. Furthermore, as discussed above, the most interesting materials show strong coupling between the magnetism, crystal structure, and electronic structures, further complicating the situation.

Another reason that intermetallic magnets remain an exciting and active research area is that the development of new experimental and theoretical techniques have frequently resulted in the discovery of new and unexpected magnetic phenomena in materials that were previously believed to be well-understood. For example, the development of magnetic neutron diffraction experiments [27] led to the discovery that the original "ferromagnet" Fe_3O_4 is actually not a true ferromagnet, but rather a ferrimagnet with two different types iron moments pointing in opposite directions. The opposing moments have different magnitudes, resulting in a net magnetization. In a

similar vein, we recently reported a study of the intermetallic MnPtGa, [28] which has been understood to be a simple ferromagnetic. When investigated with high-resolution neutron diffraction, we found that this compound actually shows a complex and beautiful series of magnetic phase transitions including noncollinear and incommensurate magnetic structures.

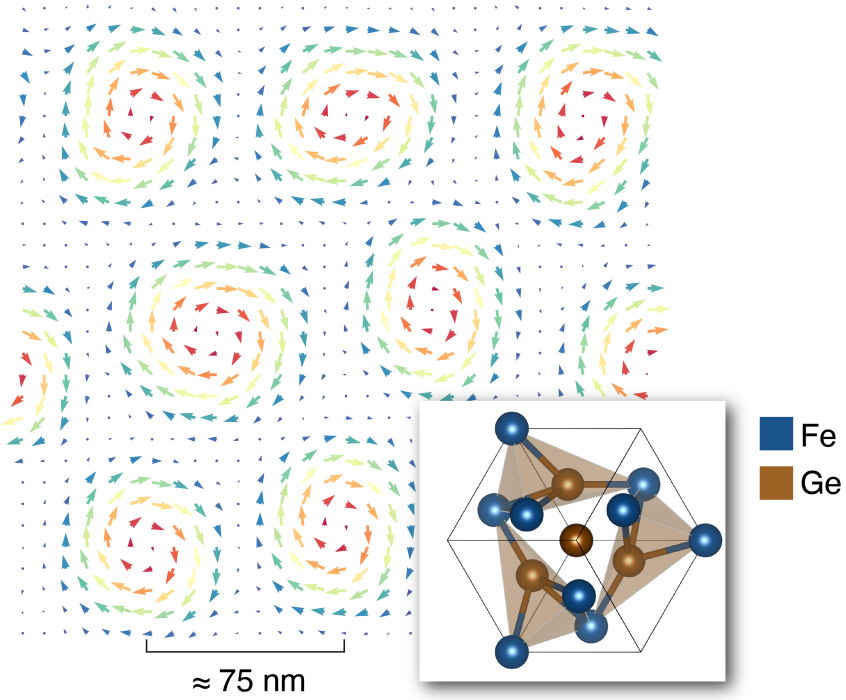

Figure 1.3: FeGe has non-centrosymmetric and non-enatiomorphic crystal structure, which allows antisymmetric Dzaloshinskii-Moriya (DM) interaction to coexist with ferromagnetic (FM) exchange. The result is long-period chiral magnetic structures, such as the hexagonal skyrmion lattice illustrated here. The vector field was generated using a classical Monte Carlo simulation of a Heisenberg magnet with DMI and FM exchanges and represents one slice of a lattice of 1-D Bloch-type skyrmions.

As another example, the development of symmetry analysis theory of noncentrosymmetric magnets by Dzyaloshinskii and Moriya concluded that chiral magnetic interactions could co-exist with ferromagnetic interactions in materials with chiral space groups. [29, 30] This led to the re-investigation of the “simple” B20 ferromagnetics

FeGe and MnSi with small angle neutron scattering, [31, 32] and it was discovered that these materials actually hosted long-period incommensurate helical magnetic ground states. [33] Locally, the spins are aligned ferromagnetically, but over the course of hundreds of unit cells, the moment direction gradually rotates to form spirals with wavelengths between about 15 nm and 1 μm. In 2009, following additional theoretical predictions, [34, 35] the situation was discovered to be even more interesting, as topologically-protected chiral vortices known as skyrmions were discovered to form in these compounds at certain temperatures and magnetic fields. [36] Since then, a variety of long-period topological spin textures have been discovered in intermetallic magnets including various vortex [37] and hedgehog-shaped skyrmions, [38] antiskyrmions, [39] merons, [40] and others. In most cases, these spin textures have been discovered in systems that were before thought of as "simple," well-understood magnets.

Therefore, while much progress has been made, the range of magnetic phenomena that can arise out of combinations of different types of magnetic interactions, crystal structures, and electronic correlations in intermetallics is still only just barely explored. In this dissertation, I will attempt to advance the effort to understand the behavior of functional intermetallic magnets through studies linking crystal structure and magnetism of several different materials. These studies fall into two major categories: those related to functionalizing magnetostructural coupling for applications in magnetic refrigeration (Chapters 2, 3, 4, and 5), and those related to understanding the formation of skyrmion lattices in materials with chiral crystal structures (Chapters 6 and 7). The goal of these studies is, broadly, to establish a predictive understanding of magnetic phenomena so that magnetic materials with optimal properties for next-generation technologies can be identified or designed. The research takes the form of

computational and experimental studies, with a focus on the development of methods and the application of those methods to key intermetallic systems.

In the remainder of this introductory chapter, a perspective review on magnetostructural coupling in magnetocaloric materials is presented, summarizing and generalizing the results of Chapters 2, 3, 4, and 5). Chapter 2 presents a simple computational proxy, the magnetic deformation, which is used to rapidly screen ferromagnets to identify potential magnetocalorics. Chapter 3 expands the utility of this proxy by introducing a method to compute magnetic deformation for alloyed systems. These two chapters establish, in a generic way, that magnetostructural coupling controls the strength of the magnetocaloric effect. Chapters 4 and 5 then proceed to use experimental and computational techniques to dive deeply into the magnetocalorics MnAs and MnB, respectively, in order to understand the specific ways in which magnetism and structure couple in real materials. Other detailed studies of individual materials from the computational search may be found in Refs. 28, 41–43.

The dissertation then pivots away from discussions of magnetocaloric materials to two chapters which focus on understanding magnetic skyrmion host materials. Chapter 6 shows how magnetic entropy measurements can serve as a robust and quantitative method of mapping out subtle magnetic phase diagrams in skyrmion host materials. This approach is used to resolve the phase diagram of the near-room-temperature skyrmion host FeGe. For other applications of this method, see refs 44, 45. Chapter 7 then uses this technique, along with neutron diffraction, density functional theory, and additional magnetic measurements, to understand the magnetic behavior of the $Co_xZn_yMn_z$ family of high-temperature skyrmion hosts. An unusual two-sublattice magnetic structure consisting of co-existing ordered and disordered magnetism is found, which can explain some of the remarkable skyrmionic properties of

this class of materials. Finally, I conclude in Chapter 8 with remarks about possible future research directions that would use the understanding established in this dissertation to control and manipulate intermetallic magnetism in new ways.

1.2 Magnetostructural coupling in magnetocalorics: A perspective review

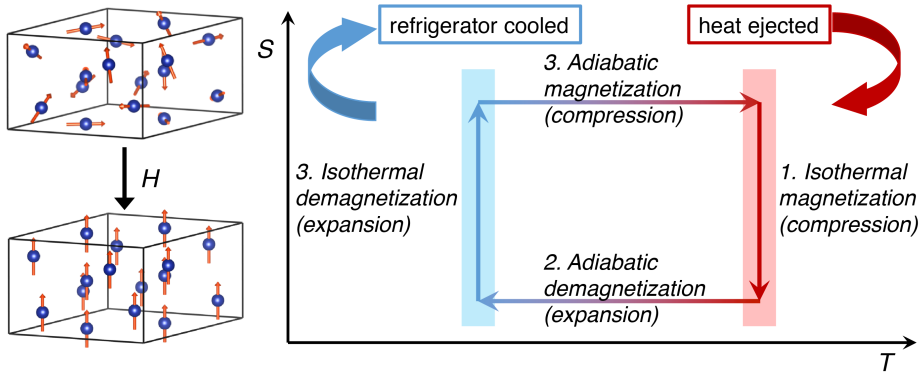

Figure 1.4: The magnetic refrigeration Carnot cycle shown on a temperature-entropy (T-S) axis. For each step of the cycle, the analogous step in the vapor compression cycle is shown in parenthesis.

When a magnetic field is quickly applied to a ferromagnetic or paramagnetic material, the temperature rises. When the field is removed, the material cools. The effect—known as the magnetocaloric effect—is due to the decrease in entropy that occurs when randomized spins align in response to an external field. If the external field is applied adiabatically (*i.e.* quickly, so that heat does not have time to leak away), the crystal lattice entropy has to increase to compensate the decreased magnetic entropy, and a temperature rise is observed. If, on the other hand, the field application is performed isothermally, the magnetocaloric material will eject heat as the overall entropy of the

material decreases. When the material is subsequently demagnetized, the opposite effect is observed. By alternating adiabatic and isothermal magnetization and demagnetization steps (Figure 1.4), one can use the magnetocaloric effect to drive a thermodynamic heat pump in direct analogy to the conventional vapor-compression heat pumps that currently are used to cool conditioners, refrigerators, freezers, air source heat pumps and gas liquifiers. This concept was first used in 1933 with paramagnetic gadolinium sulfate at cryogenic temperatures in order to achieve temperatures below 1 K. [46] Since then, low-temperature "adiabatic demagnetization" devices have become commonplace in laboratories. In 1976, Brown demonstrated that efficient magnetic refrigeration was also possible around room temperature by using ferromagnetic gadolinium metal as the active material, [47, 48] an advance which opened the door to the development of magnetic refrigerators and air conditioners for practical use outside of the laboratory. Such magnetic heat pumps can operate with high coefficients of performance and do not require the use of cloroflourocarbons, hydroflourocarbons, or any of the other harmful refrigerant gases that vapor-compression refrigeration relies on. The development of magnetic refrigeration technology is particularly timely now, given large projected increases in demand for refrigeration and air conditioning in the developing world during this century. [49] So far, developments in magnetocaloric materials and in magnetic refrigerator engineering over the past several years have led to the first prototype systems, and several companies are promising a new generation of energy-efficient refrigerators and air conditioners in the near future. [50–52]

Here, I review the magnetocaloric effect and its applications in magnetic refrigeration and thermomagnetic power generation. Principally, the importance of magnetostructural coupling in good magnetocalorics is established. This magnetostructural coupling is discussed in the context of the phenomenological model of Bean and Rod-

bell, and an interpretation of how magnetostructural coupling plays into the model is given, using the example of the material MnAs. It is shown that *competition* between magnetic and bonding considerations is the origin for the *coupling* between magnetism and structure. This concept can also be used to understand the magnetostructural coupling in other high-performing magnetocalorics, and can be used as a tool to discover and design new multifunctional materials with desirable caloric properties.

1.2.1 The case for magnetic refrigeration

Refrigeration was first commercialized in the late 1800s using a refrigeration cycle known as vapor compression refrigeration, which is still used in nearly all refrigerators, freezers, air conditioners and heat pumps today. In this process, a refrigerant gas is alternately compressed (releasing heat) and decompressed (absorbing heat) in isothermal and isobaric processes to drive a thermodynamic cycle and pump heat from the inside of a refrigerator or building to the outside. The first refrigerants used were simple gases like NH_3, SO_2, and CH_3Cl These performed well—however, they are highly toxic and therefore quite dangerous as vapor compression devices sometimes leak. In the 1920s, a new class of refrigerants called chloroflorocarbons (CFCs, *e.g.* R-12 CF_2Cl_2) was introduced. CFCs are nontoxic and nonflammable, and their adoption led to an incredible popularization of domestic refrigeration around the world. Unfortunately, it was discovered around 1976 [53] that CFCs such as freon-12 are highly ozone-depleting and that use of these refrigerants was contributing to the formation of a hole in Earth's ozone layer. In response to this discovery, the Montreal Protocol on Substances that Deplete the Ozone Layer [54] was internationally ratified in 1987 to phase-out CFC use in refrigeration and other industries. The Montreal Protocol became a remarkable example of international cooperation for the protection of

the environment, with the result that CFCs were effectively phased out of refrigerators and other products by 2010, and the ozone layer is currently recovering. [55] In most cases, the phased-out CFCs were replaced by hydroflourocarbons (HFCs, *e.g.* HFC-134a CF_3CH_2F), which are non-ozone depleting and also safe. However, it was thereafter discovered that HFCs (as well as CFCs) show extraordinarily high global warming potentials 1000 to 7000 times that of CO_2, contributing significantly to global climate change. [56] The Kigali Amendment to the Montreal protocol [57] passed in 2016 phases out these HFCs by 2047 in favor of gases like HFO-1234yf, NH_3, or flammable gases like isobutane. In the meantime, safely managing existing and future HFC-laden devices as they reach their end-of-life is among the most important climate change challenges facing humanity. [58]

In response to currently known environmental concerns, alternative gas refrigerants are being developed [59] and improved vapor compressor designs may help to limit the amount of refrigerant gases released into the atmosphere over the lifetime of new devices. At the same time, the history of vapor refrigeration should motivate us to consider alternative cooling technologies that may be inherently safer and more environmentally friendly than vapor compression. This is especially timely now, as climate change and development of warm countries like China and India are expected to lead to a massive increase in demand for refrigeration and air conditioning over the next century. [49] The leading candidates for such a replacement are solid-state based “caloric” technologies, including those based on magnetocalorics as well as electrocalorics, elastocalorics, and barocalorics. [50] The latter three classes of materials function in much the same way as magnetocalorics, except that they change temperature in response to electric field, strain, and pressure, respectively. Among caloric technologies, magnetocalorics are currently the most promising for large-scale usage

in refrigerators and air-conditioners due to the relative maturity of the field and the high efficiencies and capacities achievable. Magnetocaloric refrigerators require no refrigerant fluids except a benign heat transfer agent such as water or antifreeze, and operate without high-pressure, risk of fire, or toxic gases. Furthermore, several theoretical and experimental studies have suggested that magnetic refrigeration is inherently more energy-efficient than traditional vapor compression refrigeration. [12, 47, 60] At present, however, prototype magnetic refrigerators have struggled to obtain the cooling power, temperature spans, or wall-plug efficiencies of the best vapor compression refrigerators. [61, 62] The problem is that vapor compression refrigeration has behind it well over 100 years of engineering effort by multi-national corporations, governments, and academic labs. Magnetic refrigeration, on the other hand, has a much shorter history and a comparatively modest amount of financial and resource investment to date. Nevertheless, the results so far are promising, and given the inherent advantages of magnetic refrigeration and the growing international academic and industrial interest in magnetic refrigeration, there is cause for optimism.

1.2.2 Development of magnetocaloric materials

The first metrics considered to characterize the performance of a given magnetocaloric material are the height and width of the Carnot cycle rectangle that is depicted in Figure 1.4. The width of the box represents the adiabatic temperature change upon magnetization ΔT_{ad}, while the height of the box represents the isothermal magnetic entropy change ΔS_M. ΔS_M controls the amount of heat that can be pumped in one cycle of the refrigerator, while ΔT_{ad} controls the rate at which the refrigerator may be cycled. Both of these metrics depend strongly on the temperature at which the magnetization or demagnetization is performed, as well as the magnetic field that is applied.

For a ferromagnetic material, the maximum magnetocaloric effect is observed near the Curie temperature, where the system is on the verge of magnetic order. In this regime, an external magnetic field is able to have the largest effect polarizing randomized magnetic moments. For this reason, gadolinium metal, which is ferromagnetic with large $S = 7/2$ moments and a Curie temperature of 293 K is a natural candidate for cooling near room temperature. [47]

In Brown's 1976 device, magnetic fields of 5 T were applied using cryogenic superconducting magnets. Under these conditions, gadolinium exhibits a peak ΔS_M of about –8 J kg^{-1} K^{-1} and ΔT_{ad} of about 7 K. In a real magnetic refrigerator, the magnetic field will have to originate from a permanent magnet and therefore will be limited to fields of about 1 to 2 T. Thus, a good magnetocaloric material is one that can show large entropy and temperature changes upon application of a modest magnetic field in the correct temperature range for the given application. This temperature range of interest varies from around room temperature for refrigerators and air conditioners down to 20 K for hydrogen liquefaction. While the first material to be investigated for magnetic refrigeration near room temperature was gadolinium, which has a conventional second-order magnetic transition, it was discovered in the last decade of the 20th century that much larger effects could be achieved in materials exhibiting first-order coupled magnetostructural transitions. The first example of this was the giant (inverse) magnetocaloric effect observed in FeRh. Upon heating FeRh above 375 K, the material abruptly transforms from an antiferromagnet to a ferromagnet while simultaneously increasing its unit cell volume by 1%. Application of a magnetic field stabilizes the ferromagnetic phase relative to the antiferromagnetic phase, and therefore application of a magnetic field just below the transition temperature can cause the material to go through a magnetostructural phase transition. The result is a "giant" magnetocaloric

effect that is at least two times stronger than the effect seen at gadolinium's conventional second-order Curie transition (for an applied field of just 2 T, FeRh shows a peak $\Delta S_M = 20\,\mathrm{J\,kg^{-1}\,K^{-1}}$ and peak $\Delta T_{\mathrm{ad}} = 13$). [63]

Unfortunately, due to the large hysteresis associated with the first-order magnetostructural transition in FeRh, the observed effect is irreversible and can only be realized on the first magnetization of a sample. Therefore, using FeRh in a practical device is a challenge. However, in 1997 a reversible giant magnetocaloric effect with lower hysteresis was reported in $Gd_5Si_2Ge_2$ at 276 K, where the material exhibits a first-order magnetic transition between an orthorhombic ferromagnetic state and a monoclinic paramagnetic structure. This transition was reported to give peak $\Delta S_M = -17\,\mathrm{J\,kg^{-1}K^{-1}}$ and $\Delta T_{\mathrm{ad}} = 15$ K for an applied field of 5 T. This discovery led to an explosion of interest in practical application of magnetocaloric cooling at the turn of the millennium. Reversible giant magnetocaloric effects were reported in several more families of materials with first-order magnetostructural transitions, including several other rare-earth-based materials as well as systems containing only earth-abundant transition metal and main group elements, such as $(Mn,Fe)_2(P,Si,Ge,As)$, [64–67] $La(Fe,Si)_{13}H_x$, [68, 69] MnAs, [70, 71] and $MnNi_2X$ Heusler ferromagnetic shape memory alloys, [72, 73] among others. [12]

The specific details of the magnetic transitions vary in each of these families of giant magnetocaloric effect materials, although all of them involve transitions between ferromagnetic states and lower moment states (such as paramagnetic or antiferromagnetic) accompanied by a discontinuous change in crystal symmetry or lattice parameter. While this type of first-order transition leads to large caloric effects, it also comes with downsides. Thermal and magnetic hysteresis amount to losses, and kinetic limitations during cycling. As a result, the reversible ΔS_M and ΔT_{ad} of a first-order material are

generally significantly lower than the values observed on first cycling. [73–75] In addition, volume changes during cycling lead to mechanical degradation of the active material and introduce engineering challenges. Therefore, one research focus for the field of magnetic refrigeration is to come up with chemical or engineering strategies to mitigate the downsides of first-order magnetostructural transitions. [74–77] On the other hand, another approach is to search for materials that, like gadolinium, show continuous transitions that nevertheless exhibit substantial magnetocaloric effects. [42, 78–81] As there are many proposed applications for magnetic refrigeration, each operating under different conditions and at different temperatures, a variety of magnetocaloric materials are needed, and the discovery and optimization of new magnetocalorics will help to advance this technology towards practical application.

1.2.3 Magnetostructural coupling controls the magnetocaloric effect

The materials showing the largest magnetocaloric effects are those with strong magnetostructural coupling. This is most clearly illustrated in the "giant" magnetocaloric effect materials discussed in the previous section, which show extraordinary magnetic entropy changes at first-order coupled magnetostructural transitions. In a narrow temperature region near this type of transition, two magnetostructural states are balanced in energy such that the application of a moderate magnetic field can change the energy balance and drive the system from one state to the other. While this behavior has been well-established over the past 20 years, [82] the role of such coupling in magnetocalorics with continuous transitions is comparatively underappreciated.

Indeed, when searching for new magnetocalorics with continuous transitions, the

most common approach has been to simply search for ferromagnets with maximal saturation magnetization and a suitable transition temperature [79, 83, 84]. However, experimental, computational, and theoretical work confirms that the strength of magnetostructural coupling controls magnetocaloric performance, regardless of the order of the phase transition.

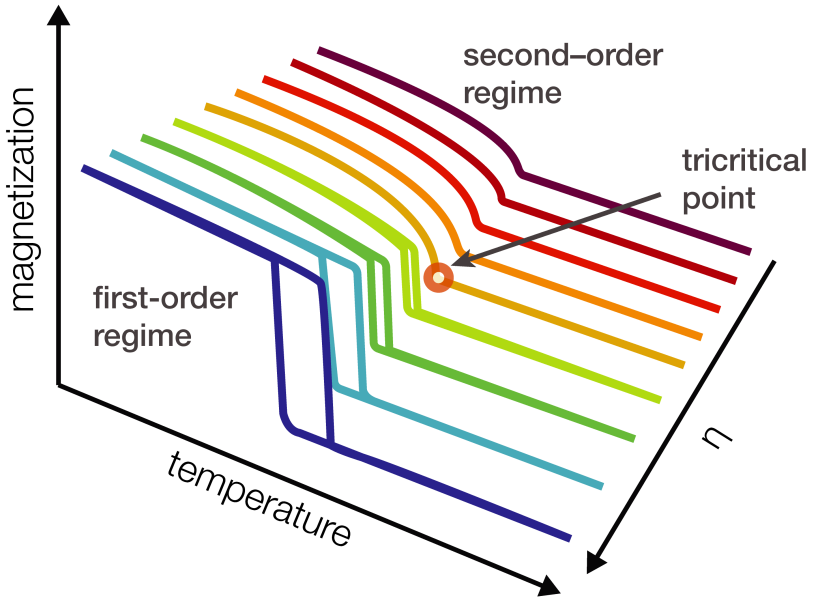

Figure 1.5: The behavior of a magnetic transition as a function of magnetostructural interaction strength, here labelled η after the parameter from the Bean and Rodbell model. For weak magnetostructural coupling, the system shows a conventional second-order phase transition. For strong coupling, the system shows a first-order magnetostructural phase transition. At some intermediate point, a tricritical point exists.

One clear way to make this point is to consider systems where chemical substitutions allow one to tune between first-order magnetostructural transitions and conventional second-order magnetic transitions, such as in $Mn_xFe_{1.25-x}P_{0.5}Si_{0.5}$ [85] or $LaFe_{13-x}Si_x$ [86]. In these systems, the compositional variable x can be used to control the strength of the magnetostructural coupling. Figure 1.5 shows schematically the basic behavior of such a system: when magnetostructural coupling is strong, a

strongly first-order transition is observed with a large $|\Delta S_M|$, latent heat, and thermal hysteresis. As magnetostructural coupling strength decreases, the material becomes more weakly first-order and shows a reduced $|\Delta S_M|$. At the "tricritical point," magnetostructural coupling strength decreases enough that the transition loses its first-order character and becomes continuous. In each case, it is experimentally observed that the ΔS_M continuously decreases through the tricritical point, and continues to decrease when magnetostructural coupling is weakened, even within the continuous second-order regime. These investigations demonstrate that compositions close to the tricritical point show hysteresis-free continuous transitions that nevertheless have enhanced magnetocaloric effects and are therefore very attractive candidates for practical application in magnetic refrigeration devices. For example, in $Mn_xFe_{1.95-x}P_{0.5}Si_{0.5}$, the $x = 1.4$ case shows a second-order phase transition with a gravimetric $-\Delta S_M$ that is about twice as high as that seen in gadolinium, despite the fact that the gravimetric saturation magnetization is only about half that of gadolinium. [85]

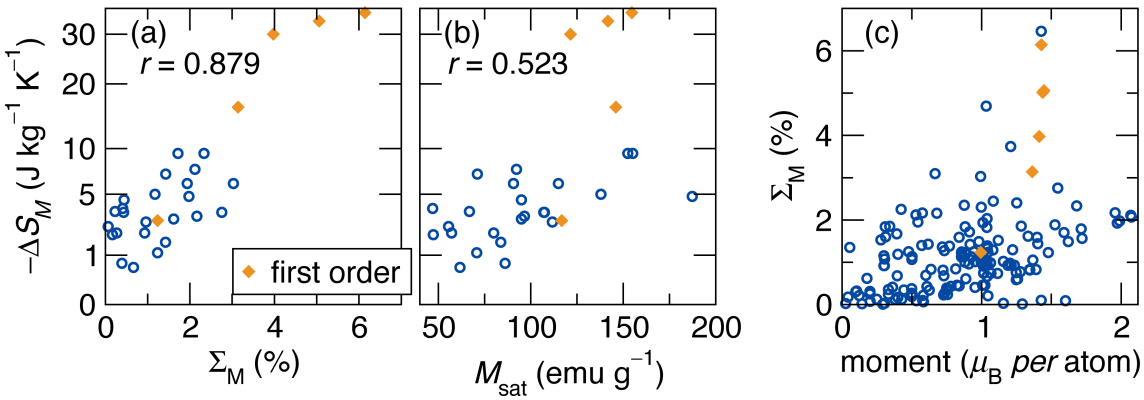

Figure 1.6: Comparison of calculated properties (a) magnetic deformation Σ_M and (b) saturation magnetization with experimental magnetocaloric effect. Pearson's r factor is indicated for each: Σ_M, which is a proxy for magnetostructural coupling, shows a much stronger correlation. The relationship between Σ_M and magnetic moment is shown in (c).

Inspired by the idea that magnetostructural coupling can drive magnetocaloric ef-

fects, Chapter 2 (ref. 18) presents a high-throughput computational study of magnetic compounds aimed at identifying materials with strong magnetostructural coupling for further study as magnetocalorics. We introduce the magnetic deformation Σ_M, a simple DFT-based proxy for magnetostructural coupling. In order to obtain Σ_M, both non-spin-polarized and spin-polarized DFT structural optimizations for a given compound are performed, and the degree of lattice deformation [87] between the two optimized unit cells is calculated. For compounds where the introduction of spin-polarization into the DFT calculation causes a large change in unit cell volume or shape, Σ_M is large and magnetostructural coupling is surmised to be strong. A Σ_M of 0%, on the other hand, indicates that the magnetism does not affect the crystal structure at all. This proxy was calculated for a survey of literature-reported magnetocaloric materials, and was found to correlate very well with experimental ΔS_M, both in materials with and materials without first-order magnetostructural transitions (Figure 1.6(a)). On the other hand, calculated magnetic moment shows a much poorer correlation (Figure 1.6b), and therefore saturation magnetization should not be considered as good a screening parameter as Σ_M. The relation between magnetic moment and Σ_M can be seen in Figure 1.6(c), which shows that a large magnetic moment does not guarantee a large Σ_M, altough there does appear to be a general trend where the maximum possible Σ_M scales with magnetic moment size. In Chapter 2, the calculation of Σ_M is limited to compounds with relatively simple "DFT-friendly" unit cells with no atomic site disorder or alloying. Chapter 3 (ref. 88) introduces methods for the calculation of Σ_M for disordered alloys and solid solutions *via* supercell averaging.

1.2.4 Magnetostructural coupling in the Bean and Rodbell model

The basic phenomenology of how magnetostructural coupling modifies a magnetic transition was largely accomplished already in 1962, with the development of the model of Bean and Rodbell. [89, 90] In this model, Weiss's standard mean-field approach to ferromagnetism is modified to include a volume dependence of the magnetic exchange. The resulting model captures much of the basic magnetic and magnetocaloric behavior outlined above, including the change from second order, to tricritical, to first order magnetic transitions as magnetostructural coupling strength is increased. In this section, a review of the key results of the Bean-Rodbell model is provided.

In order to include magnetostructural coupling in a mean field description of ferromagnetism, Bean and Rodbell introduced a volume dependence of the magnetic exchange, which manifests as a volume-dependent Curie temperature

$$T_C(v) = T_0\left(1 + \beta\frac{v - v_0}{v_0}\right) \tag{1.1}$$

where Curie temperature T_C is a function of unit cell volume v. v_0 and T_0 are volume and Curie temperature absent of magnetostructural coupling, and β is a constant that controls the strength of magnetostructural coupling, defined as $\beta = (\mathrm{d}T/\,\mathrm{d}T_0)(\mathrm{d}V/\,\mathrm{d}V_0)^{-1}$. If β is positive, the magnetic exchange energy will favor an expansion of the unit cell in the magnetically-ordered regime compared to the paramagnetic regime. This change in volume imparts a strain energy on the lattice, which will oppose the change according to the bulk modulus B.

The result of this modification to the Weiss model is that a new term arises in the Weiss molecular field, so that the magnetization σ as a function of temperature T and

applied field H is given by:

$$\sigma(T,H) = B_J\left(\frac{\mu_0 g \mu_B J}{k_B T}H + \frac{3J}{J+1}\frac{T_0}{T}\sigma + \frac{9J(2J^2+2J+1)}{(J+1)^3}T_0 T\eta\sigma^3\right) \tag{1.2}$$

where B_J is the Brillouin function, J is the total angular momentum quantum number, μ_0 is the vacuum permeability, μ_B is the Bohr magneton and k_B is the Boltzmann constant. η is a new parameter defined as:

$$\eta = \frac{\beta^2}{B}\frac{5J(J+1)}{2J^2+2J+1}Nk_B T_0 \tag{1.3}$$

where N is the number density of magnetic moments per unit volume. η turns out to be the key parameter which controls magnetostructural behavior within the Bean and Rodbell: a first-order transition is obtained for $\eta > 1$ and a second-order transition for $\eta < 1$. For $\eta = 1$, a tricritical point is observed, just as discussed in the previous section. For any nonzero value of η, the magnetically ordered phase unit cell volume shows the following behavior:

$$\frac{v - v_0}{v_0} = \frac{3J}{2(J+1)}Nk_B T_0 \frac{\beta}{B}\sigma^2 \tag{1.4}$$

Equation 1.2 can be solved numerically for different temperatures and magnetic fields, and with proper inputted values can often reproduce experimental magnetization data quite well. [91–93] In addition, the magnetocaloric effect can be calculated as a function of η by considering the changes in entropy of the magnetic moments [94]. The result is that the expected entropy increases as η increases, both in the first-order and second-order regime, just as expected from experiments. Importantly, this result is obtained even without any consideration of structural phonon entropy, highlighting

the fact that magnetostructural coupling can drive giant changes in magnetic moment entropy, even without any contribution from structural entropy.

Although the Bean and Rodbell model does not consider the microscopic interactions that drive magnetostructural coupling, the model can be used to gain insight into the giant magnetocaloric effect. We note from equation 1.3, that

$$\eta \propto \frac{\beta}{B} \tag{1.5}$$

which shows that a first-order magnetostructal transition requires a high β (magneto-volume coupling constant) and a low B (Bulk modulus). The latter condition ensures that the lattice is compressible enough to tolerate large changes in structure at the Curie temperature. When De Blois and Rodbell parametrized the model with actual values from MnAs, they arrived at $\beta = 18.9$ and $B = 22$ GPa. [95] Considered on their own, both the β value and B are quite anomalous. Tabulated bulk moduli, [96] in particular, for transition metal-based intermetallics typically range from 80 GPa to over 200 GPa, with the majority being well over 100 GPa and only rare examples of compounds as low as 40 GPa (MnSb, CrTe). Indeed, CoAs and FeAs, which are isostructural to MnAs, show bulk moduli of 123 GPa and 118 GPa, respectively. [97] Clearly, the Bean and Rodbell model's prediction of $B = 22$ GPa for MnAs is highly unexpected.

Remarkably, subsequent experimental measurements of the bulk modulus of MnAs in the paramagnetic regime confirmed the prediction of Bean and Rodbell. [98–100] Furthermore, the pressure-dependence of the Curie temperature can be used in combination with the bulk modulus to confirm the large predicted β value. Therefore, it is germane to ask: how does the extreme compressibility and strong volume-exchange coupling necessary for a first-order magnetostructural transition arise? As has already

been established, it is probably not feasible to seek out these two properties independently, as "normal" mechanisms will not provide β values high enough or B values low enough. In the next section I present a picture of competition between chemical bonding and magnetism, and show how such competition may lead simultaneously to anomalously strong coupling between the magnetism and crystal structure and anomalously high compressibility, satisfying both of the requirements of the Bean and Rodbell model for a first-order transition.

1.2.5 Extensions of the Bean-Rodbell model

Before moving on, it is important to acknowledge some limitations of the Bean-Rodbell model, and discuss which extensions can be made to it to extend its utility. The model is a mean field model, and therefore does not consider the role of local correlations and critical behavior, and therefore fails to address experimental properties such as excitations and short-range order above the Curie temperature. The model also does not consider the role of structural entropy, although a Debye-approximation for the phonon entropy in the free energy term may be added. [101] More complex is the inclusion of interactions between the spins and the phonons, which recent research is showing can play a significant and surprising role in the giant magnetocaloric effect [102]. For the purposes of our discussion of the conditions necessary to establish the strong magnetostructural coupling, however, the Bean and Rodbell model will perform quite well with just two generalizations, which are given below.

Firstly, in the original Bean and Rodbell model, the only moment-lattice interaction present is a volume-dependence of the mean-field magnetic exchange. In 1967, Goodenough and Kafalas pointed out that it is also important to consider the volume-dependence of the local moment *magnitude*. To add this into the Bean and Rodbell

model, one simply needs to note that in Weiss's mean field model T_C is proportional to $W\mu^2$, where W is the effective molecular field due to the exchange constants, and μ is the local magnetic moment. Therefore, if both exchange and magnetic moment have a volume dependence, then β becomes

$$\beta = \frac{\mathrm{d}(T_C/T_0)}{\mathrm{d}(V/V_0)} = V_0 \left(\frac{2}{\mu_0} \frac{\mathrm{d}\mu}{\mathrm{d}V} + \frac{1}{W_0} \frac{\mathrm{d}W}{\mathrm{d}V} \right) \tag{1.6}$$

Therefore, β may arise by a volume-dependence of the magnetic exchange, a volume-dependence of the magnetic moment magnitude, or a combination of both. In whichever case, strong magnetostructural coupling requires a large value for β.

The other important modification I consider here concerns the fact that structural changes arising from magnetic ordering are often not isotropic volume changes, as assumed by Bean and Rodbell. In fact, MnAs actually changes structure type through its first-order magnetsotructural transition from hexagonal at low temperature to orthorhombic at higher temperature. Although there is a volume change of about 2.5% accompanying this transition, the more physically-relevant parameter of this phase transition is the displacement of the Mn atoms from their hexagonal lattice. An alternative example is found in MnFe(P,Si), [65] which adopts the hexagonal Fe_2P structure both above and below T_C. In this material, the first-order transition involves discontinuous changes of opposite sign in the hexagonal a and c directions, so that the cell changes shape substantially with almost no change in volume. Therefore, the c/a ratio serves as the physically-relevant mode of the magnetostructural transition, instead of the unit cell volume. In either of these cases, the same phenomenology as the Bean and Rodbell model can be applied, replacing the volume-dependent magnetic interactions with a dependence on the relevant structural mode. The bulk modulus, in this case, must be replaced by the material's elastic constant with respect to the relevant struc-

tural mode. In other words, in order to show magnetostructural coupling, a structure must be "soft" with respect to some structural distortion mode and also have magnetic properties that are strongly dependent on that structural distortion mode.

1.2.6 Competition between magnetism and structure leads to magnetostructural coupling

In order to illustrate how *competition* between magnetism and structure can lead to *coupling* between magnetism and structure, I here consider the case of MnAs, the material which Bean and Rodbell originally designed their model to address. MnAs is a canonical example of a material exhibiting dramatic magnetostructural coupling. At 318 K, it exhibits a strongly first-order transition between a hexagonal ferromagnetic state at low temperature and a paramagnetic orthorhombic state at high temperature. This transition may be manipulated with temperature, pressure, strain, and magnetic field, and carries with it a giant magnetocaloric effect. [70] As a result of its wealth of multifunctional properties and simple crystal structure, MnAs has been studied extensively for the past century and has been the basis for the development of several important magnetic theories. Despite this long history, a satisfactory microscopic picture of the mechanism for magnetostructural coupling has been elusive as conflicting ideas about the nature of the magnetic phases persist.

Chapter 4 reports a density functional theory investigation of the ordered and disordered magnetic states in MnAs, which demonstrates how competition between chemical bonding and magnetic exchange works to establish magnetostructural coupling. Here, I describe how this competition simultaneously satisfies the two criteria for a first-order transition in the Bean and Rodbell model: a large dependence of magnetism

on structure (high β) and a high compressibility (low B). This competition-based mechanism has important implications for the behavior of MnAs and other strongly magnetostructurally-coupled materials. One particullarly interesting result is a prediction that the paramagnetic state of MnAs will locally exhibit large atomic displacements accompanied by the dynamic forming and breaking of bonds on the timescale of the spin fluctuations.

As discussed previously, the structure change in MnAs involves a change of symmetry. Below 318 K, MnAs adopts the hexagonal Ni_2In structure, while above 318 K it adopts the MnP structure (space group $Pnma$), which is a distortion from Ni_2In. This phase transition carries with it a 2.5% change in volume, but the primary driver of the transformation is the movement of Mn atoms off of their hexagonal lattice positions to form zigzag chains of shorter Mn-Mn contacts. Here, the magnitude of this Mn displacement in fractional units of the lattice parameter is referred to as δ_{Mn}.

The concept of magnetism-structure competition for MnAs is illustrated in Figure 1.7. At the top, a hypothetical nonmagnetic hexagonal form of MnAs with no magnetic moments is shown. This state is of high structural symmetry (because it is hexagonal) and of high magnetic symmetry (because there is no distinction between spin up and down), but it is never observed experimentally because of its high energy. As is the common paradigm in solid state materials, a high-energy state may often reduce its energy by undergoing a distortion that lowers the energy of occupied states at the expense of raising the energy of unoccupied states. It turns out in MnAs that two different types of distortion are energetically feasible. The left path shows an electronic distortion whereby the electronic structure spin-polarizes into an ordered ferromagnetic state within the hexagonal structure. The spin-polarization of the electronic structure into a filled majority spin channel and an empty minority spin channel gives

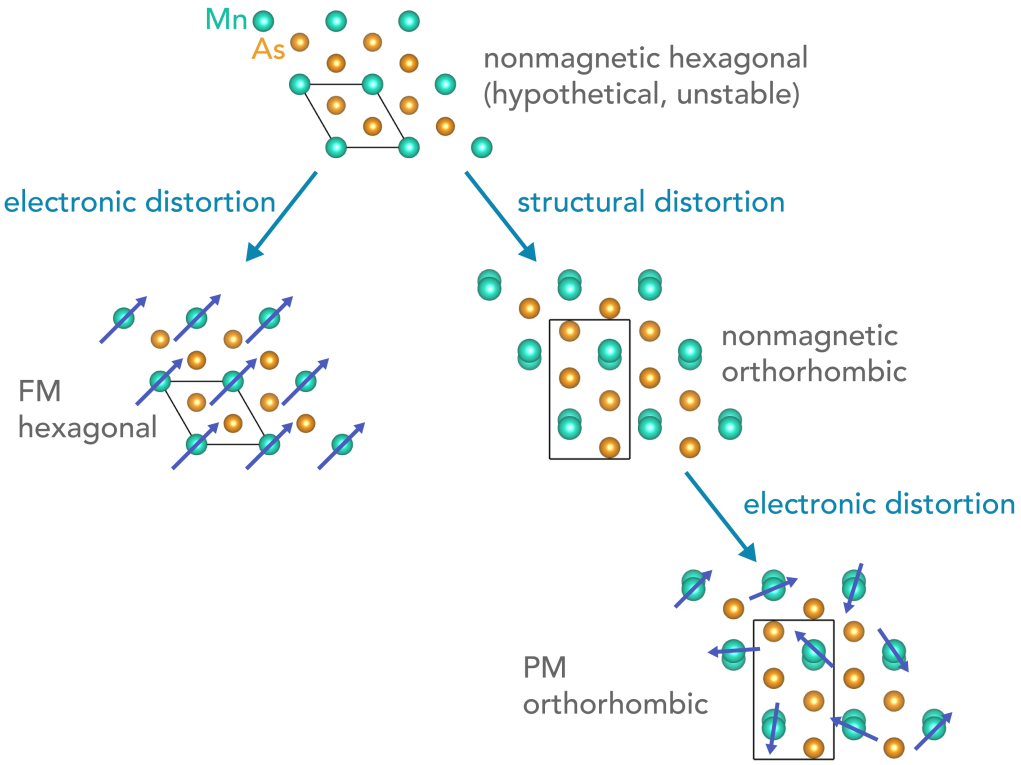

Figure 1.7: There are two mutually incompatible paths to stabilize MnAs, and the system must choose one path or the other at any given temperature.

a large Stoner-type energy reduction compared to the nonmagnetic state. In addition, strong ferromagnetic exchange between the co-aligned Mn moments further stabilizes this structure.

The right path shows a structural distortion into the MnP structure type, which better optimizes filled bonding orbitals than the hexagonal structure and therefore lowers the energy. Importantly, this orthorhombic structure brings in-plane Mn atoms close enough together that their d orbitals overlap. This is beneficial from the standpoint of bonding as it allows for the formation of a metal-metal bond, but it also precludes the possibility of ferromagnetism in the overlapping orbitals according to the Pauli exclusion principle. This is because two electrons with the same spin cannot occupy the

same bonding orbital. The orthorhombic structure can spin-polarize to further reduce its energy, but the resulting magnetic state does not share the strong in-plane magnetic exchange that the hexagonal structure features, and therefore the "right" path does not benefit from as much magnetic stabilization as the "left" path. In Figure 1.7, the magnetic state in the "right" path is shown as paramagnetic to emphasize that the orthorhombic structure has weaker magnetic exchange and therefore has a lower Curie temperature than the hexagonal structure.

As can be seen in this simple illustration, MnAs inherently shows competition between magnetism and structure. There are two possible paths to stabilization, but they are mutually exclusive. The system cannot simultaneously take advantage of the ferromagnetic electronic state and the orthorhombic nuclear structure, but must choose one or the other. It turns out that at 0 K the left path is energetically preferable, and this is the ground state observed in experiment and with DFT calculations. However, as the temperature is increased, magnetic fluctuations begin to set in, weakening the exchange stabilization of the ferromagnetic structure. At the same time, the fully disordered magnetic structure on the right path drops in free energy due to the entropy contribution. At some point, the right branch becomes lower in energy than the left branch, and the system discontinuously jumps branches through a dramatic first-order magnetostructural transition. Because the energies of the two phases will depend on temperature, magnetic field, and physical stress, this transition may be actuated with a variety of stimuli [71]. In this way, the competing structural and magnetic conditions lead to a remarkable, highly-functional coupling between the magnetism and the crystal structure.

In order to connect this picture back to the Bean-Rodbell model, Figure 1.8 schematically shows the free energy surfaces for the two magnetostructural states of MnAs. For

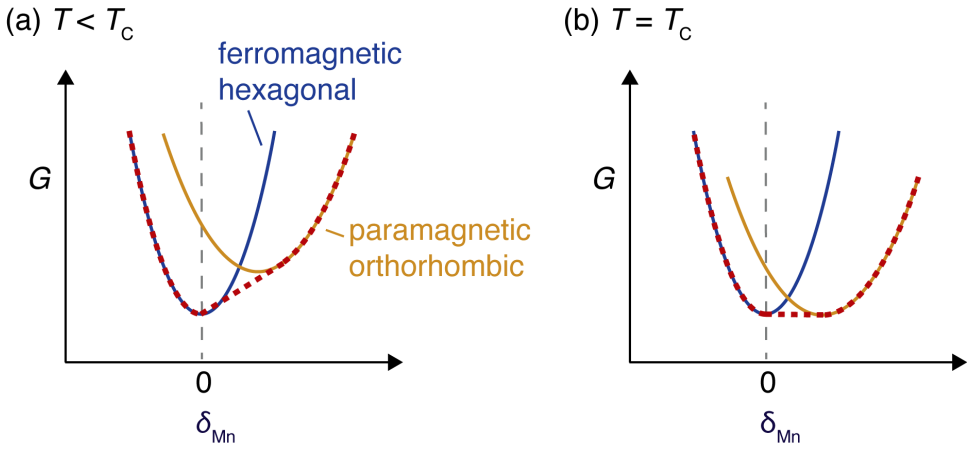

Figure 1.8: Schematic energy surfaces for ferromagnetic and paramagnetic MnAs at two different temperatures. The overall energy surface felt by the system is represented by the red dotted line. Around $T = T_C$, the system will show a very high effective compressibility.

both the hexagonal and orthorhombic structure, the energy as a function of δ_{Mn} is shown, with the hexagonal structure's curve centered at $\delta_{\mathrm{Mn}} = 0$, and the orthorhombic structure at a finite value of δ_{Mn}. Each of these phases has an elastic constant with respect to δ_{Mn}, which controls the steepness of the parabolic energy surface. At low temperature, the ferromagnetic hexagonal state is lower in energy than the orthorhombic state. As temperature is increased, however, the orthorhombic structure's free energy curve drops with respect to the hexagonal structure's curve, eventually becoming the more stable state for $T > T_C$. At the critical temperature T_C, the energy minima of the two curves equalize, as drawn in the right panel. At this temperature, the effective energy surface experienced by this system is represented by the tie line (red dotted line) between the two curves. The result of this tie line is that the system experiences a broad, flat energy surface around the transition temperature. This energy surface explains the anomalously high compressibility observed in MnAs, even though both the hexagonal and orthorhombic states on their own would likely not be compressible enough. Therefore, we can see that the compressibility requirement may be fulfilled

if a system has two competing states which differ in some structural coordinate but are close in energy. The farther-separated the two states in the structural coordinate, the more compressible the effective energy surface displayed by the material is. The β requirement can simultaneously be satisfied in this sort of system, as the two states have different strengths of magnetic exchange.

1.2.7 Competition between moment formation and boron-boron bonding in MnB

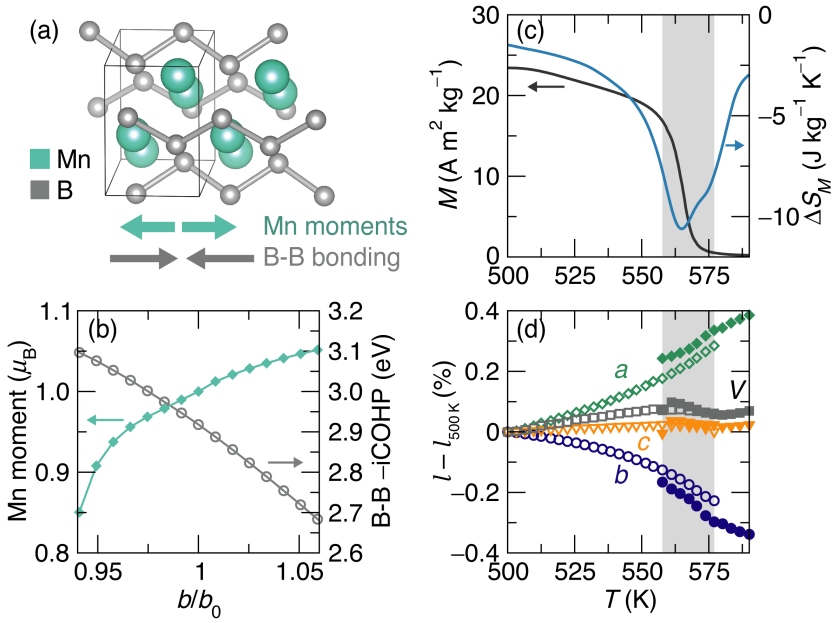

Figure 1.9: Magnetostructural competition in MnB arises as a competition between B-B bonding along the crystallographic b axis and the magnitude of the Mn moment.

Another illustrative example of how magnetostructural coupling controls the magnetocaloric effect is found in MnB (Chapter 5), an example of a material that does not show a first-order magnetostructural transition but nevertheless shows strong magnetocaloric effect. [81] MnB has a saturation magnetization that is only 60% that of

gadolinium, and yet shows a peak ΔS_M of –10.7 J kg^{-1} K^{-1} for an applied field of 5 T, which is 34% larger than that of gadolinium. In order to understand the behavior of MnB, it is instructive to compare to its isostructural cousin FeB, which has very similar magnetic properties (including a nearly identical T_C), but shows a magnetocaloric effect that is about three times smaller than in MnB.

Synchrotron diffraction through the T_C (Figure 1.9c-d) reveals that, while there is no giant magnetostructural phase transition, large anomalies in the lattice parameters are seen at the phase transition, indicating the presence of notable coupling between magnetism and lattice. FeB, on the other hand, does not show this effect, once again highlighting how magnetostructural coupling is associated with a strong magnetocaloric effect even in the absence of a first-order magnetostructural transition. Furthermore, DFT calculations comparing bond strengths and magnetic moment as a function of b lattice parameter size indicate that, like in MnAs, MnB shows distinct competition between magnetic and structural considerations. The boron-boron bonding interactions would prefer that the b lattice parameter be small, while the magnetic moment size and magnetic stability increase as b increases. Therefore, MnB is always balanced between structural and magnetic stability. As temperature increases and fluctuations set in, the magnetic considerations are weakened and the balance shifts towards structural stability. Therefore, the b lattice parameter decreases sharply, leading to the observed lattice parameter anomalies. In FeB, on the other hand, no such moment-dependence of the b lattice parameter occurs, and as a result almost no magnetostructural coupling is evident in the temperature-evolution of the lattice parameters.

MnB evidently shows a large magnetocaloric effect that is driven by magnetostructural coupling established due to competition between magnetism and bonding. How-

ever, this coupling is not strong enough to drive the system into the first-order regime as in MnAs. Based on these observations, it may be concluded that MnB is most likely quite proximal to the tricritical point illustrated on Figure 1.5, allowing it to show a substantial magnetocaloric effect without thermal hysteresis or irreversibility.

1.2.8 Outlook

Based on a review of magnetocaloric materials, computation, and theory, it may be concluded that magnetostructural coupling is the most significant driving force for strong magnetocaloric effects. Therefore, if one wishes to discover, design, or manipulate magnetocalorics, they should seek to control the strength of magnetostructural coupling. A material with extraordinarily strong magnetostructural coupling may show a giant magnetocaloric effect—but if hysteresis is undesirable then this concept may also be used within the second-order/tricritical regimes to increase magnetocaloric effects without introducing irreversibility. The Bean and Rodbell model shows that the key to strong coupling is to have magnetic interactions that depend on crystal structure (large β), and also to have a very soft lattice (low B) that can accommodate distortions. This perspective review has argued that searching for materials that independently have suitable values of β and B is probably not a viable strategy. However, in systems where magnetism and bonding compete with each other, these two parameters may be simultaneously satisfied. An investigation of magnetostructural coupling in some key materials leads to the conclusion that this is the mechanism that drives the performance of most magnetocaloric materials. This concept of magnetism-bonding competition may be used to interpret, manipulate, and control magnetocalorics.

Chapter 2

A simple computational proxy for screening magnetocaloric compounds

[1] Alternating cycles of isothermal magnetization and adiabatic demagnetization applied to a magnetocaloric material can drive refrigeration in very much the same manner as cycles of gas compression and expansion. The material property of interest in finding candidate magnetocaloric materials is their gravimetric entropy change upon application of a magnetic field under isothermal conditions. There is, however, no general method of screening materials for such an entropy change without actually carrying out the relevant, time- and effort-intensive magnetic measurements. Here we propose a simple computational proxy based on carrying out non-magnetic and magnetic density functional theory calculations on magnetic materials. This proxy, which we refer to as the magnetic deformation Σ_M, is a measure of how much the unit cell deforms when comparing the relaxed structures with and without the inclusion of spin polar-

[1] The contents of this chapter have substantially appeared in reference 18: J. D. Bocarsly, E. E. Levin, C. A. C. Garcia, K. Schwennicke, S. D. Wilson, and R. Seshadri. A simple computational proxy for screening magnetocaloric compounds. *Chem. Mater.* **29** (2017) 1613–1622. doi:10.1021/acs.chemmater.6b04729

ization. Σ_M appears to correlate very well with experimentally measured magnetic entropy change values. The proxy has been tested against 33 known ferromagnetic materials, including nine materials newly measured for this study. It has then been used to screen 134 ferromagnetic materials for which the magnetic entropy has not yet been reported, identifying 30 compounds as being promising for further study. As a demonstration of the effectiveness of our approach, we have prepared one of these compounds and measured its isothermal entropy change. MnCoP, with $T_C = 575\,\mathrm{K}$, shows a maximum $\Delta S_M = -6.0\,\mathrm{J\,kg^{-1}\,K^{-1}}$ for an applied field of $H = 5\,\mathrm{T}$.

In addition, the data collected and calculated for this project is available in interactive format in a website, currently hosted at magnets.mrl.ucsb.edu/.

This project was performed in collaboration with Emily Levin, Christina Garcia, and Kai Schwennicke and was supervised by Ram Seshadri and Stephen Wilson. I would like to thank Dr. Jason Douglas is thanked for providing the sample of $FeRu_2Sn$.

2.1 Introduction

Magnetic refrigeration, based on the magnetocaloric effect (MCE) [46], has been proposed as an energy efficient and environmentally friendly alternative to vapor compression refrigeration.[103] In a typical ferromagnet near its Curie temperature, application of a magnetic field, H, causes randomly oriented spins to align, leading to a decrease in magnetic entropy of the material, as depicted in Figure 1.4. If this magnetization is performed adiabatically, the decrease in magnetic entropy is compensated by a rise in temperature, and *vice-versa* for demagnetization. If the magnetization is performed isothermally, the material will decrease its total entropy and reject heat. By alternating adiabatic and isothermal magnetizations and demagnetizations, one can

use the magnetocaloric effect to drive a thermodynamic cycle in direct analogy to the conventional vapor-compression cycle. With the use of a regenerator, this process can cool with a large coefficient of performance near room temperature [47, 48]. Developments in magnetocaloric materials and in magnetic refrigerator engineering over the past several years have led to the first prototype systems, and several companies are promising a new generation of energy-efficient refrigerators and air conditioners in the near future. [50, 51]

To evaluate a magnetocaloric material, the isothermal entropy change $\Delta S_M(T, H)$ and adiabatic temperature change $\Delta T_{\mathrm{ad}}(T, H)$ are typically the first parameters investigated. These two parameters represent the height and width, respectively, of the Carnot cycle diagram shown in Figure 1.4. For magnetic refrigeration near room temperature, several suitable materials are being studied in detail, including (Mn,Fe)$_2$(P,Si) [66, 104], La(Fe,Si)$_{13}$ and its hydrides [105], and Heusler compounds [72, 73]. These systems are comprised of Earth-abundant, inexpensive elements and combine large ΔS_M and ΔT_{ad}, with low hysteresis, high mechanical and chemical stability, and good thermal properties. Despite great progress within these systems, discovery of new magnetocalorics with desirable properties is still important. As the first generation of magnetocalorics moves towards commercial viability, more and more diverse applications of the magnetocaloric effect are being proposed, including gas liquefaction [51], small-scale solid state cooling [106], and thermomagnetic generators [107]. These applications will each demand materials with different properties, including a range of active temperatures, cycling properties, thermal properties, and magnetic field responses.

Various competing interactions contribute to the magnetocaloric effect, creating challenges in the discovery of new magnetocaloric materials. The first materials investigated for magnetic cooling near room temperature were ferromagnets with standard

second-order paramagnetic to ferromagnetic phase transitions. The most common metric used to search for new materials is the saturation magnetization, M_S: materials with a high density of polarized spins are expected to show larger changes in entropy. For this reason, Gd, which has a saturation magnetization in excess of 250 emu/g and a Curie temperature near room temperature [108], is the prototypical second order material. Indeed, Gd shows a sizeable magnetic entropy change of 6.1 J kg^{-1} K^{-1} and adiabatic temperature change of 6.4 K for an applied field $H = 2$ T. [109] Phenomenological models can be used to describe the entropy change in these materials, but these models are descriptive rather than predictive. [110, 111]

The discovery of a "giant" magnetic entropy change in $Gd_5(Si,Ge)_4$ in 1997 created new opportunities in the search for magnetocalorics. In $Gd_5(Si,Ge)_4$, a first-order coupled magnetic and structural transition leads to a greatly enhanced ΔS_M. [82, 112, 113] After the discovery of this phenomena, several other systems with known first-order magnetostructural transitions were investigated, yielding some of the most promising magnetocaloric materials, including Fe_2P-based and $La(Fe,Si)_{13}$-based materials. In these systems, coupling of the spins and the lattice leads to a system with switchable magnetostructural state, so that a moderate magnetic field can induce a large change in the magnetic entropy of the system. [111, 112, 114]

Inspired by these ideas, we propose here the use of computational screening to aid in discovery of new magnetocalorics. Recently, several high-throughput projects have used density functional theory (DFT) to calculate the total energies and electronic structures of hundreds of thousands of known and hypothetical materials. [115–117] Many physical properties can be easily and reliably calculated with DFT. For more complicated properties such as the magnetocaloric effect, it is advantageous to design a computational "proxy" that correlates well with experimental results. The

strategy of using proxies has been employed in the search for thermoelectrics [118], phosphors[119], and battery materials[120–122]. The screening parameter is, in each case, designed based on physical understanding and is verified against relevant experimental observations before being used to identify materials that merit further experimental or computational study.

Here, we introduce the magnetic deformation Σ_M, a simple DFT-based proxy for screening of new magnetocalorics. The experimental ΔS_M is shown to correlate well with Σ_M across the full range of investigated transition metal-based magnetocalorics. We use Σ_M to screen 134 ferromagnetic materials that have not yet been characterized for magnetocaloric effect, identifying 30 candidates for further experimental study. As a preliminary validation of this strategy, we show magnetocaloric measurements on one of these candidates, MnCoP. MnCoP shows a peak ΔS_M of $-6.0\,\mathrm{J\,kg^{-1}\,K^{-1}}$ for an applied field of $H = 5\,\mathrm{T}$ near its Curie temperature of $T_C = 575\,\mathrm{K}$. This entropy change is much larger than expected for a typical ferromagnet, and MnCoP fits nicely into the trend of ΔS_M *vs.* Σ_M established in this study. In carrying out this investigation, we have aggregated experimental data and performed calculations on more than 160 magnetic materials, which can potentially aid in data-driven approaches for materials screening.

2.2 Methods

2.2.1 Data aggregation

A search of the scientific literature for magnetocaloric materials yielded 24 reported compounds and associated crystal structures, transition temperatures and maximum

isothermal magnetic entropy changes, ΔS_M, for applied fields of 2 T and 5 T. We have restricted this dataset to rare earth-free materials with simple unit cells that display ferromagnetic to paramagnetic transitions. In this case, simple unit cells means unit cells that do not contain atomic site disorder, and are therefore straightforward to model with DFT using periodic boundary conditions. In some instances where the reported unit cells contained atomic site disorder in the form of multiple atoms randomly mixed on a single crystallographic site, an ordered approximation of the unit cell was used. For example, (Mn,Fe)$_2$(P,Si) compounds are well-known to contain some mixing of Mn and Fe atoms and P and Si atoms; [123] however, MnFeP$_{2/3}$Si$_{1/3}$ was still included in the dataset because a reasonable approximate unit cell is generated by assuming all of the the Mn is ordered on the $3g$ site, the Fe on the $3f$ site, the P on the $2c$ site, and the Si on the $1b$ site. Compounds containing rare earth atoms (except Y and La) were not included in this study due to difficulties in accurately modeling f-electrons with DFT.

This dataset naturally contains a bias towards materials with large ΔS_M because poorer performing materials are seldom reported. Consequently, we supplemented the data set with new ΔS_M measurements on nine ferromagnetic materials, including several with low ΔS_M values. These values were obtained from magnetic measurements via the Maxwell relation:

$$\left(\frac{\partial S}{\partial H}\right)_T = \left(\frac{\partial M}{\partial T}\right)_H \tag{2.1}$$

This relation allows for the calculation of isothermal entropy change using:

$$\Delta S_M(H,T) = \int_0^H \left(\frac{\partial M}{\partial T}\right)_{H'} dH' \tag{2.2}$$

The temperature derivatives required by this equation were calculated from smoothed magnetization *vs.* temperature curves collected at different magnetic fields between 0.1 T and 5 T using a Quantum Design DynaCool PPMS equipped with a Vibrating Sample Magnetometer (VSM) with a high-temperature oven option. The measured materials are shown in the latter half of Table 2.1. Ni and Fe_2P were purchased, $FeRu_2Sn$ was prepared as reported in a prior report[124], and all others were prepared for this study. Details of the preparations and full ΔS_M measurements for these materials are provided in the Appendix section 2.5.1. In addition to these 33 materials with known ΔS_M, we aggregated the crystal structures and Curie temperatures of 134 transition metal-based ferromagnets with known Curie temperatures (Table 2.2, Appendix Table 2.3) that have not yet been studied for magnetocaloric performance.

One of the materials we prepared and measured, MnCoP, was chosen because it was predicted to show a strong magnetocaloric effect based on the analysis performed in the present study. The details of the preparation may be found in the Appendix section 2.5.2, along with a synchrotron X-ray diffraction structural characterization of the sample. The diffraction pattern was taken on the High Resolution Powder Diffraction beamline (11-BM) at the Advanced Photon Source, Argonne National Laboratory and was analyzed by Rietveld refinement using the software packages GSAS [125] and EXPGUI [126]. The crystal structure of MnCoP was drawn using the program VESTA. [127]

2.2.2 Density functional theory calculations

For the materials studied, optimized structures were obtained using density functional theory (DFT) with and without spin-polarization, corresponding to a collinear ferromagnetic state and a nonmagnetic state, respectively. These calculations were per-

formed using the *Vienna ab initio simulation package* (VASP) [128] using projector augmented wave (PAW) psuedopotentials [129, 130] within the Perdew-Burke-Ernzerhor (PBE) generalized gradient approximation (GGA) [131]. Spin-orbit coupling was not included. The Python packages `pymatgen` and `custodian` were used to build a Python framework to automate, manage, and analyze the VASP calculations. [132] For each material, the crystal structure was obtained from the literature and reduced to the primitive cell. In cases where the reported crystal structure contained partial atomic site disorder, an ordered approximation of the unit cell was used. k-point meshes with a density of 2000 points per Å^{-3} were used for all calculations. In the structural relaxations, the lowest energy unit cell shape was found using the conjugate-gradient algorithm, allowing ion positions to move within the cell and allowing the cell to deform and change volume. The relaxations were run iteratively until the volume change between subsequent relaxations was less than 2%. After each structure was fully converged, a final electronic optimization was performed while keeping the structure fixed. For each material, the first ferromagnetic structural relaxations were instantiated with magnetic moments of 3.0 μ_B on each transition metal ion. For all calculations, `custodian`[132] was used to automatically monitor jobs and resubmit those that failed due to common errors. From these calculations, various structural, energetic, and magnetic parameters were aggregated. The magnetic moment on each ion was approximated by the projection of the fully converged spin-polarized wavefunctions onto spherical harmonics within a Wigner-Seitz radius of each atom. The default Wigner-Seitz radii included with the VASP PAW psuedopotentials were used for this purpose.

2.2.3 Derivation of the magnetic deformation

The degree of lattice deformation has previously been employed to quantify changes in, or compare similar crystal structures.[87, 133] Here we define the magnetic deformation, Σ_M as the degree of lattice deformation between the DFT-optimized nonmagnetic and magnetic unit cells. To calculate Σ_M, the transformation matrix, $\boldsymbol{P}$, between the magnetic and nonmagnetic relaxed structures is determined from $\boldsymbol{P} = \boldsymbol{A}_{NM}^{-1} \cdot \boldsymbol{A}_M$ Where $\boldsymbol{A}_{NM}$ and $\boldsymbol{A}_M$ are respectively the lattice parameters of the non-magnetic and magnetic relaxed unit cell. In general, $\boldsymbol{P}$ may contain a rotational component, which does not contribute to deformation of the lattice. To remove this component, the Lagrangian finite strain tensor, $\boldsymbol{\eta}$, is calculated from $\boldsymbol{P}$:

$$\boldsymbol{\eta} = \frac{1}{2}(\boldsymbol{P}^T\boldsymbol{P} - \boldsymbol{I}) \tag{2.3}$$

The degree of lattice deformation is the root mean square of the eigenvalues of $\boldsymbol{\eta}$. Here, we express the magnetic deformation as a percentage:

$$\Sigma_M = \frac{1}{3}(\eta_1^2 + \eta_2^2 + \eta_3^2)^{1/2} \times 100 \tag{2.4}$$

A `python` implementation of this calculation is provided in the Appendix section 2.5.3.

2.3 Results and discussion

The experimental and computed properties for the 33 characterized magnetocalorics investigated in this study are shown in Table 2.1. For these materials, the experimental ΔS_M for applied field of both 2 T and 5 T correlate strongly with the calculated

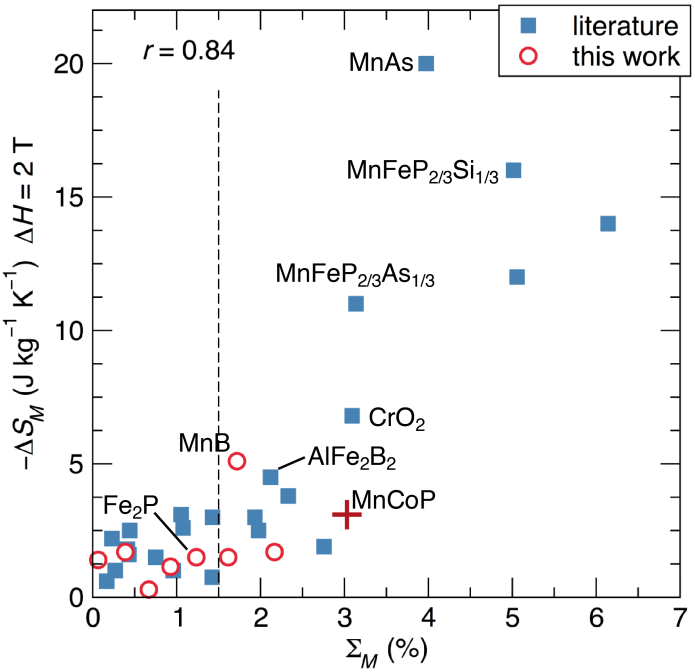

Figure 2.1: Comparison of the magnetic deformation, Σ_M and experimental maximum isothermal entropy change upon application of a 2 T magnetic field. The ΔS_M measurements include those obtained from previous studies and new measurements presented in this contribution. MnCoP, which was synthesized and measured after using Σ_M to screen candidate materials, is shown as a red plus. Pearson's r is indicated in the top left.

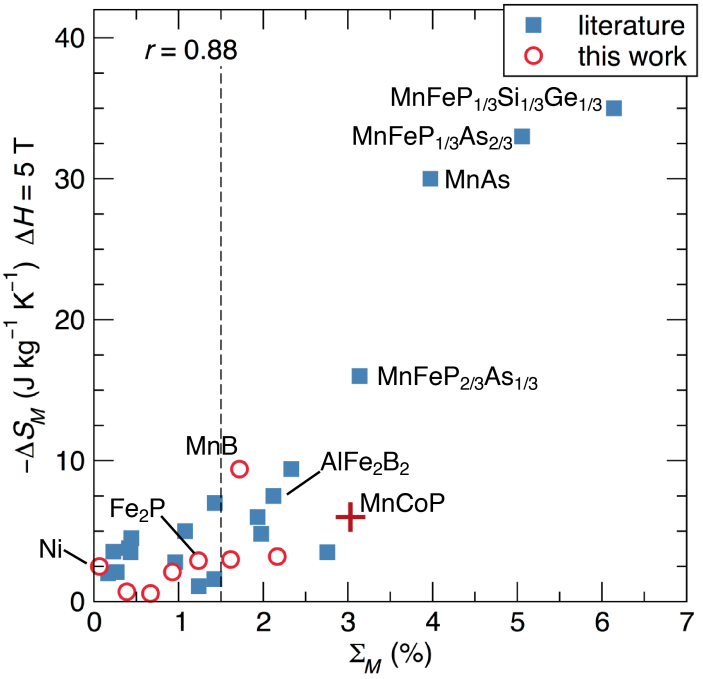

Figure 2.2: Comparison of Σ_M and maximum isothermal entropy change upon application of a 5 T magnetic field. Pearson's r is indicated in the top left.

magnetic deformation, Σ_M (Figure 2.1 and Figure 2.2). In particular, the "giant" magnetocaloric effect materials in the database (MnAs and Fe_2P-based materials) are clearly separated from all other materials by their large values of lattice deformation ($\Sigma_M > 3\,\%$). These materials have discontinuous unit cell changes at their first-order magnetic phase transition, and Σ_M appears to capture this behavior. Interestingly, ΔS_M also correlates with Σ_M for the other materials in the dataset, which are not believed to have discontinuous magnetostructural transitions. This correlation appears to hold quite well across the full dataset, which spans a large range of structure types, magnetic exchange mechanisms, and elemental compositions. It is important to note that the correlation is not perfect, and a low value of Σ_M does not guarantee a low ΔS_M. However, the correlation does suggest that materials with higher values of Σ_M are much more likely to show high ΔS_M than materials with lower values of Σ_M. $\Sigma_M =$

1.5 % serves as a good cutoff: the compounds with Σ_M >1.5 are all remarkable magnetocalorics. Based on these results, we propose that Σ_M can be used as a screening parameter to identify compounds for experimental study.

The actual meaning of Σ_M is subtle. For the case of the Fe_2P-type materials in this dataset ($MnFeP_{2/3}Si_{1/3}$, $MnFeP_{1/3}Si_{1/3}Ge_{1/3}$, $MnFeP_{1/3}As_{2/3}$, and $MnFeP_{2/3}As_{1/3}$), the relaxed magnetic and nonmagnetic unit cell shapes qualitatively mirror the differences seen in the ferromagnetic and paramagnetic structures of these materials. Specifically, the relaxed magnetic unit cell has a larger hexagonal c axis and smaller a axis than the relaxed nonmagnetic cell, much like the experimental structural transition observed at the ferromagnetic to paramagnetic transition. [85] However, for most of the materials studied, there is no discontinuous structure change, and yet Σ_M is nonzero. Formally, Σ_M is indicating differences in equilibrium structure at 0 K between a material in a nonmagnetic state and in a ferromagnetic state. This 0 K nonmagnetic state is a poor representation of the high-temperature paramagnetic states, which has dynamically disordered moments. Therefore, it is best to describe Σ_M as an indication of the degree to which structural and magnetic degrees of freedom are coupled in a material, similar to magnetovolume coupling terms in the Bean and Rodbell model, which has been quite successful in analyzing magnetocalorics. [89, 111] The strong correlation of ΔS_M with Σ_M highlights the importance of magnetostructural coupling in first order materials, but also indicates that magnetostructural coupling is important for strong magnetocaloric performance in materials displaying second-order magnetic transitions.

The major advantages of Σ_M as a screening parameter is that it is computationally inexpensive and entirely material agnostic. Where more rigorous *ab initio* descriptions of exchange-volume coupling or magnetic entropy require detailed knowledge of a system, including the nature of the magnetic moments, the magnetic exchange mech-

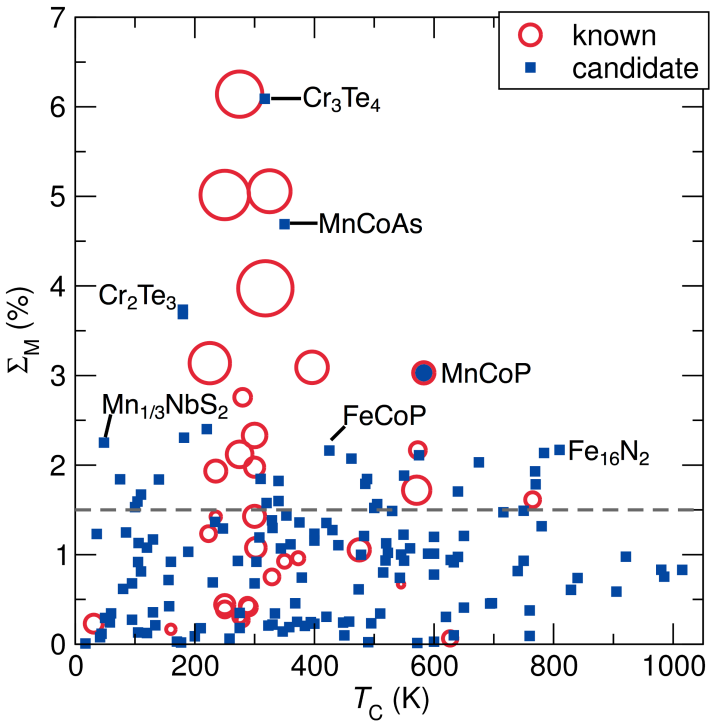

Figure 2.3: Σ_M *vs.* T_C for the known magnetocalorics and the candidate ferromagnetic materials. For the known magnetocalorics, the area of the circle is proportional to the material's peak ΔS_M with an applied field of 2 T. The grey line indicates $\Sigma_M = 1.5$; candidates above this line are predicted to show large ΔS_M. MnCoP, a candidate material with $\Sigma = 3.03\%$ which we have synthesized and measured, is shown with area proportional to its ΔS_M. [155–214]

anism, and the nature of the phase transition, Σ_M can be rapidly calculated for any material given only an ordered unit cell and no additional human input. Figure 2.3 shows Σ_M calculated for all 167 materials in this study, including the 134 that have not yet been studied for magnetocaloric effect, plotted against the experimental T_C. Thirty ferromagnets with $\Sigma_M > 1.5$ are identified and listed in Table 2.2. Based on the correlations observed in known magnetocalorics, these materials are likely to show strong magnetocaloric effect and are therefore excellent candidates for experimental study.

We report here a first experimental verification of these predictions. MnCoP, an othorhombic material with the TiNiSi structure ($Pnma$)[215], has $\Sigma_M = 3.03$ and

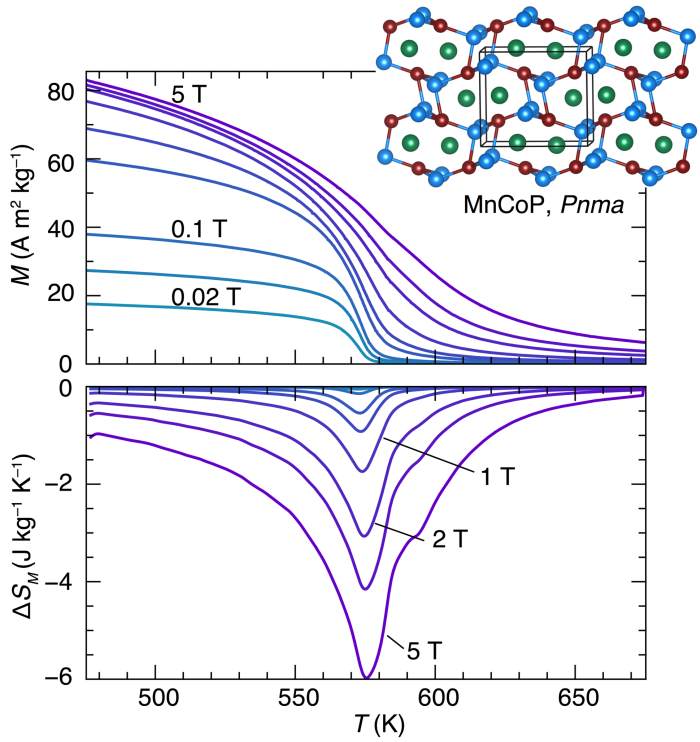

Figure 2.4: Magnetocaloric characterization of MnCoP, which shows a high Σ_M of 3.03%. Top: Magnetization *vs.* temperature at different magnetic fields. Bottom: ΔS_M, calculated from equation 2.2. The fields are 0.02 T, 0.05 T, 0.1 T, 0.3 T, 0.5 T, 1.0 T, 2.0 T, 3.0 T, and 5.0 T.

is therefore expected to have strong ΔS_M near its Curie temperature of 583 K. We prepared this compound and measured its isothermal entropy change, as shown in Figure 2.4. MnCoP shows a maximum ΔS_M of 3.1 kg^{-1} K^{-1} for an applied field of 2 T and 6.0 $J\,kg^{-1}$ K^{-1} for an applied field of 5 T. As shown in Figure 2.1 and Figure 2.2, these values fit well into the observed correlation between ΔS_M and Σ_M.

Currently, the most commonly used parameter in the search for new magnetocalorics is the saturation magnetization, M_S. Within systems, including some first order systems, the magnitude of ΔS_M is found to scale with M_S and looking for high magnetization compounds has often been a design principal in searching for new magnetocalorics [79, 83, 216]. The theoretical M_S of each of the materials in this dataset is easily

calculated from the magnetic DFT calculations. Surprisingly, despite the widespread acceptance of M_S as a key determiner of ΔS_M, the data shows poor correlation between M_S and ΔS_M. This can be seen in Figure 2.5, which is a visualization of the cross-correlation matrix for the properties investigated in this study. MnAs and the Fe_2P-based "giant" magnetocalorics show larger ΔS_M than Gd, despite having lower M_S. For the giant magnetocaloric effect materials, the failure of M_S as a predictor of ΔS_M can be understood as arising from the dominant role that the first-order magnetostructural transition plays in determining the entropy change. However, even for second order materials with no known discontinuous structural transition at the Curie temperature, deviation is expected. Using the Arrott-Noakes equation of state [217] for a second order magnetic transition and making the mean field approximation gives the following: [110]

$$\Delta S_M(H_1) = -\frac{1}{2}a\big[M(H_1) - M(0)\big] \tag{2.5}$$

Where the maximum entropy change upon isothermal application of a field H_1 is determined by a, a phenomenological parameter dependent on the critical exponents. $\big[M(H_1) - M(0)\big]$ is the difference between the magnetization under a field of H_1 and the spontaneous magnetization. Therefore, while large M_S provides the potential for large $\big[M(H_1) - M(0)\big]$, the value of $\Delta S_M(H_1)$ will ultimately depend heavily on the critical exponents and field-dependence of the magnetization curves.

The surprisingly poor correlation between calculated M_S and experimental ΔS_M can therefore be explained in both in materials displaying first- and second-order magnetic transitions. In both cases, the possible entropy change of the spin system upon magnetization is determined by the M_S, but the portion of that total change that can be caused by a finite magnetic field (*e.g.* 2 T or 5 T) is limited by other material properties that are not captured in a calculation of M_S.

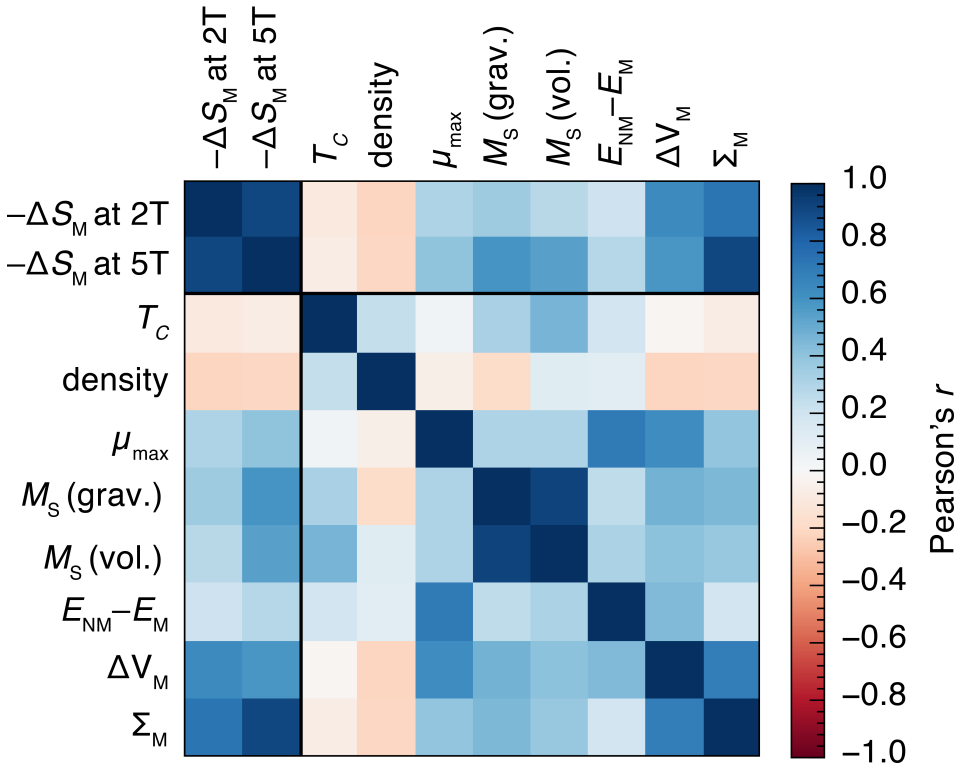

Figure 2.5: Visualization of the cross-correlation matrix for experimental (ΔS_M and T_C) and computed properties (all others). $\mu_{\max}$ is the maximum localized on any ion in the compound, and $E_{NM} - E_M$ is the energy difference between the structure calculated without and with spin-polarization, in eV/atom. For each square, the color represents Pearson's r, which ranges from -1 (perfect negative correlation) to $+1$ (perfect positive correlation) through 0 (no correlation). Correlations involving ΔS_M use the 33 magnetocaloric materials (Table 2.1), while all other correlations use the full dataset of 167 materials (Table 2.2 and Appendix Table 2.3).

Analysis of aggregated materials data has become an important and insightful way of understanding physical phenomena, especially as large databases of experimental and computational data have been established. [75, 218–224] Statistical analysis, interactive visualization, and machine learning allow for new and insightful ways of understanding materials behavior and guiding research efforts. The experimental and computed data in this study, provided in full in the Appendix and in an interactive website currently hosted online at magnets.mrl.ucsb.edu, afford opportunities for this type of analysis. For example, Figure 2.5 contains a cross-correlation analysis of the parameters investigated in this study, including measured ΔS_M and T_C and several properties extracted from the DFT calculations. This analysis shows that ΔS_M for applied fields of both 2 T and 5 T is more strongly correlated with Σ_M than with any other calculated property investigated. The percentage volume change between the nonmagnetic unit cell and the magnetic unit cell also shows some correlation with ΔS_M, although less than the magnetic deformation. While the cell volume captures some of the structural differences that arise between the magnetic unit cell and nonmagnetic unit cell, it fails to account for cases where significant unit cell shape changes occur without large changes in cell volume. These sort of structural transitions can be important in magnetocaloric materials, for example in the case of the Fe_2P-type compounds discussed earlier. Numerous other correlations are found between various parameters. For example, $E_{\mathrm{NM}} - E_{\mathrm{M}}$, which can be viewed as the energy benefit of a material becoming magnetic, is much more strongly related to the maximum ionic moment size $\mu_{\max}$ than to any other parameter, including the overall magnetization M_S. This suggests that a large ionic moment is a sign of a highly stable magnetic ground state. Interestingly, this analysis also shows that none of the investigated parameters correlates particularly well with T_C. As T_C is an important parameter in screening magnets for a variety of applications, including magnetocalorics, it will be valuable to investigate simple and

general computational methods of predicting T_C.

2.4 Conclusion

This contribution introduces a simple computational proxy for the screening of magnetic materials for magnetocaloric performance, Σ_M, the magnetic deformation. This proxy is validated using ΔS_M values from reported magnetocalorics and new ΔS_M measurements. Based on application of this proxy to ferromagnets that have not yet been measured for ΔS_M, we propose 30 likely candidates for strong magnetocaloric performance. The calculation of Σ_M requires no knowledge of a material beyond it's crystal structure, so the method is easily applied to a large number of compounds. While this study has restricted screening to known ferromagnets with relatively simple unit cells and no rare earth elements, the proxy is quite general and could be used across a large variety of systems. For example, by combining this proxy with phase stability analysis, [219] this proxy could be applied to screen large numbers of hypothetical materials that are expected to be thermodynamically stable but have not yet been experimentally investigated. Alternatively, this proxy can be used to screen compositions within a single system to suggest compositions with optimal properties. Furthermore, as many known magnetocaloric materials have magnetic transitions other than the transition from paramagnetic to ferromagnetic states, it would be profitable to expand this proxy to a wider range of materials by comparing the structures of materials with other kinds of magnetic orderings, such as antiferromagnets and ferrimagnets.

	T_C	ΔS_M (J kg^{-1} K^{-1})		ref.	Σ_M	M_S	ΔV_M
	(K)	$H = 2$ T	$H = 5$ T		(%)	(emu/g)	(%)
MnAs	318	−20	−30	134	3.97	121.5	13.2
$MnFeP_{2/3}Si_{1/3}$	250	−16		135	5.02	171.1	7.10
$MnFeGe_{1/3}P_{1/3}Si_{1/3}$	275	−14	−35	136	6.14	154.7	5.80
$MnFeP_{1/3}As_{2/3}$	325	−12	−33	137	5.06	141.7	6.63
$MnFeP_{2/3}As_{1/3}$	225	−11	−16	137	3.14	146.0	7.10
CrO_2	396	−6.8		138	3.09	133.0	3.90
$AlFe_2B_2$	275	−4.5	−7.5	139	2.12	92.3	1.77
Mn_5Ge_3	300	−3.8	−9.4	140	2.33	152.5	11.3
Fe_3C	475	−3.1		141	1.05	170.2	5.53
$LaMnO_3$	300	−3	−7	142	1.43	71.2	7.42
MnCoGe	235	−3	−6	143	1.93	90.7	4.67
Mn_5PB_2	302	−2.6	−5	144	1.08	138.0	4.03
Y_2Fe_{17}	300	−2.5	−4.8	145	1.98	187.3	10.4
Mn_3GaC	250	−2.5	−4.5	146	0.44	95.0	2.31
MnSi	31	−2.2	−3.55	147	0.23	66.9	1.20
Mn_3Sn_2	280	−1.9	−3.5	148	2.76	107.3	8.15
MnP	290	−1.8	−3.8	149	0.41	46.9	1.22
Mn_3AlC	288	−1.6	−3.5	150	0.43	107.0	2.26
$MnNi_2Ga$	329	−1.5		151	0.75	93.7	3.93
Fe_5Si_3	373	−1	−2.8	140	0.96	111.7	3.13
La_2MnNiO_6	280	−1	−2.1	152	0.27	57.2	1.40
MnFeGe	235	−0.75	−1.6	143	1.42	83.8	3.68
$SrRuO_3$	160	−0.6	−2	153	0.17	47.3	0.84
Fe_3GeTe_2	225		−1.1	154	1.24	70.8	6.12
Ni	627	−1.4	−2.6	18	0.07	55.6	0.34
Fe_2P	223	−1.5	−2.9	18	1.23	116.7	3.64
MnB	571	−5.1	−9.4	18	1.72	155.1	3.64
FeB	573	−1.7	−3.2	18	2.17	96.6	1.52
MnNiSb	765	−1.5	−3.0	18	1.61	94.9	8.50
$MnNi_2Sn$	350	−1.2	−2.1	18	0.93	80.0	4.85
$FeRu_2Sn$	545	−0.3	−0.6	18	0.67	61.7	3.49
$MnFe_2Si$	250	−0.6	−1.6	18	0.39	86.1	2.03
MnCoP	583	−3.1	−6.0	18	3.03	114.9	5.53

Table 2.1: Selected experimental and calculated data for the magnetocalorics investigated in this study. The Curie temperature (T_C) and peak isothermal entropy change (ΔS_M) columns represent experimental results, either aggregated from literature (top section) or from new magnetic measurements in this study (bottom section). The magnetic deformation (Σ_M), saturation magnetization (M_S), percentage volume difference between the magnetic unit cell and the nonmangetic unit cell (ΔV_M), and density (ρ) are from DFT calculations performed in the present study. In each case, the ΔS_M is for the ferromagnetic to paramagnetic transition. MnB has also been measured by Fries et al. [80]

Table 2.2: Ferromagnetic compounds with large values of magnetic deformation, Σ_M ($>$1.5), indicating potential for good magnetocaloric properties. For each material, T_C is the experimental magnetic transition temperature (found in given reference). Σ_M and saturation magnetization (M_S) are the result of DFT calculations. The complete list of candidate compounds and calculated parameters can be found in the Appendix, Table 2.3.

	T_C (K)	ref.	Σ_M (%)	M_S (emu/g)
Cr_3Te_4	317	155	6.09	83.7
MnCoAs	350	156	4.69	91.7
Cr_2Te_3	180	157	3.73	69.3
MnCoP	583	215	3.03	114.9
MnPtGa	220	158	2.40	65.5
CrNiAs	182	159	2.31	90.0
$MnNb_3S_6$	48	160	2.25	45.0
$Fe_{16}N_2$	810	161	2.17	213.4
FeCoP	425	156	2.16	78.0
Fe_5SiB_2	784	162	2.14	147.2
Fe_3Pd	575	163	2.11	168.8
Fe_3Pt	462	164	2.07	127.8
Fe_4CoSiB_2	675	165	2.03	117.9
Fe_4N	769	161	1.93	232.0
Fe_3N	550	166	1.88	187.8
$MnGa_2Sb_2$	310	167	1.85	34.7
Fe_2CoN	488	168	1.84	155.4
$MnTa_4S_8$	75	169	1.84	21.7
CrNiP	140	156	1.84	104.3
$MnGeAs_2$	340	170	1.82	83.6
$Fe_{23}Y_6$	485	171	1.79	152.8
Fe_4MnSiB_2	770	165	1.79	141.5
Fe_3Ge	640	172	1.70	147.8
Ba_2MnReO_6	110	173	1.67	35.8
$MnGe_4$	340	174	1.60	25.2
$Sr_3Ru_2O_7$	104	175	1.59	39.7
$MnGeP_2$	320	170	1.58	98.9
Fe_3RhN	505	176	1.56	168.9
$MnNb_4S_8$	100	169	1.53	29.7
MnPdSb	500	177	1.52	66.3

2.5 Appendix: Supplemental material

2.5.1 Sample synthesis and $\Delta S_M(\Delta H, T)$ measurements

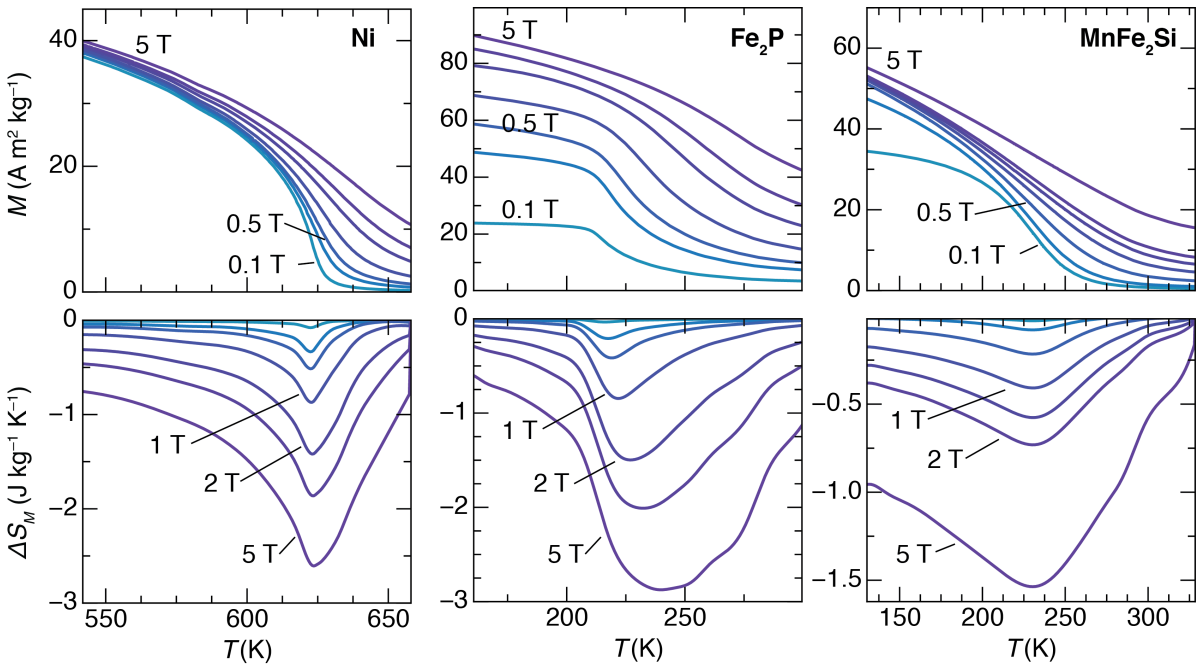

Figure 2.6: Magnetocaloric characterization of Ni foil, Fe_2P and Heusler $MnFe_2Si$ *via* magnetic measurements. For Ni and Fe_2P, the $M(T)$s were taken at fields of 0.1 T, 0.3 T, 0.5 T, 1 T, 2 T, 3 T, and 5 T. For $MnFe_2Si$, the $M(T)$s were taken at fields of 0.1 T, 0.2 T, 0.5 T, 1 T, 1.5 T, 2 T, and 5 T.

Ni foil (0.125 mm thickness, $\geq$99.9 % purity) and **Fe_2P** powder (99.5% purity) were obtained from Aldrich.

The Heusler **$MnFe_2Si$** was prepared by a rapid assisted microwave synthesis method, which has been shown to be an effective way to synthesize intermetallics. [225] Stoichiometric amounts of Mn, Fe, and Si powders, totaling about 1 g in mass, were weighted and ground together with a mortar and pestle. The powder was pressed into a pellet 6 mm in diameter and sealed in an evacuated silica ampoule which was then placed in an alumina crucible filled with 7 g activated charcoal. The charcoal

acts as a microwave susceptor. This crucible was placed in an alumina foam housing, loaded into a 1200 W domestic Panasonic microwave (model NN-SN651B) and heated at 70% power (840 W) for 2.5 minutes and then 90% power (1080 W) for 3 minutes. The resulting compound was annealed in the evacuated ampoule for 5 days at 650°C to promote homogenization of the final product. The sample was confirmed to be the correct phase by laboratory powder X-ray diffraction.

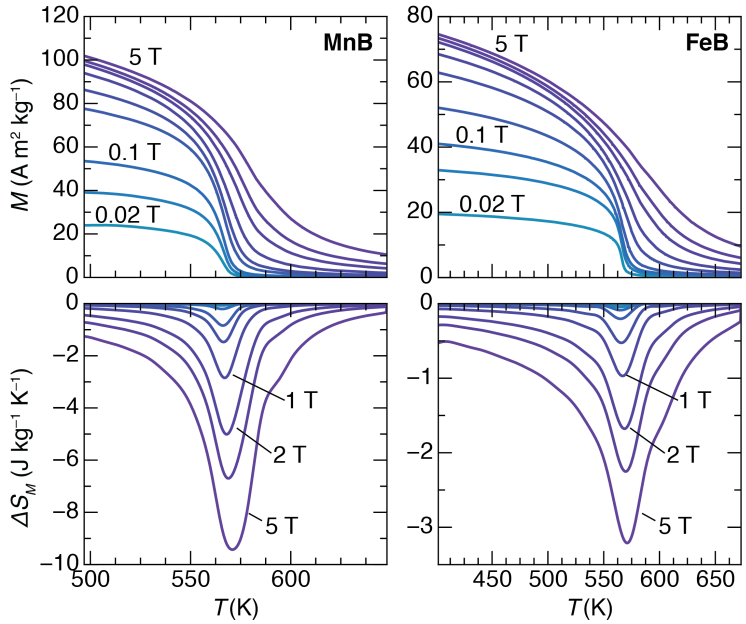

Figure 2.7: Magnetocaloric characterization of MnB and FeB *via* magnetic measurements. For MnB, the $M(T)$s were taken at fields of 0.02 T, 0.05 T, 0.1 T, 0.3 T, 0.5 T, 1 T, 2 T, 3 T, and 5 T. For FeB, the $M(T)$s were taken at fields of 0.02 T, 0.06 T, 0.1 T, 0.2 T, 0.5 T, 1 T, 2 T, 3 T, and 5 T.

The compounds **MnB** and **FeB** were prepared by assisted microwave synthesis, using a procedure similar to $MnFe_2Si$. Stoichiometric amounts of elemental Mn or Fe and B powders were weighed out, including an extra 2 wt.% B to account for losses during heating. The powders were ground and pressed into 300 mg pellets 6 mm in diameter. Each pellets was sealed in an evacuated fused silica ampoule. The ampoule was placed

in a crucible with 6.5 g activated charcoal which had been preheated in the microwave to about 150°C, and this was placed in an alumina foam housing. The samples were microwaved at 70% power (840W) for 3 minutes and allowed to cool in the microwave. Melting of the pellet was not observed. Pellets were annealed in evacuated ampoules at 1100°C for 2 days, followed by air quenching. Weight loss of 1.9% was observed in the FeB sample, which we attribute to loss of boron during the microwave step. Formation of FeB and MnB were confirmed by laboratory powder X-ray diffraction.

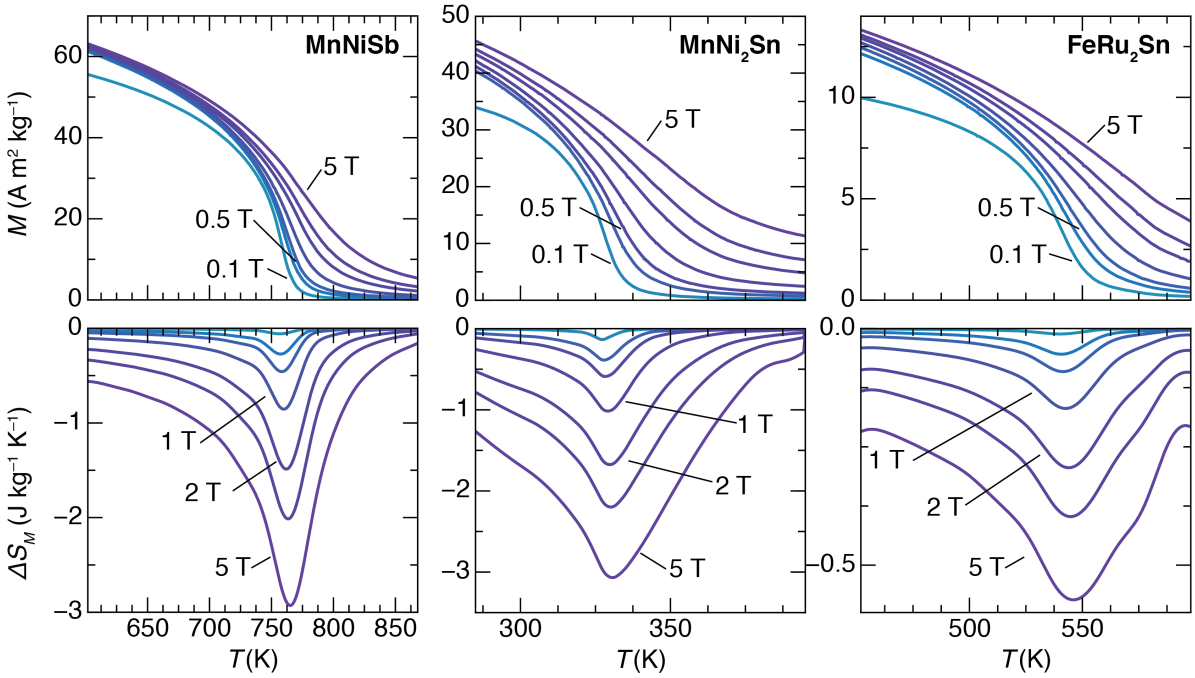

Figure 2.8: Magnetocaloric characterization of half-Heusler MnNiSb and full-Heuslers $MnNi_2Sn$ and $FeRu_2Sn$ *via* magnetic measurements. The $M(T)$s were taken at fields of 0.1 T, 0.3 T, 0.5 T, 1 T, 2 T, 3 T, and 5 T.

Half-Heusler **MnNiSb** and Heusler **$MnNi_2Sn$** were similarly prepared using assisted microwave synthesis. The pure elements were ground together and pressed into 1 g pellets and then sealed in evacuated silica ampoules and loaded into the microwaves as described for MnB and FeB. MnNiSb was microwaved at 70% power (840 W) for 2.5 minutes and then annealed in the evacuated ampoule at 650°C for 7 days before

air quenching. $MnNi_2Sn$ was microwaved for 100% power (1200 W) for 3 minutes and then annealed in the evacuated ampoule at 850°C for 4 days before air quenching. The phases were verified by laboratory X-ray diffraction.

$FeRu_2Sn$ was prepared as described previously. [124]

2.5.2 Sample synthesis and structural characterization of MnCoP

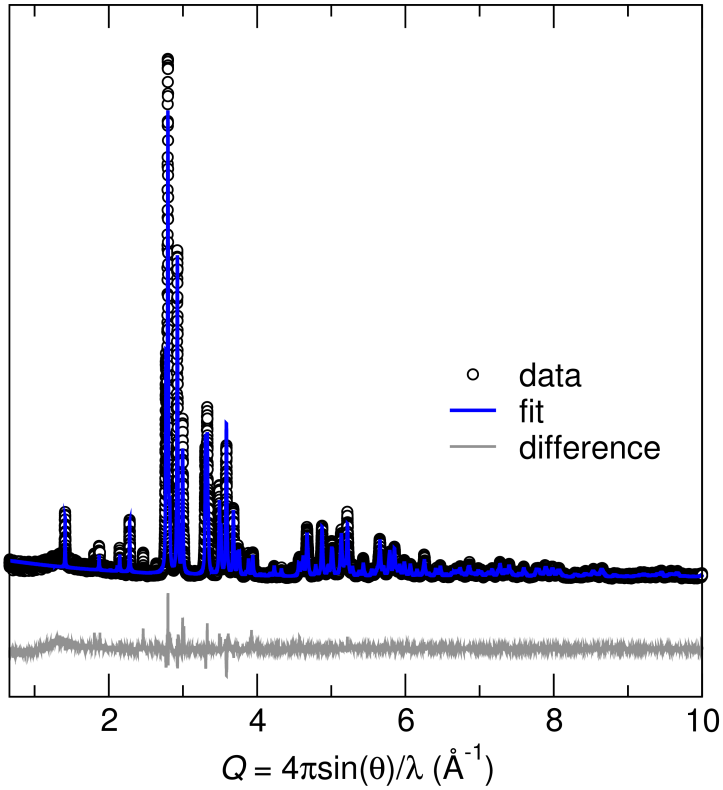

Figure 2.9: Rietveld refinement of the synchrotron XRD pattern of the MnCoP sample. The pattern shows good agreement with the structural model previously reported (TiNiSi-type, $Pnma$). [215]

MnCoP was made by assisted microwave reaction. Stoichiometric amounts of Mn_3P_2, Co, and red P powders were ground in a mortar and pestle and pressed into a pellet 6 mm in diameter, which was then sealed in an evacuated silica ampoule. The

ampoule was placed in an alumina crucible surrounded by 7 g of activated charcoal that had been preheated to 100°C, which acts as a susceptor material in the microwave. This crucible was then placed in a thermally insulating housing made from alumina foam and microwaved at 70% power (840 W) for 2.5 minutes. The silica ampoule was then transferred to a conventional furnace and the sample was annealed at 950°C for 17 hours before quenching in water. The sample was verified to show the $Pnma$ TiNiSi-type structure *via* Rietveld refinement of the synchrotron X-ray diffraction pattern (Figure 2.9).

2.5.3 Calculation of the magnetic deformation Σ_M

The following `python` functions can be used to calculate the degree of lattice deformation between two unit cells. Tested on `python 2.7.10` with `numpy 1.10.1` and `pymatgen 3.2.10` [132].

```
__copyright__ = "Copyright 2017, Joshua D. Bocarsly"
__license__   = "MIT"

from os.path import join as j
import numpy as np
from numpy import linalg as LA
import pymatgen as mg

def magnetic_deformation(nm_struct, m_struct):
    '''
    Calculates the magnetic deformation, which is the degree of
    lattice deformation between an optimized nonmagnetic structure
    (non spin-polarized) and an optimized magnetic structure
    (spin-polarized).

    nm_struct and m_struct are pymatgen.core.structure.Structure
    objects containing the nonmagnetic optimized cell and the magnetic
    optimized cell.
```

```
    Returns the magnetic deformation expressed as a percentage (float).
    '''
    lmn = nm_struct.lattice_vectors().T
    lm  = m_struct.lattice_vectors().T
    return degree_of_lattice_deformation(lmn, lm)

def degree_of_lattice_deformation(L1, L2):
    '''
    Calculates the degree of lattice deformation between two
    unit cells.

    The unit cells are provided as a 3x3 matrix, with each
    column containing the cartesian representation of one
    of the lattice vector.

    Returns the degree of lattice deformation as a
    percentage (float)
    '''
    #calculate the transformation matrix from 1 to 2
    L1_i = LA.inv(L1)
    P = np.dot(L1_i, L2)
    #calculate the lagrangian finite strain tensor, eta
    I = np.identity(3)
    eta = 0.5*(np.dot(P.T,P)-I)
    #calculate the 3 eigenvalues of eta and return the
    root mean square
    w, v = LA.eig(eta)
    dold = 100*(1./3.)*np.sqrt(w[0]**2 + w[1]**2 + w[2]**2)
    return dold
```

2.5.4 Calculated and collected data for ferromagnets

Table 2.3: Experimental Curie temperature T_C and calculated properties for the ferromagnetic candidate materials investigated in this study.

formula	T_C (K)	ref.	Σ_M (%)	M_s (emu/g)	ΔV_M (%)	ρ (g/cm^3)	E_{NM-M} (eV/atom)	$\mu_{\max}$ (μ_B)
Cr_3Te_4	317	155	6.09	83.7	22.67	6.40	0.27	3.4
MnCoAs	350	156	4.69	91.7	7.97	8.15	0.20	3.0
Cr_2Te_3	180	157	3.73	69.3	16.39	6.41	0.32	3.2
MnPtGa	220	158	2.40	65.5	8.22	11.74	0.37	3.7
CrNiAs	182	159	2.31	90.0	7.35	7.64	0.12	3.0
$MnNb_3S_6$	48	160	2.25	45.0	8.42	4.78	0.05	3.9
$Fe_{16}N_2$	810	161	2.17	213.4	11.47	7.73	0.04	2.8
FeCoP	425	156	2.16	78.0	3.28	7.45	0.09	1.8
Fe_5SiB_2	784	162	2.14	147.2	5.00	7.05	0.07	2.1
Fe_3Pd	575	163	2.11	168.8	11.16	8.86	0.27	2.8
Fe_3Pt	462	164	2.07	127.8	10.96	11.65	0.19	2.8
Fe_4CoSiB_2	675	165	2.03	117.9	3.76	7.23	0.05	1.6
Fe_4N	769	161	1.93	232.0	10.20	7.27	0.26	3.0
Fe_3N	550	166	1.88	187.8	6.89	7.48	0.16	2.1
$MnGa_2Sb_2$	310	167	1.85	34.7	4.85	6.85	0.06	2.9
Fe_2CoN	488	168	1.84	155.4	5.90	7.68	0.12	2.2
$MnTa_4S_8$	75	169	1.84	21.7	7.57	7.13	0.05	3.9
CrNiP	140	156	1.84	104.3	5.32	6.70	0.05	2.5

Table 2.3: Experimental Curie temperature T_C and calculated properties for the ferromagnetic candidate materials investigated in this study.

formula	T_C (K)	ref.	Σ_M (%)	M_s (emu/g)	ΔV_M (%)	ρ (g/cm^3)	E_{NM-M} (eV/atom)	$\mu_{\max}$ (μ_B)
$MnGeAs_2$	340	170	1.82	83.6	9.62	4.84	0.18	3.8
$Fe_{23}Y_6$	485	171	1.79	152.8	9.45	6.98	0.15	2.5
Fe_4MnSiB_2	770	165	1.79	141.5	4.43	7.00	0.08	2.1
Fe_3Ge	640	172	1.70	147.8	7.18	8.37	0.22	2.2
Ba_2MnReO_6	110	173	1.67	35.8	8.81	7.27	0.12	4.3
$MnGe_4$	340	174	1.60	25.2	1.10	6.68	0.02	1.8
$Sr_3Ru_2O_7$	104	175	1.59	39.7	1.89	5.90	0.01	1.4
$MnGeP_2$	320	170	1.58	98.9	8.14	3.93	0.05	3.1
Fe_3RhN	505	176	1.56	168.9	8.24	8.39	0.17	2.6
$MnNb_4S_8$	100	169	1.53	29.7	6.32	4.72	0.04	3.7
MnPdSb	500	177	1.52	66.3	8.01	8.15	0.23	3.2
FePt	750	178	1.49	72.1	7.84	14.91	0.34	2.9
$MnCu_2Sn$	530	179	1.49	72.9	7.83	8.28	0.35	3.7
Fe_3P	716	166	1.47	157.3	5.76	7.44	0.13	2.2
Mn_3ZnC	353	180	1.44	161.7	7.56	6.94	0.14	2.7
$CuCr_2Te_4$	329	181	1.38	44.3	7.27	6.40	0.33	3.0
Fe_2NiN	234	168	1.37	126.3	4.73	7.64	0.13	2.1
$CuCr_2S_4$	375	181	1.36	94.9	7.15	4.13	0.24	2.7
Sr_2FeMoO_6	420	173	1.35	7.3	7.11	5.56	-0.04	0.7

Table 2.3: Experimental Curie temperature T_C and calculated properties for the ferromagnetic candidate materials investigated in this study.

formula	T_C (K)	ref.	Σ_M (%)	M_s (emu/g)	ΔV_M (%)	ρ (g/cm^3)	E_{NM-M} (eV/atom)	$\mu_{\max}$ (μ_B)
$TaMn_2B_4$	780	182	1.32	66.7	2.34	8.99	0.08	2.1
MnPtSn	330	183	1.30	55.5	6.82	10.25	0.56	3.8
$MnPd_2Sb$	247	179	1.29	62.0	6.79	9.60	0.51	4.0
$CuCr_2Se_4$	430	184	1.27	59.3	6.69	5.71	0.30	2.9
$CdCr_2S_4$	86	185	1.25	97.2	6.55	4.19	0.38	2.9
Fe_3Al	400	186	1.23	169.9	6.48	6.88	0.24	2.4
$HgCr_2S_4$	36	187	1.23	77.3	6.47	5.22	0.36	2.9
Fe_3Y	549	171	1.22	82.4	5.51	7.18	0.10	2.1
Fe_4MnPB_2	650	165	1.21	140.7	4.23	7.19	0.08	2.2
$MnCu_2Al$	600	179	1.20	94.9	6.29	6.68	0.27	3.4
Ba_2FeMoO_6	308	173	1.19	42.8	6.26	6.41	0.10	3.7
$CdCr_2Se_4$	130	185	1.17	63.0	6.14	5.53	0.41	3.0
Sr_2FeReO_6	400	173	1.16	32.7	6.07	6.73	0.10	3.7
$HgCr_2Se_4$	106	187	1.13	53.9	5.93	6.39	0.39	3.0
$MnCu_2In$	520	179	1.13	69.9	5.91	8.33	0.36	3.6
$MnNi_2Sb$	360	179	1.12	75.6	5.86	8.80	0.35	3.6
$CrMn_2B_4$	440	182	1.11	90.9	1.92	6.15	0.04	1.8
$CrTa_3Se_6$	120	160	1.08	16.0	4.08	8.78	0.07	3.1
WMn_2B_4	560	182	1.07	58.4	1.26	9.37	0.06	1.8

Table 2.3: Experimental Curie temperature T_C and calculated properties for the ferromagnetic candidate materials investigated in this study.

formula	T_C (K)	ref.	Σ_M (%)	M_s (emu/g)	ΔV_M (%)	ρ (g/cm^3)	E_{NM-M} (eV/atom)	$\mu_{\max}$ (μ_B)
$MnNi_2Sn$	344	179	1.07	78.7	5.61	8.71	0.35	3.6
$MnPd_2Sn$	189	179	1.03	60.1	5.41	9.73	0.49	3.9
Fe_7C_3	523	188	1.02	151.3	3.71	7.86	0.07	2.0
$MoMn_2B_4$	590	182	1.01	78.7	1.54	6.96	0.06	1.8
Fe_2Zr	600	189	1.01	84.3	5.30	7.80	0.11	2.0
$ScFe_2$	545	190	1.00	94.2	3.80	6.23	0.09	1.8
MnCoSb	478	183	1.00	70.9	5.24	7.98	0.38	3.2
Co_5Y	921	191	0.98	105.2	4.82	7.72	0.11	1.6
Fe_5PB_2	640	165	0.97	143.1	4.94	7.26	0.07	2.0
Mn_5SiB_2	628	162	0.94	131.5	3.64	6.83	0.07	1.7
Fe_5C_2	519	192	0.93	153.2	4.81	7.83	0.09	2.1
Fe_2Y	550	193	0.93	86.0	4.89	7.04	0.17	2.0
Ni_3Mn	750	161	0.93	119.4	4.88	8.52	0.26	3.2
Mn_3InC	272	194	0.93	116.0	4.88	7.89	0.13	2.5
$CrNb_3S_6$	160	160	0.92	32.1	3.73	4.90	0.06	2.8
Ba_2FeReO_6	303	173	0.92	27.3	4.82	7.50	0.14	3.7
$CrNb_3Se_6$	105	160	0.92	21.1	3.43	6.57	0.08	3.0
$ZrFe_2$	633	195	0.91	83.7	4.79	7.85	0.11	2.0
$FeCo_2Ge$	980	196	0.83	126.1	4.35	8.74	0.32	2.9

Table 2.3: Experimental Curie temperature T_C and calculated properties for the ferromagnetic candidate materials investigated in this study.

formula	T_C (K)	ref.	Σ_M (%)	M_s (emu/g)	ΔV_M (%)	ρ (g/cm^3)	E_{NM-M} (eV/atom)	$\mu_{\max}$ (μ_B)
$FeCo_2Si$	1015	196	0.83	148.9	4.34	7.58	0.30	2.8
Fe_3Ge	740	172	0.82	125.2	4.27	8.60	0.28	2.6
$BaFeO_3$	110	197	0.81	83.8	4.25	6.42	0.22	3.0
Fe_4CoPB_2	515	165	0.80	108.6	3.51	7.46	0.05	1.6
Fe_3Si	600	198	0.78	146.0	4.07	7.42	0.25	2.6
$MnCo_2Si$	985	179	0.75	138.9	3.94	7.51	0.36	3.0
$MnNi_2Ga$	379	179	0.74	93.7	3.89	8.26	0.31	3.4
$FePd_3$	543	164	0.74	63.5	3.88	10.65	0.35	3.3
CoPt	840	199	0.74	49.0	3.12	15.73	0.16	1.9
Co_2B	156	200	0.72	83.1	1.02	8.23	0.05	1.0
La_2MnCoO_6	230	201	0.69	68.7	3.58	6.82	0.15	2.9
FeNiP	95	156	0.68	45.6	1.46	7.37	0.05	1.4
FeCoAs	300	156	0.68	64.5	2.95	8.51	0.14	2.1
$MnTa_3S_6$	80	160	0.62	12.6	1.27	7.78	0.01	1.8
Co_3B	474	200	0.61	105.6	2.09	8.35	0.08	1.3
$MnCo_2Sn$	829	179	0.61	96.5	3.17	9.07	0.43	3.2
$MnCo_2Ge$	905	179	0.59	113.7	3.07	8.69	0.39	3.1
$MnCo_2Al$	697	202	0.46	112.6	2.39	7.21	0.31	2.7
Fe_3ZnC	368	180	0.46	93.8	2.38	7.60	0.11	1.7

Table 2.3: Experimental Curie temperature T_C and calculated properties for the ferromagnetic candidate materials investigated in this study.

formula	T_C (K)	ref.	Σ_M (%)	M_s (emu/g)	ΔV_M (%)	ρ (g/cm^3)	E_{NM-M} (eV/atom)	$\mu_{\max}$ (μ_B)
$MnCo_2Ga$	694	179	0.45	94.3	2.37	8.67	0.32	2.8
MnB_2	157	203	0.42	133.3	1.71	5.63	0.14	1.8
MnAl	650	161	0.41	129.8	1.99	5.35	0.17	1.9
VMn_2Al	760	202	0.38	59.5	1.97	6.38	0.06	1.4
CoS_2	130	204	0.36	45.2	1.86	4.92	0.01	0.9
$BaRuO_3$	60	205	0.34	43.3	1.80	7.11	0.02	1.5
$CrCo_2Al$	334	202	0.34	85.2	1.79	7.06	0.12	1.6
Fe_3GaC	510	180	0.34	70.1	1.78	7.80	0.04	1.2
Sr_2CrMoO_6	420	173	0.31	26.7	1.60	5.73	0.07	0.5
Sr_2CrReO_6	620	173	0.31	10.8	1.59	6.96	0.07	1.1
$CrBe_{12}$	50	206	0.29	47.4	1.06	2.49	0.01	1.7
VCo_2Sn	95	202	0.27	57.3	1.42	8.80	0.06	1.1
Sr_2CrWO_6	458	173	0.25	22.0	1.31	6.86	0.07	2.3
$TiCo_2Sn$	371	207	0.25	39.4	1.30	8.40	0.04	1.1
$HfCo_2Sn$	394	208	0.25	26.9	1.28	11.31	0.04	1.1
VCoSb	58	209	0.24	24.1	1.27	7.80	0.04	1.2
$ZrCo_2Sn$	448	208	0.24	34.1	1.26	8.80	0.05	1.1
$CrCo_2Ga$	495	202	0.23	70.5	1.22	8.54	0.13	1.6
$CoPt_3$	400	199	0.23	25.2	1.19	18.36	0.11	2.0

Table 2.3: Experimental Curie temperature T_C and calculated properties for the ferromagnetic candidate materials investigated in this study.

formula	T_C (K)	ref.	Σ_M (%)	M_s (emu/g)	ΔV_M (%)	ρ (g/cm^3)	E_{NM-M} (eV/atom)	$\mu_{\max}$ (μ_B)
Mn_3GeC	330	180	0.22	65.1	1.14	7.61	0.08	1.2
TiCoSn	134	210	0.21	9.2	1.10	6.50	0.00	0.6
$MnNi_2In$	323	179	0.21	81.3	1.08	8.95	0.36	3.5
$TiCo_2Ge$	384	207	0.20	47.2	1.07	7.96	0.04	1.0
VCo_2Ga	358	226	0.19	46.8	0.99	8.32	0.05	0.9
$CrFe_2Al$	210	186	0.18	5.0	0.93	7.00	0.00	0.2
$NbCo_2Sn$	105	208	0.13	29.0	0.68	9.32	0.02	0.9
$TiCo_2Al$	120	211	0.13	28.8	0.65	6.47	0.01	0.6
Au_4V	44	212	0.12	12.7	0.56	16.36	0.06	1.8
Ni_3Pt	450	199	0.10	34.8	0.51	12.70	0.04	0.8
FePd	760	178	0.09	110.2	0.46	10.48	0.39	2.9
NiPt	200	199	0.09	23.4	-0.46	15.85	0.01	0.7
Ni_3Al	41.5	212	0.08	22.2	0.40	7.47	0.00	0.3
WMn_2Sn	258	202	0.06	0.0	0.33	12.07	0.00	0.0
$CrTa_3S_6$	170	160	0.03	21.7	0.15	7.70	0.04	2.7
Co_7La_2	490	214	0.02	2.2	0.03	7.86	0.00	0.4
$Co_3Sn_2S_2$	177	188	0.02	11.6	-0.08	7.23	0.01	0.4
MnPtSb	572	183	0.01	58.2	-0.07	11.20	0.20	3.6
$ZrZn_2$	17	212	0.01	22.1	0.05	7.31	0.02	0.5

Chapter 3

Computational screening of magnetocaloric alloys

[1] The magnetic deformation proxy introduced in Chapter 2 provides a way to rapidly screen potential magnetocalorics to identify the strongest candidates for further experimental study. As with most high-throughput density functional theory (DFT) screens, this study was restricted to compounds with simple, well-defined crystallographic unit cells due to difficulties in simulating atomic site disorder. However, experimentally, it is often found that the highest-performing functional materials, for a variety of applications, are alloys and disordered materials which would be overlooked in conventional searches. Here we extend the DFT-based magnetic deformation proxy presented in Chapter 2 to screen magnetocaloric materials with atomic site disorder. This is accomplished by thermodynamic averaging of the magnetic deformation for ordered supercells across a solid solution. We show that the highly nonmonotonic magnetocaloric

[1]The contents of this chapter have substantially appeared in reference 88: C. A. C. Garcia, J. D. Bocarsly,* and R. Seshadri. Computational screening of magnetocaloric alloys. *Phys. Rev. Mater.*, **4** (2020) 024402. *corresponding author.

properties of the disordered solid solutions $Mn(Co_{1-x}Fe_x)Ge$ and $(Mn_{1-x}Ni_x)CoGe$ are successfully captured using this method.

This project was performed in collaboration with Christina Garcia and under the mentorship of Ram Seshadri.

3.1 Introduction

Recent advances in computing and automated materials science frameworks [115–117, 218, 227, 228] have enabled high-throughput *in silico* screening of crystalline solids aimed at identifying candidate materials for a variety of applications including structural materials [229–231], battery electrodes [227, 232], thermoelectrics [118], photovoltaics [233, 234], and magnetocalorics [18], among many others. In these projects, automated density functional theory (DFT) calculations are performed on a large number of candidate structures and compositions that have either been pulled from the literature or generated using a set of rules. Properties of interest are predicted from the results of these first principles calculations, often making use of a proxy: a simple quantifiable parameter that serves as an indicator of the more complex physical phenomenon [18, 119, 235]. While this strategy has met with success and has expanded the breadth of materials systems under consideration for various applications, a major limitation is that these efforts have generally been limited to evaluating compounds with simple unit cells, and without atomic site disorder (alloying). Consequently, alloyed and solid-solution materials are excluded from these searches, despite experiments suggesting that the highest-performing materials for a variety of applications often come from these families.

The importance of screening compositionally disordered materials is especially ap-

parent in the field of magnetocalorics, where many of the highest-performing materials rely on substantial unit cell disorder and nonstoichiometry for their remarkable properties, including $(Mn,Fe)_{2-\delta}(P,Si)$ [64–67], $La(Fe,Si)_{13}H_x$ [68, 69], $Gd_5(Si,Ge)_4$ [82, 236], and a variety of substituted MnCoGe-based compounds [237, 237–239]. In these materials, application of a magnetic field causes randomly oriented spins to align, reducing the entropy of the spin system. Alternating cycles of adiabatic and isothermal magnetization and demagnetization of a magnetocaloric can be used to drive a thermodynamic cycle and build an efficient magnetic heat pump [47]. Such devices promise to provide an energy-efficient and environmentally-friendly alternative to conventional vapor-compression refrigeration and air conditioning [50, 103], which typically rely on hydrofluorochlorocarbons, which are now known to be associated with high global warming potential [240]. The primary metric used to quantify the performance of a magnetocaloric is the entropy change experienced by the material upon isothermal application of a magnetic H field at a temperature T, $\Delta S_M(T, H)$. This parameter reaches its peak value near a magnetic transition temperature T_c, where the spins are most susceptible to an external field. An effective magnetocaloric should therefore show a large peak $|\Delta S_M(T, H)|$ at a useful temperature range.

For the high-performing magnetocaloric materials mentioned above, magnetic moments are strongly coupled to crystal structure, causing their magnetic transitions to couple to discontinuous changes in the crystal symmetry or lattice parameters. Such systems can show greatly enhanced (giant) magnetocaloric effects [82] around their first-order magnetostructural phase transitions. In fact, magnetostructural coupling can lead to an enhanced magnetocaloric effect even without this type of first-order transition present [81, 85, 86, 241]. We previously introduced a simple DFT-based proxy for magnetostructural coupling known as the magnetic deformation [18] Σ_M —

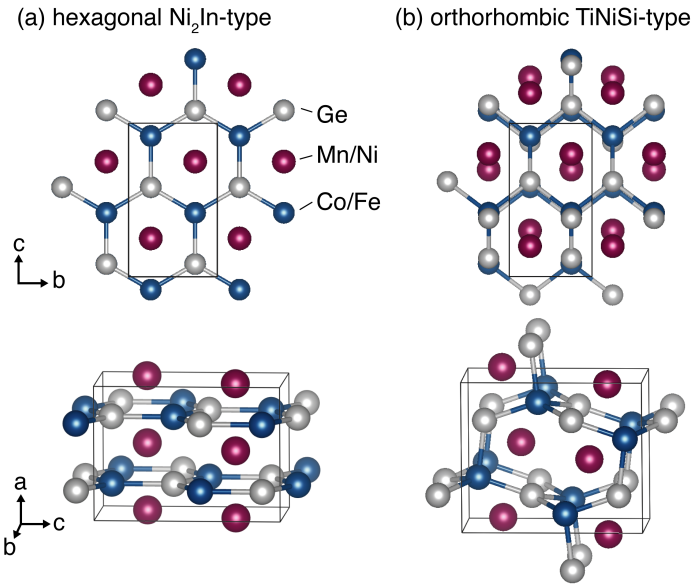

Figure 3.1: (a) Hexagonal and (b) orthorhombic structure types of MnCoGe, depicted in the orthorhombic setting. The orthorhombic structure can be accessed from the hexagonal structure by a displacive phase transition involving corrugation of the honeycomb Co-Ge network.

a stand-in for magnetostructural coupling — obtained through comparing the degree of lattice deformation between magnetic and nonmagnetic DFT structural optimizations. In systems where the inclusion of magnetism in the DFT calculation causes a large change in the optimized structure, we surmise that magnetostructural coupling must be strong. In a survey of reported magnetocalorics without substantial unit cell disorder, we found that Σ_M correlates well with the experimental peak ΔS_M for transition metal-based compounds, both for materials with known first-order magnetostructural transitions and for those with no such transitions [18]. Consequently, Σ_M can be used to computationally screen magnetic compounds to identify promising magnetocalorics.

While the application of the magnetic deformation proxy was previously limited to DFT-friendly compounds with no consideration of atomic site disorder, here we introduce a method to allow for the calculation of Σ_M in disordered solid solutions. In

order to accomplish this, we consider the test case of MnCoGe-based alloys. MnCoGe, an orthorhombic $Pnma$ compound with a TiNiSi-type structure, shows an intermediate peak ΔS_M of -6 J kg^{-1} K^{-1} for an applied field $H = 5$ T [242]. This effect is in agreement with the calculated value of Σ_M = 1.93% [18]. However, it was reported in 2010 that inclusion of just two or three percent boron (*e.g.* $MnCoGeB_{0.02}$) in the material leads to a giant magnetocaloric effect with peak ΔS_M of up to $-47.3\,\mathrm{J\,kg^{-1}\,K^{-1}}$ [237]. This doped MnCoGe shows a coupled first-order magnetostructural transition, with a higher-symmetry hexagonal Ni_2In paramagnetic phase (Figure 3.1(a)) transforming to a magnetic phase with a mixture of TiNiSi (Figure 3.1(b)) and Ni_2In structures. The TiNiSi structure is described by a subgroup ($Pnma$) of the spacegroup of the Ni_2In structure ($P6_3/mmc$), and is formed by a displacive phase transition involving corrugation of the honeycomb Co-Ge lattice [243], as illustrated in Figure 3.1. Similar effects to those of boron-doping can also be realized with a number of other atomic substitutions, with giant magnetocaloric effects seen at disordered compositions including $MnCoGeC_{0.03}$ [237], $Mn_{0.9}Ni_{0.1}CoGe$ [238], $MnCoGe_{0.95}Ga_{0.05}$ [239], and $Mn_{0.98}CoGe$ [237].

Here, we propose a method by which the magnetic deformation proxy Σ_M can be used to screen compositionally disordered magnetic materials to identify promising magnetocaloric compositions. Σ_M for a compositionally disordered material is calculated by taking a Boltzmann-weighted average of the individual Σ_M values for enumerated ordered supercells of the disordered material. Using this technique, the qualitative magnetocaloric behavior of two solid solutions of MnCoGe are successfully reproduced: $Mn(Co_{1-x}Fe_x)Ge$ [242] and $(Mn_{1-x}Ni_x)CoGe$ [238]. In the first system, substitution of Fe for Co has has been shown to cause a modest increase in peak $-\Delta S_M$ at the intermediate composition $x = 0.2$ [242]. In the second, substitution of Ni for

Mn has been shown to lead to a much larger increase in $-\Delta S_M$, with a giant magnetocaloric effect observed at $x = 0.1$ [238]. In both cases, we show that the highly nonmonotonic behavior of the solid solution is remarkably captured by the ensembled magnetic deformation calculations, with only minor deviations. We investigate the potential energy surfaces relevant to the DFT structural optimizations of individual supercell calculations for Mn($Co_{1-x}Fe_x$)Ge and find that key cells experience double-well potentials with local minima at the hexagonal and orthorhombic structures of MnCoGe. This indicates that the ability of the structural optimization algorithm to traverse from one local minima to the other is an important consideration with regard to the results obtained from the magnetic deformation proxy calculations.

3.2 Methods

3.2.1 Supercell enumeration

For the solid solution systems studied, all possible orderings of the supercells up to a specified multiple of the volume of the 12 atom MnCoGe primitive cell ($Pnma$, TiNiSi structure) were enumerated. For the Mn($Co_{1-x}Fe_x$)Ge system, we chose two times the primitive cell volume, allowing for x increments of 1/8 across the full composition range $x = 0$ to $x = 1$. For ($Mn_{1-x}Ni_x$)CoGe, supercells up to 3 times the primitive cell volume were considered from $x = 0$ to 0.25, allowing for $x = 1/12$ and $x = 1/6$ compositions to be probed in addition to $x = 0$, 1/8 and 1/4. The Clusters Approach to Statistical Mechanics (CASM) code [244–246] was used to enumerate these symmetrically distinct configurations and determine the multiplicity of each configuration. These ordered supercells may vary in cell shape and are not, in general, simple $2\times1\times1$

or 3×1×1 stackings of the primitive cell. However, all cells do start with unit cell parameters and atomic positions consistent with the MnCoGe $Pnma$ symmetry, if the atom identity on the mixed site is ignored. Table 3.1 lists the compositions for which we apply this method along with the number of supercell configurations generated and the maximum supercell size for each composition.

For the $Mn(Co_{1-x}Fe_x)Ge$ system, a parallel set of supercells was also enumerated with the same unit cell orderings but with the atom positions and unit cell parameters adjusted to correspond to the Ni_2In-type hexagonal ($P6_3/mmc$) structure. The necessary transformation is possible for every supercell of the TiNiSi structure because $Pnma$ is a subgroup of $P6_3/mmc$ and therefore the Ni_2In structure type can always be expressed within a $Pnma$-compatible unit cell.

$MnCo_{1-x}Fe_xGe$			$Mn_{1-x}Ni_xCoGe$		
x	count	$V_{\max}$	x	count	$V_{\max}$
0	1	1	0	1	1
0.125	7	2	0.0833	9	3
0.25	29	2	0.125	7	2
0.375	41	2	0.1667	71	3
0.5	58	2	0.25	184	3
0.625	41	2			
0.75	29	2			
0.875	7	2			
1	1	1			

Table 3.1: Compositions considered (labeled by x) and the number (count) of symmetrically distinct, ordered supercells with composition x for the $Mn(Co_{1-x}Fe_x)Ge$ and $(Mn_{1-x}Ni_x)CoGe$ systems. For each composition, $V_{\max}$ is the volume of the largest supercells enumerated, in multiples of the primitive cell volume.

3.2.2 Magnetic deformation

For each enumerated cell, the magnetic deformation Σ_M was calculated following the procedure given in Ref. 18. The optimized structure for each configuration was acquired using density functional theory (DFT) with and without spin polarization. Calculations were performed using the Vienna *ab initio* simulation package (VASP) [128] using the generalized gradient approximation (GGA) exchange-correlation functional as parameterized by Perdew, Burke and Ernzerhof [129, 131]. Spin-orbit coupling was not included. For each configuration, the spin-polarized relaxations were initialized with magnetic moments of 3.0 μ_B on each transition metal ion.

Meshes for DFT calculations were automatically generated with the number of k-points set to 2500 divided by the number of atoms in the cell. Structural optimizations were performed using the conjugate gradient algorithm with an energy convergence criterion of 10^{-3} eV. The structural relaxations were run iteratively until the volume change between subsequent relaxations was less than 2%. Once this convergence parameter was met, a final electronic optimization was performed for each enumeration while keeping the structure fixed. The Python packages `pymatgen` and `custodian` [132] were used to automate, monitor, and analyze the VASP calculations.

Based on the obtained optimized structures, the magnetic deformation Σ_M is calculated as the degree of lattice deformation (%) [87, 133] between the DFT optimized nonmagnetic and magnetic structures. This is obtained by finding the transformation matrix between the two relaxed structures: $\mathbf{P} = \mathbf{A}_{\mathrm{NM}}^{-1}\mathbf{A}_{\mathrm{M}}$, where $\mathbf{A}_{\mathrm{NM}}$ and $\mathbf{A}_{\mathrm{M}}$ are the lattice vectors of the nonmagnetic and magnetic relaxed unit cell, respectively. The Lagrangian finite strain tensor (which removes any rotational component of $\mathbf{P}$) is then calculated as $\boldsymbol{\eta} = \frac{1}{2}(\mathbf{P}^{\mathrm{T}}\mathbf{P} - \mathbf{I})$, and the magnetic deformation is obtained as the root-

mean-squared eigenvalues of $\boldsymbol{\eta}$:

$$\Sigma_M = \frac{1}{3}(\eta_1^2 + \eta_2^2 + \eta_3^2)^{1/2} \times 100\,\%. \tag{3.1}$$

For the Mn($Co_{1-x}Fe_x$)Ge system, in addition to the magnetic deformation calculated using only orthorhombic starting cells, a global Σ_M was calculated for each cell based on the lowest energy nonmagnetic and the lowest energy magnetic structure obtained in either the run that started with the hexagonal structure or the run that started with the orthorhombic structure.

Although it is well-established that DFT often fails to localize $3d$ transition metal electrons enough to accurately model the moments in magnetic intermetallics, we chose not to include any Hubbard U correction terms in order to keep the calculations as simple (and generalizable) as possible, and to maintain compatibility with our previous work [18] where it was found that Σ_M performs well as a proxy for magnetocaloric effect across a diverse range of compounds without the use of U. While we believe a GGA+U approach could allow for the more faithful reproduction of magnetic and structural ground states observed in experiment, this method increases computational cost and requires careful selection of U terms for each individual transition metal element in the compound, making it difficult to generalize to a high-throughput search.

3.2.3 Modeling disorder

We consider the aggregate Σ_M for a given composition labeled by x to be determined by an ensemble of the ordered supercells. The aggregation may be done by a weighted average of the calculated Σ_M for each ordering i using the multiplicity Ω_i as the weight:

$$\Sigma_{M,\text{avg.}} = \frac{\sum_i \Omega_i \Sigma_{M,i}}{\sum_i \Omega_i} . \tag{3.2}$$

A more complete picture, however, considers the calculated energy of each enumeration, considering that low energy states are more likely to be present in a true sample of a disordered alloy. To approximate this, we define the Boltzmann weight of a configuration i with composition x as

$$w_i = \Omega_i \exp\left(\frac{E_i - E_0}{k_B T}\right) \tag{3.3}$$

such that the Boltzmann-weighted average Σ_M is

$$\Sigma_{M,\text{Boltzmann}} = \frac{\sum_i w_i \Sigma_{M,i}}{\sum_i w_i} . \tag{3.4}$$

Here, E_i is the spin-polarized energy of supercell i, expressed *per* the maximum supercell size (*i.e.* in units of eV *per* 24 or 36 atoms). E_0 is the energy of the lowest-energy enumeration for the composition x, and k_B is the Boltzmann constant. The temperature T was set to 300 K. In addition, we also tested setting the temperature to the preparation temperatures of the alloys (around 1000 K), and this did not dramatically change the presented results.

In addition to enumerating small supercells, we also tried calculations of Σ_M on special quasirandom structures, a different method commonly used for DFT modeling of alloys [247, 248]. In this method, an alloy composition is modeled by a single large supercell (here, 48 atoms) with occupation of the atomic sites chosen so as to match the near-neighbor correlations of the true infinite disordered compound as well as possible.

Unfortunately, this method was not as successful as the supercell enumeration method for the tasks investigated presently. For a discussion of these calculations, the reader is directed to the Appendix section 3.4.1.

3.2.4 Transition paths

In order to investigate the potential energy surfaces which control the DFT structural relaxations used to calculate Σ_M, we performed transition path calculations on a few selected atomic supercells of Mn($Co_{0.75}Fe_{0.25}$)Ge between their hexagonal and orthorhombic structures. Lattice parameters and atom positions of structures along the path are interpolated between the end members, which are the relaxed hexagonal ($d = 0$) and orthorhombic ($d = 1$) structures. The energies of structures along this path were calculated without structural relaxation.

3.3 Results and Discussions

Experimental peak $-\Delta S_M$ values and computed Σ_M data for the Mn($Co_{1-x}Fe_x$)Ge system are shown in Figure 3.2. MnCoGe and MnFeGe are both ferromagnets, and the full solid solution between them can be prepared experimentally [242]. This solid solution features a transition from the orthorhombic $Pnma$ structure of MnCoGe at $x < 0.2$ to the hexagonal $P6_3/mmc$ structure of MnFeGe at $x > 0.2$ [242]. Across this series, peak $-\Delta S_M$ decreases as x increases, except for at the phase boundary ($x = 0.2$), where a peak in $-\Delta S_M$ reaching $9\,\mathrm{J\,kg^{-1}K^{-1}}$ for an applied field of 5 T is observed. Figure 3.2(c) shows the energies of the individually enumerated supercells relative to the energies of the corresponding mixture of MnCoGe and MnFeGe. Many orderings

across the full compositional range show negative formation energies, consistent with the experimental observation that the solid solution forms and does not phase segregate. As seen in Figure 3.2(b), the calculated Σ_M values for individual ordered cells span a range of values, from about 0.75% to 2.25%. The simple average of these Σ_M values somewhat follows the experimental trend of a general decrease in ΔS_M with increasing x interrupted by a peak near the middle of the compositional range. However, the position and magnitude of the peak in Σ_M are far off from the experimental results, and therefore the correspondence between computation and experiment is poor. On

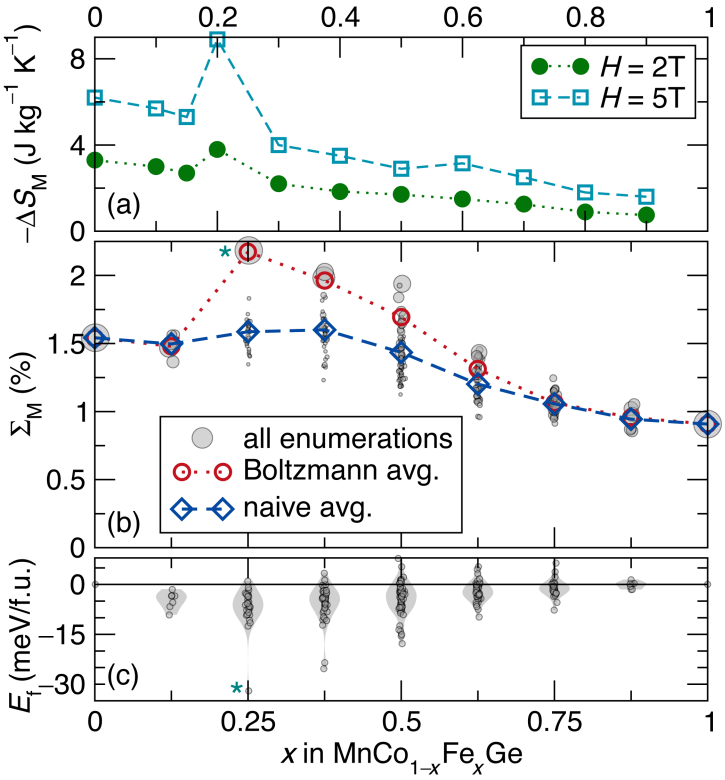

Figure 3.2: Comparison of (a) peak ΔS_M values as measured by Lin *et al.* for applied fields of 2 T and 5 T [242] and (b) calculated Σ_M *vs.* x for Mn(Co$_{1-x}$Fe$_x$)Ge. In (b), each gray circle represents a single enumerated cell, with the area of each circle proportional to its Boltzmann weight as calculated in equation 3.3. Both Boltzmann (equation 3.4) and naive (equation 3.2) averages of Σ_M for composition x are overlaid. (c) Energy of formation *vs.* x for each cell. The asterisk indicates the cell indicated as cell B in Figure 3.5. The gray shaded areas (violin plot) visualize the distribution of the supercell energies.

the other hand, the Boltzmann-weighted average gives an excellent qualitative match, with a maximum Σ_M at $x = 0.25$, the closest computed composition to the peak in the experimental data ($x = 0.2$). The peak in Σ_M is broader than that seen in the ΔS_M data; however, the qualitative match is remarkable given the simplicity of the computational model and the many variables involved in the experimental preparation and measurement of a magnetocaloric material.

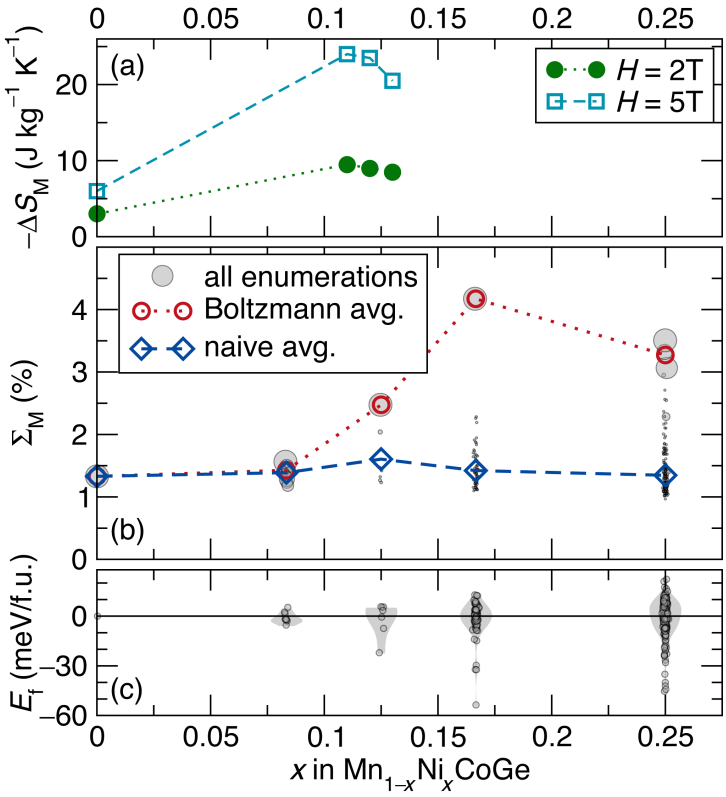

Figure 3.3: Comparison of (a) experimental peak ΔS_M values as measured by Zhang *et al.* [238] and (b) calculated Σ_M for $(Mn_{1-x}Ni_x)CoGe$ ($x \leq 0.25$). (c) Energies of formation *vs.* x for the enumerated cells. Refer to the Figure 3.2 caption for additional definitions.

Figure 3.3 shows the same analysis for a different solid solution of MnCoGe, the $(Mn_{1-x}Ni_x)CoGe$ system. In this case, introduction of a small amount of Ni ($\approx 11\%$) has been found to result in a giant magnetocaloric effect with peak $-\Delta S_M$ reaching $24\,J\,kg^{-1}K^{-1}$ for an applied field of 5 T [238]. As in the $Mn(Co_{1-x}Fe_x)Ge$ system, this

is due to the coincidence of magnetic and structural transitions, *i.e.* due to a first-order magnetostructural transition, observed for samples with x between 0.08 and 0.12 (for $x < 0.08$ and x slightly greater than 0.12, the structural and magnetic transitions occur at different temperatures). As alloying across the whole composition space $0 \leq x \leq 1$ has not yet been reported, in order to set a reasonable limit to the computational cost, Σ_M was calculated only for $x \leq 0.25$ for this system (Figure 3.3). For this compositional range, the calculations presented here reproduce the experimental ΔS_M reports with a similar level of success as the study of the Mn($Co_{1-x}Fe_x$)Ge system discussed above. While the maximum Σ_M is slightly misaligned from the experimental largest $-\Delta S_M$ ($x = 0.167$ *vs.* $x = 0.11$, respectively), the qualitative shape and the magnitude of the Σ_M curve matches nicely to the experiment.

A direct comparison of the two systems under study reveals that the maximum Σ_M is 2.1 times larger in the ($Mn_{1-x}Ni_x$)CoGe system than in the Mn($Co_{1-x}Fe_x$)Ge system. Similarly, the ratio of the maximum Boltzmann averaged Σ_M values is 2.7. Even without experimental references, a computational screen comparing these two systems would correctly conclude that ($Mn_{1-x}Ni_x$)CoGe is a more promising candidate system of experimental study. Furthermore, such a conclusion would be reached even if we had only considered supercells of up to size $V_{\max} = 2$ (24 atoms) for both systems. While the peak in Σ_M at $x = 0.167$ (1/6) in ($Mn_{1-x}Ni_x$)CoGe would not have been captured, the Σ_M at $x = 0.25$ is still large enough relative to any values in the Mn($Co_{1-x}Fe_x$)Ge system to suggest that Ni is a more interesting dopant. A comparison of Σ_M and ΔS_M values for the two systems on the same scale may be found in the Appendix Figure 3.10.

In addition to Σ_M and cell energy, we obtain information from our calculations about the evolution of magnetic moments in these solid solutions. Figure 3.4 shows the

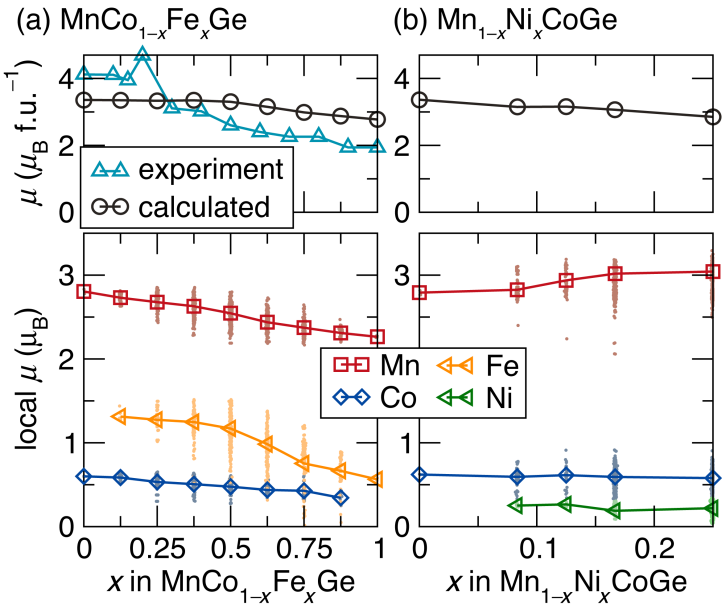

Figure 3.4: Total (top) and local (bottom) evolution of the DFT magnetic moments for (a) $Mn(Co_{1-x}Fe_x)Ge$ and (b) $(Mn_{1-x}Ni_x)CoGe$. All of the individual transition metal local moments from individual enumerated cells are shown as small dots, while the Boltzmann-averaged local and total moments are shown as larger symbols connected by lines. For $Mn(Co_{1-x}Fe_x)Ge$, experimentally measured 5 K saturated total magnetic moments from Lin *et al.* [242] are plotted for comparison.

DFT total moment (top) and projected local moments (bottom) for $Mn(Co_{1-x}Fe_x)Ge$ and $(Mn_{1-x}Ni_x)CoGe$. As with the ensembled Σ_M calculations, the total and local moments shown are a Boltzmann-weighted average of all of the moments in all of the enumerated supercell calculations. However, in this case, there are not substantial differences between Boltzmann-weighted and simple averages. In the case of $Mn(Co_{1-x}Fe_x)Ge$, a comparison to the reported experimental saturated moments at 5 K is included [242], while we were unable to find such data for $(Mn_{1-x}Ni_x)CoGe$. From this comparison, we see that the calculated moment is underestimated for MnCoGe and overestimated for MnFeGe. As discussed in the methods section, it is likely that a more faithful reproduction of the experimental moments would require a GGA+U approach. However, the general trend of decreasing moment with increasing Fe content is captured by our calculations, and we can therefore use these results to draw insight

into the local magnetic moment evolution. As Fe atoms are substituted in, they are found to hold a larger local moment than the Co atoms they replace (about 1 μ_B *vs.* 0.5 μ_B). However, at the same time, the large Mn moments decrease in magnitude with increasing x. The net effect is a decrease in total moment with x. In $(Mn_{1-x}Ni_x)CoGe$, a decrease in total moment with x is also predicted; however, in this case, the decrease is driven by the replacement of high-moment Mn atoms (3 μ_B) with Ni atoms which have very small moments (about 0.25 μ_B).

Returning to the Σ_M results, we noticed that for the compositions showing maximal Boltzmann-averaged Σ_M ($x = 0.25$ for $Mn(Co_{1-x}Fe_x)Ge$ and $x = 0.175$ for $(Mn_{1-x}Ni_x)CoGe$), the Boltzmann averages are dominated by a single enumerated cell which has significantly lower energy than the rest of the cells. For example, in Figure 3.2(c), the energy of formation for all of the enumerated cells is plotted *versus* x. At $x = 0.25$, the cell marked with an asterisk is about 20 meV f.u.$^{-1}$ lower in energy than all the other cells, and therefore contributes dominantly to the Boltzmann-averaged Σ_M. This special unit cell also exhibits a larger Σ_M than any of the other enumerations, and as a result this single cell is entirely responsible for the peak at $x = 0.25$ in the Boltzmann-averaged Σ_M. Inspection of the calculations for this special cell revealed that the magnetic structural optimization resulted in a cell with atom positions consistent with the hexagonal structure (Figure 3.1(a)), while the nonmagnetic structural optimization stayed in the orthorhombic structure (Figure 3.1(b)) with which the calculation was initialized. For the other enumerations at $x = 0.25$, both the magnetic and nonmagnetic unit cells remained in the orthorhombic structure.

To understand this, we turned to calculations of the transition path energies between the hexagonal and orthorhombic structures of two representative enumerated cells with $x = 0.25$: cell A is a cell that stayed in the orthorhombic structure for both

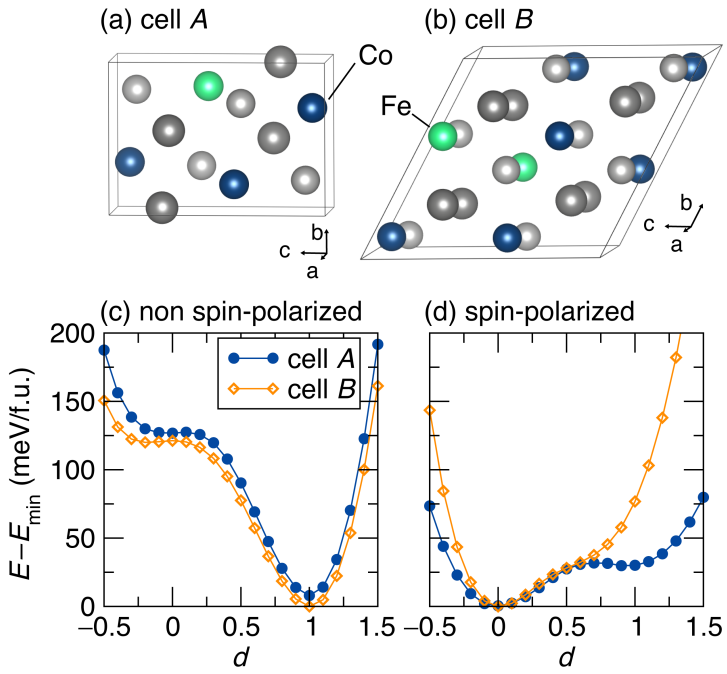

Figure 3.5: Transition path energies between the hexagonal (MnFeGe-like, $d = 0$) and orthorhombic (MnCoGe-like, $d = 1$) structures of two different enumerated configurations of $MnCo_{0.75}Fe_{0.25}Ge$, (c) without and (d) with spin polarization. (a) Cell *A* shows a transition path landscape which is characteristic of that experienced by the majority of the enumerated cells, which remain orthorhombic after both nonmagnetic and magnetic structural relaxations. (b) Cell *B* is the special cell marked by an asterisk in Figure 3.2, which transformed to the hexagonal structure during the spin-polarized relaxation.

magnetic and nonmagnetic optimizations, and cell B is the special cell that changed structures during the magnetic optimization. For each cell, Figure 3.5 shows the energies of the transition paths with and without spin-polarization as functions of the fractional hexagonal distortion d, with $d = 0$ corresponding to the hexagonal structure, and $d = 1$ to the orthorhombic structure. Interestingly, for both cells, the nonmagnetic calculation shows a global minimum at the orthorhombic structure while the magnetic calculation shows a global minimum at the hexagonal structure. As the enhanced magnetocaloric effect around $x = 0.2$ in $Mn(Co_{1-x}Fe_x)Ge$ is believed to arise from coupling of the magnetic transition to a structural transition, it is interesting to note that the

inclusion of magnetism in the DFT calculation changes the predicted structural ground state. However, it is also important to note that the nonmagnetic DFT calculation should not be considered a realistic model for the true high-temperature paramagnetic state.

The transition path energies without spin polarization look qualitatively similar for cell A and cell B, with a very shallow local minimum at the hexagonal structure and a global minimum at the orthorhombic structure. In contrast, with spin polarization, greater differences between the two cells are evident. Cell A exhibits a double well potential with a barrier between the wells, while cell B has no barrier to relaxation into the global minimum hexagonal structure. As the optimizations used to calculate Σ_M were initialized with an orthorhombic starting configuration, cell A relaxed into the orthorhombic local minimum, while cell B was able to relax into the global minimum structure. As a result of this feature of its potential energy surface, the DFT calculations on cell B result in a lower energy and larger magnetic deformation than all other cells enumerated at this composition. We can therefore conclude that the effectiveness of the magnetic deformation proxy in identifying the extremal magnetocaloric composition in this system is driven by the ability to conveniently identify a potential energy surface with competing structural ground states whose energies are coupled to the system magnetism, and which has low barriers to relaxation from one state to the other. These features are consistent with the thermodynamic conditions necessary for a first-order magnetostructural transition leading to an enhanced magnetocaloric effect.

Based on this analysis, we proceed to consider what role the incomplete structural relaxations in cells like cell A played in the evaluation of the overall Σ_M. To address this, a parallel set of DFT calculations was run with the enumerated supercells initialized in the hexagonal structure, instead of the orthorhombic structure. The

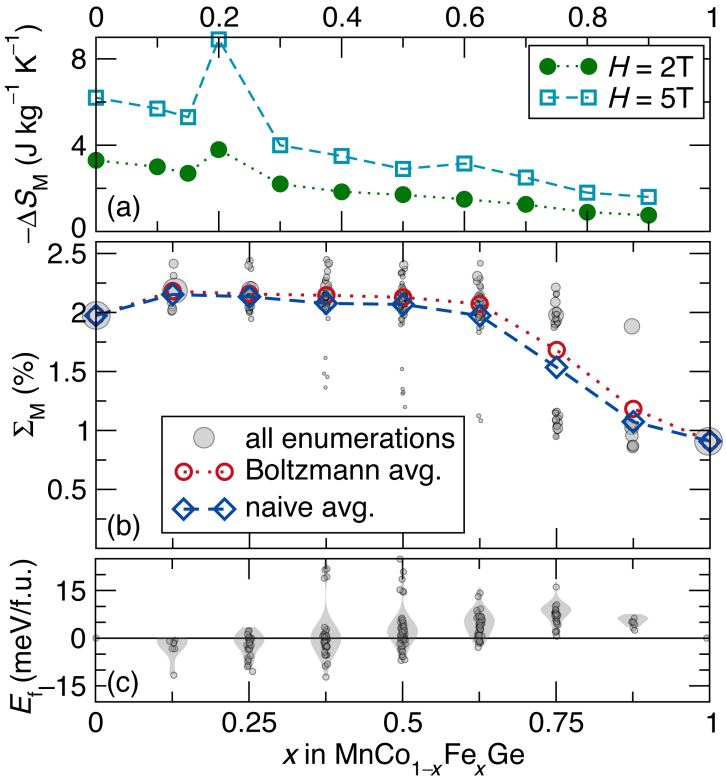

Figure 3.6: Comparison of peak ΔS_M values as measured by Lin *et al.* [242] (a) and calculated Σ_M *vs.* x (b) for Mn(Co$_{1-x}$Fe$_x$)Ge using global Σ_M values computed from calculations starting from both the orthorhombic and hexagonal structures, as discussed in the text. Please refer to the Figure 3.2 caption for definitions.

nonmagnetic and magnetic structures used in calculating Σ_M were then each taken from the calculation that reached a lower energy state. The results are shown in Figure 3.6, which can be compared to Figure 3.2 in which only the orthorhombic initialization was considered. Providing an alternate path to relaxation for each cell increases the likelihood that the global energetic minimum is reached for each of the nonmagnetic and magnetic optimizations. As a result, more cells change structure type between the nonmagnetic and magnetic unit cells and the $\Sigma_{M,i}$ values increase. Both the Boltzmann and simple weighted averages of Σ_M are seen to increase for all $x < 0.8$ in the Mn(Co$_{1-x}$Fe$_x$)Ge system such that the strong peak seen before at $x = 0.2$ for the Boltzmann-averaged Σ_M is smeared out and the qualitative match with the experimen-

tal data is weakened. Nevertheless, the composition and magnitude of the peak in Σ_M remains very similar to the original calculations. Furthermore, this approach results in the Boltzmann and naive averages converging to nearly the same values for each composition. Therefore, if using this strategy to screen magnetocaloric systems, one does not necessarily need to exhaustively perform DFT calculations on all possible enumerations; rather, reasonably accurate results could be obtained by averaging together a small number of $\Sigma_{M,i}$ values (*i.e*, 5 – 10 cells) for each composition x.

Summary and Conclusions

In this work, we introduce a method for screening experimental magnetocaloric behavior in disordered compounds (alloys) which employs the magnetic deformation proxy Σ_M in conjunction with the enumeration of relatively small supercells of various compositions. We validate its screening utility by direct comparison to reported experimental ΔS_M measurements in Mn($Co_{1-x}Fe_x$)Ge and ($Mn_{1-x}Ni_x$)CoGe, two systems where the magnetocaloric performance depends on x in a highly nonmonotonic manner. In both cases, the method successfully predicts the presence and magnitude of enhanced magnetocaloric effects in the solid solutions compared to MnCoGe, reproducing the qualitative shape of the ΔS_M *vs.* x curves and identifying the compositions of the largest magnetocaloric effect with errors of $\delta x \approx 0.05$.

Figure 3.7 provides a summary of these results, showing the correspondence between predicted Σ_M and experimental peak ΔS_M as compared to previous results applying Σ_M to 33 ferromagnets without substantial atomic site disorder [18]. On this plot, all of the calculated x points from the Mn($Co_{1-x}Fe_x$)Ge system (Figure 3.2) are plotted against the $-\Delta S_M$ of the nearest composition experimentally reported by Lin *et*

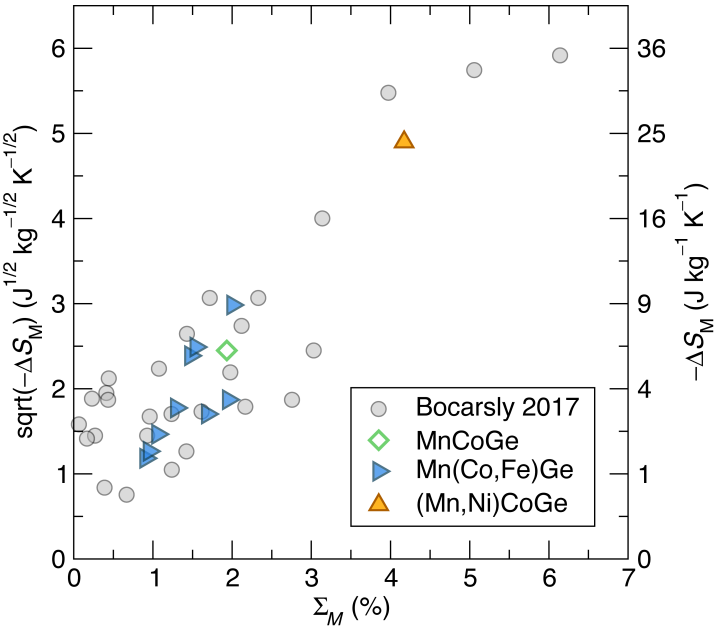

Figure 3.7: Correspondence between peak values of experimental $-\Delta S_M$ for an applied field of 5 T and magnetic deformation Σ_M. Gray circles show the results from Ref. 18, which considered only ordered magnets.

al. [242]. In $(Mn_{1-x}Ni_x)CoGe$, where the experimental data are more sparse and the composition with maximal Σ_M somewhat deviates from the reported largest $-\Delta S_M$ [238], the maximum Σ_M (at $x = 0.167$) is plotted against the maximum $-\Delta S_M$ (at $x = 0.11$). This plot demonstrates that the magnetocaloric effects of these complex disordered systems are being screened with comparable accuracy to prior predictions of ordered magnets.

The success of Σ_M in predicting behavior of these complex MnCoGe-based magnetocalorics demonstrates that screening disordered magnetocalorics is a promising route towards the discovery of exceptional magnetocaloric effects at unstudied compositions. This screening technique requires no information about the system other than the known crystal structure of the parent compound (here, MnCoGe), and therefore we believe this approach will be quite generally applicable. Due to the many supercells sampled (on the order of 200 for each system), the computational cost of

obtaining Σ_M on solid solutions is much larger than the cost of screening compounds without compositional disorder. Nevertheless, it would be feasible to apply this screening method to searches on the order of tens, or perhaps hundreds, of systems. For example, this method could be used to exhaustively screen elements for promise as dopants for MnCoGe or another magnetocaloric material of interest.

3.4 Appendix: Supplemental material

3.4.1 Special Quasi-random Structure calculations

Special quasirandom structures (SQSs) with different values of x in Mn($Co_{1-x}Fe_x$)Ge ($0 \leq x \leq 1$) and ($Mn_{1-x}Ni_x$)CoGe ($x \leq 0.25$) were generated using the `mcsqs` utility [248]. An SQS is a single disordered supercell of finite size, constructed such that the local atomic correlation distributions match well those of an infinite randomly distributed alloy. In this case, SQS unit cells containing 48 atoms (four times the primitive orthorhombic TiNiSi-structured cell) were generated to have pair, triplet, and quadruplet correlations of radius ≤ 6 Å that best match the random state. The 48-atom cells allow for compositions with x-spacing of 0.0625.

As shown in Figure 3.8 and Figure 3.9, this approach results in Σ_M that closely matches the naive (non-energy-weighted) average of the enumerated supercells, but deviates from the Boltzmann average. This makes sense, as the SQS attempts to reproduce a fully random alloy, with no preference for energetically favorable local configurations. Unfortunately, this means that the SQS does not do a good job of predicting experimental ΔS_M in this system.

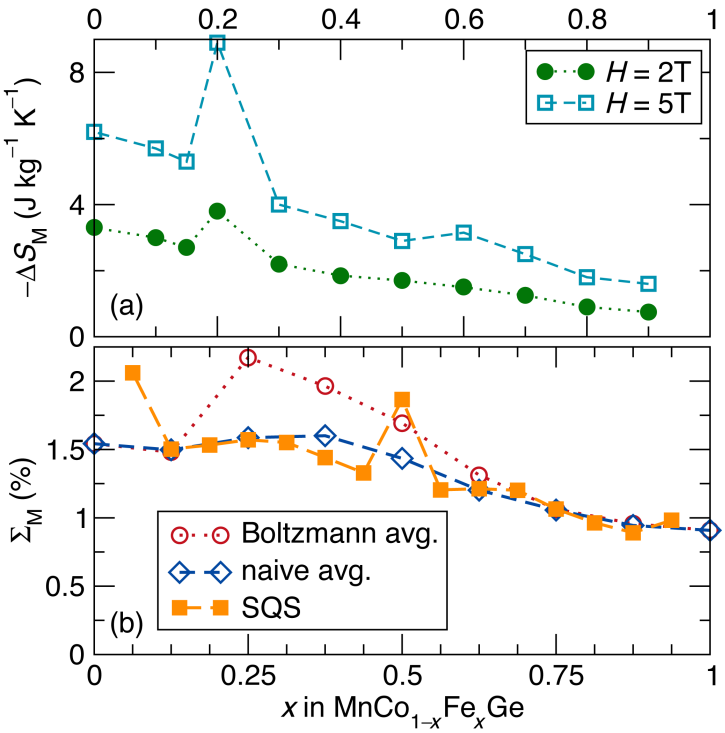

Figure 3.8: (b) Σ_M for Mn(Co$_{1-x}$Fe$_x$)Ge calculated using special quasirandom structures (SQSs) with 48 atoms each is shown compared to Σ_M calculating using the supercell approach (main text Figure 3.2) with either naive averaging (equation 3.2) or Boltzmann averaging (equation 3.4). (a) shows the experimental peak ΔS_M for applied fields of 2 T and 5 T, as reported by Lin *et al.* [242]. The SQS approach gives results similar to the naive average of the supercells, with some deviations.

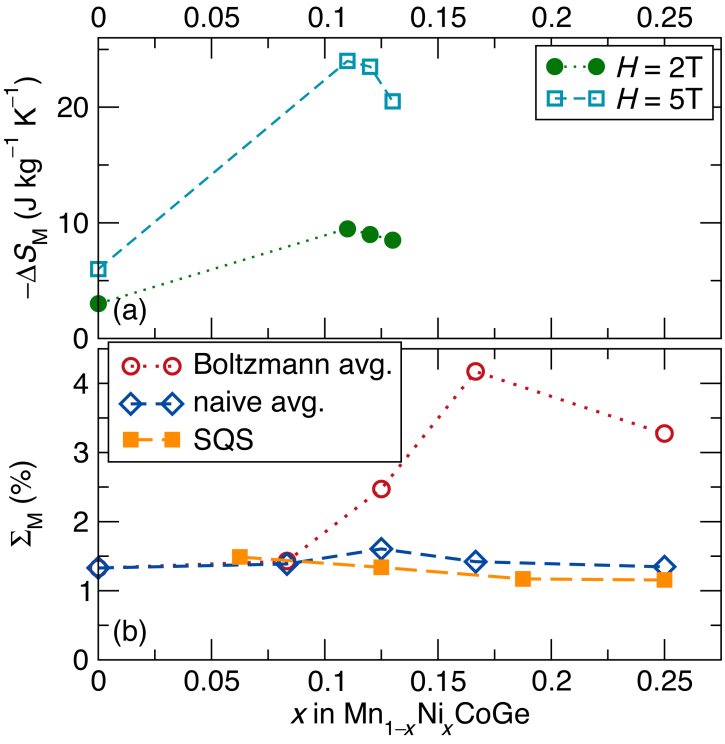

Figure 3.9: (b) Σ_M for $(Mn_{1-x}Ni_x)CoGe$ ($x \leq 0.25$) calculated using special quasirandom structures (SQSs) with 48 atoms each is shown compared to Σ_M calculating using the supercell approach (main text Figure 3.3) with either naive averaging (equation 3.2) or Boltzmann averaging (equation 3.4). (a) shows the experimental peak ΔS_M for applied fields of 2 T and 5 T, as reported by Zhang *et al.*[238]. The SQS structure gives results similar to the naive average of the supercells.

3.4.2 Comparison of Σ_M and peak ΔS_M for Mn(Co$_{1-x}$Fe$_x$)Ge and (Mn$_{1-x}$Ni$_x$)CoGe

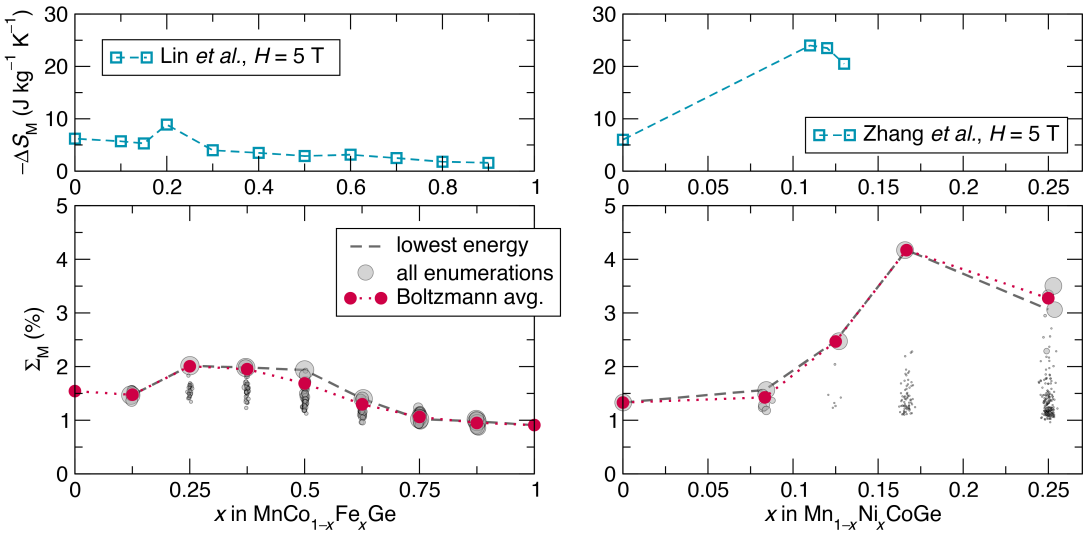

Figure 3.10: Direct comparison of computed Boltzmann-averaged magnetic deformation (Σ_M) and reported peak ΔS_M [238, 242] for Mn(Co$_{1-x}$Fe$_x$)Ge and (Mn$_{1-x}$Ni$_x$)CoGe ($x \leq 0.25$). This data is reproduced from the main text Figure 3.2 and Figure 3.3, but presented with the same y-axis scaling to show the magnitude differences between the two systems.

Chapter 4

Competition between magnetism and bonding drives magnetostructural coupling in MnAs

[1] Chapters 2 and 3 have demonstrated that magnetostructural coupling, in a generic sense, controls the magnetocaloric effect. Here, density functional theory calculations are used to investigate the specific origins and implications of the coupling between magnetism and crystal structure in one material. An understanding of the origins of giant magnetostructural coupling is developed for the compound MnAs, a magnetic material that has served as a prototype for many promising technologies including caloric refrigeration, magnetic actuation, and spintronics. Electronic structure calculations reveal that the strong coupling between magnetism and crystal structure arises from an orbital-specific competition between exchange energies and kinetic (bonding) energies and that thermally activated spin-fluctuations drive the unusual first-order phase tran-

[1] This chapter is adapted from a manuscript in preparation: J. D. Bocarsly, M. Johannes, S. D. Wilson, R. Seshadri, Magnetostructural coupling from competing exchange and chemical bonding.

sition from high to low symmetry upon heating. The underlying mechanism raises the prospect of an exotic paramagnetic state featuring local fluctuations in atomic positions and bonding on the time scale of the moment fluctuations. The results should inform the design of new materials with enhanced magnetostructural coupling, at the border between structural and magnetic stability.

This project was performed in collaboration with Michelle Johannes and was supervised by Stephen Wilson, and Ram Seshadri. Professor Chris Van de Walle is thanked for helpful discussions in the early stages of this project.

4.1 Introduction

Since the 1950s [89, 95, 249–252], MnAs has served as the prototypical material for strong coupling between magnetism and crystal structure. A dramatic first-order magnetostructural phase transition is observed at $T_C = 318\,\mathrm{K}$, whereupon the ferromagnetic (FM) hexagonal structure transforms to a paramagnetic (PM) orthorhombic structure with a 2.5% smaller unit cell volume. As the temperature is further increased, the hexagonal structure is recovered *via* a continuous transition around $T_t = 398\,\mathrm{K}$. The transition at T_C is of great interest because it can be actuated by temperature, field, and mechanical stress. In particular, a moderate magnetic field can be used to drive giant entropy changes in MnAs, enabling magnetic refrigeration based on the magnetocaloric effect [12, 70, 82]. Other promising magnetocalorics, such as $Gd_5(Si,Ge)_4$, MnFe(P,X), and doped $LaMnO_3$ display similarly strong magnetostructural coupling [18, 85, 102, 236, 253]; it is evident that, to advance magnetocaloric technology, a microscopic and mechanistic understanding of giant magnetostructural coupling is needed. More generally, it is of interest to determine how the various interactions in

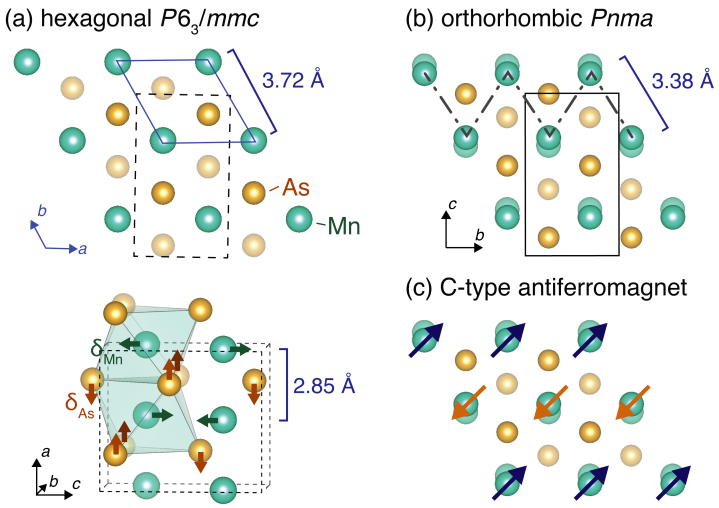

Figure 4.1: Structure of MnAs in its (a) hexagonal and (b) orthorhombic forms. In (a), the orthohexagonal cell is shown in dashed lines and, at the bottom, the arrows indicate the directions of the atomic displacements that create the orthorhombic structure. (c) The previously proposed C-type antiferromagnetic structure of the orthorhombic phase. All correlations out of the shown plane are ferromagnetic.

metallic magnets, including Hund's coupling, magnetic exchange, and chemical bonding can be leveraged to couple degrees of freedom towards multifunctional behavior.

In the ground state hexagonal structure of MnAs, Mn atoms are arranged on a hexagonal lattice (Figure 4.1). The Mn atoms have large spacing (3.72 Å) within the basal plane, while there is short spacing (2.85 Å) perpendicular to the plane, through face-connected octahedra. Upon heating above 318 K or applying pressures above 2 kbar [254], first-order transitions to orthorhombic symmetry are observed (Figure 4.1(b)). During these transitions, alternating rows of Mn atoms move towards each other within the plane to create Mn–Mn zigzag chains with contacts lengths of 3.38 Å, while alternating rows of As atoms move a similar distance in the perpendicular direction. In this letter, we refer to the magnitudes of these modes within the orthorhombic cell as $\delta_{\mathrm{Mn}} = \Delta\,\mathrm{Mn}_z/c$ and $\delta_{\mathrm{As}} = \Delta\mathrm{As}_x/a$, indicating deviations of the atoms' fractional coordinates from their ideal hexagonal position. At 318 K and ambient pressure, δ_{Mn}

and δ_{As} are about 0.027 and 0.025, respectively [255].

There have been numerous attempts to explain the behavior of MnAs [89, 95, 252, 256–259]. Goodenough and coworkers proposed that the transitions are Mn^{3+} high-spin to low-spin transformations [71, 252, 254]. Conversely, Bean and Rodbell proposed a phenomenological model where a first-order transition can be realized in a sufficiently compressible material with a strongly volume-dependent magnetic exchange [89, 95]. This approach has found widespread success in modeling materials with magnetostructural coupling, but does not provide a microscopic mechanism for the phenomenology. Recent computational effort has come to the conclusion that the orthorhombic structure above T_C is actually antiferromangetic (AFM), with the Mn moments alternating direction along the zigzag chains (C-type AFM, Figure 4.1(c)) [114, 256, 260, 261]. However, neutron diffraction points to a PM state without long-range order [251], and paramagnetic scattering experiments [262, 263] and chemical substitution studies [264] indicate ferromagnetic correlations and a local moment magnitude that remains approximately constant across T_C. Microscopic understanding consistent with the experimental situation has, so far, clearly been missing. Furthermore, a variety of unusual physical properties reported in MnAs are largely unexplained, including the presence of large amounts of local disorder [100, 265], anomalous elastic properties [98, 99], and extremely low thermal conductivity [266]

Here, we use electronic structure calculations on ordered and disordered magnetic states to establish physical mechanisms for both the pressure-driven and temperature-driven phase transitions in MnAs. Both transitions are found to arise from an orbital-specific competition between exchange energies (intra-atomic Hund's coupling and inter-atomic magnetic exchange), which favor the hexagonal state, and kinetic energy/chemical bonding, which favors the orthorhombic states. Furthermore, our calcu-

lations suggest that this competition becomes dynamic in the paramagnetic phase as magnetic fluctuations are coupled to large atomic displacements accompanied by the formation and dissolution of chemical bonds.

4.2 Results and discussions

We began our investigation by performing density functional theory-based calculations (DFT) [128–130] on MnAs using a generalized gradient approximation (PBEsol [131, 267]). Starting with the experimental ambient pressure hexagonal [268] and orthorhombic [255] structures and ferromagnetic moments, we fully relaxed the lattice parameters and internal atomic coordinates. This resulted in cells with volumes respectively 13% and 19% *smaller* than experiment, in contrast with the typical slight overestimation of volumes associated with the PBEsol approximation [269]. Additionally, the DFT energy of the orthorhombic cell was found to be lower than that of the hexagonal cell by 181 meV f.u.$^{-1}$, a result that is clearly unphysical given that, experimentally, the ground state is ferromagnetic and hexagonal. Previous DFT studies have not addressed this inconsistency [114, 270], presumably because a full relaxation into the global orthorhombic minimum was not investigated.

Employing the DFT+U electron correlation correction, using the $U - J = U_{\text{eff}}$ formalism of Dudarev [271], localizes the Mn d states that are systematically too diffuse in standard DFT [272] and brings both the lattice parameters and magnetic moments (3.4 μ_B *per* Mn) of the hexagonal cell into good agreement with experiment for $U_{\text{eff}} = 1.2$ eV (see Appendix Figures 4.8 and 4.9). Perhaps more importantly, this U_{eff} proves to be the critical variable to correct the trend in energetics, and the hexagonal cell is now 92 meV f.u.$^{-1}$ lower in energy than the orthorhombic one. The orthorhom-

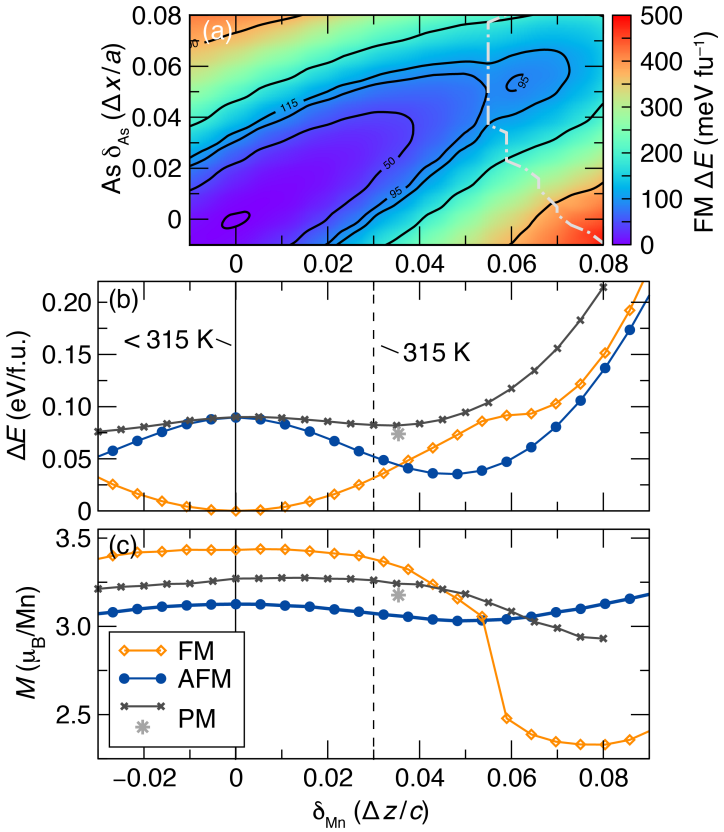

Figure 4.2: (a) 2D energy surface of ferromagnetic MnAs as a function of Mn distortion and As distortion. (b) 1D energy surfaces of ferromagnetic (FM), antiferromagnetic (AFM), and paramagnetic (PM) MnAs as a function of Mn distortion. (c) Corresponding Mn local moment magnitudes.

bic cell has a smaller moment of 2.4 μ_B *per* Mn, which, along with its lattice parameters, closely matches the experimental state obtained at low-temperatures by applying pressure [273]. This indicates that the pressure-driven phase transition is consistent with the Goodenough picture of a high-moment to low-moment transition. However, the volume of this cell is 16% smaller than the ambient pressure orthorhombic cell observed above T_C and has a much larger Mn distortion (δ_{Mn} of 0.061 *vs.* 0.027); therefore this low-moment cell cannot explain the thermally-driven transition at T_C.

Proceeding with $U_{\mathrm{eff}} = 1.2$ eV, we investigated the energy surface of ferromagnetic MnAs during its transition from high-moment hexagonal to low-moment orthorhom-

bic, as a continuous function of δ_{Mn} and δ_{As}. Figure 4.2(a) shows 2D energy surface composed of 900 calculations where Mn z and As x positions were held fixed, while all other coordinates and the cell were allowed to freely relax. We obtain a double-welled energy surface with local minima at the hexagonal structure (0,0) and in the heavily-distorted low-moment orthorhombic structure discussed above (0.061, 0.053). This analysis shows that the transition is driven primarily by the Mn distortion: moving the Mn atoms without movement of the As atoms can trigger the transition, but not *vice-versa*. We therefore proceed to plot the 1D energy surface and local Mn magnetic moment as a function of δ_{Mn} only (Figure 4.2(b-c)), where the As x position is now allowed to freely relax along with the other structural parameters. The most notable feature is the sharp drop in the magnetic moment from 3.4 μ_{B} to 2.4 μ_{B} as the hexagonal-to-orthorhombic phase boundary is crossed.

When we instead impose the C-type AFM structure, the energy surface looks very different, with the hexagonal structure now at a maximum in energy. The double well is replaced by a single energy minimum found at $\delta_{\mathrm{Mn}} = 0.05$, and the local magnetic moment dependence becomes virtually independent of δ_{Mn}. The magnetic stabilization energy (FM minus AFM), which is proportional to Mn-Mn exchange energy along the zigzag chain, is at its most negative at $\delta_{\mathrm{Mn}} = 0$, and changes sign to positive (favoring AFM) at $\delta_{\mathrm{Mn}} = 0.035$, consistent with the extended Heisenberg model investigation by Rungger and Sanvito [270]. We note that the experimentally-observed ambient-pressure orthorhombic cell δ_{Mn} values (≤ 0.027) remain within the regime where ferromagnetic exchange dominates, confirming the experimentally observed ferromagnetic correlations.

The calculated crossover between FM and AFM energies near the δ_{Mn} of the experimentally-observed orthorhomic structure is consistent with a spin-fluctuation-based paramag-

netic state. Since the dynamics of such a state are out of reach for DFT calculations, we simulate this state using a special quasirandom structure (SQS) methodology [247], which has recently been applied to paramagnets [274–276]. This approach involves constructing a supercell (we used the 96-atom supercell shown in Figure 4.6(a)) and adjusting quasirandom up and down moments on the Mn atoms such that the local spin-spin correlations of the cell match the correlations of an infinite paramagnet (see Appendix for details). When this disordered local moment cell is fully relaxed (gray star in Figure 4.2(b-c)), it adopts an orthorhombic structure with an average $\delta_{\mathrm{Mn}} = 0.035$, a much better agreement with experiment ($\delta_{\mathrm{Mn}} = 0.027$ at 318 K) than was seen in the antiferromagnetic or low-moment ferromagnetic calculations. An energy surface of the SQS cell was also calculated, showing a very shallow minimum around the experimental orthorhombic structure and a maximum at $\delta_{\mathrm{Mn}} = 0$. By construction, the SQS cells are higher than the FM and AFM states, as the fluctuations which stabilize the paramagnet are not considered in the energy calculation. Nevertheless, we can immediately see that any transition away from a high-moment FM state to a PM, AFM, or low-moment FM state in MnAs will be accompanied by a distortion from hexagonal to orthorhombic. Thus it is the high-moment ferromagnetism itself that establishes the high-symmetry lattice and any pressure or temperature sufficient to disrupt this magnetic configuration will simultaneously drive the structural distortion.

To understand the origins of this behavior, we investigated the orbital bonding properties of MnAs. While Mn sits in a nearly perfect octahedron in the hexagonal structure, we found that the expected octahedral crystal field splitting is absent from the electronic structure (see Appendix Figure 4.10). This indicates that direct Mn-Mn interactions beyond the immediate Mn-As coordination shell play a large role in the electronic structure, reminiscent of the FeAs family of superconductors which also exhibit

a strong and unusual magnetostructural coupling [277, 278].

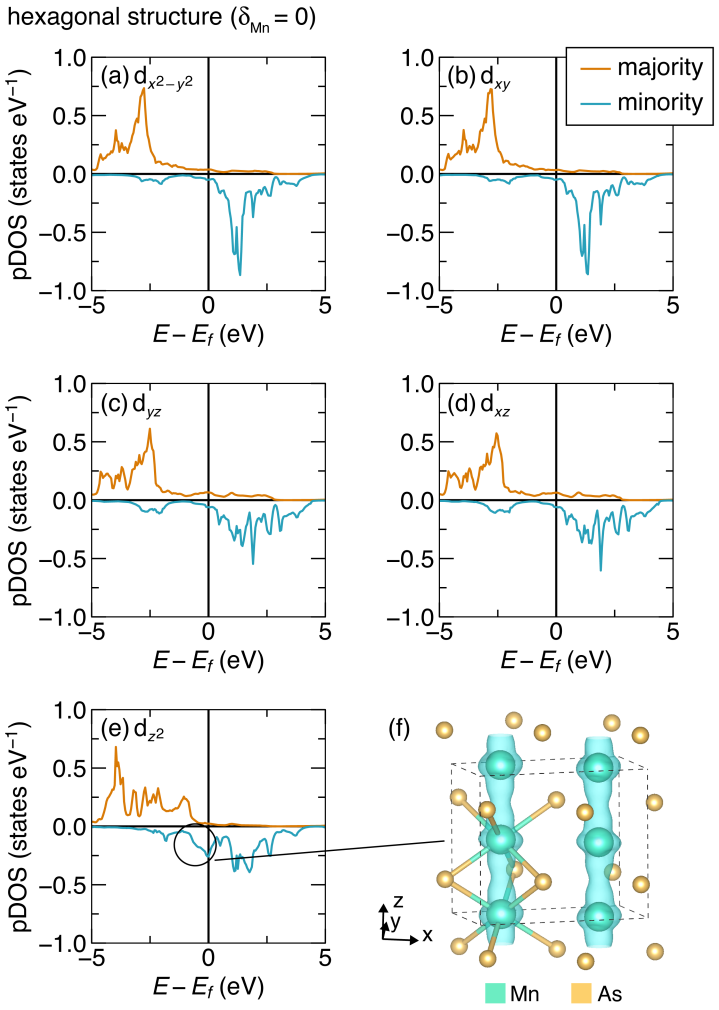

Figure 4.3: Hexagonal, FM MnAs projected partial densities of states (pDOS) for the five Mn d orbitals in the non-conventional orbital projection scheme described in the text (the x, y, and z axes for this scheme are labelled in panel (f)). In the hexagonal structure, all of the d orbitals except d_{z^2} show pDOS characteristic of complete spin polarization, with the majority spin states localized in a peak below the Fermi level (E_f) and the minority states localized about E_f. The d_{z^2} orbital, on the other hand, shows a much more dispersive structure with a lower magnetic moment, consistent with the short Mn-Mn contact (2.75 Å) along the z axis causing d-orbital overlap and a chain of metal-metal bonding along the z axis. This d_{z^2} hybridization is illustrated in (f), which shows the minority spin density from $E_f - 1$ eV to E_f forming a 1-D band along the z axis.

We therefore moved to an unconventional d orbital basis oriented according to the

Mn-Mn contacts, as illustrated in Figure 4.3. In this scheme, the d_{z^2} orbital lobes point out of the plane, along the nearest-neighbor Mn-Mn contact, while one lobe of the $d_{x^2-y^2}$ orbital points along the Mn-Mn zigzag contact that is activated by the distortion. In the hexagonal structure, all of the Mn d orbitals except the d_{z^2} orbital show partial DOS that are approximately half-filled with the majority spin states localized 2.5 eV below the Fermi level with unoccupied minority spin states above, as shown in Figure 4.3(a-d). This electronic structure is stabilized by Hund's coupling (*i.e.* the intra-atomic exchange), which lowers the energy of the spin-polarized occupied states. On the other hand, the d_{z^2} orbital shows a much more dispersive DOS consistent with a band formed by Mn-Mn bonding along the short contacts, as shown in Fig 4.3(e). For this orbital, it is the kinetic energy benefit associated with chemical bonding that stabilizes the electronic structure.

In this projection scheme, the $d_{x^2-y^2}$ orbital shows large changes when a Mn distortion is introduced, while the other d orbitals are comparatively unaffected (Figure 4.4). As the distortion mode forces Mn atoms together in the x direction, overlap of the $d_{x^2-y^2}$ neighboring orbitals makes full spin-polarization untenable due to the Pauli exclusion principle, as electrons with the same spin cannot overlap spatially. This precipitates an electronic transition as seen by the reorganization of the DOS in Figure 4.5(d). The new electronic structure loses the Hund's coupling stabilization, but partially compensates the loss by forming Mn-Mn bonds. A newly formed zigzag bonding band can be visualized as the partial charge density of the newly occupied minority states (Figure 4.5(e)). The competition between Hund's coupling and bonding is clearly seen in Figure 4.5(c), which shows the $d_{x^2-y^2}$ moment and bond strength (estimated using the integrated crystal orbital Hamilton population (–iCOHP) [279–283]) as a function of δ_{Mn}. As δ_{Mn} increases, the moment drops precipitously while a metal-metal bond forms.

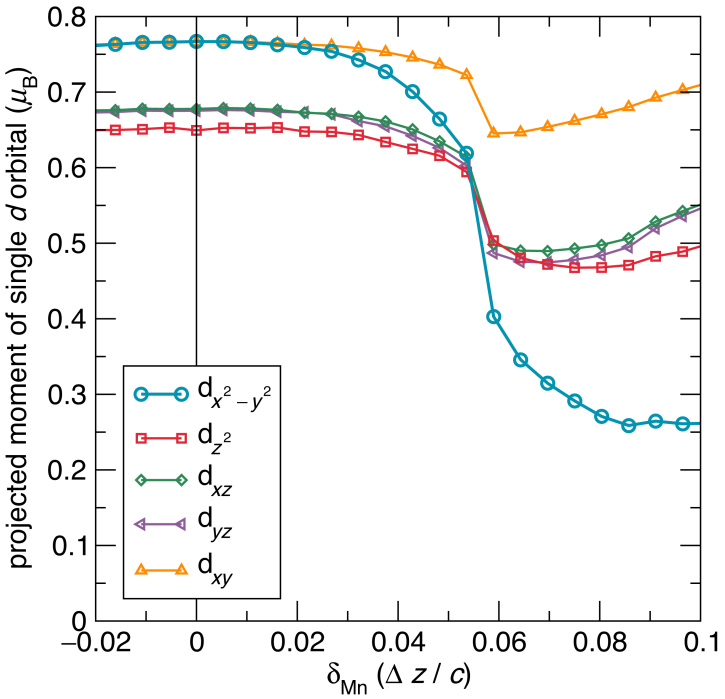

Figure 4.4: Changes in the moment of each Mn d orbital as a function of Mn distortion (δ_{Mn}) for the ferromagnetic case. The $d_{x^2-y^2}$, which points one of its lobes along the Mn-Mn zigzag contact that is activated by the Mn distortion mode, experiences a drastic reduction in moment of 55% between the hexagonal and low-moment orthorhombic structure. On the other hand, the changes in the other orbitals are much smaller, emphasizing the importance of the $d_{x^2-y^2}$ orbital to the structural transition.

Furthermore, the orthorhombic distortion also increases the Mn-As and As-As –iCOHPs (see Appendix Figure 4.12) as the asymmetric coordination optimizes bond distances. Altogether, these bonding interactions explain the local stability of the low-moment orthorhombic state.

Therefore, we can see that the high-moment hexagonal to low-moment orthorhombic transition experienced by MnAs under pressure can be understood as arising from a competition between Hund's coupling and chemical bonding. This scenario is similar to the competition between moment magnitude and chemical bonding which drives the magnetostructural coupling in MnB [81]. At ambient pressure in MnAs, the Hund's coupling stabilization outweighs the bonding/kinetic energy consideration. However,

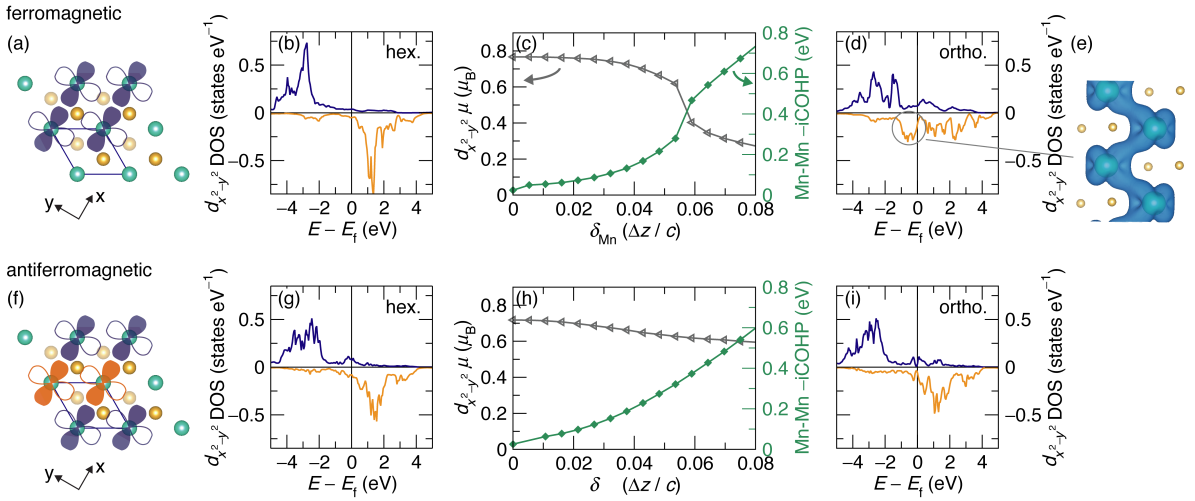

Figure 4.5: Single-orbital properties of MnAs in the FM (a-e) and C-type AFM (f-i) structures. (a) Mn $d_{x^2-y^2}$ orbitals in the specially chosen basis, oriented along Mn-Mn contacts. (b,d) Projected partial $d_{x^2-y^2}$ DOS for the hexagonal and orthorhombic structures, respectively. (c) Projected $d_{x^2-y^2}$ moment and negative integrated crystal orbital Hamilton populations as a function of Mn distortion. (e) Partial charge density of the minority spin channel within 1 eV below the fermi level for ferromagnetic, orthorhombic MnAs. (f-i) show the same data as (a-e), except for the AFM case.

the application of pressure forces a reorganization of the electrons to comply with the Pauli principle, destabilizing the high-volume high-moment state in favor of a lower-moment, more strongly bonded structure.

It is also instructive to look at the orbital changes in the AFM case [Fig 4.5(f-i)], even though this magnetic structure is never observed experimentally, in order to understand how spin flips modify the system. In the AFM case, the Mn atoms that are brought together by the distortion have opposite spins and the Pauli exclusion principle does not come into play. As the $d_{x^2-y^2}$ orbitals begin to overlap, they are able to hybridize and form a bond with similar strength to the ferromagnetic case, but without disrupting the spin polarization. For this reason, the Mn local moment magnitudes remain approximately constant as a function of δ_{Mn}, and bonding and moment can all be simultaneously optimized at $\delta_{\mathrm{Mn}} = 0.05$. The resulting state is still higher in en-

ergy than the ferromagnetic hexagonal state, however, due to the Mn-Mn *interatomic* magnetic exchange (*i.e.* FM − AFM energy in Figure 4.2(b)), which is maximized at $\delta_{\mathrm{Mn}} = 0$.

Based on the analysis of the ordered FM, AFM and SQS states, we are now equipped to understand why the ambient-pressure transition from ferromagnetic to paramagnetic is coupled to a large structural distortion. The hexagonal ground state is not optimized from a bonding perspective, but maximizes magnetic exchange energy and is therefore lower in energy than all competing states. As temperature rises and spin-flip fluctuations begin to set in, this exchange energy benefit is weakened, and, at 315 K, it becomes more favorable to structurally distort, forgoing the interatomic exchange energy in favor of the kinetic/bonding stabilization of the orthorhombic state. The spin fluctuations aid this transition by introducing AFM pairs of Mn atoms along the zigzag chains, allowing many of the $d_{x^2-y^2}$ orbitals to maintain their Hund's coupling stabilization when distorting. All the competition, interestingly, takes place in the $d_{x^2-y^2}$ orbital channel. The small Mn-Mn contact length along the z^2 orbital causes is to remain in the bonded state at all temperatures, while very long Mn-Mn contacts in the other orbital directions cause them to stay in their spin-polarized Hund's coupled states at all temperatures. Therefore, the key to this transition is the competition between exchange and bonding energies in half-filled Mn-Mn orbitals that are just on the verge of possible overlap.

This interplay between magnetic exchange, magnetic moment, and structural distortion has interesting implications for the paramagnetic orthorhombic state. In MnAs, when fully relaxing the SQS cell, individual Mn atoms move away from their symmetrical sites by up to 0.2 Å leading to very different local environments for different Mn atoms. These large local distortions has not been seen other paramagnets simulated

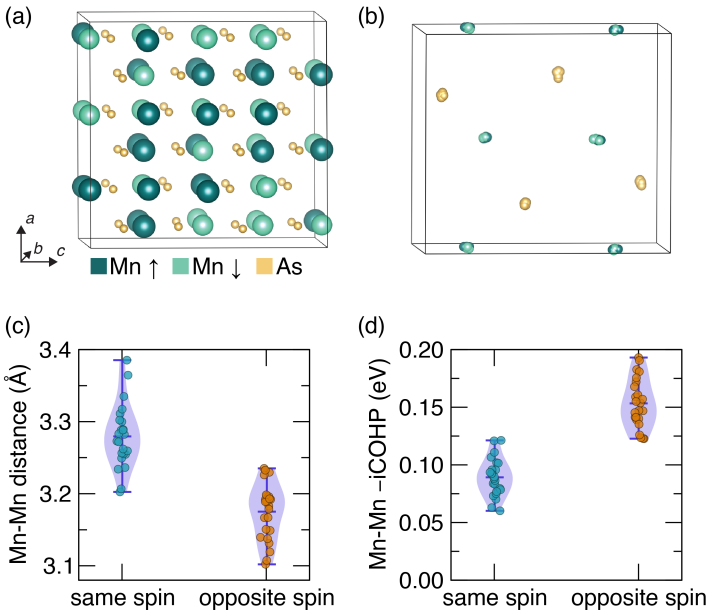

Figure 4.6: (a) Structurally-relaxed SQS used to simulate the paramagnetic state. (b) Projection of the supercell atomic positions into a single orthorhombic cell, showing Mn and As occupying a distribution of positions along the structural distortion modes. (c) Distributions of bond distance and (d) negative integrated crystal orbital Hamilton population for the 48 unique Mn-Mn zigzag contacts.

using this method [274–276]. Figure 4.6(a) shows the relaxed SQS cell, and Figure 4.6(b) shows the same cell with all of the atoms projected into a single primitive orthorhombic unit cell. The Mn and As atoms cluster into elongated clouds along the hexagonal-to-orthorhombic distortion modes, indicating that the paramagnetic state is most stable with a distribution of δ_{Mn} and δ_{As}. In Figure 4.6(c-d), we have extracted all 48 Mn-Mn contacts along the zigzag chains in the SQS cell, and plotted their bond length (c) and bond strength ($-$iCOHP, (d)) as a function of whether the pairs of atoms have the same spin direction or opposite spin direction. On average, the AFM pairs have bond distances 0.1 Å shorter than ferromagnetic pairs, and bond strengths about twice as strong. On the other hand, similar analysis for the other Mn-Mn contacts in the structure finds no dependence of the bond lengths or strengths on the spin correlation (Figure 4.7), highlighting once again that the competition-driven coupling

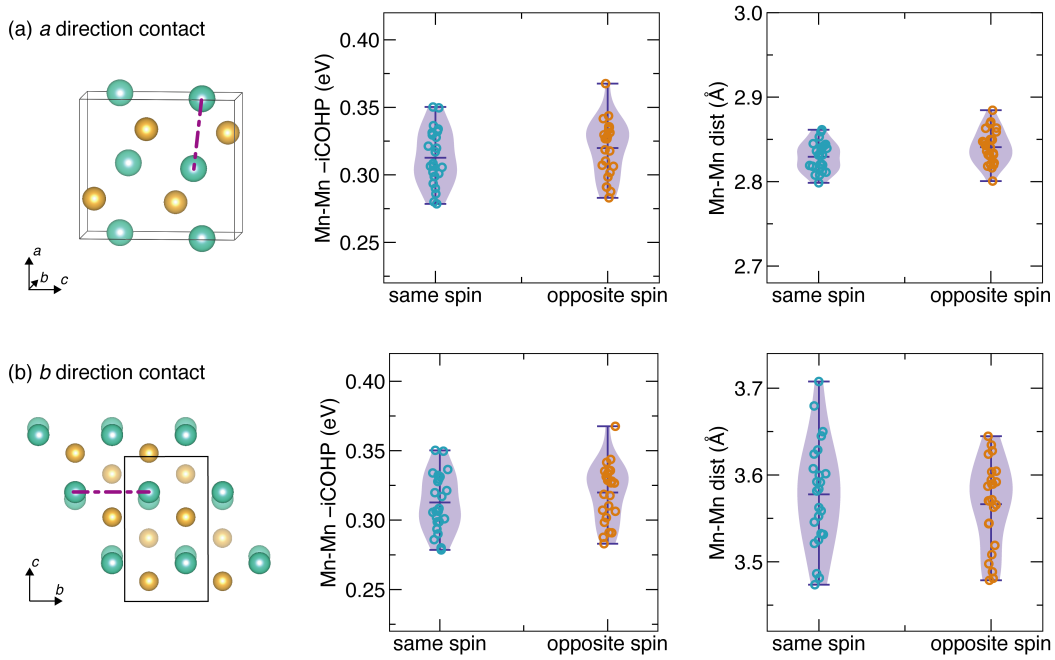

Figure 4.7: Distributions of bond distances and –iCOHPs extracted from the relaxed SQS cell, for (a) the out-of-plane Mn-Mn contacts and (b) the Mn-Mn contacts along the orthorhombic b direction. These data are analogous to the data shown for the Mn-Mn zigzag contact in Figure 4.6. Unlike the zigzag contact, the two contacts shown here do not exhibit a dependence of bond length or –iCOHP on the spin correlation. This observation highlights that the competition-driven magnetostructural coupling is only active in a single Mn d orbital, the $d_{x^2-y^2}$ orbital discussed in the main text.

in MnAs occurs selectively in the Mn $d_{x^2-y^2}$ orbitals.

This fascinating result implies that in the paramagnetic state of MnAs, thermal spin fluctuations can be expected to couple to large atomic displacements accompanied by the dynamic formation and breaking of metal-metal bonds. We predict this exotic state is detectable by large and dynamic local-symmetry breaking [100, 265], as well as anomalous phonons, magnons, and thermal and spin transport. In particular, this state may be invoked to explain the extremely low thermal conductivity [266] and the abnormal elastic properties [98, 99]. In understanding all of these properties, and it becomes evident that traditional notions of spin and lattice independence will not

be sufficient. Furthermore, the mechanisms for magnetostructural coupling driven by competition between exchange and kinetic energy scales described here are expected to be a general feature of other systems displaying strong magnetostructural coupling.

4.3 Appendix: Supplemental material

4.3.1 Electronic structure calculation methods

Density functional theory calculations of ordered magnetic states

Electronic structure calculations were performed using density functional theory (DFT), as implemented in the Vienna *Ab initio* Simulation Package (VASP) [128] with projector augmented wave (PAW) pseudopotentials [129, 130] within the Perdew-Burke-Ernzerhof generalized gradient approximation (GGA) revised for solids (PBEsol) [131, 267]. A DFT+U approach was adopted, using the $U - J = U_{\text{eff}}$ formalism of Dudarev [271], with the U_{eff} applied to the Mn d orbitals.

Once the appropriate $U_{\text{eff}} = 1.2$ eV value was chosen (see below), calculations of the orthohexagonal unit cell (Figure 4.1(b)) with varying amounts of Mn distortion and As distortion were performed. During the experimentally observed structural distortion from hexagonal to orthorhombic, the Mn atoms move principally along the c lattice direction, while the As atoms move along the a lattice parameter. Therefore, the parameters $\delta_{\text{Mn}} = \Delta\text{Mn}_z/c$ and $\delta_{\text{As}} = \Delta\text{As}_x/a$ were used to parameterize the distortion space. 900 calculations were performed on a 30×30 grid of δ_{Mn} and δ_{As} values ranging from –0.03 to 0.08. The Mn z parameter and As x parameter were kept fixed, while all of the other atomic coordinates and the unit cell were allowed to freely relax. Structural relaxations with an ionic convergence criterion of 1×10^{-4} eV were performed three

times iteratively to ensure convergence, and then static calculations with an electronic convergence criterion of 1×10^{-6} eV were performed. Monkhorst-Pack k-point grids of $6 \times 8 \times 6$ were used, and all calculations were initialized with ferromagnetic moments of 3 μ_B on each Mn atom. Spin-orbit coupling was not included. In all calculations, the final configurations maintained $Pnma$ symmetry and ferromagnetic ordering.

Similarly, linear potential surfaces only as a function of δ_{Mn} were calculated, with the As z coordinate now being allowed to relax freely. For these calculations, an increased k-point grid of $6 \times 11 \times 5$ was used. The lattice parameters were initialized by linearly interpolating between the lattice parameters of the fully relaxed hexagonal structure ($\delta_{\mathrm{Mn}} = 0$) and the local minimum energy orthorhombic structure, and then allowed to relax freely. These calculations were performed using both ferromagnetic and C-type antiferromagnetic moment initializations, and in all cases the magnetic ordering type stayed consistent with the initialization during relaxation. The results from each of these calculations were analyzed to obtain the crystal orbital Hamilton population (COHP) for nearby atoms and projected densities of states using the `LOBSTER` code [279–283]. The projected densities of states were calculated using a non-standard orientation of the d orbital basis set, as described in the main text. In order to do this, the static `VASP` calculations that fed into the `LOBSTER` calculations were performed with the MnAs structure rotated in 3d space such that correct Mn-Mn contacts were oriented along the cartesian z and x directions. `pymatgen` [132] was used to perform some of the cell manipulations and analysis, and `VESTA` [127] was used to visualize the structures and charge densities.

Simulation of paramagnetic state using special quasirandom structures

The paramagnetic state of MnAs was simulated using special quasi random structures (SQS) [247] obtained using `mcsqs` program [248] included within the ATAT package. A paramagnetic SQS is a supercell which is decorated with up and down moments on the Mn atoms in such a way as to accurately reproduce the local spin-spin correlations expected in a random, dynamic paramagnet using just a single cell. A 96-atom SQS with supercell size $2 \times 3 \times 2$ of the the primitive orthorhombic cell was generated such that the 12 smallest pair correlations (radius up to 6 Å) and its first triplet correlation (radius 3.4 Å) match those of the random state. A full structural optimization was performed on this cell, starting with lattice parameters and atom positions from the lowest-energy AFM cell. The Mn atoms were each initialized with magnetic moments of positive or negative 3 μ_B based on the constructed SQS, and symmetry was switched off such that the individual Mn and As atoms are each allowed to move in any direction and break the $Pnma$ structural symmetry, and the cell is allowed to change shape arbitrarily. A Γ-centered k-point grid of $3 \times 3 \times 3$ was used. This structural optimization was performed several times iteratively, always resetting the initialized magnetic moments, until a final force convergence of –0.005 meV Å^{-1} for all atoms was reached. The atoms all moved substantially away from their $Pnma$ positions, and the quasirandom magnetic moments on each Mn atom remained stable with an overall cell moment of nearly zero. A static calculation with energy convergence of 1×10^{-6} eV was then performed, and the COHP was calculated.

Additionally, a 64-atom $2 \times 2 \times 2$ SQS was generated such that the 17 smallest pair correlations (radius up to 6.8 Å) match the random state. This cell was used to approximately obtain an energy surface of the random state as a function of δ_{Mn} by performing selective dynamics structural relaxations on the SQS with fixed values of

the Mn z parameters while all other atomic coordinates were allowed to fully relax. Structural optimizations were performed using a Γ-centered k-point grid of size $2\times4\times2$ and an energy convergence for the ionic loop of 0.001 eV. For each calculation in the energy surface, these optimizations were performed three times iteratively to ensure convergence.

4.3.2 Supplementary figures

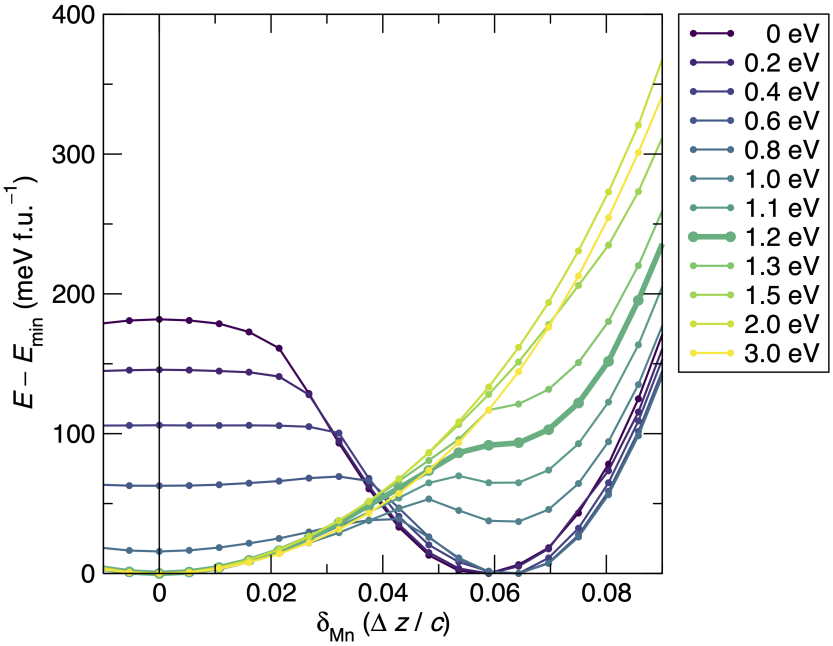

Figure 4.8: Dependence of the MnAs distortion energy landscape on the $U_{\text{eff}} = U - J$ parameter added to the Mn d-orbitals. With $U_{\text{eff}} = 0$, the distorted orthorhombic low–moment structure is erroneously lower in energy than the true (experimentally observed) hexagonal ground state ($\delta_{\text{Mn}} = 0$). Upon adding the U correction, the hexagonal state is stabilized relative to the orthorhombic state and becomes lower in energy for U_{eff},= 1.0 eV and above. The curve for the U value selected for use in this study ($U_{\text{eff}} = 1.2$ eV) is shown in bold. It should be noted that the chosen value of U_{eff} is dependent on the details of DFT calculations. For example, when we attempted to use the standard PBE GGA instead of PBEsol, the qualitative behavior of the energy curves remained the same but the optimal U_{eff} was found to be 0.5 eV.

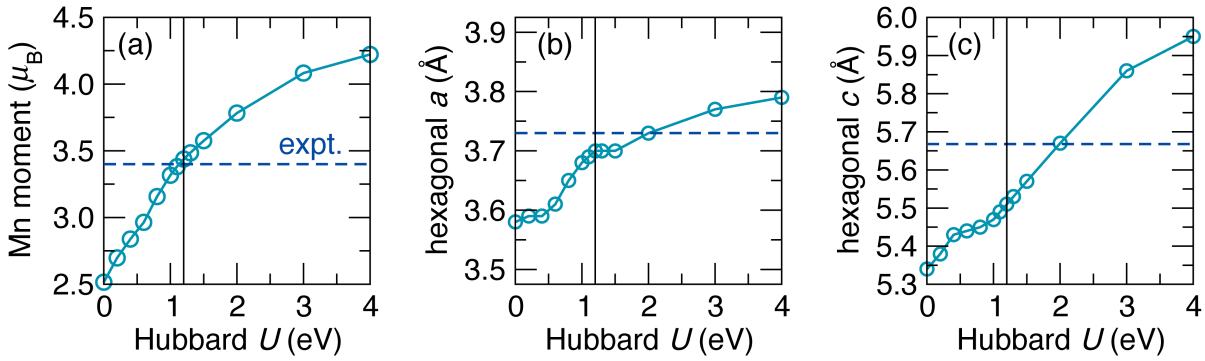

Figure 4.9: Dependence of (a) the local Mn moment and (b-c) fully relaxed lattice parameters for hexagonal MnAs on U_{eff}. For each parameter, the experimental value [254, 255] is shown as a horizontal line. $U = 0$ gives very large deviations from the experimental situation, while a U_{eff} value of 1.2 eV correctly models the moment and underestimates the hexagonal a and c parameters by just 0.8 % and 2.7 %, respectively.

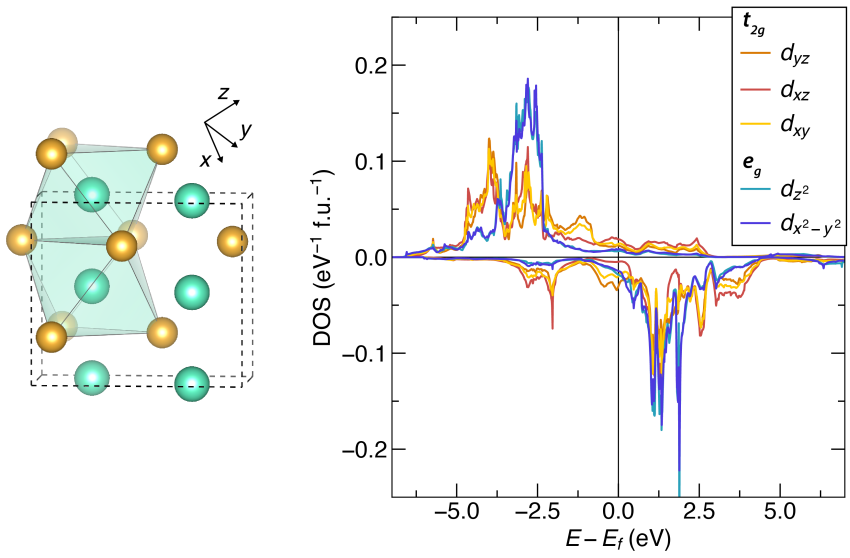

Figure 4.10: Hexagonal FM state partial densities of states (pDOS) for the Mn d orbitals in the conventional octahedral projection scheme. While the t_{2g} and e_g sets of orbitals are each approximately degenerate, both sets show multiple peaks and the overall electronic structure does not exhibit the traditional splitting between localized t_{2g} and e_g manifolds. For this reason, we found this projection scheme to be of limited utility in studying the behavior of MnAs and moved to a projection scheme oriented around the Mn-Mn contacts (below).

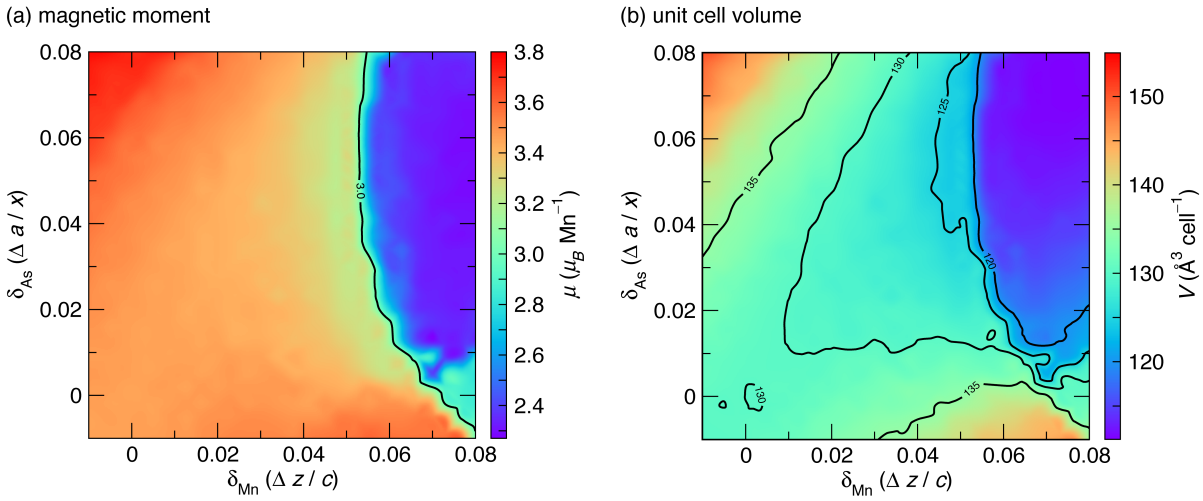

Figure 4.11: Maps of magnetic moment and unit cell volume as a function of Mn and As distortion magnitudes, from the calculations shown in main text Figure 4.2(a).

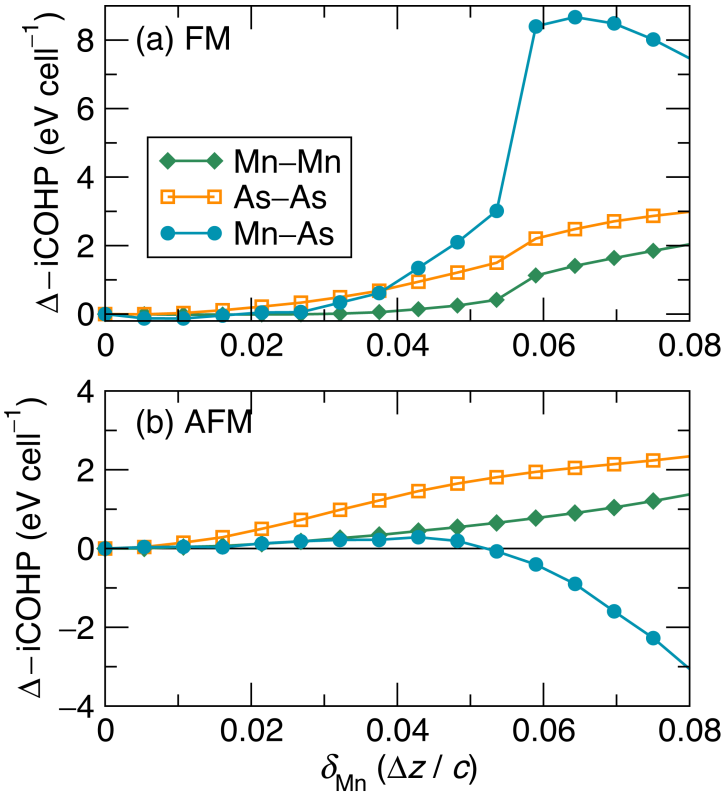

Figure 4.12: Changes in MnAs bond strengths (estimated using the *per* cell change in negative integrated crystal orbital Hamilton population, Δ–iCOHP) as a function of δ_{Mn} for (a) the ferromagnetic spin arrangement and (b) C-type antiferromagnetic spin arrangement. The largest change in –iCOHP for a single bond is observed in the Mn-Mn zigzag contact, as shown in the main text Figure 4.5. However, since there are many more Mn-As and As-As contacts within the unit cell, the total changes in Mn-As and As-As –iCOHPs per cell are generally than the Mn-Mn contribution. From these calculations, it can be see that the overall bonding is optimized around $\delta = 0.06$ for the FM case, and $\delta = 0.05$ for the AFM case.

Chapter 5

Magnetostructural Coupling Drives Magnetocaloric Behavior: The Case of MnB *versus* FeB

[1] As seen in Chapter 4, materials with strongly coupled magnetic and structural transitions can display a giant magnetocaloric effect, which is of interest in the design of energy-efficient and environmentally-friendly refrigerators, heat pumps, and thermomagnetic generators. There also exist however, a class of materials with no known magnetostructural transition that nevertheless show remarkable magnetocaloric effects. MnB has been recently suggested as such a compound, displaying a large magnetocaloric effect at its Curie temperature (570 K) showing promise in recovering low-grade waste heat using thermomagnetic generation. In contrast, we show that isostructural FeB displays very similar magnetic ordering characteristics, but is not an effective

[1]The contents of this chapter have substantially appeared in reference 81: J. D. Bocarsly, E. E. Levin, S. A. Humphrey, T. Faske, W. Donner, S. D. Wilson, and R. Seshadri. Magnetostructural coupling drives magnetocaloric behavior: The case of MnB versus FeB. *Chem. Mater.* **31** (2019) 4873–4881. doi:10.1021/acs.chemmater.9b01476 © 2019 American Chemical Society, reprinted with permission.

magnetocaloric. Temperature- and field-dependent diffraction studies reveal dramatic magnetoelastic coupling in MnB, which exists without a magnetostructural transition. No such behavior is seen in FeB. Furthermore, the magnetic transition in MnB is shown to be subtly first-order, albeit with distinct behavior from that displayed by other magnetocalorics with first-order transitions. Density functional theory-based electronic structure calculations point to the magnetoelastic behavior in MnB as arising from a competition between Mn moment formation and B–B bonding.

This project was performed in collaboration with Emily Levin and Sam Humphrey, who made the samples, and Tom Faske and Wolfgang Donner who collected the in-field diffraction patterns. The project was supervised by Ram Seshadri and Stephen Wilson. I wish to thank Dr. Saul Lapidus (Argonne National Lab Beamline 11-BM) for assistance with the data collection and Professor Barbara Albert for helpful discussions on the subject of borides.

5.1 Introduction

While the Curie transition from a paramagnet to a ferromagnet is canonically a continuous transition, there exist ferromagnets that display discontinuous first-order transitions. This phenomenon can arise when magnetic and structural degrees of freedom are so strongly coupled that the magnetic phase transition is accompanied by a structural transition. Materials displaying such coupled transitions, including MnAs,[70, 71] ferromagnetic, hole-doped $LaMnO_3$,[253] $Gd_5(Si, Ge)_4$,[82, 113, 236, 284, 285] $(Mn,Fe)_2(P,Si,Ge,As)$,[64–67, 104] and $La(Fe,Si)_{13}H_x$[68, 69] are of great interest for their unusual functionality, including, variously, colossal magnetoresistance, giant magnetovolume effects, and, most recently, giant magnetocaloric effects. The

magnetocaloric properties stem from the fact that this type of first-order transition can often be actuated using a modest magnetic field, leading to relatively small fields ordering a significant fraction of paramagnetic spins. By alternating cycles of adiabatic and isothermal magnetization and demagnetization, these changes in entropy can be leveraged to drive an environmentally-friendly and energy-efficient heat pump.[47] Conversely, changes of temperature can be employed to build efficient thermomagnetic waste heat regenerators.[107, 286, 287] The primary metric for magnetocaloric performance is the peak entropy change that can be accomplished during isothermal application of a given magnetic field, $\Delta S_{M,\mathrm{peak}}(H)$. For commercial applications, earth-abundant materials that have substantial peak isothermal magnetic entropy changes at low fields (*ie.* $H = 1\,\mathrm{T}$ to $2\,\mathrm{T}$) are attractive.

Giant first-order magnetostructural phase transitions are recognized by the usual hallmarks of an abrupt change in the magnetization at the transition temperature accompanied by a peak in heat capacity, thermal hysteresis, and phase coexistence of the two phases at the transition temperature. The structural phase transition may either be from one crystallographic space group to another (*e.g.* the $P6_3/mmc$ to $Pnma$ transition seen in MnAs[71]), or it may involve two phases within the same structure but with distinct lattice parameters (*e.g.* the transition in $(Fe,Mn)_2(P,Si)$[85]). The latter case is often termed a magnetoelastic transition.

While the giant magnetic entropy changes associated with first-order magnetostructural phase transitions are useful in applications, they pose engineering challenges. The thermal and magnetic hysteresis associated with first-order transitions leads to inefficiencies and rate limitations when the material is cycled between magnetic states. Large changes in structure during cycling can lead to fatigue and mechanical degradation. Furthermore, thermal hysteresis greatly reduces the reversible adiabatic tem-

perature change of a magnetocaloric. While these challenges can often be alleviated using chemical tuning and device engineering,[74–76] a different solution that has gained popularity recently is to change the composition of a first-order material in order to weaken the magnetostructural coupling so that the transition becomes increasingly second-order. At the border between first- and second-order transitions, one may find a tricritical transition which has no hysteresis while maintaining a large ΔS_M.[50, 85, 86, 104, 288, 289] In contrast, for systems without magnetostructural first-order transitions, the main strategy for improving ΔS_M has been to increase the magnetic moment.[79, 83, 84] However, there exist several materials such as $AlFe_2B_2$,[78, 290] Mn_5Ge_3,[291] CrO_2,[292] MnCoP,[18] and MnB[18, 80] which show promising magnetocaloric properties without any known first-order magnetostructural or magnetoelastic transitions. All of these materials have ΔS_M values that are competitive with, or exceed that of Gd metal despite having gravimetric magnetic moments at saturation that are only between 30 % and 60 % as large.[108] All these materials also have large values of magnetic deformation Σ_M, a density functional theory-based indicator of the strength of magnetostructural coupling,[18] suggesting that magnetostructural coupling may play an underappreciated role in the good magnetocaloric properties of these materials.

Here, we present the case study of MnB *vs.* FeB to demonstrate that magnetostructural coupling is the driving force behind a large magnetocaloric effect, even in a system with no obvious first-order magnetostructural transitions. MnB and FeB are both ferromagnets with the same structure (FeB-type, shown in Figure 5.1) and comparable magnetic properties, but MnB has a large ΔS_M of $-10.7\,\mathrm{J\,kg^{-1}\,K^{-1}}$ for an applied field of 5 T while FeB has an effect three times smaller. Interestingly, some anomalous structural behavior near the Curie temperature of MnB was reported as early as

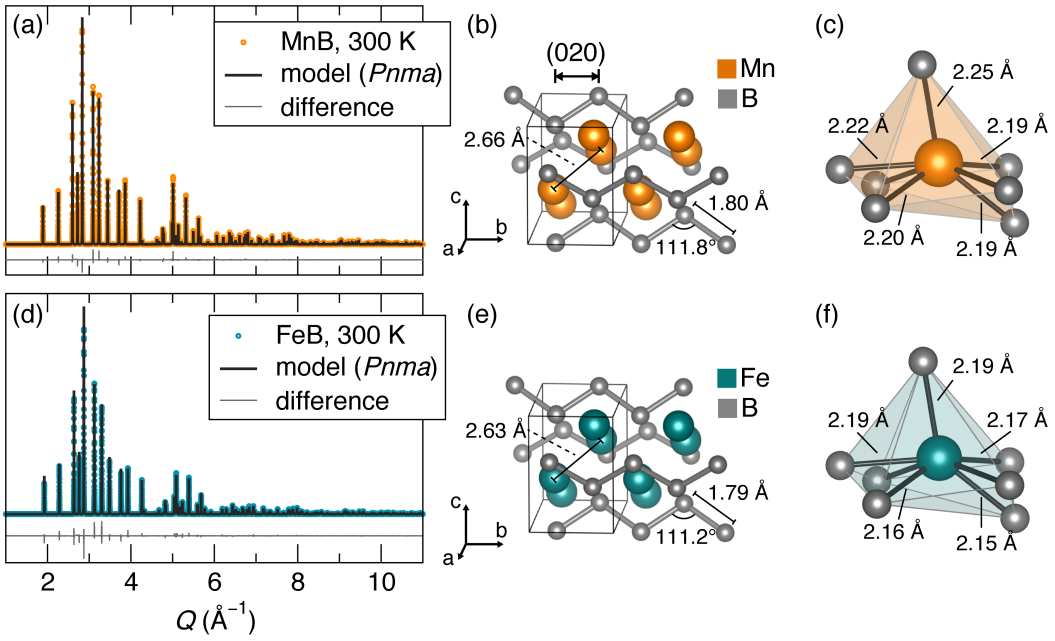

Figure 5.1: Crystal structures at 300 K of MnB (a-c) and FeB (d-f) determined from high-resolution synchrotron X-ray diffraction. (a) and (c) show the diffraction patterns, along with their Rietveld refinement fits. Both samples have the "FeB" structure (space group $Pnma$, no. 62) consisting of tightly bonded 1-D chains of B atoms with the metal ions arranged around them, as can be seen in (b) and (e). The B–B chain is almost unchanged between the structures, but slightly larger Mn-B contacts lead to the MnB cell having a 4.3% larger unit cell volume. The difference in a, b, and c lattice parameters are 1.1%, 0.97%, and 2.2%, respectively.

1975.[293, 294] However, this phenomenon was not explained, and MnB has not received much attention until recently.[18, 80, 295–297]

We use high-resolution temperature-dependent synchrotron powder diffraction and diffraction under a magnetic field to study the magnetostructural coupling in MnB and FeB. We find that despite the similarities between the two compounds, MnB shows dramatic anisotropic coupling between its lattice and magnetism while FeB does not. We employ density functional theory calculations to understand the origin of this magnetostructural coupling as a competition between manganese moment formation (and the associated volume effects) and B–B bonding. This competition leads MnB to be del-

icately balanced between competing magnetic and structural considerations, yielding a system where a small stimulus can drive large changes in structure and magnetism. Furthermore, we determine the magnetic transition in MnB is in fact subtly first-order, as revealed by phase coexistence between two isostructural phases with slightly different lattice parameters at the magnetic transition temperature. However, this subtly first-order transition appears to be distinct from the giant magnetostructural or magnetoelastic transitions seen in other magnetocalorics. The present observation is enabled by the very high resolution of the synchrotron diffraction experiments. We propose that similar behavior may also be revealed in other magnetocaloric compounds if they were to be examined in similar resolution.

5.2 Materials and methods

Phase-pure powders of MnB and FeB were prepared by assisted microwave synthesis, as reported previously[18]. Briefly, Mn (Alfa Aesar, 99.95%) or Fe (Aldrich, 99.9%) powders were ground in air with 2 % stoichiometric excess of crystalline B powder (Alfa Aesar, 99.5%), pressed into pellets, and sealed in evacuated silica ampoules. The ampoules were placed in a carbon-filled crucible and heated in a 1200 W domestic microwave oven (Panasonic, model NN-SN651B) at 70% power (840 W) for 3 min. The pellets were then annealed in evacuated ampoules at 1100°C for 2 days, followed by air quenching. The samples were confirmed to be phase-pure MnB or FeB prior to and after the final anneal. The excess B required is believed to be due to incomplete reaction of the boron starting material. The samples showed no signs of oxidation or air-sensitivity, and are treated as air stable.

Magnetic measurements were performed on a Quantum Design Physical Property

Measurement System (PPMS DynaCool) equipped with a Vibrating Sample Magnetometer (VSM) oven option which allows for the collection of magnetic data between 300 K and 1000 K. The magnetocaloric isothermal entropy change upon magnetization ($\Delta S_M(H,T)$) for each sample was determined using the appropriate Maxwell relation, from magnetization M *vs.* T measurements taken while sweeping temperature through the magnetic transition at several fixed magnetic fields between H = 0.1 T and H = 5 T. The temperature derivatives of magnetization were calculated using Tikhonov regularization,[298] as described in detail previously.[299] Raw measurement data are presented in the Appendix Figure 5.11.

High-resolution synchrotron powder diffraction data were collected on Beamline 11-BM at the Advanced Photon Source (APS), Argonne National Laboratory using an average wavelength of 0.414581 Å. Room temperature data were collected between 2θ of 0.5° and 50°. Temperature-dependent data was collected between 0.5° and 34° for MnB (10 minute collection time per pattern), and between 0.5° and 28° for FeB (5 minute collection time per pattern). A calibrated Cyberstar Hot Gas Blower was used to control the temperature. Patterns were collected continually while temperature was ramped slowly cooled through the magnetic transition such that one diffraction pattern was taken at every 3 K interval. Resulting patterns were refined using Topas Academic, using sequential and parametric[300] refinement.

Temperature and magnetic-field dependent X-ray powder diffraction measurements were performed on a custom-built laboratory diffractometer in transmission geometry (Mo Kα radiation, λ_1 = 0.709320 Å, λ_2 = 0.713317 Å, using the 2θ range from 7° to 67° with a step size of 0.0097°). The instrument has been described in detail elsewhere.[301] The sample powder was mixed with NIST 640d standard reference silicon for correction of geometric errors. Temperature in the range from 300 K to 700 K

was controlled by means of a custom SHI closed-cycle Helium cryofurnace. The heating rate between the measurements was 10 K min^{-1} and the sample temperature was stabilized for 15 min. before data collection. Magnetic fields of up to 5 T were applied for isofield warming and cooling protocols, as well as for isothermal field-application experiments. Pawley analyses of the obtained diffraction patterns were carried out sequentially using TOPAS Academic. Example data and fits are available in the Appendix Figures 5.13 and 5.14.

Spin-polarized density functional theory calculations were performed using the Vienna Ab initio Simulation Package (VASP)[128] using projector augmented wave (PAW) pseudopotentials[129, 130] within the Perdew-Burke-Ernzerhof (PBE) generalized gradient approximation (GGA).[131] First, the eight-atom unit cells of MnB and FeB were relaxed with a force convergence of 0.001 eV Å^{-1} and a starting magnetic moment of 3 μ_B per transition metal ion. This resulted in lattice parameters a, b, c of 5.36, 2.96, and 4.07 Å for MnB and 5.32, 2.93, and 3.96 Å for FeB, which are within reasonable agreement of the room temperature lattice parameters (given in Appendix Table 5.1). Based on these structures, unit cells with systematically expanded and contracted b lattice parameters were generated and ion-only relaxations were performed. On these relaxed structures, static spin-polarized and nonspin-polarized calculations were performed. The Crystal Orbital Hamilton Population (COHP) between pairs of B atoms in the chain were calculated with the help of the LOBSTER code.[279–283]

5.3 Results and discussion

The results of Rietveld refinement of high-resolution MnB and FeB patterns collected at room temperature are shown in Figure 5.1 and Table 5.1. Both patterns

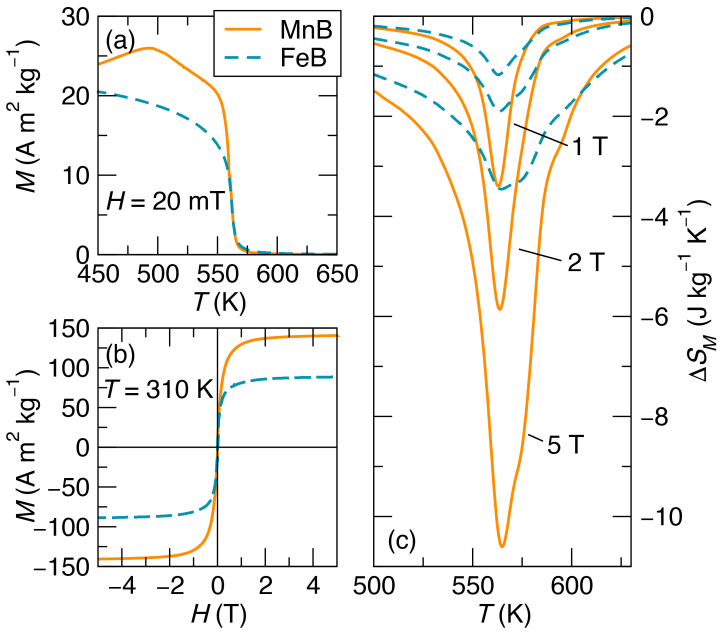

Figure 5.2: Comparison of the magnetism of MnB and FeB. (a) The two materials show a nearly identical magnetic transition temperature, but MnB shows an unconventional shape of the $M(T)$ curve. (b) MnB has a saturation magnetization about 50% larger than that of FeB, (c) but shows a peak $-\Delta S_M$ about three times larger.

match the known orthorhombic $Pnma$ structure ("FeB-type"),[302, 303] which consists of 1D zigzag chains of closely spaced (1.8 Å) B atoms running along the b crystallographic axis with Mn or Fe arranged in a distorted hexagonal network around these chains. This results in a highly bonded framework, with each metal atom coordinated by seven boron atoms within a sphere of 2.3 Åand six additional metal atoms within 2.7 Å. These diffraction patterns display anisotropic peak widths, which can be well-fit using the Stephens peak-shape function[304] which accounts for (hkl)-dependent peak broadening by assuming that different crystallographic directions may have different amounts of inhomogenous strain. The anisotropy in peak shape is consistent with the highly one-dimensional nature of the crystal structure.

MnB and FeB show very similar bond lengths and contacts, albeit with slightly larger metal-B contacts in MnB leading to larger lattice parameters and a 4.3% larger unit cell

volume for MnB. It should be noted the B–B bond lengths and the lattice parameter in their direction of propagation are very similar in the two materials.

Figure 5.2 shows the magnetic characterization of pure samples of MnB and FeB. MnB and FeB show remarkably similar magnetic ordering temperatures (560 K), despite the magnetic behavior appearing to display some key differences. Under low applied fields (less than about 0.1 T), M *vs.* T of FeB behaves as expected for a ferromagnet, uniformly increasing as temperature is lowered. MnB on the other hand, shows an atypical maximum in the magnetization around 500 K, whose origin is not known but may represent a spin reorientation or other magnetic transition. The gravimetric saturated magnetic moment of MnB is about 50% larger than that of FeB (1.65 $\mu_{\mathrm{B}}/\mathrm{Mn}$ and 1.05 $\mu_{\mathrm{B}}/\mathrm{Fe}$). This difference in saturated moment is not nearly enough to explain the dramatic difference in the magnetocaloric properties, with MnB showing a three times larger magnitude of peak ΔS_M. No resolvable thermal hysteresis was seen in either material.

The large ΔS_M in MnB compared to FeB is surprising, given the similarities in structure, ordering temperature and ordered magnetic moment. However, when the temperature-dependence of the synchrotron X-ray diffraction is examined (Figure 5.3), striking differences become evident. In FeB, all of the peaks shift uniformly towards higher Q upon cooling through the magnetic transition, demonstrating conventional positive thermal expansion. In MnB, different peaks shift in different directions, indicating highly anisotropic effects. Furthermore, pronounced kinks are visible in the thermal evolution of most of the peaks at the magnetic transition temperature, suggesting that the crystal structure is much more strongly linked to the magnetism in MnB than in FeB.

Figure 5.4 shows the temperature evolution of the (020) peak of the two com-

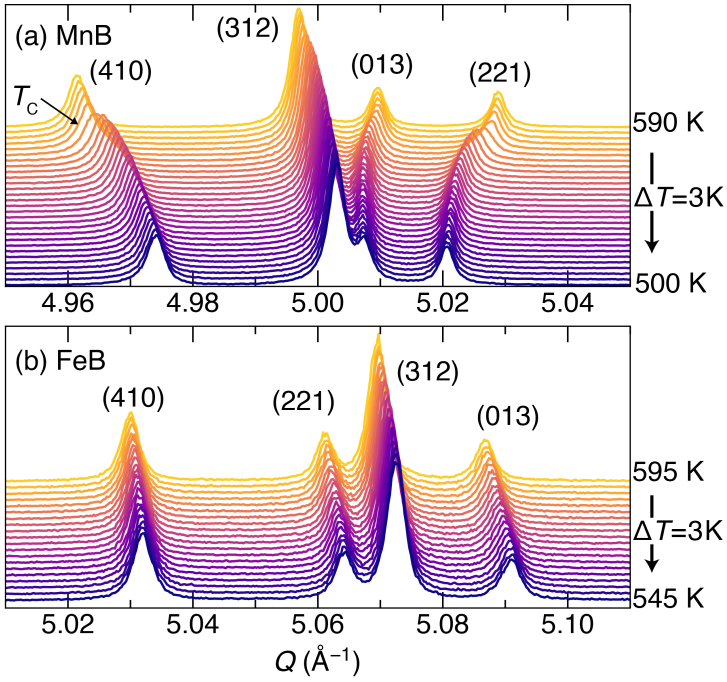

Figure 5.3: A section of the temperature-dependent diffraction dataset for (a) MnB and (b) FeB. MnB shows highly anisotropic thermal evolution of the diffraction peaks, including pronounced kinks at the Curie temperature. FeB, on the other hand, shows only conventional thermal expansion.

pounds which corresponds to the lattice spacing parallel to the B–B chain direction. In MnB, this peak shifts towards lower Q upon cooling, showing a negative coefficient of thermal expansion in the b lattice parameter. Furthermore, around the magnetic transition temperature, the peak broadens dramatically and can be seen to form a distinct shoulder (Figure 5.4b), indicating that two closely spaced peaks are present. This effect is subtle enough that it would be undetectable at the resolution of most diffraction experiments, including laboratory X-ray diffraction or powder neutron diffraction. However, with the resolution of the present experiment, the splitting of one peak into two around the magnetic transition temperature is seen on all peaks with substantial h or k character. In addition to the data shown in 5.4, a pattern taken at the fixed temperature 576.1 K after temperature equilibration also shows this two-phase coexistence, confirming that it is not a transient effect (Appendix Figure 5.12). This behavior

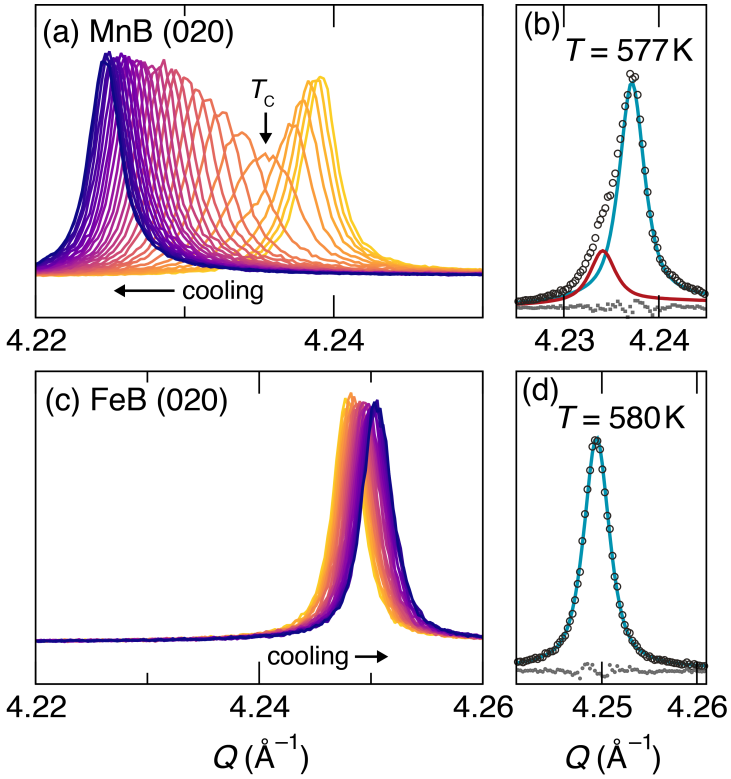

Figure 5.4: Temperature evolution of the (020) peak in MnB and FeB through the magnetic transition temperature. In MnB, the peak shifts dramatically to the left upon cooling (a), and broadens near the magnetic transition temperature. Below and above the magnetic transition, the peak has a well-behaved Lorentzian shape, but near the Curie temperature, it requires two peaks to fit, indicating coexistence of two phases (b). In FeB, the peak shifts to the right upon cooling (c) and maintains a constant-width Lorentzian shape at all temperatures, including at the magnetic transition temperature (d).

indicates that there is a region of phase coexistence between two phases around the magnetic transition in MnB, a hallmark that the transition is actually first-order. In FeB, on the other hand, no such behavior is observed.

In order to examine the thermal evolution of the structure, parametric Rietveld refinements on both data sets were performed, allowing the noise in the refined parameters to be minimized. Results for FeB are shown in 5.5. The lattice parameters and unit cell volume of FeB display well-behaved linear thermal expansion of all three

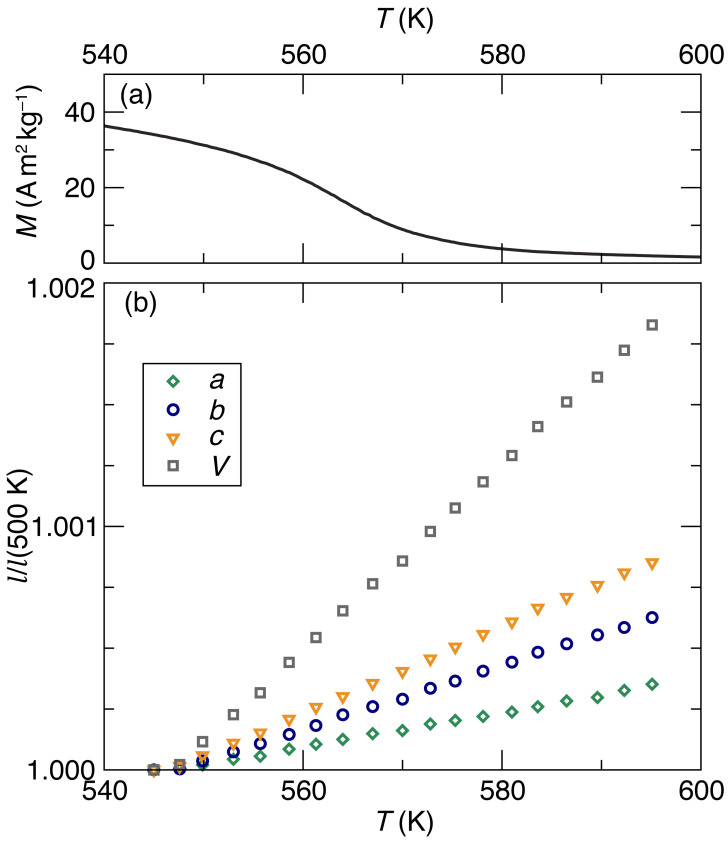

Figure 5.5: Comparison of magnetic moment *vs.* temperature (a) and lattice parametric from parametric Rietveld refinement of temperature-dependent synchrotron diffraction data (b) for FeB. In contrast to MnB, the lattice parameters of FeB all show linear, moderate positive thermal expansion, with no obvious anomaly at the magnetic transition temperature. Some anisotropy in thermal expansion can be seen, evidenced by a larger coefficient of thermal expansion in the c direction than the a and b direction.

cell parameters, with no observable change in slope at the magnetic transition temperature. Some anisotropy is seen in the thermal expansion, with average coefficients of thermal expansion of 7 ppm K^{-1}, 12 ppm K^{-1}, and 17 ppm K^{-1} in the a, b, and c directions, respectively.

In contrast, the results of parametric refinement for MnB (Figure 5.7) demonstrate anomalous behavior. If the refinement for MnB is set up so that only one crystallographic phase exists in each pattern, the patterns well below and well above the

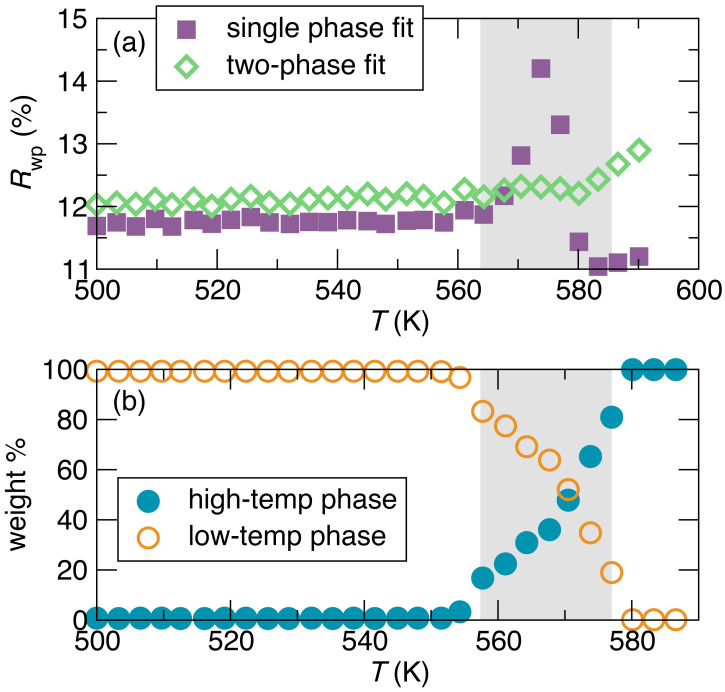

Figure 5.6: (a) Quality of fit (R_{wp}) for parametric fit of temperature-dependent synchrotron diffraction data. The purple squares show that case when a single crystallographic phase is allowed, with the peak profile (Bragg peak widths) allowed to vary independently for each pattern. This case cannot adequately fit the Bragg peak splitting observed near the magnetic transition temperature, and a spike in R_{wp} is observed in the grey boxed region. On the other hand, when two phases with slightly different lattice parameters and each with a constant peak profile are included, the R_{wp} is constant through the magnetic transition. The weight fractions of the two phases refined from this fit are shown in (b), demonstrating that the magnetic transition is concurrent with the conversion from one crystallographic phase to the other, confirming a first-order transition.

transition are described appropriately, but near the transition, R_{wp} (a measure of the error in a Rietveld fit) increases dramatically, even if the peak profile is allowed to refine independently for each temperature (Figure 5.6(a)). However, if two isostructural $Pnma$ phases with slightly different lattice parameters (about 0.05% difference in the a and b directions) are included in the fit, the R_{wp} remains constant across the magnetic transition. The two phases are found to coexist in a temperature region between 558 K and 577 K, transitioning from 100% of the low-temperature phase at 558 K to 100% of

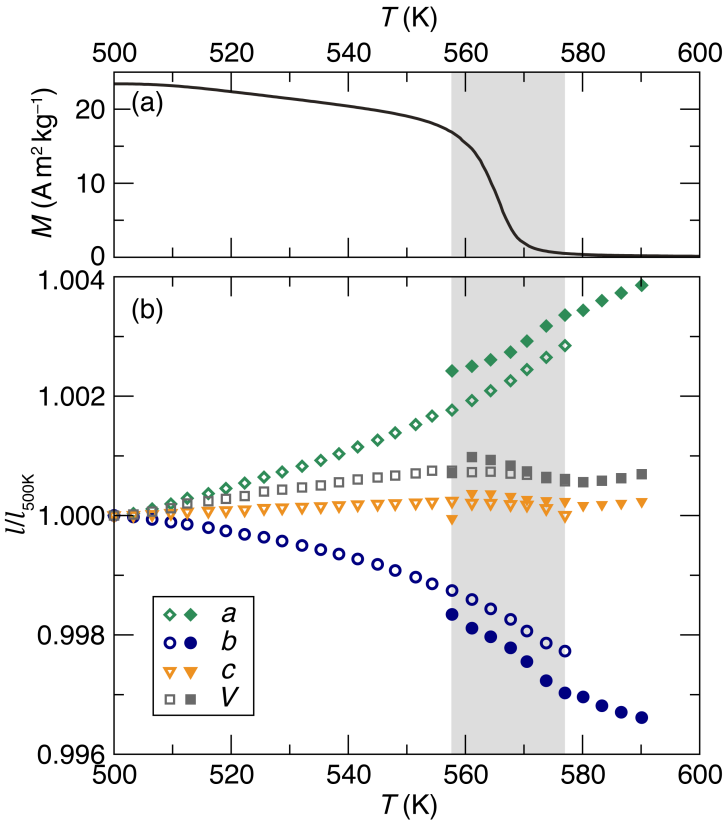

Figure 5.7: Results of parametric two-phase Rietveld refinement of temperature-dependent synchrotron diffraction data for MnB, compared with magnetization data. (a) Magnetization as a function of temperature under an applied field $H = 20\,\mathrm{mT}$. (b) MnB lattice parameters are shown relative to their 500 K value, and show highly anisotropic thermal expansion including large negative thermal expansion in the b direction. Furthermore, phase coexistence between two isostructural phases is seen in a 19 K window around the magnetic transition temperature, indicated with a gray box.

the high-temperature phase at 577 K (Figure 5.6(b)). As can be seen in Figure 5.7, the temperature-range of this two-phase transition corresponds exactly to the width of the magnetic transition. Taken together, these observations confirm that the magnetic transition in MnB is first-order. The phase coexistence over a temperature span of 20 K is reminiscent of the first-order transitions in shape memory alloys, where strain buildup causes the transformation to occur progressively, rather than all at once.[305] However, it is important to note that the differences in lattice parameters of the coexisting MnB phases are not anywhere near as large as those seen in magnetocalorics displaying

giant magnetocaloric effects at coupled first-order magnetostructural or magnetoelastic transitions (often 1% or more). In fact, the changes in lattice parameters between the two phases are less than the thermal expansion of each phase within the phase coexistence region, and therefore the the structural part of the phase transition cannot be considered primary. Rather, this transition appears to represent a different kind of first-order phase transition than those previously seen in magnetocalorics. Its origin and behavior are the subject of ongoing investigation.

Outside of the two-phase coexistence region, the thermal evolution of the lattice parameters of MnB is also unusual. The a lattice parameter experiences a very large positive thermal expansion across the full temperature range, with an average linear coefficient of thermal expansion of 43 ppm K^{-1} across the dataset. On the other hand, the b lattice parameter shows a similarly large negative coefficient of thermal expansion, -38 ppm K^{-1}. In the a and b directions, the positive or negative thermal expansion is strongest at the magnetic transition temperature. The c lattice parameter is relatively invariant with temperature, and the overall unit cell volume shows slight positive expansion. Both the c lattice parameter and the volume show some irregular behavior at the magnetic transition temperature.

Like the lattice parameters, the bond lengths in MnB show anisotropic thermal evolution (5.8). Notably, the closest Mn–B and B–B contacts decrease slightly as temperature is increased, as does the average Mn–Mn distance. However, the changes in bond length are all small, and with no dramatic changes at the transition temperature that would indicate a change in bond order. Rather, these anisotropic changes in bonding indicate that some electronic redistribution is occurring as temperature is changing, as will be discussed in the final section.

The structure evolution of MnB is clearly strongly affected by the magnetism, as

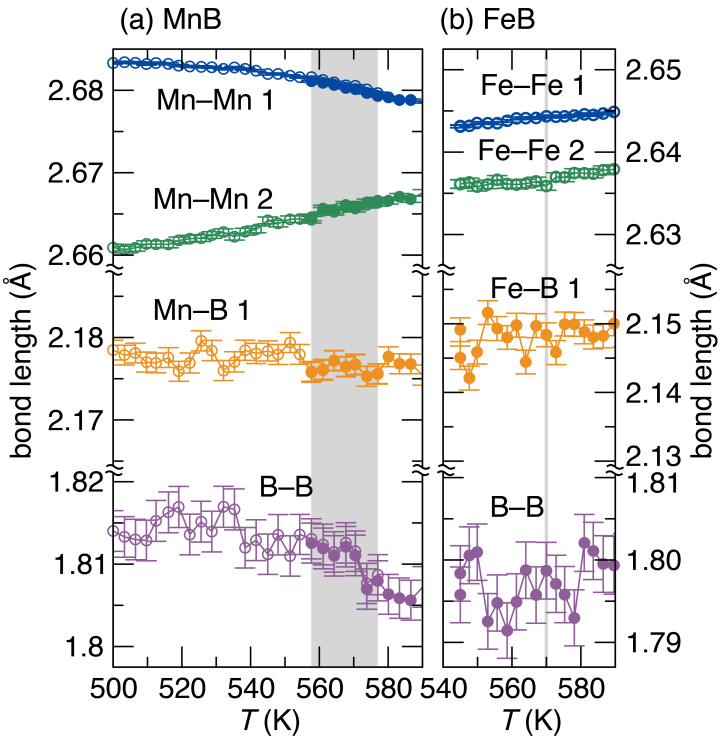

Figure 5.8: Thermal evolution of selected bond lengths and contacts in MnB and FeB, as fit from the parametric refinements. For MnB, the high-temperature phase is indicated with solid symbols, and the low-temperature phase with empty symbols. The atomic positions were constrained to be the same in the two phases for the patterns where both phases exist, which is consistent with the positions above and below the transition. In each compound, there exist two distinct metal-metal contacts with length below 2.7 Å, seven distinct metal-boron contacts with length less than 2.3 Å(only the nearest is shown), and one distinct boron-boron contact. MnB shows anisotropic thermal expansion of its bonds, while FeB shows only mild increases in bond length as temperature is raised. Magnetic transition temperatures are represented as grey box for MnB (signifying the temperature range of phase co-existence), and a grey line for FeB.

evidenced by the structural anomalies seen at the magnetic transition temperature. For this reason, MnB was originally compared to invar (Fe-Ni) alloys, wherein low thermal expansion is known to be caused by a magnetovolume effect.[293, 294] The magnetovolume effect, which is based on theories of itinerant electron magnetism, relies on the fact that large magnetization causes lattice parameters to expand.[306, 307] At low temperatures, the moment is at its largest, and its effect on expanding

the crystal lattice is also at its largest. As temperature increases, fluctuations set in and the magnetic moment weakens, causing a negative contribution to the thermal expansion. This contribution may partially or completely offset the normal thermal expansion of the material due to anharmonic phonons. Above the magnetic Curie temperature, the thermal expansion typically returns abruptly to positive. In MnB however, magnetostructural effects manifest in quite a different way. The thermal expansion is marked by a change in cell shape, inducing both a strong negative thermal expansion in the b direction and a strong positive thermal expansion in the a direction. In addition, these effects persist, although somewhat weakened in magnitude, at least 150°C (see Appendix Figure 5.15) above the magnetic transition temperature, which is quite unusual, even in magnetocalorics with exceptionally large magnetostructural coupling.[301, 307–309] This persistence suggests that the magnetism in MnB has at least partly local character, and that the magnetostructural interaction is related to a coupling between the moment magnitude and the Mn ion size. This coupling may persist above the Curie temperature because the local moments still exist in the paramagnetic regime.

5.3.1 Field Induced Magnetoelasticity

In order to directly probe magnetostructural coupling in MnB, we carried out X-ray diffraction experiments as a function of temperature under a magnetic field. Diffraction patterns were collected between 300 K and 700 K under no applied field and under an applied field of 5 T. The difference in lattice parameters fit from these patterns is shown in the top panel of Figure 5.9. Well above and well below the transition temperature, no consistent effect can be resolved above the noise. However, near the Curie temperature where the system is most susceptible to an external field, a substantial change

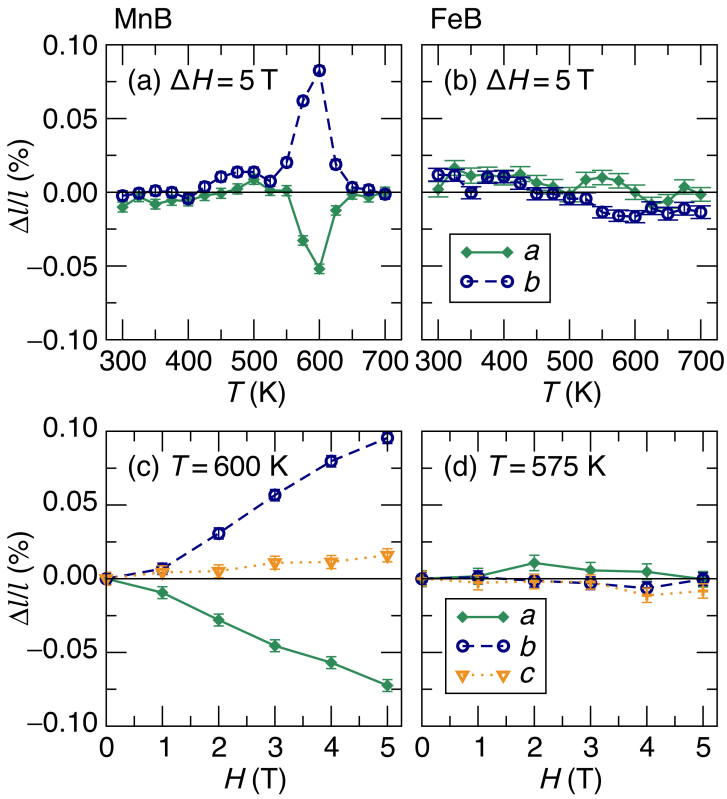

Figure 5.9: Changes in lattice parameters induced by magnetic field. The top row shows the relative change in lattice parameters upon application of a 5 T field, monitored as a function of temperature. (a) MnB shows large induced magnetoelasticity around its magnetic transition temperature, with a positive change in the b lattice parameter and a negative change in the a lattice parameter. No changes are clearly resolvable above the noise in FeB (b). The bottom panel shows how the lattice parameters evolve with magnetic field at fixed temperature near the magnetic transition temperature. Once again, the changes are not clearly resolved in FeB (d), but are seen to be large in MnB (c). Diffraction patterns were collected by Tom Faske and Wolfgang Donner at TU Darmstadt.

in lattice parameters is seen upon application of the field in MnB, an effect which we will term "induced magnetoelasticity." As with the thermal expansion, this effect is anisotropic: the a lattice parameter decreases upon application of the field, while the b lattice parameter increases by nearly 0.1 %. In FeB, no induced magnetoelasticity is resolvable. The observation of a maximum effect at 600 K in MnB as opposed to 570 K as seen in the magnetic measurements and synchrotron diffraction is most likely

due to the large applied field increasing the transition temperature, as well as as slight differences in the sample.

In the temperature-dependent experiment, the induced magnetoelasticity in the c lattice parameter was not determined as the c lattice parameter displayed a sample history-dependence, presumably related to the build-up and release of strains in the material. However, the induced magnetoelasticity in all three lattice parameters was resolvable in isothermal experiments, where the sample was held at a constant temperature near the magnetic transition while fields ranging from 0 T to 5 T were applied. These results are shown in the bottom row of Figure 5.9. Once again, no lattice parameter changes could be resolved in FeB above the noise. In MnB at 600 K, on the other hand, the b lattice parameter expands upon the application of a magnetic field, reaching a maximum expansion of 0.095(4)% (or 950 ppm) at 5 T, while the a lattice parameter contracts, reaching a contraction of $-0.072(4)\%$. The c lattice parameter shows a smaller expansion, which reaches 0.016(4)%. The Q-space resolution of the in-field diffractometer is insufficient to identify the two coexisting structural phases that were seen in the synchrotron diffraction, so it is somewhat ambiguous whether these large magnetoelasticities are caused by intrinsic effects in the two coexisting phases themselves or by the field transforming part of the sample from one phase to the other. However, because the lattice parameter changes are almost twice as large as the maximum difference in lattice parameter between the two phases in the temperature-dependent synchrotron diffraction experiment, we can conclude that intrinsic magnetoelasticity in the phases is at least partially responsible for the effect. This is also consistent with a visual inspection of the diffraction patterns (see Appendix Figure 5.14), which shows that the diffraction peaks shift with applied field, rather than change shape. The observed lattice parameter changes are large compared to conventional Joule magnetostriction

found in all magnets (typical measured in ppm), but are smaller than values would be observed at a giant first-order magnetostructural transition (often 1% or more). This behavior positions MnB in an intermediate regime in terms of magnetostructural coupling, suggesting that MnB is proximal to a magnetostructural tricritical point. The explains the large, but not hysteretic ΔS_M.

This observed anisotropic magnetovolume effect in MnB explains the strange thermal expansion behavior. As MnB is heated from low temperature, its magnetic moment falls as fluctuations set in, and therefore the moment's influence on structure is decreased. On the other hand, when an external magnetic field is applied, the moment strengthens and the inverse happens. Therefore, the changes in lattice upon application of a field provide information about the magnetic contribution to the observed thermal expansion. In FeB, this magnetostructural coupling is small, so the thermal expansion is more or less unaffected by the magnetism. In MnB on the other hand, the anisotropic magnetoelastic effect modifies the standard thermal expansion. In the b direction, the magnetoeleastic effect is positive and large, which overwhelms the standard positive thermal expansion and leads to a strong negative thermal expansion. In the a direction, the negative magnetoelastic effect strengthens the positive thermal expansion leading to an exceptionally large positive thermal expansion. In the c direction, the weaker positive effect offsets the thermal expansion leading to a fairly temperature-independent lattice parameter, as is the case in invar.

5.3.2 Competing Interactions and Magnetostructural Coupling

In order to understand the origins of the unconventional thermal expansion and magnetoelastic effect in MnB, we employ density functional theory (DFT) calculations on both MnB and FeB. Noting that the strongest bonds in the system are the covalent B–

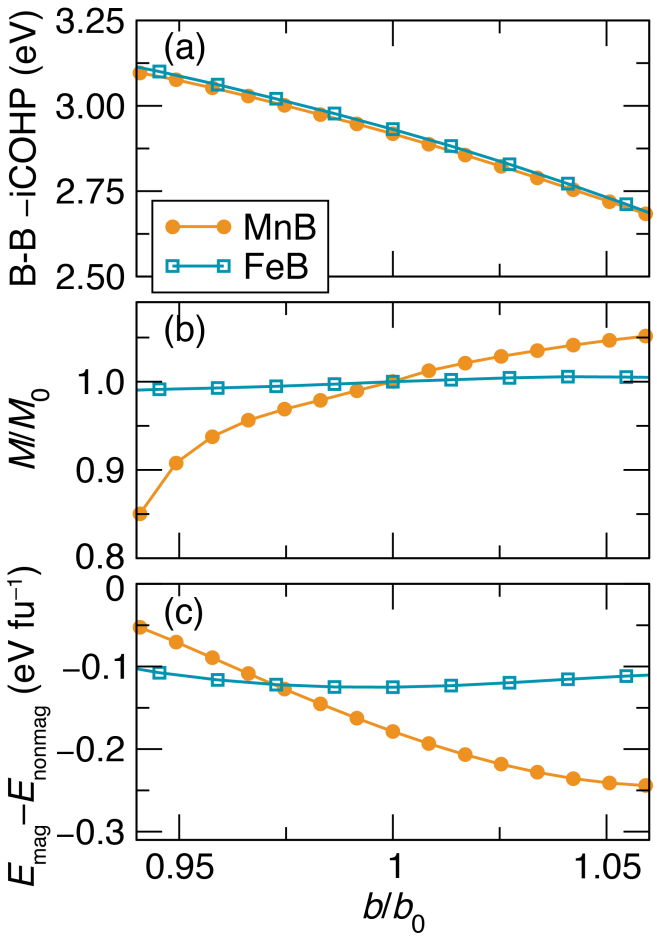

Figure 5.10: Results of DFT calculations for MnB and FeB cells with contracted and expanded b lattice parameter. (a) Integrated crystal orbital Hamilton population (iCOHP) between B–B atoms in the chain, an indicator of the bond strength, with more negative values indicating greater stability. (b) Evolution of the local moment magnitudes (normalized to their equilibrium values M_0), which decrease as b is contracted in MnB but stay constant in FeB. Similarly, (c) shows that the energy stabilization from magnetization (difference in energy between a spin-polarized and non-spin-polarized calculations) decreases as b is contracted in MnB, but stays constant in FeB. These results demonstrate that MnB displays direct competition between Mn moment formation and B–B bond formation, while FeB does not.

B bonds which run in a zig-zag chain along the b lattice parameter, we show the results of DFT calculations for FeB and MnB unit cells with expanded and contracted b lattice parameters in Figure 5.10. B–B bond strength (as indicated by the integrated Crystal Orbital Hamilton Population, $-$iCOHP), Mn or Fe moment magnitude, and magnetic

stabilization energy ($E_{\mathrm{mag}} - E_{\mathrm{nonmag}}$) are shown. In both compounds, contraction of the b lattice parameter (up to about 20%) leads to an increase in the B–B bond strength, indicating that the B–B are more elongated than they would prefer to be, absent of other forces in the structure. On the other hand, contraction of the b lattice parameter leads to a decrease in moment magnitude and magnetic stabilization in MnB, indicating that the manganese magnetism would favor an expanded b lattice parameter. Therefore, the equilibrium lattice parameter in MnB can be understood as resulting from the result of a competition between moment magnitude and B–B bond strength. In FeB, on the other hand, the moment size and magnetic stabilization are virtually independent of b-lattice parameter, and no such competition exists.

We propose that it is the competition between stabilizing the magnetism and the bonding in MnB that leads to the strong and anisotropic magnetoelastic coupling. As temperature is increased and magnetic fluctuations set in, the magnetic stabilization weakens and the B–B bonds are able to exert their contractive forces on the structure, leading to negative thermal expansion in the b direction and a decrease in the B-B bond length and the closest Mn-B bond length. In this picture, the a lattice parameter responds to the driving forces in the b lattice direction with a positive Poisson ratio, alleviating some of the volumetric strain associated with the large decrease in b lattice parameter. This causes the negative magnetoelastic effect in the a direction. The c lattice direction is intermediate between these two cases since the B–B zigzag chains sit mostly in the b-c plane. In addition to explaining the thermal evolution of the lattice parameters, the competition-induced magnetostructural coupling in MnB can explain its extraordinary magnetocaloric effect. Because MnB sits in an active balance between magnetic and structural degrees of freedom, changes in magnetism or b lattice parameter can energetically compensate each other. This provides a low energy pathway for

changing Mn moment magnitude, allowing a small stimulus (magnetic field) to cause a large change in magnetic state and therefore magnetic entropy.

FeB has a smaller transition metal cation than than MnB, due to the increased nuclear charge as well as the lower magnetic moment. Comparing the room-temperature crystal structures, the unit cell volume and metal-B bond lengths are all larger in MnB than in FeB. However, the b lattice parameter and B–B bond lengths only show a small increase, suggesting that the larger size of MnB is straining against the available size of the metal site in the FeB structure, which is constrained by the strong B–B bonding. In fact, MnB sits at a phase boundary: moving one column to the left on the periodic table yields CrB, a transition metal monoboride with a modified structure (space group $Cmcm$) from the $Pnma$ structure of the common forms of MnB, FeB, and CoB. In fact, MnB itself can be stabilized in either the $Pnma$ (as studied presently) or a low-temperature $Cmcm$ structure.[302] Therefore, we expect that FeB does not show the moment-bonding competition, and associated magnetostructural coupling that MnB does because the smaller size of the Fe atoms is not straining the B–B bonds.

5.4 Conclusion

We have demonstrated that MnB shows anisotropic magnetoelastic coupling that is driven by competition between Mn moment formation and B–B bond strength. These results explain why MnB shows a large magnetocaloric effect of $-10.7\,\mathrm{J\,Kg^{-1}K^{-1}}$ at 5 T, while isostructural FeB with otherwise similar magnetic properties shows a much smaller effect. While there is no change in the space group across the magnetic transition in MnB, coupling of magnetism and structure is evidently an important driver of the magnetocaloric performance. Based on this result, MnB appears to be proximal

to a magnetostructural tricritical point which allows for a transition with a large ΔS_M while maintaining negligible hysteresis.

In addition, we have shown that the magnetic transition in MnB is in fact very subtly first-order with clear phase-coexistence at the magnetic transition, albeit the behavior of the transition is quite distinct from the giant first-order coupled magnetostructural transitions displayed by other magnetocalorics.

5.5 Appendix: Supplemental material

Table 5.1: Refined crystal structure of MnB and FeB from room temperature high-resolution synchrotron diffraction data (λ=0.414581 Å). GOF indicates the goodness of fit, which is defined as the ratio between the weighted profile R factor R_{wp}, and expected R factor, R_{exp}. Numbers in parentheses are standard uncertainties in the last given digit(s) from Rietveld refinement.

	MnB (300 K)	FeB (300 K)
spacegroup	$Pnma$	$Pnma$
a (Å)	5.5632	5.5020
b (Å)	2.9769	2.9482
c (Å)	4.1473	4.0596
V (Å)^3	68.682	65.852
GOF	1.93	1.57
metal		
x	0.17588(2)	0.17709(3)
y	0.25	0.25
z	0.12083(3)	0.11988(4)
B_{iso}	0.158(2)	0.162(2)
boron		
x	0.0341(2)	0.0363(2)
y	0.25	0.25
z	0.6128(3)	0.6141(3)
B_{iso}	0.35(1)	0.29(1)

Table 5.2: Refined lattice parameters and weight fractions for the high-temperature phase of MnB from the temperature-dependent synchrotron diffraction data. Numbers in parentheses are standard uncertainties in the last given digit(s) from Rietveld refinement. The values for temperatures from 590.1 K to 580.1 K are from the single-phase parametric refinement, while the values for temperatures between 577.0 K and 557.7 K are from the two-phase parametric refinement, with the lattice parameters and weight fractions for the other (low temperature) phase given in Table 5.3.

T (K)	a (Å)	b (Å)	c (Å)	V (Å)	weight fraction (%)
590.1	5.60293(1)	2.96463(1)	4.15299(1)	68.9836(1)	100
586.6	5.60221(1)	2.96490(1)	4.15287(1)	68.9790(1)	100
583.3	5.60149(1)	2.96522(1)	4.15278(1)	68.9761(1)	100
580.1	5.60059(1)	2.96566(1)	4.15272(1)	68.9744(1)	100
577.0	5.60014(1)	2.96586(1)	4.15300(1)	68.9781(2)	77.0(3)
573.8	5.59912(2)	2.96646(1)	4.15306(1)	68.9805(3)	59.0(3)
570.5	5.59771(3)	2.96742(2)	4.15314(2)	68.9868(6)	43.3(4)
567.7	5.59668(4)	2.96811(3)	4.15335(2)	68.9936(9)	27.2(5)
564.3	5.59596(6)	2.96865(4)	4.15353(3)	69.000(1)	18.7(5)
561.1	5.59536(7)	2.96909(5)	4.15355(4)	69.003(2)	13.4(4)
557.7	5.59492(8)	2.96977(5)	4.15181(5)	68.985(2)	10.3(4)

Table 5.3: Lattice parameters and weight fractions refined for the low-temperature phase of MnB from the temperature-dependent synchrotron diffraction data. The values for temperatures from 577.0 K to 557.7 K are from the two-phase parametric refinement, with the lattice parameters and weight fractions for the other (high-temperature) phase given in Table 5.2. The values for temperatures from 554.3 K to 500.0 K are from the single-phase parametric refinement.

T (K)	a (Å)	b (Å)	c (Å)	V (Å)	weight fraction (%)
577.0	5.59729(3)	2.96794(1)	4.15204(2)	68.9754(5)	23.0(3)
573.8	5.59619(2)	2.96834(1)	4.15252(1)	68.9791(3)	41.0(3)
570.5	5.59505(2)	2.96894(1)	4.15276(1)	68.9829(3)	56.7(4)
567.7	5.59400(1)	2.96952(1)	4.15280(1)	68.9842(3)	72.8(5)
564.3	5.59307(1)	2.97005(1)	4.15288(1)	68.9866(2)	81.3(5)
561.1	5.59215(1)	2.97051(1)	4.15289(1)	68.9859(2)	86.6(4)
557.7	5.59126(1)	2.97096(1)	4.15303(1)	68.9876(2)	89.7(4)
554.3	5.59070(1)	2.97130(1)	4.15296(1)	68.9876(1)	100
551.5	5.58991(1)	2.97163(1)	4.15291(1)	68.9845(1)	100
548.0	5.58914(1)	2.97196(1)	4.15286(1)	68.9820(1)	100
545.0	5.58845(1)	2.97227(1)	4.15282(1)	68.9798(1)	100
541.6	5.58782(1)	2.97253(1)	4.15278(1)	68.9775(1)	100
538.4	5.58718(1)	2.97278(1)	4.15272(1)	68.9743(1)	100
535.3	5.58656(1)	2.97300(1)	4.15265(1)	68.9707(1)	100
532.1	5.58601(1)	2.97321(1)	4.15261(1)	68.9682(1)	100
528.7	5.58547(1)	2.97343(1)	4.15256(1)	68.9658(1)	100
525.6	5.58499(1)	2.97362(1)	4.15253(1)	68.9636(1)	100
522.3	5.58443(1)	2.97376(1)	4.15243(1)	68.9584(1)	100
519.1	5.58393(1)	2.97393(1)	4.15237(1)	68.9550(1)	100
516.1	5.58345(1)	2.97409(1)	4.15233(1)	68.9524(1)	100
512.5	5.58301(1)	2.97426(1)	4.15228(1)	68.9498(1)	100
509.7	5.58248(1)	2.97437(1)	4.15218(1)	68.9443(1)	100
506.5	5.58202(1)	2.97450(1)	4.15210(1)	68.9404(1)	100
503.3	5.58159(1)	2.97463(1)	4.15204(1)	68.9371(1)	100
500.0	5.58140(1)	2.97470(1)	4.15202(1)	68.9359(1)	100

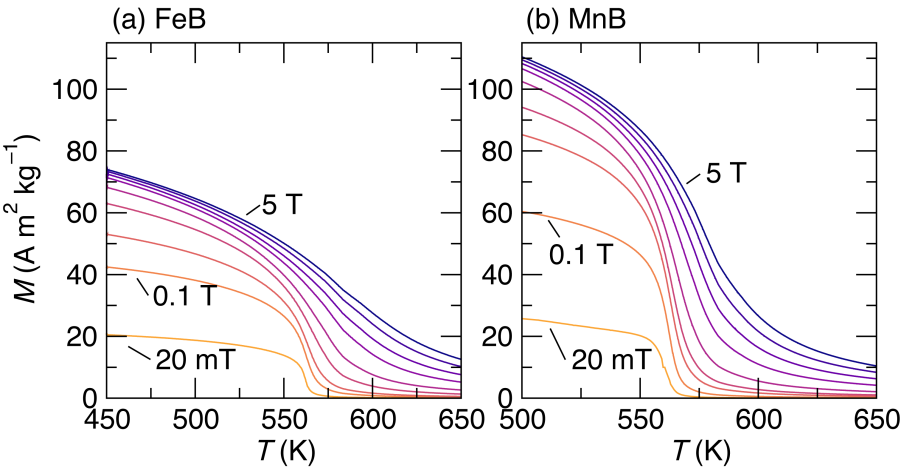

Figure 5.11: Magnetization *vs.* temperature under a nine applied fields for FeB (a), and MnB (b). These data are processed into the ΔS_M data presented in the main text Figure 5.2. At high field, the FeB $M(T)$ broadens out considerably while the MnB remains relatively sharp, leading to a much larger peak ΔS_M for MnB.

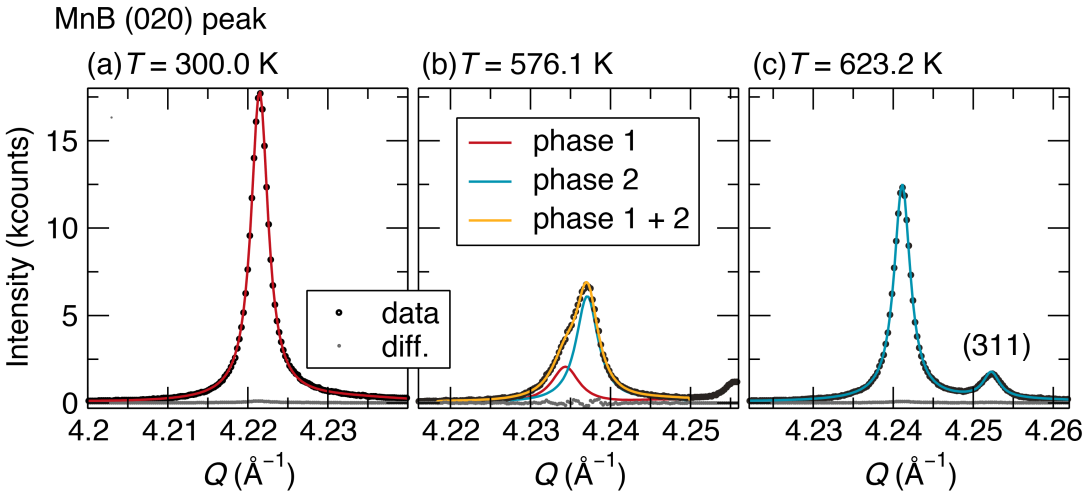

Figure 5.12: MnB (020) synchrotron diffraction peak from patterns taken while equilibrated at temperatures well below the magnetic transition (a), near the magnetic transition (b), and well-above the magnetic transition (c). This data is similar to the data in the main text Figure 4, except that these patterns are taken at static temperature after temperature equilibration. In (a) and (c), the diffraction peaks can be fit with a single Lorentzian peak, while around the magnetic transition two Lorentzians are required, indicating phase coexistence of two phases.

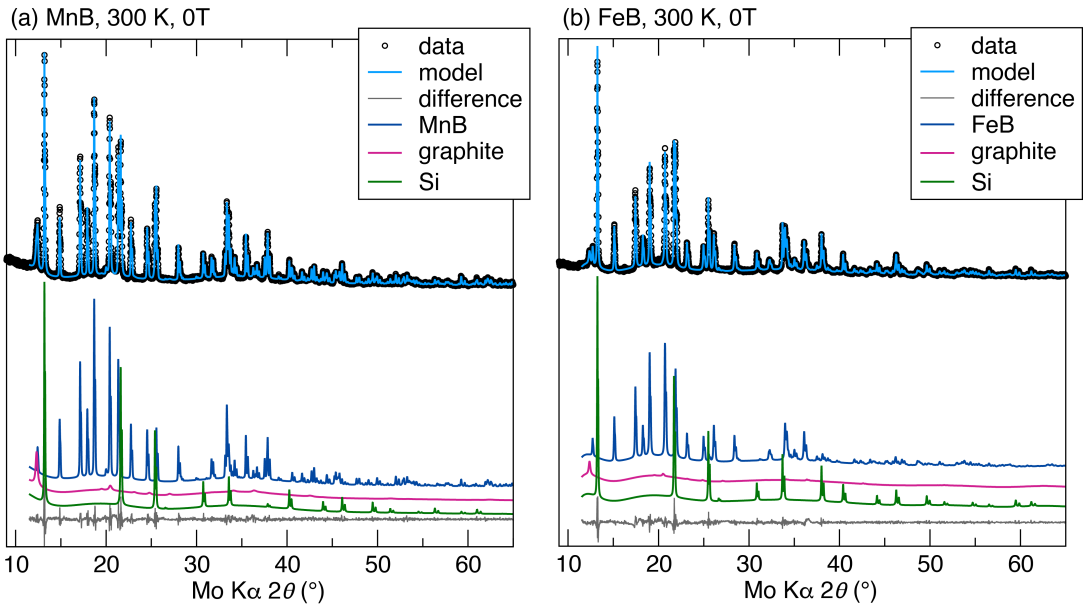

Figure 5.13: Example Pawley fits of the diffraction data from the in-field, variable temperature X-ray diffractometer (in this case, taken at 300 K with no applied field). The samples (single phase MnB or FeB) have been mixed with NIST 640D standard reference silicon and mounted on a graphite support. Both silicon and graphite phases are included in the Pawley refinement, and the known silicon lattice parameter is used to correct instrumental geometric errors.

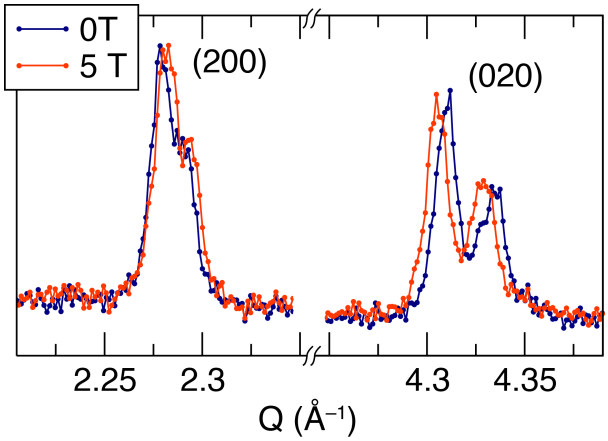

Figure 5.14: Detailed view of the difference in MnB diffraction pattern under zero applied field and 5 T applied field, taken at 600 K. Only the (200) and (020) peaks are shown. The doublet peaks are from Mo Kα_1 and Kα_2 radiation. Upon application of the field, an anisotropic magneto-elastic effect is seen, with some lattice peaks with substantial h character moving to the right, and lattice peaks with substantial k character moving to the left. The full patterns (along with those taken at other fields) were fitted to give the data shown in the main text Figure 5.9(c).

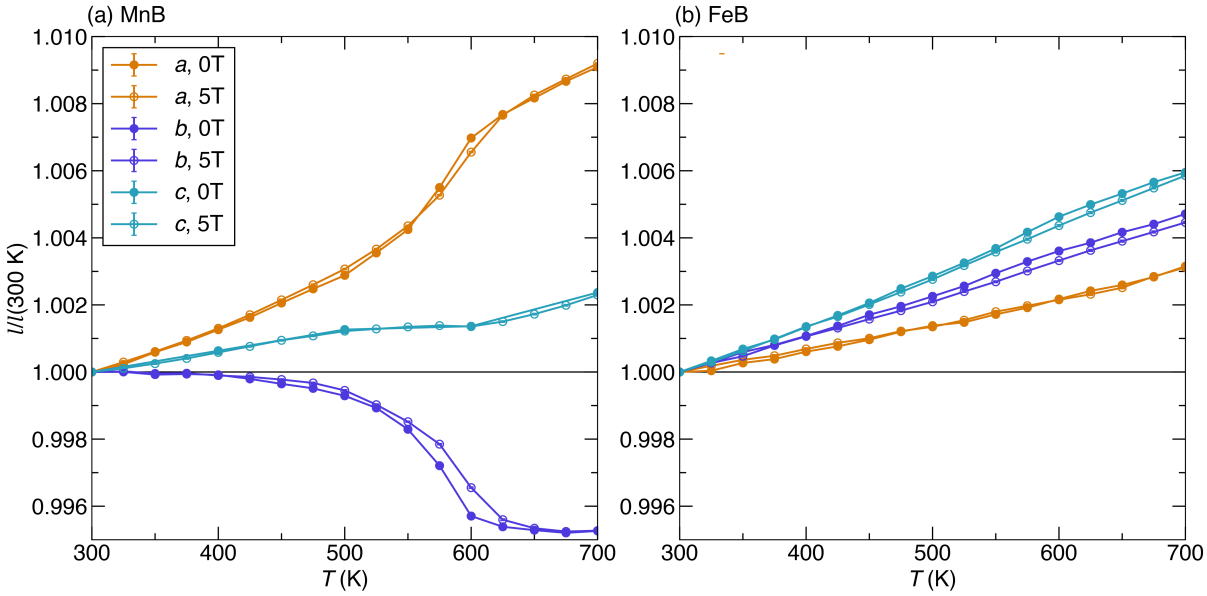

Figure 5.15: Lattice parameters fit from temperature and field-dependent XRD patterns of MnB and FeB, normalized to their 300 K values at zero field. These refinements were used to generate the induced magnetoelasticity (difference in lattice parameters upon application of a magnetic field) data shown in the main text, Figure 5.9. Due to a sample history effects observed in MnB in the c lattice parameter, c, 0 T data are fit from a later run, after the sample had been cycled to remove any history. Error bars, which are in general smaller than the data points, represent standard uncertainties from the Pawley refinements. Diffraction patterns were collected by Tom Faske and Wolfgang Donner at TU Darmstadt.

Chapter 6

Magnetoentropic signatures of skyrmionic phase behavior in FeGe

[1] At this point in the dissertation, we move away from the study of magnetocalorics and focus on understanding long-period chiral magnetic structures in intermetallics, using many of the same methods employed in the previous chapters. In this chapter, we demonstrate that magnetocaloric measurements can rapidly reveal details of the phase diagrams of high temperature skyrmion hosts, concurrently yielding quantitative latent heats of the field-driven magnetic phase transitions. Our approach addresses an outstanding issue in the phase diagram of the skyrmion host FeGe by showing that DC magnetic anomalies can be explained in terms of entropic signatures consistent with a phase diagram containing a single pocket of skyrmionic order and a Brazovskii transition.

[1]The contents of this chapter have substantially appeared in reference 299: J. D. Bocarsly, R. F. Need, R. Seshadri, and S. D. Wilson. Magnetoentropic signatures of skyrmionic phase behavior in FeGe. *Phys. Rev. B* **97** (2018) 100404. doi:10.1103/PhysRevB.97.100404

This project was a collaboration with Ryan Need, who grew the crystals, and was supervised by Ram Seshadri and Stephen Wilson.

6.1 Introduction

Magnetic anomalies corresponding to skyrmion lattice ordering or "precursor" states are well known in chiral helimagnets such as MnSi and FeGe [31–34, 310–313] and were observed long before the first reciprocal space [36, 314] or real space [315] observations of magnetic skyrmions. In general, these anomalies appear as subtle bumps and kinks in the magnetization expected for a ferromagnet near its magnetic transition temperature, as illustrated in Figure 6.1. In skyrmion hosts, these features represent magnetization steps expected for the first-order phase transitions between topologically distinct spin states. Unfortunately, in real materials these discontinuities are always smeared out by experimental convolution and inherent thermal/configurational disorder. This often renders mapping the bulk magnetic phase diagrams of skyrmion hosts a subtle endeavor, and discrepancies have arisen regarding the number of distinct topological phases that exist in key materials [35, 316–320].

This problem is exacerbated in high temperature skyrmion hosts, where direct calorimetric techniques identifying topological phase boundaries (*e.g.* heat capacity studies) suffer from large lattice background signals. The B20 near-room-temperature skyrmion host FeGe is a prominent example of this challenge, where several reports suggest that the skyrmion *A* phase in FeGe is in fact broken into several sections, each hosting distinct skyrmionic states [35, 316–318]. The inability to directly quantify the entropic response from each of these phases in FeGe hearkens to parallel studies of the low temperature skyrmion host MnSi, where similar multiple "*A*-phase" states were

proposed [321] but eventually precluded *via* high resolution heat capacity measurements [319, 322]. Resolving whether there is only a single pocket in the "*A* phase" that hosts skyrmionic spin texture or multiple in FeGe remains an open question.

More broadly, the continued unveiling of magnetic skyrmions in materials near and above room temperature and their potential uses in practical applications [323–330] has further highlighted the need to quantify the thermodynamically distinct spin states in their high-temperature magnetic phase diagrams. New materials continue to be discovered, many with near-room-temperature skyrmion states [39, 325, 331–334]. Precise and quantitative techniques for rapidly interpreting magnetic anomalies in this new realm of materials and for ultimately surveying thermodynamically distinct magnetic states in their phase diagrams are needed.

Here we present a rapid DC magnetization technique for mapping the magnetocaloric response of skyrmion hosts. This method is effective even at high temperatures and is sensitive to the field-driven entropy changes associated with entering/exiting the first-order phase boundaries expected for topologically distinct spin states. As a result, the magnetic phase diagram for a given compound can be mapped in under 24 hours, and the entropy changes associated with a given state can be quantified. We leverage this technique to address an outstanding issue in the phase diagram of the near-room-temperature skyrmion host material FeGe by demonstrating that the entropic response can be understood *via* a single skyrmion "*A*-phase" and a nearby line of first-order phase transitions representing Brazovskii transitions into a fluctuation disordered state.

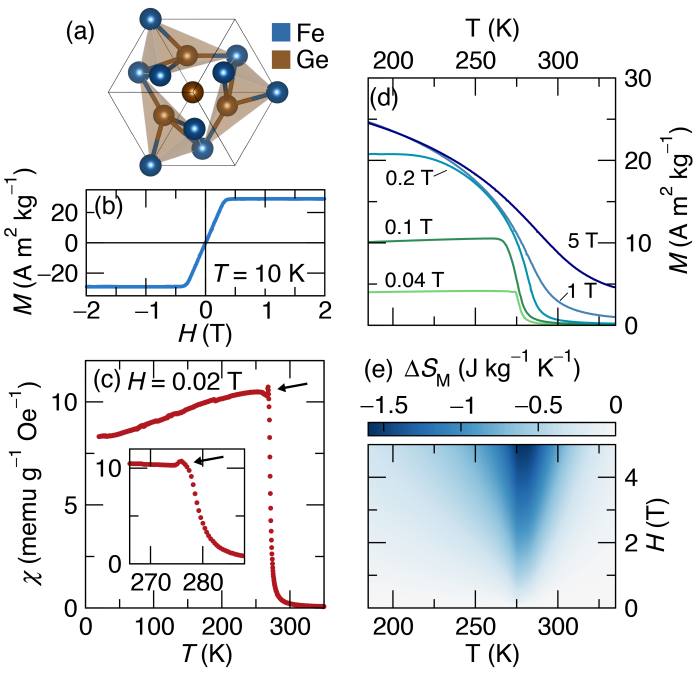

Figure 6.1: (a) Crystal structure of cubic B20 FeGe (spacegroup $P2_13$), shown along the (111) axis. (b) Magnetization as a function of field collected at 10 K is very sharp, saturates at low field, and shows no hysteresis. (c) Magnetization as a function of temperature collected under applied field $H = 20$ mT shows an anomaly near T_C. (d) $M(T)$ collected under different applied fields. This is a subset of the data set (18 total fields) used to calculate the course-grained map of $\Delta S_M(H,T)$ shown in (e).

6.2 Methods

Magnetocaloric effects can be quantified as the magnitude of isothermal entropy change upon magnetization, $\Delta S_M(H,T)$, near a magnetic phase transition. $\Delta S_M(H,T)$ is obtained from the Maxwell relation $(\mathrm{d}S/\mathrm{d}H)_T = (\mathrm{d}M/\mathrm{d}T)_H$, where S is the total entropy, H is the magnetic field, M is the magnetization, and T is the temperature. This allows the isothermal entropy change upon application of field H to be calculated from bulk DC magnetic measurements at many fields and temperatures using

$$\Delta S_M(T,H) = \int_0^H \left(\frac{\mathrm{d}M}{\mathrm{d}T}\right)_{H'} dH' \tag{6.1}$$

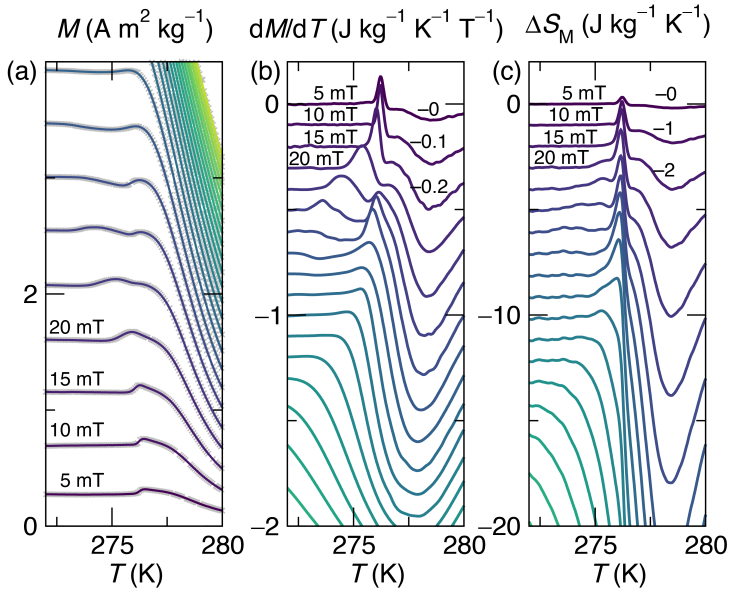

Figure 6.2: The process for obtaining high-resolution magnetoentropic information using equation 6.1. (a) DC $M(T)$ data taken at many closely-spaced fields (24 fields between 5 and 120 mT) (b) Temperature derivatives of magnetization $\mathrm{d}M/\mathrm{d}T = \mathrm{d}S/\mathrm{d}H$ are calculated directly using Tikhonov regularization. For visual clarity, the curves are each offset by 0.1 J kg^{-1} K^{-1} T^{-1}. The antiderivatives of the calculated derivatives are shown as colored lines in (a), and match the raw data (grey crosses) very well. (c) Integrals of the $\mathrm{d}M/\mathrm{d}T$ curves with respect to field give the isothermal magnetic entropy change at each temperature and applied field. Curves are each offset by 1 J kg^{-1} K^{-1}.

Comparisons to heat capacity measurements carried out under field have validated the use of this approach, even for the analysis of first-order phase transitions if suitable measurement parameters are chosen [335–337]. Measuring $M(T)$ under different applied magnetic fields and calculating $\mathrm{d}M/\mathrm{d}T$ allows a map of $\Delta S_M(T, H)$ to be obtained using equation 6.1.

To date, applications of these methods have been largely limited to using DC magnetization to calculate $\Delta S_M(T, H)$ at a few temperatures and fields to evaluate materials for applications in magnetic refrigeration [103] and to determine critical constants [338]. For these applications, low data densities and simple numerical methods are adequate. However, in order to apply these techniques to measure, in resolution, the

entropic effects of the subtle field-driven phase transitions in magnetic skyrmion hosts, far higher data densities are required and more sophisticated data processing is needed to separate signal from noise.

To demonstrate this concept, single crystals of the high temperature skyrmion host FeGe were grown using a standard iodine vapor transport technique (see Appendix section 6.4.2) and a Quantum Design DynaCool Vibrating Sample Magnetometer (VSM) was used to collect two datasets: a "course-grained" set taken while sweeping temperature at a rate of 7 K min^{-1} with fields ranging from 20 mT to 5 T and a "fine-grained" set taken while sweeping at a rate of 1 K min^{-1} at closely-spaced fields around the magnetic transition. The former was taken to evaluate the general high field magnetocaloric response and the latter to analyze the skyrmion phase transition. By operating the VSM continuously, tens of thousands of data points are collected in an ≈18 hour measurement span. The $\mathrm{d}M/\mathrm{d}T$ numerical derivatives cannot be calculated using traditional finite differences without introducing unnacceptable noise. Rather, a statistical technique based on Tikhonov regularization [298] was employed. Briefly, the derivatives are determined so as to simultaneously minimize the deviation of their antiderivatives from the data and the roughness. From these smooth derivatives, the integrals with respect to field were evaluated to obtain $\Delta S_M(T, H)$. Details of the technique are included in the Appendix section 6.4.1.

6.3 Results and discussion

Figure 6.1(a) shows the B20 magnetic lattice of FeGe looking along the (111) axis of the cubic unit cell. A chiral spin state is known to manifest below 280 K in this system with the helix propagating along this (111) wave vector and moments rotating

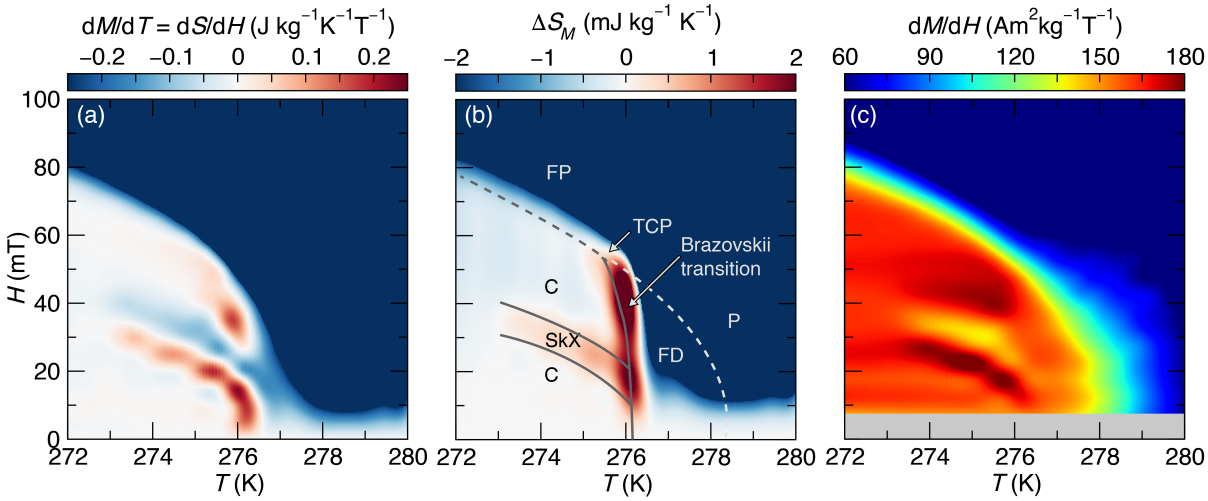

Figure 6.3: Detailed magnetoentropic maps of FeGe near the ordering temperature. (a) A map of $\mathrm{d}M/\mathrm{d}T = \mathrm{d}S/\mathrm{d}H$ reveals clear ridges (red) and valleys (blue) indicating lines of first-order phase transitions. Note that the ridges and valleys are actually continuous; the segmented appearance is an artifact of the 2-D interpolation. (b) Map of $\Delta S_M(T, H)$. (c) $\mathrm{d}M/\mathrm{d}H$ calculated from the DC magnetization dataset. (a) is used to find the phase boundaries of the phase diagram drawn on (b), where solid lines represent first-order phase transitions.The dashed line between C and P indicates a continuous transition. The dashed line between FD and FP represents a crossover. P: paramagnetic, FD: fluctuation disordered, FP: field polarized, C: conical, SkX: skyrmion lattice, TCP: tricritical point.

in the plane orthogonal to this axis. Upon applying a modest field, this helical spin state rapidly tilts into a conical phase and eventually into a polarized ferromagnet state as shown in Figure 6.1(b). The low-field susceptibility $\chi(T)$ is shown in Figure 6.1(c) and the characteristic cusp near T_C is apparent. Magnetization data at higher fields are shown in Figure 6.1(d) while the resulting ΔS_M determined from this course-grained sampling of the phase diagram is shown in Figure 6.1(e). As expected, a negative peak in ΔS_M is seen near the magnetic ordering temperature as the magnetic field aligns paramagnetic spins and decreases the entropy of the system.

At lower fields, however, the magnetization and magnetocaloric behavior are more complex. Figure 6.2(a) illustrates how the low-field magnetization evolves as a function of temperature under a series of closely spaced fields near the magnetic ordering

temperature. This rich behavior is then processed into $\mathrm{d}M/\mathrm{d}T$ at each temperature and field point as shown in Figure 6.2(b). The final integrated ΔS_M curves are plotted in Figure 6.2(c). These data are then presented in Figure 6.3 as (T, H) maps of $\mathrm{d}M/\mathrm{d}T$, ΔS_M, and instantaneous DC susceptibility $\mathrm{d}M/\mathrm{d}H$ near the onset of the "*A* phase" cusp.

$\mathrm{d}M/\mathrm{d}T = \mathrm{d}S/\mathrm{d}H$ can be viewed as a thermodynamic capacity which gives complementary information to traditional measurements of heat capacity $C = T(\mathrm{d}S/\mathrm{d}T)$. Peaks and valleys in $\mathrm{d}S/\mathrm{d}H$ can indicate field-driven first-order phase transitions and ultimately can give entropies of transitions. In the map shown in Figure 6.3(a), the high-field region is blue, indicating the conventional (negative) magnetocaloric behavior of a ferromagnet discussed above. At lower fields and temperatures, however, a white region ($\mathrm{d}S/\mathrm{d}H \approx 0$) can be seen with clear ridges (red lines) and valleys (blue lines) corresponding to phase transformations within that region.

When integrated over field (ΔS_M), the phase regions separated by features in $\mathrm{d}S/\mathrm{d}H$ are visualized in terms of their entropy, as seen in Figure 6.3(b). The sharp nearly-vertical phase line near 276 K denotes a line of first-order phase transitions between the ordered state and the fluctuation disordered state, as discussed later. At temperatures below this first-order line, a single, small pocket of increased entropy (about 0.3 $\mathrm{J\,kg^{-1}\,K^{-1}}$) is observed about the expected skyrmion phase. All other points in the white region, which corresponds to the ordered helical and conical phases, can be reached without a change in entropy from the zero-field state. The observation that the skyrmion lattice shows distinctly higher entropy than the conical phase is consistent with the idea that the skyrmion lattice is stabilized by thermal fluctuations. As further reference, Figure 6.3(c) shows a map of static $\mathrm{d}M/\mathrm{d}H$ illustrating the onset of an enhanced susceptibility at ≈ 279 K, far above the first-order line and indicative of the onset of the fluctuation disordered regime. Anomalies in the susceptibility map of

Figure 6.3(c) bracket both the upper and lower field phase boundaries of the single "*A* phase" skyrmion state resolved in the ΔS_M map.

The assignment of a skyrmion lattice pocket approximately 3 K in width and 10 mT in height within the conical phase is consistent with previous phase diagrams of FeGe based on AC and DC susceptibility, specific heat, and small angle neutron scattering measurements. [35, 316–318] However, variations in AC susceptibility and SANS neutron scattering intensities caused speculation that the conventional skyrmion state, termed the A_1 pocket, was neighbored by between one and three additional "A phase" pockets. Notably none of the signatures of these new "A phase" pockets arise from thermodynamic measurements nor via the identification of broken symmetries, and here, our thermodynamic magnetoentropic measurements resolve that none of those regions except the expected main A-phase show increased entropy relative to the helimagnetic state. Therefore, we conclude that the previous signatures of additional states near the "A phase" arise from dissipative processes or mixed phase regions due to the nearby line of first order Brazovskii transitions. Any true thermodynamic phases must have much smaller skyrmion numbers than the skyrmion lattice phase and entropies nearly indistinguishable from the topologically trivial helical and conical phases.

To further quantify the entropies associated with the phase boundaries in Figure 6.3(a), Figure 6.4(a) shows $\mathrm{d}S/\mathrm{d}H$ *vs.* H cuts at fixed temperatures across the phase diagram of FeGe. At temperatures below the skyrmion lattice phase (Figure 6.4(a)), the conical to field polarized phase transition can be seen as a sudden change in slope of the $\mathrm{d}S/\mathrm{d}H$ *vs.* H curve. At all fields below this critical field, it can be seen that $\mathrm{d}S/\mathrm{d}H$ is zero. This indicates that there is no change in entropy as the system is polarized from the helical magnetic state, through the conical state until the collinear ferromagnetic state is reached. Once in the ferromagnetic state, application of a magnetic field

suppresses spin fluctuations, reducing entropy as expected. One consequence of this constant entropy in the low-field phase, is that there is no signature in $\mathrm{d}S/\mathrm{d}H$ for the helical to conical phase transition at low field.

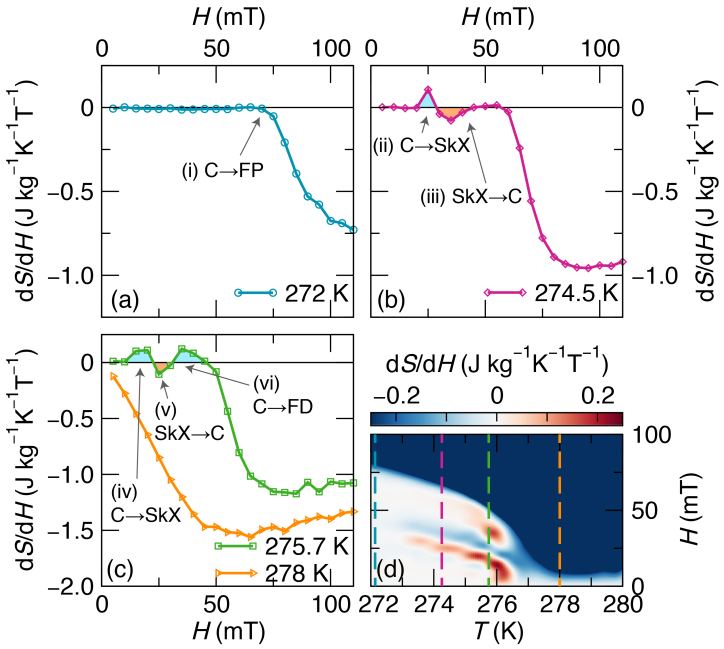

Figure 6.4: (a-c) shows $\mathrm{d}S/\mathrm{d}H$ *vs.* H at four representative temperatures. Field--driven phase transitions are easily found: first-order transitions show up as peaks (ii-vi) in the this thermodynamic capacity, while continuous phase transitions show up as changes in the slope (i). Integration of the peaks gives entropies of transitions and latent heats, as shown in Table 6.1. (d) gives a reproduction of the heatmap of $\mathrm{d}S/\mathrm{d}H$ *vs.* T and H, as shown in Figure 6.3b with the slices shown in (a-c) overlaid as dashed colored vertical lines. Refer to the caption of Figure 6.3 for the definitions of the phase abbreviations.

Turning to Figure 4 (b), $\mathrm{d}S/\mathrm{d}H$ cuts along H near 274.5 K show there is both a peak and a valley prior to entering the field polarized state. Hence as field is increased, there is first an absorption of heat and then a release of heat. This is consistent with the expected entropic signature of first-order phase transitions into and out of the skyrmion lattice phase based on heap capacity measurements of low-temperature skyrmion hosts [317, 320, 322]. These peak and valley features form the extended ridges in (H,T) space (Figure 6.3(b)) that define the top and bottom of the skyrmion lattice phase.

Table 6.1: Latent entropies and heats of transitions as determined by integrating the $\mathrm{d}S/\mathrm{d}H$ curves shown in Figure 6.4. The errors are a generous estimate based on performing the integration at several closely-spaced temperatures.

	transition	ΔS (mJ kg^{-1} K^{-1})	Q (mJ kg^{-1})
(i)	C $\rightarrow$ FP	*na*	*na*
(ii)	C $\rightarrow$ SkX	0.25(5)	69(14)
(iii)	SkX $\rightarrow$ C	$-$0.35(5)	$-$96(14)
(iv)	C $\rightarrow$ SkX	0.9(1)	248(28)
(v)	SkX $\rightarrow$ C	$-$0.29(2)	$-$80(6)
(vi)	C $\rightarrow$ FD	0.81(3)	223(8)

At higher temperature ($T \approx 276$ K), the nearly vertical ridge in the $\mathrm{d}S/\mathrm{d}H$ is split into a lower and an upper section by the intersection of the skyrmion phase boundaries (Figure 6.4(d)). This vertical ridge indicates another line of first-order phase transitions where the application of a magnetic field disorders the system. This is consistent with the theory of a Brazovskii scenario of a strong fluctuations driving the magnetic ordering into a line of first-order transitions terminating in a tricritical point at nonzero field (here, around 50 mT) [339–341]. Crucially, because the slope of this ridge in (T, H) space is negative, application of a field drives the system from the ordered helimagnetic state to the fluctuation disordered state: hence the sign of the $\mathrm{d}S/\mathrm{d}H$ is positive. Therefore, this unique transition appears as a striking line of anomalous (positive) $\mathrm{d}S/\mathrm{d}H$ on the magnetocaloric maps. The entropies associated with crossing each of these phase boundaries are summarized in Table 6.1.

This global picture shows that the very complex shape of the DC magnetic anomalies in FeGe can in fact be elegantly associated with the magnetoentropic response expected for a phase diagram containing a single thermodynamic A phase (skyrmion lattice) contained within the conical phase that borders out of a line of first-order Brazovskii transitions. To verify that features of this phase diagram were not affected by the use of several single crystals, the same procedure was carried out on a fixed single crystal

(≈ 0.1 mg) and yielded the same phase diagram (see Appendix Figure 6.7). This is consistent with observations of very low anisotropy fields in FeGe [311].

In summary, we have demonstrated a rapid magnetoentropic mapping technique that harnesses DC magnetization data to resolve the magnetic entropies associated with the complex phase diagrams of helimagnets in very high resolution. This technique allows for the clear demarcation of thermodynamic phase boundaries in FeGe, which have been difficult to study in traditional calorimetry measurements due to a high ordering temperature and accompanying large lattice background. We observe clear entropic signatures of transitions into and out of a single skyrmion lattice phase as well as observe a nearly vertical line of first-order transitions terminating in a tricritical point, consistent with the first-order Brazovskii transition observed in MnSi. The technique presented here is expected to be of significant utility for the rapid discovery and study of new skyrmion hosts, especially those with transitions near and above room temperature.

6.4 Appendix: Supplemental information

6.4.1 Mapping magnetoentropy using a vibrating sample magnetometer

Principles of measurement and data analysis

In the study of magnetocaloric materials, the isothermal change in entropy upon application of a magnetic field, $\Delta S_M(T, H)$, is routinely calculated from magnetization data by leveraging the thermodynamic Maxwell relation:

$$\left(\frac{\partial S}{\partial H}\right)_T = \left(\frac{\partial M}{\partial T}\right)_H \tag{6.2}$$

Here, S is the total entropy, H is the magnetic field, M is the magnetization, and T is the temperature. This implies that the isothermal entropy change upon application of field H can be calculated from magnetic measurements by equation 6.1, reproduced here:

$$\Delta S_M(T, H) = \int_0^H \left(\frac{\mathrm{d}M}{\mathrm{d}T}\right)_{H'} dH'$$

In this contribution, we use a vibrating sample magnetometer to rapidly collect $M(T, H)$ data to evaluate equation 6.1 in high resolution. The data is collected continuously while slowly ramping temperature at different fixed magnetic fields. This procedure gives a very high density of data points along the temperature axis (many points per Kelvin). While in principle this data density is beneficial, the small T and M differences between neighboring points means that simple numerical differentiation

via the finite difference method ($\mathrm{d}M/\mathrm{d}T \approx \Delta M/\Delta T$) gives extremely large errors that far outweigh the signal. This problem persists even if spline smoothing is applied to each $M(T)$ before the finite differences are taken. To avoid this problem and use the data density to our advantage, we employ a statistical Tikhonov regularization procedure to calculate the numerical derivative. In this method, a derivative curve of a dataset is directly calculated such that it has minimum roughness while still having an antiderivative that matches the magnetization data closely. Given a set of observations (measurements) of magnetization, $\hat{M}$, this means finding a curve, M', that minimizes:

$$Q(M') = \int_{T_{\min}}^{T_{\max}} |M(T) - \hat{M}(T)| dT + \lambda \int_{T_{\min}}^{T_{\max}} |M''(T)|^2 dT \tag{6.3}$$

The first term is the total deviation of the M, the antiderivative of M', from the observations $\hat{M}$. The second term is the roughness of the derivative curve. λ is a regularization parameter that determines the relative importance of the two terms such that larger values of λ lead to a smoother calculated derivative, potentially at the cost of fidelity to the observations. A procedure to calculate these derivatives has been implemented by Stickel in the Python package `scikit.datasmooth` [298]. A suitable λ may be inferred from the data directly; however, it is generally better to manually set this parameter by eye, as shown in Figure 6.6.

Numerical integration does not present the same noise issues as numerical derivation, so the integration step may be performed using the standard trapezoid method.

Measurement Procedure and data analysis

Here, we include an example procedure used to collect DC magnetization data and transform it into mangetoentropic maps. Sample Python code (`magentro.py`) to

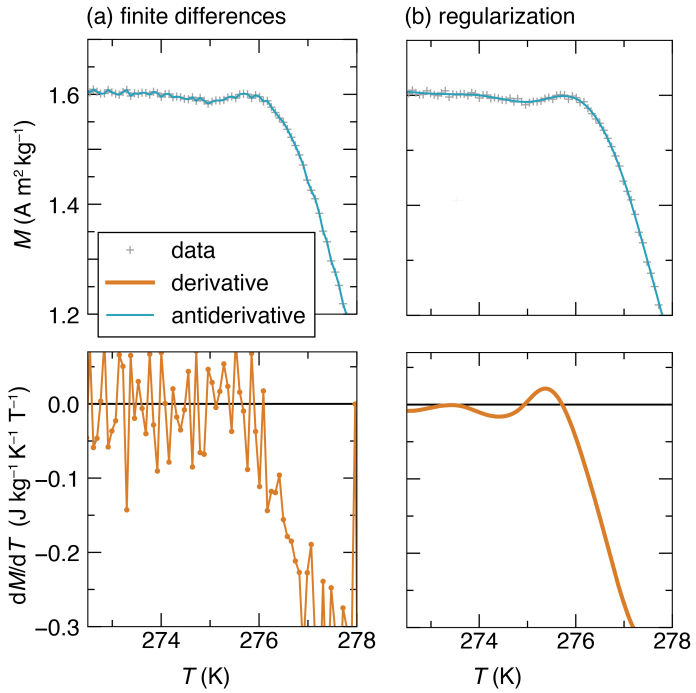

Figure 6.5: Comparison of finite differences and Tikhonov regularization for calculating the derivative of magnetization as a function of temperature ($H = 30$ mT) taken on a single crystal of FeGe (see Section III, below). The top graphs show the magnetization data and antiderivatives of the calculated derivatives, which are shown on the bottom graphs. (a) The finite difference method gives an unusable derivative dominated by noise. (b) The regularization method gives a smooth derivative that matches the input data well.

analyze DC magnetization data to create magnetoentropic maps is included with the Supplemental Material of ref. 18.

1. The $M(T, H)$ data set must be collected with high data density along the temperature axis. In the case of the fine-grained magnetoentropic mapping of 0.75 mg of FeGe, the data points were taken with 5 seconds of averaging of the VSM signal while sweeping temperature at a rate of 1 K/min from 282 K to 268 K (approximately 12 points/ K). This temperature sweep was repeated under 24 different applied fields, ranging from 5 mT to 120 mT in increments of 5 mT. The sweep rate and averaging time were chosen so that many points would be

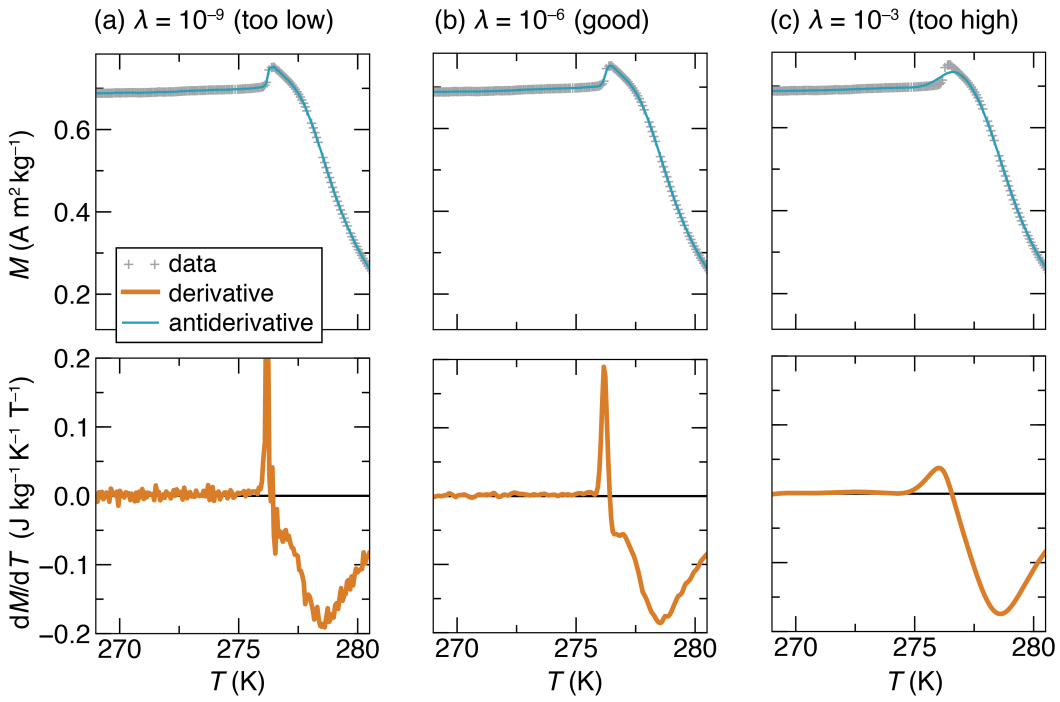

Figure 6.6: Calculation of regularized derivative of FeGe $M(T)$ data collected at $H = 10\,\mathrm{mT}$ with different choices of the regularization parameter λ in equation 6.3. (a) λ is too small. The antiderivative matches the input data well, but the derivative itself is unnacceptably noisy. (b) λ is chosen appropriately. The calculated derivative is reasonably smooth and has an antiderivative that matches the input data well. (c) λ is too large. The derivative is oversmoothed and the antiderivative no longer matches the data. Note that λ must be determined for each data set.

collected across each feature of interest (magnetic anomaly). Faster sweep rates and shorter averaging times are possible for samples with larger moments.

2. Abnormal measurement points are removed and placed the data set is placed into S.I. units. If using a Quantum Design VSM, this can be accomplished using the function `magentro.prep_qdvsm_file()`. Data for all fields should be be included in a single measurement data file. In addition, if there are random outlier measurements, it may be beneficial to manually remove them at this stage.

3. The data set is split into individual $M(T)$ sweeps at fixed fields. For each one, the numerical derivative is performed by minimizing equation 6.3. In general,

this step should be tried with multiple values of λ to visually choose an optimum value that is acceptably smooth while still having an antiderivative that matches the input data. Larger values will give smoother derivatives, while smaller values will match the input data more closely. Oftentimes the same λ can be used for all fields. Sometimes, however, it is advantageous to choose a different λ for each applied field, moving from smaller values at low fields to larger values at high fields. Figure 6.6 shows an example of correctly choosing λ. The function `magentro.process_MTs()` calculates the derivatives for a data set given a λ value (or λ values for each field). Note that the derivative curve is effectively continuous, but it is actually calculated and provided as a collection of discrete (temperature, value) points.

Alternatively, good values of λ may be inferred from the data using a variety of numerical methods, as outlined in Ref. [298]. However, we have found that it is generally easier to simply choose the λ parameters manually.

4. Numerical integrations of the derivatives with respect to field are performed using the trapezoid method at each temperature to give $\Delta S_M(T, H)$. This step is also performed by `magentro.process_MTs()`.

5. The smoothed magnetization, derivatives ($\mathrm{d}M/\mathrm{d}T = \mathrm{d}S/\mathrm{d}H$), and ΔS_M have now been obtained as a function of temperature at the fixed measurement fields. This may be plotted as is (`magentro.plot_property_as_lines()`) or further processed into 2-D (T, H) heat maps (`magnetro.plot_property_as_map()`). Furthermore, cuts may be taken along the field direction at any temperature to create figures like Figure 4 in the main text (`magentro.plot_H_cut()`).

6.4.2 Details of the preparation of B20 FeGe single crystals

FeGe crystals in the B20 structure ($P3_12$) were grown using iodine vapor transport from precursor powder and iodine in a 130:1 mass ratio. The precursor FeGe powder was generated by arc melting pieces of Fe and Ge (99.999%, Sigma Aldrich) together under an argon atmosphere. The arc melted pellet was flipped and remelted at least 12 times to increase mixing and homogeneity, and subsequently annealed under vacuum in a sealed quartz ampoule at 580°C for a period of 7 days. This procedure resulted in FeGe powder that was 25% B20 and 75% B35 as determined by Rietveld analysis of x-ray powder diffraction data. The powder and iodine (99.999% Alfa Aesar) were then sealed in one end of a quartz ampoule under vacuum below 5 $\times$ 10^{-5} mbar. The ampoule was placed in a three zone tube furnace with the precursors held at 570°C, the middle zone at 565°C, and the far end at 570°C for fourteen days. The middle portion of the ampoule, with smooth side walls, was chosen to be the cold deposition region to reduce the number of nucleation sites. In subsequent crystal growths subsequent, small ($<$100 um diameter) B20 crystals were placed in the middle of the ampoule to act as nucleation sites. Successful crystal growth using this procedure resulted in B20 crystals roughly 250 um in diameter with a truncated octahedron morphology. The B20 phase of these crystals was confirmed *via* single crystal X-ray diffraction and SQUID magnetometry.

6.4.3 Magnetoentropic map of a single FeGe single crystal

In order to verify that the magnetoentropic maps presented in the main text were not largely influenced by the use of multiple single crystals, we performed the same measurement on a single crystal (about 0.03 mg, arbitrarily oriented). The results

are shown in Figure 6.7. The results are qualitatively the same, although there is much more noise in the single crystal measurement due to weak signal. Due to the very small size of the crystal, the weight is not known precisely, and therefore the magnitude of the values in Figure 6.7 should not be treated as exact.

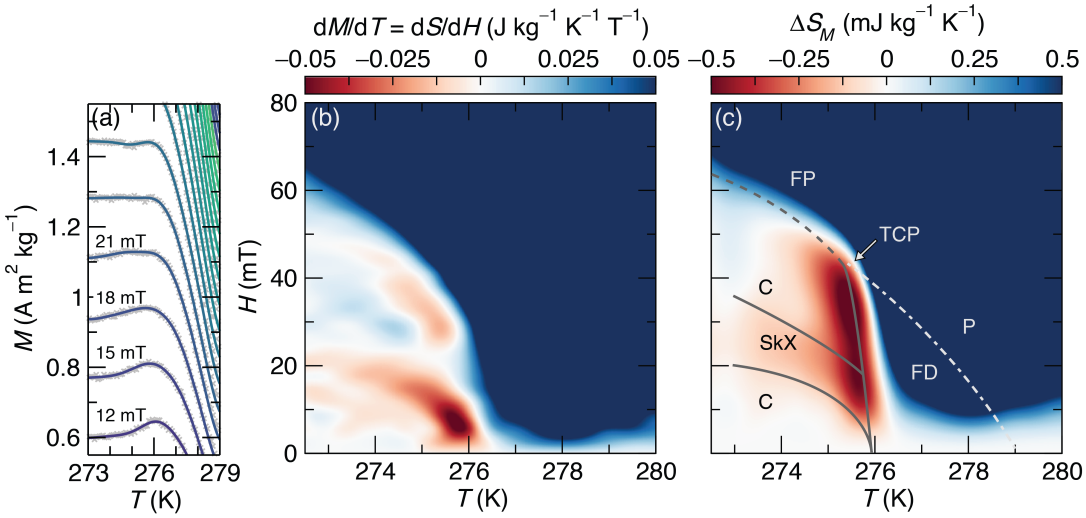

Figure 6.7: Magnetoentropic maps of a single FeGe crystal. (a) Sample of the DC magnetization data (grey crosses) overlayed with the antiderivatives of the regularized derivatives, showing a very good fit despite experimental noise. (b) Map of $\mathrm{d}M/\mathrm{d}T$ showing ridges and valleys matching those in Figure 3 in the main text. (c) Map of $\Delta S_M(T, H)$ with phase diagram overlayed. Solid lines indicate first-order transitions. The dashed line between C and P indicates a continuous transition. The dashed line between FD and FP represents a crossover. P: paramagnetic, FD: fluctuation disordered, FP: field polarized, C: conical, SkX: skyrmion lattice, TCP: tricritical point.

Chapter 7

Deciphering structural and magnetic disorder in the chiral skyrmion host materials $Co_xZn_yMn_z$ ($x+y+z=20$)

[1] $Co_xZn_yMn_z$ ($x+y+z=20$) compounds crystallizing in the chiral β-Mn crystal structure are known to host skyrmion spin textures even at elevated temperatures. As in other chiral cubic skyrmion hosts, skyrmion lattices in these materials are found at equilibrium in a small pocket just below the magnetic Curie temperature. Remarkably, $Co_xZn_yMn_z$ compounds have also been found to host metastable non-equilibrium skyrmion lattices in a broad temperature and field range, including down to zero-field and low temperature. This behavior is believed to be related to disorder present in the materials. Here, we characterize the atomic and magnetic disorder in $Co_xZn_yMn_z$ us-

[1] The contents of this chapter have substantially appeared in reference 342: J. D. Bocarsly, C. Heikes, C. M. Brown, S. D. Wilson, and R. Seshadri. Deciphering structural and magnetic disorder in the chiral skyrmion host materials $Co_xZn_yMn_z$ ($x+y+z=20$). *Phys. Rev. Mater.* **3** (2019) 014402. doi:10.1103/PhysRevMaterials.3.014402 .

ing neutron and synchrotron diffraction, density functional theory calculations, DC and AC magnetic measurements, and the magnetoentropic mapping method introduced in Chapter 6. We demonstrate that Co has a strong site-preference for the diamondoid 8c site in the crystal structure, while Mn tends to share the geometrically frustrated 12d site with Zn, due to its ability to develop a large local moment on that site. This magnetism-driven site specificity leads to distinct magnetic behavior for the Co-rich 8c sublattice and the Mn on the 12d sublattice. The Co-rich sublattice orders at high temperatures (compositionally tunable between 210 K and 470 K) with a moment around 1 μ_B/atom and maintains this order to low temperature. The Mn-rich sublattice holds larger moments (about 3 μ_B) which remain fluctuating below the Co moment ordering temperature. At lower temperature, the fluctuating Mn moments freeze into a reentrant disordered cluster-glass state with no net moment, while the Co moments maintain order. This two-sublattice behavior allows for the observed coexistence of strong magnetic disorder and ordered magnetic states such as helimagnetism and skyrmion lattices.

This project was performed in collaboration with Colin Heikes and Craig Brown, who helped with the neutron data collection, and was supervised Ram Seshadri and Stephen Wilson. I would like thank Weiwei Xie for helpful insights and Neil Dilley for help with the high-temperature magnetic measurements.

7.1 Introduction

Chiral magnetic nanostructures, including skyrmions and other long-wavelength modulated spin structures, have been the subject of intense and increasing research attention in the past decade. From an applications viewpoint, skyrmionic spin textures

are exciting because they promise to enable magnetic racetrack memory and other kinds of low-power, high-density spintronics [13]. From a scientific viewpoint, the discovery of skyrmion spin textures has revealed the tremendous diversity of magnetic nanostructures that can form spontaneously in seemingly simple magnetic materials [36, 38, 39, 315, 333, 343].

A goal in the search for new bulk skyrmion hosts has been to find materials that can exhibit these spin textures in a broad temperature range around room temperature. In most bulk skyrmion hosts, stable skyrmion lattices are only observed in a narrow temperature and field pocket just below the magnetic Curie temperature [299, 319, 320, 344]. The stability of skyrmion lattices in this pocket is understood to arise from a combination of long-range magnetic interactions and thermal fluctuations [36, 345]. A true room-temperature skyrmion lattice in a bulk material was first reported in 2015 with the discovery of a hexagonal lattices of Bloch skyrmions in β-Mn structured $Co_xZn_yMn_z$ ($x+y+z$ =20, $z \leq 7$) [325] compounds. This family has Curie temperatures than can be compositionally tuned between about 210 K and 470 K, with each composition hosting skyrmions near its Curie temperature.

Beyond the equilibrium phase diagram, the topological protection of skyrmions implies the possibility of long-lived metastable skyrmions outside of the narrow pockets of stability. Indeed, by starting in the stable skyrmion lattice phase and quenching temperature, long-lived metastable skyrmion lattices have been observed in several bulk skyrmion hosts. In the chemically well-ordered material MnSi, cooling rates of hundreds of kelvins per second are needed to achieve this state [346]. In a high-pressure cell, this state is achieved with moderate cooling rates [347], a phenomenon that has been attributed to disorder induced by pressure inhomogeneities. Alternately, the intrinsically chemically disordered B20 compound $Fe_{1-x}Co_xSi$ exhibits long-lived

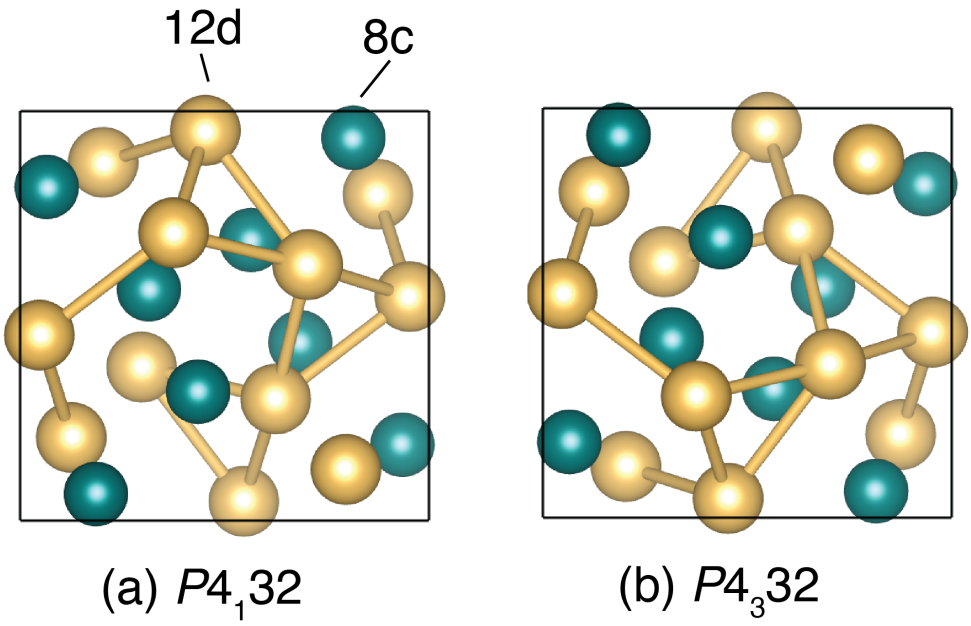

Figure 7.1: The β-Mn crystal structure, comprising 8c and 12d atomic sites, is displayed in its two chiral enatiomers, $P4_132$ (a) and $P4_332$ (b). The two structures differ only in handedness, and therefore should have the same formation energy, with individual crystallites of a sample forming in one or the other configuration. The origin of each cell has been translated by 1/4 of a unit cell from the standard setting such that the chiral four-fold screw axis (4_1 or 4_3) is centered in the cube face. The connecting lines indicate 12d–12d contacts of length ≈2.7 Å, showing how the 12d sublattice is constructed of equilateral triangles arranged in a helix. The 8c sublattice, on the other hand, can be viewed as a distorted diamond lattice.

metastable skyrmions with moderate cooling rates at ambient pressure [344].

As in $Fe_{1-x}Co_xSi$, a metastable skyrmion lattice may be formed in $Co_xZn_yMn_z$ by cooling through the stable skyrmion lattice pocket at moderate rate. This metastable phase is observed in a broad temperature and field range, including down to zero field and from above room temperature down to at least 20 K [332, 348]. At low temperatures and fields, the skyrmion lattice in $Co_8Zn_8Mn_4$ goes through a reversible transition from hexagonal to square symmetry, while approximately maintaining the overall number of skyrmions. Remarkably, this ordering appears to coexist with disordered spin glass behavior at low temperature [37]. For a Mn-rich composition, $Co_7Zn_7Mn_6$, a

second type of stable skyrmion lattice has recently been observed at low temperature in addition to the typical hexagonal lattice which is formed near the Curie temperature [37]. This low-temperature skyrmion lattice is disordered, and is suggested to be stabilized by short-range frustrated magnetic fluctuations in the $Co_xZn_yMn_z$ magnetic ions, as opposed to the thermal fluctuations which stabilize the skyrmion lattice near the Curie temperature. Given these observations, it is clear that the disorder in $Co_xZn_yMn_z$ drives new and interesting magnetic behavior. However, little has been done to characterize the atomic and magnetic disorder in this system, and understand its origins and couplings.

A large amount of atomic and magnetic disorder is possible in the highly-flexible β-Mn structure, which is shown in Figure 7.1. This structure consists of two crystallographic sites: a small eightfold site (8c) which forms a distorted diamondoid network, and a larger twelvefold site (12d), which forms a geometrically frustrated hyperkagome lattice. β-Mn itself is proposed to show a spin liquid state [349], a property which is driven by geometric frustration in the 12d sublattice. Certain substitutions into β-Mn drive the system into a spin-glass with antiferromagnetic correlations [349, 350], while nanoparticles of ϵ-Co, which have β-Mn structure, appear to be ferromagnetic [351]. Other compositions include the superconductors $Li_2(Pt/Pd)_3B$ [352] and Rh_2Mo_3N [353].

$Co_xZn_yMn_z$ compounds crystalize in this structure across a broad volume of the ternary phase diagram stretching from β-Mn itself, to $Mn_{0.6}Co_{0.4}$ and CoZn [354]. Due to the similar electronegativities and atomic radii of Mn, Co, and Zn, it is expected that the elements could mix on either of these two sites, leading to a material with a large amount of compositional disorder within the unit cell. Establishing the atomic distribution over the two sites is crucial to understanding the magnetic properties of

this system, as ions on the two atomic sites are expected to have different magnetic properties due to the different sizes and topologies of the two sites. In fact, in pure elemental β-Mn, Mn atoms on the 12d site are found to have much stronger local magnetic moments than on the 8c site [349, 355].

In this contribution, we characterize the nature of the atomic and magnetic disorder in the skyrmion host materials $Co_xZn_yMn_z$ using neutron and synchrotron diffraction, density functional theory calculations, and DC and AC magnetic measurements. The high-temperature diffraction and DFT results demonstrate that the Co atoms have a site-preference for the 8c site, while Mn and Zn atoms tend to distribute randomly on the larger 12d site, which is geometrically frustrated. The Mn site preference is driven by the Mn atoms' ability to develop a large moment (about 3 μ_B) when sitting on this site. The magnetization measurements and low-temperature neutron diffraction reveal distinct magnetic behavior between the Co sublattice and the Mn/Zn sublattice. The Co atoms order ferromagnetically at high temperature (between 100 K and 470 K, depending on composition) and remain ordered down to low temperature. The large Mn moments tend not to align completely with the ferromagnetic Co matrix, but rather maintain dynamically fluctuations below the Co moment ordering temperature and even at high magnetic fields. At lower temperatures, the dynamic Mn moments freeze into a completely disordered re-entrant cluster spin glass state while the Co sublattice remains mostly ferromagnetically ordered. This two-sublattice behavior allows for the coexistence of disordered and spin-glass magnetic states with ordered magnetic states, such as helimagnetic, conical, and skyrmion lattices.

7.2 Methods

7.2.1 Sample preparation

Five samples of $Co_xZn_yMn_z$ with nominal compositions $Co_{10}Zn_{10}$, $Co_9Zn_9Mn_2$, $Co_8Zn_{10}Mn_2$, $Co_8Zn_9Mn_3$, and $Co_7Zn_7Mn_6$ were prepared from the elements, using a procedure similar to previous reports [325, 353]. Stoichiometric amounts of Co powder, Zn shot, and Mn pieces totaling 0.5 g were weighed and sealed in an evacuated silica ampoule. The ampoule was heated to 1000 °C for 24 hours and then slowly cooled to 925 °C over the course of 75 hours. Finally, the sample was held at 925 °C for 48 hours before quenching to room-temperature in a water bath. For $Co_8Zn_9Mn_3$ and $Co_7Zn_7Mn_6$ this same procedure was performed with 5 g of starting material for neutron diffraction experiments. This solidification procedure yielded shiny metallic slugs. In cases where Mn was present, some green spots on the slug or green powder was found in the ampoule. X-ray diffraction revealed this green powder to be mainly MnO, and in all but the most Mn-rich sample ($Co_7Zn_7Mn_6$), this powder was easily removed from the metallic slug. The slugs were then pulverized for study by X-ray and neutron diffraction and magnetization.

7.2.2 Diffraction and Rietveld Refinement

After preparation, samples were initially checked for rough phase composition using a Pananalytical Empyrean X-ray diffractometer with Cu Kα radiation (λ(Kα1) = 1.54056 Å, λ(Kα2) = 1.54439 Å) equipped with a PIXcel 1D detector. Powdered samples were placed on a zero background plate and measured in Bragg-Brentano (reflection) geometry. In order to minimize the effects of Co and Mn fluorescence in the CuKα beam, the

detector was set to reject low-energy photons.

High resolution synchrotron powder diffraction data were collected on the $Co_{10}Zn_{10}$, $Co_8Zn_9Mn_3$, and $Co_7Zn_7Mn_6$ samples using beamline 11-BM at the Advanced Photon Source (APS), Argonne National Laboratory using an average wavelength of 0.414581 Å. Patterns for $Co_8Zn_9Mn_3$ were collected at 350 K and 100 K, for $Co_7Zn_7Mn_6$ at 300 K and 100 K, and for $Co_{10}Zn_{10}$ at 300 K.

Neutron powder diffraction data were collected on the $Co_8Zn_9Mn_3$ and $Co_7Zn_7Mn_6$ samples using the BT-1 32 detector neutron powder diffractometer at the NCNR, NIST. A Cu(311) monochromator with a 90° take-off angle, λ = 1.5402(2) Å, and in-pile collimation of 60 minutes of arc were used. Data were collected over the range of 3-168° 2θ with a step size of 0.05°. Samples were sealed in vanadium containers of length 50 mm and diameter 6 mm inside a dry He-filled glovebox. A closed-cycle He cryofurnace was used for temperature control between 14 K and 350 K. Patterns were collected for $Co_8Zn_9Mn_3$ at 350 K, 100 K, and 14 K, and for $Co_7Zn_7Mn_6$ at 300 K, 150 K, 100 K, and 14 K.

Rietveld refinement of all patterns was performed using the TOPAS Academic software. The synchrotron patterns were fit using full-Voight peaks with peak width determined by a standard crystallite size term and a microstrain term for the Lorentzian and Gaussian components (four parameters). In most cases, the Gaussian components of the Voight peaks refined to zero and purely Lorentzian peak shapes were used. Diffractometer peak asymmetry was handled using a fixed axial divergence asymmetry correction based on the instrument geometry. The neutron diffraction patterns were fit using purely Gaussian Stephens peak shapes [304] (two parameters) as well as a standard Gaussian size broadening term (one parameter).

For $Co_8Zn_9Mn_3$ and $Co_7Zn_7Mn_6$, synchrotron and neutron diffraction patterns were

collected on identical samples at identical temperatures above and below the magnetic ordering temperatures. These pairs of patterns were simultaneously corefined to yield an optimal structure. In the corefinements, synchrotron and neutron phases were allowed to have different lattice parameters, peak shapes, and instrumental parameters. Atom positions, atomic displacement parameters, and weight percent of a MnO impurity in the $Co_7Zn_7Mn_6$ sample were kept fixed between the two patterns. To limit possible systematic errors in the refinement results caused by the very large intensity of the synchrotron diffraction patterns compared to the neutron diffraction patterns, the weights of the synchrotron data points were globally decreased by a constant factor (0.2 for $Co_8Zn_9Mn_3$ and 0.65 for $Co_7Zn_7Mn_6$). This factor was chosen so that $\sum_i w_i(Y_{\mathrm{obs}} - Y_{\mathrm{calc}})^2/N_{\mathrm{data}}$ was approximately equal for the synchrotron and neutron data sets.

The $Co_8Zn_9Mn_3$ sample was analyzed for composition using X-ray fluorescence on a Rigaku Primus IV using semiquantitative analysis. A bulk piece of the sample was polished flat, and measured at 10 different 1mm spots across the surface of the sample to obtain an average composition and standard deviation. The room temperature densities of $Co_8Zn_9Mn_3$ and $Co_7Zn_7Mn_6$ powder samples were measured using a micromeritics AccuPyc II 1340 helium pycnometer. Ten measurements of the volume of each sample were performed and used to calculate an average and standard deviation of the density.

7.2.3 Density Functional Theory

In order to evaluate the relative energetics of atomic site preferences, density functional theory calculations were performed using the Vienna Ab initio Simulation Package (VASP) [128] using projector augmented wave (PAW) psuedopotentials [129, 130]

within the Perdew-Burke-Ernzerhor (PBE) generalized gradient approximation (GGA) [131]. Spin-orbit coupling was not included. Symmetrically distinct colorings of the disordered 20-atom cubic unit cell were generated using the CASM code [244, 246]. The energies of each ordering were calculated by first performing two sequential structural optimizations (conjugate gradient algorithm), and then a static calculation with the relaxed structure. Energy convergence criteria of 10^{-5} eV for the electronic loops and 10^{-4} eV for the ionic loops were used. During the structural optimizations, unit cell shape, volume, and ion positions were allowed to relax. All atoms were initialized with an initial collinear magnetic moment of 3 μ_B.

7.2.4 Magnetic measurements

Magnetic measurements were performed using a Quantum Design DynaCool PPMS equipped with a Vibrating Sample Magnetometer (VSM), using both the low-temperature mode (2K to 400 K) and the high-temperature oven option (300 K to 900 K). For the low-temperature mode, powdered samples were measured in polypropylene capsules. For the high-temperature mode, as-cast pieces were sanded into thin, flat pieces (1 mg to 5 mg) and cemented onto the high-temperature oven stick using alumina cement (Zircar). Various measurements at fixed fields and temperatures were performed for each sample. In order to probe the paramagnetic Curie-Weiss behavior, magnetization as a function of temperature under an applied field of 1 T was collected upon warming above the magnetic transitions to temperatures up to 800 K. At temperatures between 600 K and 900 K, each of the samples showed a kink in the magnetization that appeared irreversible and therefore was assumed to indicate some reaction with the sample environment. Therefore, data at and above this magnetic feature was discarded. Given these experimental constraints, linear Curie-Weiss fits with no residual magnetization

term were obtained for all samples except $Co_{10}Zn_{10}$.

AC magnetic susceptibility was obtained on the $Co_7Zn_7Mn_6$ sample using a Quantum Design MPMS XL. The real (χ') and imaginary (χ'') parts of the susceptility as a function of temperature was measured on the sample of $Co_7Zn_7Mn_6$ under a DC field $H = 20$ mT with various excitation frequencies. The sample was measured upon warming, after cooling under the 20 mT DC field.

In addition, indirect magnetocaloric measurements were performed using DC magnetization. The magnetic entropy change associated with isothermal magnetization of a material ΔS_M, which is a function of the temperature T and applied magnetic field H, is obtained from magnetization data using the Maxwell relation:

$$\left(\frac{\partial S}{\partial H}\right)_T = \left(\frac{\partial M}{\partial T}\right)_H \tag{7.1}$$

In this equation, S is the total entropy, H is the magnetic field, M is the magnetization, and T is the temperature. Therefore, the isothermal entropy change upon application of field H can be calculated from magnetic measurements at many fields and temperatures by:

$$\Delta S_M(H,T) = \int_0^H \left(\frac{\partial M}{\partial T}\right)_{H'} dH' \tag{7.2}$$

The underlying magnetization data for this calculation was collected as continuously collected magnetization *vs.* temperature sweeps under several different fields (Appendix Figure 7.13). The derivatives were calculated using a regularization procedure [298], as described in Ref. 299, and the integrals were calculated using the trapezoid method.

7.3 Results and discussion

7.3.1 Atomic structure and site preferences

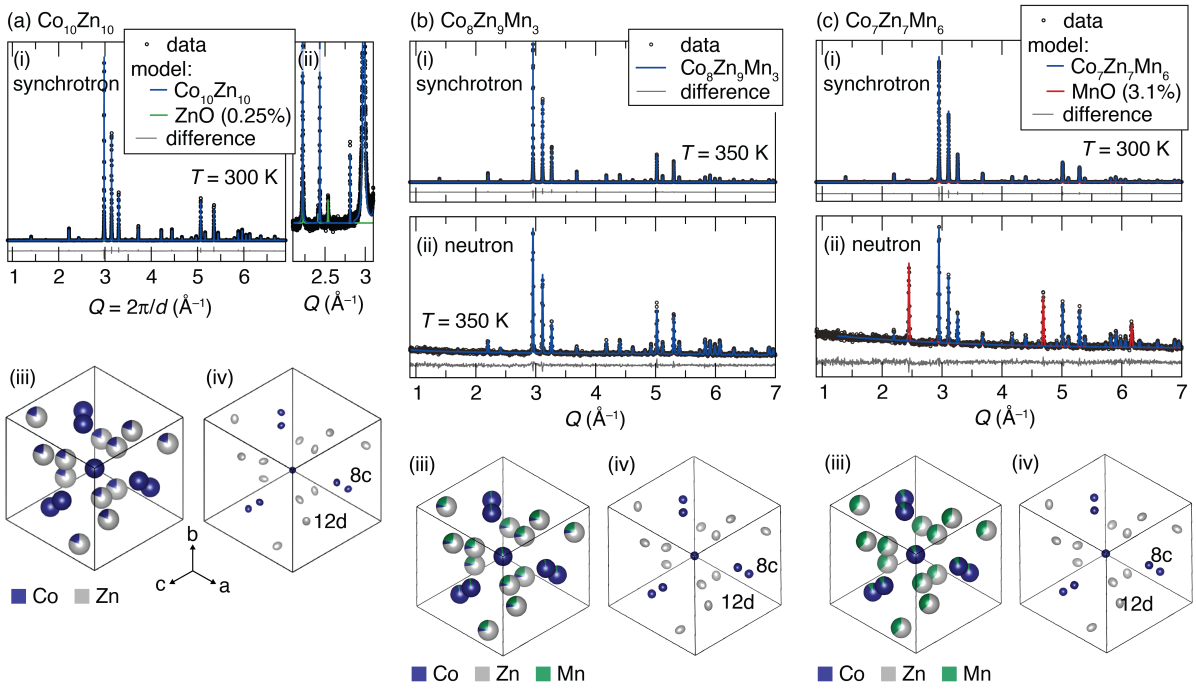

Figure 7.2: Synchrotron and paramagnetic neutron diffraction patterns for (a) $Co_{10}Zn_{10}$, (b) $Co_8Zn_9Mn_3$, and (c) $Co_7Zn_7Mn_6$. For $Co_{10}Zn_{10}$ (a), the synchrotron diffraction pattern is shown along with Rietveld fit to the $P4_132$ β-Mn structure (i). A 0.25 wt.% ZnO secondary phase is observed, which can be seen in an expanded view (ii). Refined structures are shown both with partial occupancies indicated by the atom coloring (iii) and anisotropic atomic displacement parameters displayed as 90% probability ellipsoids (iv). For $Co_8Zn_9Mn_3$ (b) and $Co_7Zn_7Mn_6$ (c), combined synchrotron (i) and neutron (ii) Rietveld refinements above the magnetic Curie temperatures are shown. The $Co_8Zn_9Mn_3$ shows only the β-Mn phase, while the $Co_7Zn_7Mn_6$ sample shows a 3.12(3) wt.% MnO secondary phase, which, due to structure factor differences between X-ray and neutron diffraction, appears much stronger in the neutron pattern. The refined structural details are described in table 7.1 and 7.2.

Rietveld refinement of synchrotron powder diffraction for $Co_{10}Zn_{10}$ is shown in Figure 7.2a., the reported β-Mn structure ($P4_132$) [356] fits the observed synchrotron diffraction pattern at room temperature very well, with a small wurtzite ZnO [357]

impurity (0.25(2) wt%). The 8c site is found to be uniformly occupied by Co, while the 12d site has a random distribution of about 80% Zn and 20% Co, giving a final composition of $Co_{10.24(14)}Zn_{9.76(14)}$, very close to the nominal starting composition of $Co_{10}Zn_{10}$. No peaks violating this model are found, and the data quality is sufficient to refine well-behaved anisotropic displacement parameters (Figure 7.2a-iv). The structural parameters determined using this refinement can be found in tables 7.1 and 7.2.

As Mn is added to this structure, the site preferences become more complex to determine. X-ray diffraction, which is sensitive to the electron density of a crystal structure, is poorly suited to distinguishing between elements with similar electron count, such as Mn and Co. On the other hand, neutrons are scattered by nuclear interactions and magnetization density, and can therefore give complementary information to X-ray diffraction. At first glance, the large contrast between the neutron scattering lengths of Co, Zn and Mn (2.48 fm, 5.68 fm and -3.73 fm, respectively) would seem to make neutron powder diffraction an ideal tool to study the atomic site preferences in these materials. However, since there are only two sites in the β-Mn structure, only a single compositional degree of freedom may be stably refined using the Rietveld method (other degrees of freedom will correlate with the pattern scale factor). In other words, when performing Rietveld refinement, one cannot allow occupancies for Co, Zn, and Mn on the two sites to refine independently, but must constrain the compositions such that only a single compositional parameter is refined. Simultaneous refinements between synchrotron XRD and neutron diffraction can improve the overall fit and allow for refinement of an additional compositional degree of freedom, although the compositional information given by the synchrotron pattern is fairly limited. Therefore, in order to determine the correct ordering in $Co_xZn_yMn_z$ compounds, we jointly refine the synchrotron and neutron data using several plausible models, and distinguish between

equally-well-fitting models by comparing their predicted results to reference measurements such as X-ray Fluorescence compositional analysis and density measurements performed using helium gas pycnometry.

Figure 7.2b shows neutron and synchrotron diffraction patterns taken on a single sample of material with nominal composition $Co_8Zn_9Mn_3$. A joint Rietveld refinement between the two histograms has been performed. Both datasets shows no peaks except those expected for the β-Mn phase, indicating that the sample is phase pure. Rietveld refinement was performed using several compositional models. Given that the 8c site is entirely filled by Co in Co-Zn compounds [353], a natural starting guess is a configuration where the 8 Co atoms per unit cell sit on the 8c site and 9 Zn atoms and 3 Mn atoms are randomly distributed on the 12d site. This gives a reasonably good fit to the data (overall R_{wp}=12.38). If Mn has a strong site-preference for the 8c site, on the other hand, it would be expected to displace Co from the 8c site to the 12d site, which gives far worse fit (R_{wp}=13.78). In addition, various models with Zn on the 8c all give very poor fits.

The fit may be improved by allowing a fraction of the Mn (14%) to move to the 8c site, displacing an equivalent amount of Co to the 12d site (R_{wp} = 12.36). No such improvement is found when allowing Zn to move onto the 8c site. This model fits the synchrotron and neutron data very well and gives physically reasonable refined structural parameters with the overall composition $Co_8Zn_9Mn_3$. However, we may expect that the sample deviates from the nominal composition due to the observation that MnO was formed and discarded during the sample preparation. Therefore, we analyzed the sample using X-ray fluorescence (XRF) compositional analysis, which gave an Mn-deficient composition, $Co_{8.302(14)}Zn_{8.869(15)}Mn_{2.829(6)}$. Rietveld refinements assuming this empirical composition were also performed, and yielded very similar results to the

nominal composition refinements, with a slightly better overall fit ($R_{wp} = 12.35$). In this model, 18% of the Mn is found on the 8c site while 82% is on the 12d site, giving a site configuration of $(Co_{7.58(3)}Mn_{0.42(3)})^{8c}(Zn_{8.87}Mn_{2.41(3)}Co_{0.72(3)})^{12d}$. The refined density (7.805(7) g cm^{-3}) is in agreement with the density determined by helium pycnometry (7.78(5) g cm^{-3}). The fit given by this model, as well as drawings of the determined structure, is shown in Figure 7.2b. In addition, refined parameters are reported in tables 7.1 and 7.2.

We also performed synchrotron and neutron corefinements for data collected on a $Co_7Zn_7Mn_6$ sample, which is a relatively Mn-rich $Co_xZn_yMn_z$ composition (Figure 7.2c). This sample was found to contain about 3% MnO by weight, present in equal quantities in the neutron diffraction pattern and the synchrotron diffraction pattern. Fortuitously, this impurity serves as an internal standard between the two scans, fixing the scale factor of the neutron pattern relative to the synchrotron pattern. This constraint allows for stable refinement of an additional compositional degree of freedom, and, as a result, there is much less ambiguity in this refinement than in the refinement of $Co_8Zn_9Mn_3$. Based on the structures of the $Co_{10}Zn_{10}$ and $Co_8Zn_9Mn_3$ samples, a natural first guess for the structure of $Co_7Zn_7Mn_6$ is a model with Co and Mn sitting on the 8c site, and Mn and Zn on the 12d site.

The compositions of both sites may be independently refined, yielding a structure that matches both the synchrotron and neutron patterns very well, as shown in Figure 7.2c and reported in tables 7.1 and 7.2. This refinement gives a total composition of $Co_{7.04(4)}Zn_{7.43(3)}Mn_{5.53(5)}$, with a 3.12(3)% MnO secondary phase. The mixture of these phases (neglecting oxygen) gives a total composition of $Co_{6.85(2)}Zn_{7.23(2)}Mn_{5.92(4)}$, very close to the nominal composition. In addition, the mixture density is calculated to be 7.56(2) g cm^{-3}, in agreement with a measurement of the density determined by He

Table 7.1: Composition, phase analysis, and lattice parameters from Rietveld refinement of synchrotron and neutron diffraction of $Co_xZn_yMn_z$ samples. Samples are refined in the $P4_132$ spacegroup (No. 213). Numbers in parentheses are standard uncertainties in the last given digit(s) from Rietveld refinement. For site-specific properties and magnetic moments refined from these datasets, see table 7.2 and table 7.6.

composition nominal (determined)	secondary phases	T (K)	source[1]	a (Å)	R_{wp}	R_p	R_{exp}
$Co_{10}Zn_{10}$ $(Co_{10.24(14)}Zn_{9.76(14)})$[2]	ZnO (0.25(2)%)	300	S	6.322506(3)	15.58	12.18	9.37
$Co_8Zn_9Mn_3$ $(Co_{8.302(14)}Zn_{8.869(15)}Mn_{2.829(6)})$[3]	none observed	350	S	6.380518(6)	13.44	10.32	6.43
			N	6.3787(1)	6.09	4.96	6.65
		100	S	6.359298(4)	11.31	8.59	6.32
			N	6.3862(1)	6.39	5.06	6.47
		14	N	6.3558(1)	6.52	5.29	6.60
$Co_7Zn_7Mn_6$ $(Co_{7.04(4)}Zn_{7.43(3)}Mn_{5.53(5)})$[2]	MnO (3.12(3)%)	300	S	6.39108(1)	9.84	7.96	8.69
			N	6.3889(2)	4.27	3.52	4.80
		150	N	6.3745(2)	5.91	4.79	6.71
		100	S	6.37253(1)	9.62	8.19	10.16
			N	6.3705(1)	4.44	3.67	4.81
		14	N	6.3692(1)	3.52	2.90	3.50
$Co_9Zn_9Mn_2$	none observed	300	L	6.35441(9)	3.68	2.87	3.33
$Co_8Zn_{10}Mn_2$ $(Co_{8.8}Zn_{8.7}Mn_{2.5})$[4]	$Co_{2.6}Zn_{10.0}$ (20.1(6)%)	300	L	6.3645(2)	4.14	3.23	3.75

[1] synchrotron (S), laboratory X-ray (L), or neutron (N)
[2] determined by Rietveld refinement
[3] determined by x-ray fluorescence
[4] determined by phase balance with nominal composition

Table 7.2: Site-specific structural properties of $Co_xZn_yMn_z$ samples from Rietveld refinement of synchrotron and neutron diffraction. The 8c site has coordinates (x,x,x), and the 12d site has coordinates ($\frac{1}{8}$,y,$y+\frac{1}{4}$). Numbers in parentheses are standard uncertainties in the last given digit(s) from Rietveld refinement. The type column indicates the type of diffraction data used: synchrotron (S), neutron (N), or joint synchrotron and neutron (S+N).

	T (K)	type	site properties			
			site	composition	8c x or 12d y	B_{eq}
$Co_{10}Zn_{10}$	300	S	8c	Co_8	0.06429(5)	0.419(9)
			12d	$Co_{2.24(15)}Zn_{9.76(15)}$	0.20296(4)	0.588(7)
$Co_8Zn_9Mn_3$	350	S+N	8c	$Co_{7.58(3)}Mn_{0.42(3)}$	0.06479(4)	0.670(8)
			12d	$Co_{0.72(3)}Zn_{8.87}Mn_{2.41(3)}$	0.20279(3)	0.812(6)
	100	S+N	8c		0.06522(3)	0.269(5)
			12d		0.20299(2)	0.345(4)
	14	N	8c		0.0652(4)	0.25(5)
			12d		0.2029(2)	0.27(4)
$Co_7Zn_7Mn_6$	300	S+N	8c	$Co_{7.04(4)}Mn_{0.96(4)}$	0.06477(3)	0.521(5)
			12d	$Zn_{7.43(3)}Mn_{4.57(3)}$	0.20271(2)	0.703(5)
	150	N	8c		0.0637(7)	0.6(1)
			12d		0.2029(4)	0.30(6)
	100	S+N	8c		0.06489(2)	0.100(4)
			12d		0.20270(2)	0.190(3)
	14	N	8c		0.0649(4)	0.1(1)
			12d		0.2029(2)	0.17(4)

pycnometry (7.53(2) g cm^{-3}).

Samples of $Co_9Zn_9Mn_2$ and $Co_8Zn_{10}Mn_2$ were also prepared and checked for phase content with laboratory XRD. The patterns are found in Appendix Figure 7.12. The $Co_9Zn_9Mn_2$ sample is found to be pure β-Mn, with no observable secondary phases at the resolution of the experiment. $Co_8Zn_{10}Mn_2$ was found to contain about 20% of γ-brass $Co_{2.6}Zn_{10}$, which is observed in Co-Zn materials when the Zn:Co ratio deviates too far above 1:1 [358]. By mass balance, the remaining 80% β-Mn phase is expected to have the composition $Co_{8.8}Zn_{8.7}Mn_{2.5}$, which has a nearly 1:1 Zn:Co ratio. The γ-brass has a very low magnetic moment and therefore is not expected to have a significant impact on bulk magnetization measurements, and so this sample was included in the magnetization studies with the mass corrected to remove the nonmagnetic impurity.

Although all samples exhibit slight deviations from the nominal compositions, the samples will be referred to by their nominal compositions for the remainder of this article. The experimental compositions are used in calculating moments and in performing magnetic neutron refinements. Crystallographic information files containing the final refined structures, including anisotropic atomic displacement parameters, for the $Co_{10}Zn_{10}$, $Co_8Zn_8Mn_3$, and $Co_7Zn_7Mn_6$ samples are included in the Appendix.

7.3.2 Energetics of site preferences

In order to verify and rationalize the observed patterns of site preferences and site mixing in $Co_xZn_yMn_z$, we performed density functional theory (DFT) calculations. Table 7.3 and Table 7.4 show the result of DFT calculations for various hypothetical unit cells with the overall compositions $Co_{10}Zn_{10}$ and $Co_8Zn_9Mn_3$, respectively. In each case, we start with a presumed "ground state" for each composition with Co completely occu-

pying the 8c site and the remaining elements randomly occupying the 12d site. Then, we consider alternate configurations generated by taking between one and three Zn or Mn atoms from the 12d site and swapping them with Co atoms from the 8c site. Because all of the configurations studied, including the "ground state", involve atomic site disorder, five randomly selected colorings of the single 20-atom β-Mn unit cell were considered for each configuration, with the average energy (with standard deviation) of those five cells reported.

As can be seen in tables 7.3 and 7.4, the energy of the unit cell increases monotonically as Zn is switched onto the 8c site in $Co_{10}Zn_{10}$ and as Mn or Zn is switched onto the 8c site in $Co_8Zn_9Mn_3$. Linear regression of the calculated cell energies *vs.* the number of non-Co atoms on the 8c atoms gives a rough estimate of the energy penalty associated with these sorts of anti-site defects. In $Co_{10}Zn_{10}$, this penalty is 516(20) meV per Zn atom moved onto the 8c site. In $Co_8Zn_9Mn_3$, the penalty is 210(20) meV/Mn atom on the 8c site and 540(30) meV/Zn atom on the 8c site.

Our experimental samples were prepared by heating to high temperature, slowly cooling to 925°C = 103 meV/k_B and then quenching to room temperature. Therefore, we expect the room temperature samples to contain some amount of disorder frozen in

Table 7.3: DFT calculations of $Co_{10}Zn_{10}$ with various atomic configurations. For each configuration, five unit cells with randomly selected orderings of Co and Zn have been calculated, and average properties (with standard deviations) are reported. Energies are given in reference to the energy of Co_8-Co_2Zn_{10}.

configuration	Zn on	ΔE	Co moment (μ_B)		volume
([8c]-[12d])	8c site	(meV)	8c	12d	(Å^3)
Co_8-Co_2Zn_{10}	0	0(114)	1.33(7)	1.2(3)	248.0(6)
Co_7Zn_1-Co_3Zn_9	1	596(64)	1.32(12)	1.43(7)	249.1(3)
Co_6Zn_2-Co_4Zn_8	2	1067(69)	1.31(15)	1.48(7)	249.8(5)
Co_5Zn_3-Co_5Zn_7	3	1564(88)	1.29(11)	1.47(7)	251.0(4)

Table 7.4: Results of spin-polarized DFT calculations of $Co_8Zn_9Mn_3$ with various atomic configurations. For each configuration, five unit cells with randomly selected orderings of Co, Zn, and Mn have been calculated, and average properties (with standard deviations) are reported. The final column refers to non-spin-polarized DFT calculations on the same unit cells. Energies are provided relative to the Co_8-Zn_9Mn_3 calculations from either spin-polarized (column 2) or non-spin-polarized (final column) calculations. The non-spin polarized reference is 2.518 eV higher in energy than the spin-polarized reference.

configuration	non-Co atoms	ΔE	Mn moment (μ_B)		Co moment (μ_B)		volume	nonmag. ΔE
([8c]-[12d])	on 8c site	(meV)	8c	12d	8c	12d	(Å^3)	(meV)
Co_8-Zn_9Mn_3	0	0 (63)	-	3.28(5)	1.39(4)	-	253.5(2)	0(359)
	Zn on 8c site							
Co_7Zn_1-$Co_1Zn_8Mn_3$	1	676(118)	-	3.23(4)	1.33(5)	1.31(9)	253.5(3)	216(139)
Co_6Zn_2-$Co_2Zn_7Mn_3$	2	1260(54)	-	3.21(7)	1.21(14)	1.26(15)	253.5(4)	555(114)
Co_5Zn_3-$Co_3Zn_6Mn_3$	3	1595(99)	-	3.24(8)	1.16(18)	1.39(7)	254.0(7)	1218(308)
	Mn on 8c site							
Co_7Mn_1-$Co_1Zn_9Mn_2$	1	182(51)	2.39(8)	3.26(6)	1.23(12)	1.25(5)	251.1(2)	-67(197)
Co_6Mn_2-$Co_2Zn_9Mn_1$	2	441(113)	2.1(7)	3.18(6)	1.13(19)	1.35(9)	249(1)	-648(183)
Co_5Mn_3-Co_3Zn_9	3	628(134)	2.40(11)	-	1.0(3)	1.39(8)	249.2(7)	-1014(159)

during the quench from high temperature. However, based on the quench temperature (103 meV/k_B), we expect that Zn atoms swapped onto the 8c site (ΔE = 516 meV to 540 meV) will be quite rare in both $Co_{10}Zn_{10}$ and $Co_8Zn_9Mn_3$. In $Co_8Zn_9Mn_3$, however, Mn may be swapped onto the 8c site at a far lower energy penalty (210 meV $\approx 2k_BT$) and therefore we expect a substantial amount of Mn to be found on the 8c site in the samples prepared by quenching, even though this disordered configuration represents a non-minimum internal energy. This prediction matches our refined structure for $Co_8Zn_9Mn_3$ exactly, which has Mn predominantly on the 12d site, with some mixing (0.43(3) Mn per 20 atom unit cell) onto the 8c site. Based on this energetic analysis, we expect that that quantity of Mn on the 8c site could be reduced by slowly cooling to room temperature (300 K = 26 meV) rather than quenching from high temperature, although we have not explored this experimentally.

In addition to validating the Rietveld refinements, the DFT calculations also allow us to probe the origin of the site preferences exhibited by Co, Zn, and Mn. According to Xie *et al.* [356], the site preference of Co for the 8c site in CoZn may be explained by the smaller size of metallic Co compared to Zn (125 pm and 134 pm 12-coordinate atomic radii [359].) Indeed, tables 7.3 and 7.4 show the unit cell volume is seen to increase as Zn is switched to the 8c site in both $Co_{10}Zn_{10}$ and $Co_8Zn_9Mn_3$, indicating that configurations with Zn on the 8c have non-optimal packing, due to a size mismatch.

The case of Mn, on the other hand, is more complex. Mn has 12-coordinate atomic radius of 127 pm, and therefore should behave similarly to Co on the basis of size arguments. However, the DFT calculations show that unit cell volume actually decreases as Mn is switched to the 8c site, despite the energy of the cell increasing. This suggests that atomic packing considerations favor Mn on the 8c site, even more strongly than Co. However, the calculations reveal a key difference between Co and Mn: magnetism.

In both $Co_{10}Zn_{10}$ and $Co_8Zn_9Mn_3$, each Co atom generally holds a local moment of between 1.1 and 1.4 μ_B, with no clear systematic difference between the 8c and 12d site. Mn, on the other hand, holds a moment of between 3.2 and 3.3 μ_B if it is on the 12d site and a moment between 2.1 and 2.4 μ_B if it is on the 8c site (Table 7.4).

The larger Mn moment observed when the Mn is on the 12d site makes sense, as the larger site allows the Mn d-orbitals to localize more than the smaller 8c site. The formation of a large local moment on Mn provides a magnetic energy savings for the structure, which is seen in the difference in the non-spin-polarized DFT energies (last column of Table 7.4) and spin-polarized DFT energies for the two structures. As Mn is moved to the 8c site, and its moment decreases, the stabilization due to spin-polarization of the electronic structure decreases. In fact, the non-spin-polarized calculations show that, in the absence of magnetism, Mn prefers to sit on the 8c site, displacing Co to the 12d site. Therefore, we may conclude that the Mn site-preferences are driven by a competition between size and magnetism: the non-optimal packing associated with having Mn on the 12d site is offset by the energy savings associated with the development of large local moment on the Mn atoms when they are on the 12d site.

In the case of $Co_7Zn_7Mn_6$, there is not enough Co to fill the 8c site and so the lowest energy state is expected to contain 7/8 Co and 1/8 Mn on the 8c site. DFT calculations of this configuration (Co_7Mn_1-Zn_7Mn_5) give Mn moments of 3.18(7) μ_B and 1.9(1.0) μ_B for the 12d and 8c sites, respectively and Co moments of 1.30(14) μ_B for the 8c site. These moments are very similar to the moments calculated for $Co_{10}Zn_{10}$ and $Co_8Zn_9Mn_3$, suggesting that the atoms, and in particular Mn on the 12d sites, hold largely localized magnetic moments. While a full energetic analysis of the site preferences of this highly disordered composition has not been performed, we expect the

energy cost of switching additional Mn or Zn atoms from the 12d site to the 8c site in $Co_7Zn_7Mn_6$ to be similar to those calculated for $Co_{10}Zn_{10}$ and $Co_8Zn_9Mn_3$. However, because the 8c site is already substantially disordered in $Co_7Zn_7Mn_6$, switching additional Mn onto that site will yield only a modest increase in entropy compared to switching Mn onto the completely ordered 8c site in $Co_8Zn_9Mn_3$. This explains why we do not observe a significant amount of Co on the 12d site in the $Co_7Zn_7Mn_6$ sample.

Based on neutron and synchrotron powder diffraction data, compositional probes, and density functional theory calculations, we can build up a picture of how the 8c and 12d sites are expected to be populated in arbitrary $Co_xZn_yMn_z$ compounds. The preference for the 8c site is as follows: Co $>$ Mn $\gg$ Zn. Therefore, given a $Co_xZn_yMn_z$ composition, up to 8 Co atoms will fill the 8c site, with the remainder (if $x < 8$) being filled by Mn. The remaining Co, Zn, and Mn atoms will be found on the 12d site. If $x \geq 8$, and there is Mn present, a fraction of the Mn is likely to mix onto the 8c site, particularly in samples quenched from high temperature. This means that, in all samples containing Mn, there is substantial compositional disorder on both atomic sites, although the 12d site is generally more disordered. While atomic packing considerations would favor Mn on the 8c site, it instead favors the larger 12d site because of its ability to develop a large (approximate 3 μ_B) local moment on that site.

7.3.3 Magnetic Properties

While it is known that at low field these materials form various long-wavelength modulated magnetic structures, including helimagnetic, conical, and skyrmion lattice phases, [37, 325, 332, 348] the local magnetic structure that is being modulated is not well established. In particular, the magnetic behavior appears to indicate some glassy character to the magnetism at low temperature [37]. In this section, we carefully

Table 7.5: Magnetic properties of $Co_xZn_yMn_z$. a refers to the lattice parameter, T_C is the onset temperature of magnetic ordering, θ_{CW} and $\mu_{\mathrm{eff,CW}}$ refer to the results of Curie-Weiss fits of high-temperature magnetic susceptibility taken at H =1 T, and M_{sat} refers to saturation magnetization at low temperature, expressed either in gravimetric units or in Bohr magnetons per formula unit or per magnetic ion (Mn and Co). ΔS_M^{pk} is the peak value of the entropy change upon isothermal magnetization to $H = 2$ T or $H = 5$ T.

	a	T_C	θ_{CW}	M_{sat}, $T = 2$ K, $H = 5$ T			μ_{eff}	ΔS_M^{pk} (J kg^{-1} K^{-1})	
composition	(Å)	(K)	(K)	(Am^{2}kg^{-1})	(μ_{B}/f.u)	(μ_{B}/mag. ion)	(μ_{B}/f.u.)	$H = 2$ T	$H = 5$ T
$Co_{10}Zn_{10}$	6.3226[1]	470	- -[3]	54.0	12.0	1.20	- -[3]	–0.86	–1.58
$Co_9Zn_9Mn_2$	6.3544[2]	415	432(2)	67.9	14.9	1.35	11.9	–1.06	–1.94
$Co_8Zn_{10}Mn_2$	6.3645[2]	395	395.5(4)	70.0	15.3	1.53	11.5	–1.16	–2.20
$Co_8Zn_9Mn_3$	6.3806[1]	340	363.7(9)	58.8	12.9	1.17	10.3	–0.94	–1.79
$Co_7Zn_7Mn_6$	6.3911[1]	210	183.1(9)	33.5	7.2	0.55	11.9	–0.46	–0.97

[1] synchrotron XRD
[2] laboratory XRD
[3] not obtained due to experimental complications

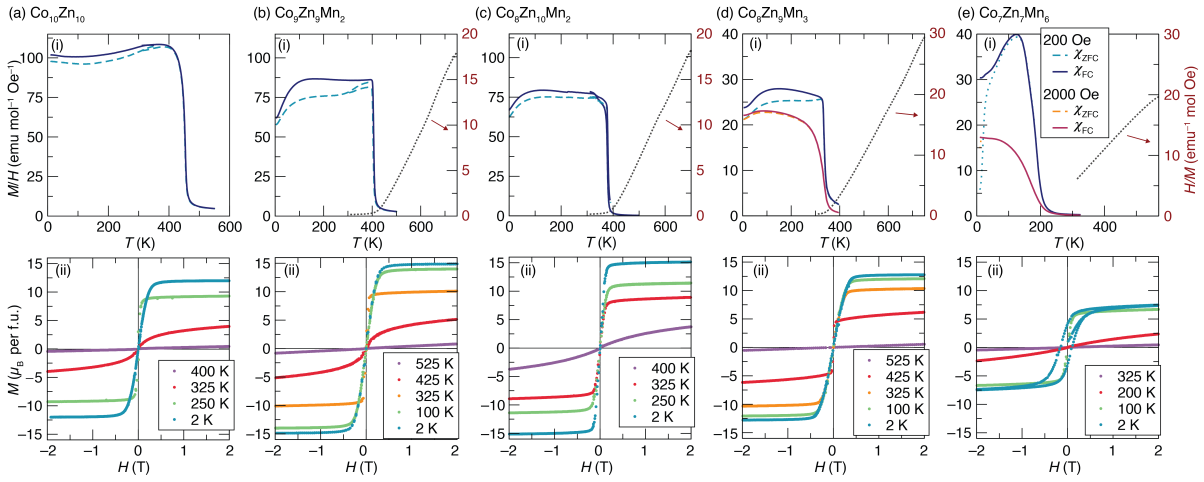

Figure 7.3: Magnetization data for $Co_xZn_yMn_z$ samples. The top row shows susceptibility M/H as a function of temperature under an applied field $H = 20$ mT, showing both zero-field cooled (ZFC, dashed dashed-lines) and field-cooled (FC, solid lines) measurements. For $Co_8Zn_9Mn_3$ (d) and $Co_7Zn_7Mn_6$ (e), measurements taken at $H = 200$ mT, are also shown. For all samples except $Co_{10}Zn_{10}$, the high-temperature magnetization, taken under an applied field $H = 1$ T is shown as inverse susceptibility (χ^{-1}, dotted lines), demonstrating Curie-Weiss behavior at high temperature. The bottom row shows magnetization M as a function of applied field H at various temperatures for each material. For each temperature, a full five-branch hysteresis loop is shown, although no significant magnetic hysteresis is observed in any loop except for at 2 K in $Co_7Zn_7Mn_6$. The unit emu mol^{-1} Oe^{-1} is equal to $4\pi \times 10^{-6}$ m^3.

consider magnetization data on the five $Co_xZn_yMn_z$ compositions in light of the atomic distributions determined in the previous sections, building up a picture of the local magnetic structure of $Co_xZn_yMn_z$.

Figure 7.3 shows DC magnetization data collected on five different $Co_xZn_yMn_z$ compositions. Magnetization as a function of temperature under a low applied field ($H = 20$ mT), displayed in the top row, shows that all five compositions display an onset of magnetic order that looks generally like ferromagnetic ordering, with Curie temperatures ranging from 470 K for the most Co-rich sample ($Co_{10}Zn_{10}$) to 210 K for the most Mn-rich sample($Co_7Zn_7Mn_6$).

Below the ordering temperature, however, the susceptibility deviates from that ex-

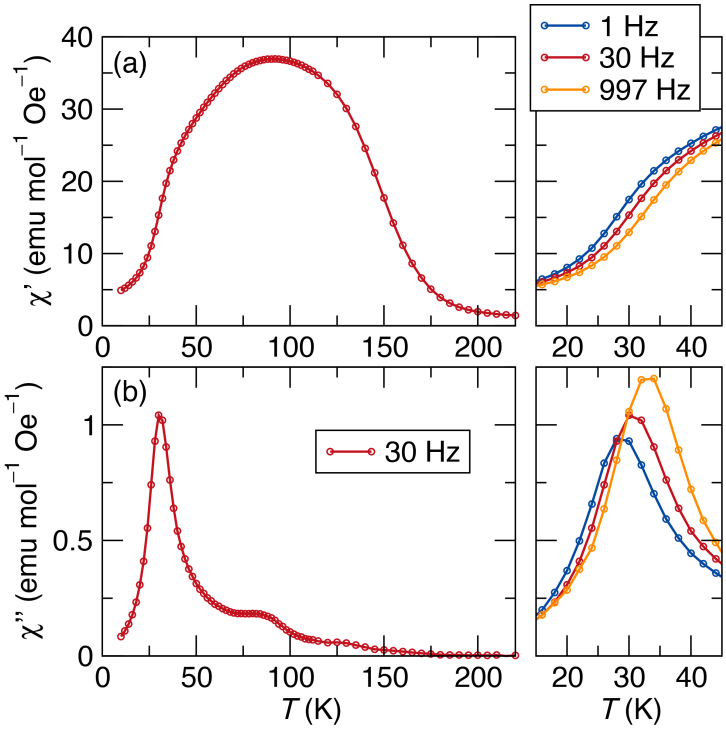

Figure 7.4: AC magnetic susceptibility measurements of $Co_7Zn_7Mn_6$. (a) Shows the real (in-phase, χ') part of the AC susceptibility, while (b) shows the imaginary (out--of-phase, χ'') part. At high temperatures, the AC susceptibility resembles the DC susceptibility shown in Figure 7.3. However, at low temperatures, χ' drops and there is a peak in χ'' indicating glassy dynamics of the spins. The right side of the figure shows the dependence of this feature on the frequency of the applied AC field. The locations of the peak in χ'' increases by about 4.5 K as the excitation field frequency is increased from 1 Hz to 997 Hz. The measurements were collected while warming, after cooling under a DC field $H = 20$ mT. The unit emu mol^{-1} Oe^{-1} is equal to $4\pi \times 10^{-6}$ m^3.

pected for a standard ferromagnet. In particular, in samples with nonzero Mn content, an additional magnetic feature is observed in the low-field susceptibility. Upon cooling to around 120 K, there is a pronounced downturn in both the ZFC and FC magnetization, as has been previously reported in these compounds [37, 325]. The magnitude of this downturn seems to generally increase with increasing Mn content, and in the most Mn-rich composition ($Co_7Zn_7Mn_6$), the downturn is accompanied by a large increase in the difference between the ZFC and FC curves. This divergence is concurrent

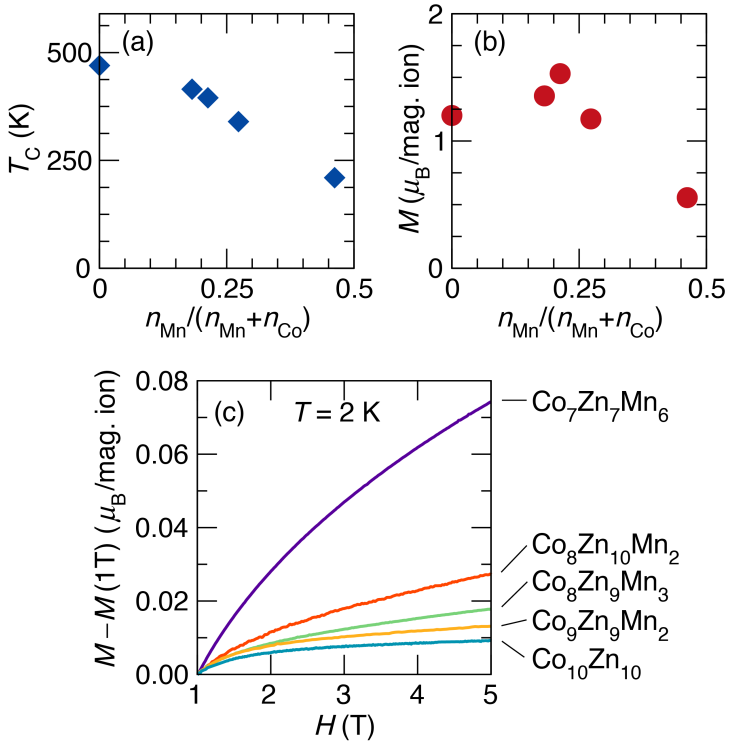

Figure 7.5: Magnetic properties of $Co_xZn_yMn_z$ alloys derived from the data in Figure 7.3. (a) and (b) show properties as a function of the amount of Mn relative to Co in the sample. (a) With increasing Mn, the Curie temperature drops from 470 K ($Co_{10}Zn_{10}$) to 210 K ($Co_7Zn_7Mn_6$). (b) Upon addition of Mn into $Co_{10}Zn_{10}$, the average saturated moment on the magnetic ions (Mn and Co) initially increases up until Mn makes up about 20% of the magnetic ions in the structure. Adding additional Mn results in a decrease in the average moment. The average moments are obtained from the magnetization at $T = 2$ K and $H = 5$ T. For (a) and (b), the data points correspond to, in order from left to right, $Co_{10}Zn_{10}$, $Co_9Zn_9Mn_2$, $Co_8Zn_{10}Mn_2$, $Co_8Zn_9Mn_3$, and $Co_7Zn_7Mn_6$. (c) shows a comparative view of the high-field portions of the 2K. $M(H)$ loops that are shown in Figure 7.3. For each sample, the magnetization at 2 K is expressed in units of μ_B per magnetic ion and the magnetization at $H = 1$ T is subtracted in order to highlight the size of the moment change experienced by the material at high field. For $Co_{10}Zn_{10}$, only a small moment change is seen, indicating that the moments in $Co_{10}Zn_{10}$ are (very nearly) completely polarized by a 1 T field. For $Co_7Zn_7Mn_6$, on the other hand, the moment rises by about 0.08 μ_B per magnetic ion (around 14%) between 1 T and 5 T, indicating that the material still contains unpolarized spins at 1 T. Samples with smaller amounts of Mn fall in between $Co_{10}Zn_{10}$ and $Co_7Zn_7Mn_6$.

with the onset of magnetic hysteresis as observed in loops of the magnetization as a function of magnetic field (Figure 7.3e-ii, 2 K). Both of these observations point to mag-

netic irreversibility in $Co_7Zn_7Mn_6$ at low temperature. For all other compositions, and for $Co_7Zn_7Mn_6$ at higher temperatures, no such hysteresis is observed and a relatively small difference between the ZFC and FC magnetization curves is seen.

Figure 7.4 shows AC magnetic susceptibility for $Co_7Zn_7Mn_6$, the most Mn-rich composition in this study. AC susceptibility as a function of temperature was measured on the sample of $Co_7Zn_7Mn_6$ with three different excitation frequencies (f = 1 Hz, 30 Hz, and 997 Hz). Above about 70 K, the real part of the susceptibility (χ') mirrors the field-cooled DC susceptibility shown in Figure7.3e-i. Above the Curie temperature (around 200 K), the imaginary part of the susceptibility (χ'') is very nearly zero, indicating that the system responds quickly to applied magnetic field. This is expected for a magnetic material in its paramagnetic regime. Below 200 K, a small χ'' signal appears, consistent with the small loss expected due to the onset of magnetic order.

Below 70 K, the real part of the susceptibility deviates from the field-cooled DC susceptibility, dropping precipitously. Simultaneously, the imaginary part of the susceptibility increases, comes to a peak around 30 K, and then falls off again. As seen on the right part of Figure 7.4 Both χ' and χ'' show a clear dependence on the excitation frequency—the onset of the downturn in χ' and the peak in χ'' increase in temperature by about 4.5 K as the excitation frequency is increased from 1 Hz to 997 Hz. These features in χ' and χ'' are a clear hallmark of glassy behavior.

The shift in freezing temperature as a function of applied frequency gives information about the magnetic interactions involved in the freezing process of a glassy magnetic system [360]. The relative shift in freezing temperature per decade of frequency, $\delta T_f = \Delta T_f/(T_f \Delta \log_{10}(f))$ is 0.038. Canonical spin glasses, such as dilute Mn in Cu or Au, have values of δT_f of the order of 0.005. On the other hand, superparamagnets show much larger values on the order of 0.1 to 0.3. The intermediate value

of δT_f in $Co_7Zn_7Mn_6$ is consistent with that of a “cluster glass", where clusters of spins, rather than individual spins, make up the building blocks of the spin glass. This is the expected state for a spin glass with a large concentration (larger than a few percent) of magnetic ions, as is the case with the 12d sublattice of $Co_7Zn_7Mn_6$.

As can be seen in the magnetization *vs.* field loops, the saturated magnetization of all of the compounds monotonically increases as temperature is lowered, indicating that the low- temperature downturn seen in the 20 mT $M(T)$ is purely a low-field phenomenon. For $Co_8Zn_9Mn_3$ and $Co_7Zn_7Mn_6$, we also show ZFC and FC measurements taken at $H = 200$ mT (Figure 7.3d-e). At this higher field, the low-temperature downturn in susceptibility has nearly disappeared and the irreversibility between ZFC and FC measurements has closed.

Magnetic properties extracted from the data in Figure 7.3 are shown in table 7.5 and plotted in Figure 7.5. As seen in Figure 7.5, many of the magnetic properties follow trends with the relative amount of Mn to Co in the unit cell, quantified as $n_{\mathrm{Mn}}/(n_{\mathrm{Mn}} + n_{\mathrm{Co}})$. The magnetic transition temperature T_c monotonically decreases as Mn is added (Figure 7.5a), indicating that ferromagnetic exchange is weakening. The average magnetic saturation per magnetic ion (Co and Mn), on the other hand, shows non- monotonic behavior (Figure 7.5b). The moment first rises as small amounts of Mn are added to the structure, then falls as larger amounts (3 or more Mn per unit cell) are added (Figure 7.5). This behavior, at least at first glance, appears to disagree with the density functional theory calculations, which indicate that each Co should contribute a moment of about 1.3 μ_B while each Mn contributes a moment of about 3.2 μ_B (or 2.4 μ_B if it is on its minority 8c site). Based on these calculations, we would expect that addition of Mn will uniformly increase the saturated magnetic moment. For $Co_{10}Zn_{10}$, $Co_9Zn_9Mn_2$ and $Co_8Zn_{10}Mn_2$, the measured magnetic moment per formula

unit is reasonably consistent with these local moment values (within 15%). For the more Mn-rich compositions $Co_8Zn_9Mn_3$ and $Co_7Zn_7Mn_6$, the experimental saturated moment is far smaller than predicted.

This apparent disagreement can be explained by non-collinearity of the Mn spins. The DFT calculations considered only collinear ferromagnetic moments; therefore, while the calculations highlight the importance of a large local moment on the Mn atoms (energy scale on the order of eV), they do not necessarily inform the lowest energy orientation of those moments (energy scale on the order of meV). Here, we propose an understanding of the magnetic structure of $Co_xZn_yMn_z$ that is consistent with both the DFT and the magnetic measurements. In our model, $Co_{10}Zn_{10}$ behaves as a local ferromagnet, with Co spins collinearly aligned within a unit cell. When a small number of Mn atoms are added to this system, they hold, as predicted by the DFT, a large local moment. These local moments order via the dominant exchange field established by the surrounding Co moments and tend to align ferromagnetically with the Co moments, increasing the susceptibility and saturation magnetization of the system. As more Mn is added, Mn atoms become more likely to have Mn-rich neighborhoods and therefore are less subject to the ferromagnetic exchange field established by the Co moments. The Mn moments tend less toward order, and more towards the native behavior of Mn in the β-Mn structure, which has a disordered ground state. Therefore, we see that after the addition of about two Mn atoms per unit cell, the saturated moment begins to decline with the addition of Mn.

In this picture, the Mn spins are more-or-less dynamically disordered at temperatures below the apparent ordering temperature of the Co moments, with a partial tendency to align with the Co spins. The low-temperature downturn in susceptibility, then, can be understood as glassy freezing of clusters of the Mn spins into a stati-

cally disordered spin glass, at which point the Mn spins no longer respond to a small magnetic field. In the most Mn-rich sample, this transition is even accompanied by a dramatic increase in magnetic hysteresis, consistent with the onset of sluggish magnetic dynamics in the frozen state.

Figure 7.5c shows a detailed view of the high-field portion of the magnetization as a function of field for each sample at 2 K with the magnetization at 1 T subtracted off to highlight differences in the high-field magnetic behavior. In this high-field regime, the chiral magnetic modulations are believed to be completely field-polarized such that no long-wavelength structures persist. $Co_{10}Zn_{10}$ experiences very little change in moment between 1 T and 5 T. The total moment in samples containing Mn, on the other hand, increases with application of large magnetic fields. In particular, the moment of $Co_7Zn_7Mn_6$ rises about 0.08 μ_B/mag. ion (14%). This suggests that the moments are not fully polarized at 1 T, or even 5 T, consistent with our model of disordered Mn on the 12d site.

7.3.4 Sublattice-specific magnetic ordering

Based on the magnetization data, we have inferred that the Mn and Co moments behave very differently in $Co_xZn_yMn_z$ materials. In order to clarify this behavior, low-temperature neutron diffraction measurements were performed on the $Co_8Zn_9Mn_3$ and $Co_7Zn_7Mn_6$ samples. The long-wavelength helimagnetic groundstate will, in principle, give a neutron diffraction pattern that looks very much like the diffraction pattern of the unmodulated unit cell, except with magnetic satellite peaks around some of the magnetic Bragg peaks. In this case, however, the modulation period is so long that the expected reciprocal-space splitting will be too small to see in the resolution of our powder neutron diffraction experiment. Because of this, we are able to model the

neutron diffraction patterns as if the long-period modulation does not exist, refining for only the local magnetic structure.

Figure 7.6 shows low-temperature neutron diffraction patterns, along with Rietveld fits, for the $Co_8Zn_9Mn_3$ sample. The site occupancies have been fixed from the paramagnetic (350 K) synchrotron-neutron corefinement. The 100 K pattern is corefined with a synchrotron pattern taken at the same temperature (shown in Appendix Figure 7.11a), while the 14 K pattern is refined on its own. Upon cooling through the magnetic transition, the intensity of several peaks is increased, and two new peaks at low Q (1.4 $Å^{-1}$ and 3.67 $Å^{-1}$) appear. These two peaks can be indexed as the allowed peaks (110) and (111) in the β-Mn unit cell, which have a very low structure factor in the paramagnetic phase. No magnetic peaks are observed at structurally-forbidden positions, indicating that the magnetic unit cell and the paramagnetic unit cell are the same.

For magnetic Rietveld (co)refinements on this sample, a simple collinear ferromagnetic spin structure was assumed. In this model, the Co and Mn on the 8c site have a single, linked moment, and the Co and Mn on the 12d site have a different linked moment. This means that the refinement is probing the average ordered moment of the Co and Mn on the 8c and 12d sites. As can be seen in Figure 7.6, this model fits the neutron patterns at both 100 K and 14 K data well, with no discripencies in peak intensities between the model and the magnetic peaks in the data. At 100 K, the 8c magnetic ions are found to hold moments of 1.00(6) μ_B and the 12d magnetic ions are found to hold moments of 0.99(28) μ_B (table 7.6). For the 8c site, which is mainly comprised of Co, this value is of reasonable agreement with the DFT moment (about 1.3 μ_B). On the 12d site, however, the magnetic ions are mostly Mn, and this refined moment is smaller than the DFT moment (3.3 μ_B). This is consistent with our understanding of

the Mn spins as dynamically disordered, with only a partial tendency to align in the direction of the Co spins at 100 K.

At 14 K, below the glass freezing temperature, similar magnetic diffraction is observed. A close look at the pattern reveals that the magnetic intensity is actually weaker in the 14 K pattern than the 100 K pattern. Such behavior is unusual in ferromagnets, where at low temperature fluctuations are suppressed and the observed ordered moment is at its largest. As seen in Table 7.6, refining the 14 K pattern gives moments on the 8c and 12d site of 0.80(8) μ_B and $0.1(4)\,\mu_B$, respectively. The moments on both sites have decreased relative to the 100 K data, but the moment on the Mn-rich 12d site has decreased much more than that on the Co-rich 8c site. This supports our hypothesis that the frustrated and glassy behavior observed in the magnetization data is driven by the Mn spins on the 12d site, while the Co atoms on the 8c site remain largely ferromagnetic. At 100K, the Mn spins may be dynamically disordered with some preference to align themselves with the ferromagnetic exchange field of the Co atoms, while at 14 K the disordered Mn spins are frozen into a glassy state with no long-range alignment or net moment. The minor drop in moment on the 8c site may be attributed to the small amount of Mn-Co antisite mixing, which was noted earlier.

Table 7.6: Results of magnetic Rietveld refinement of neutron diffraction data. M_{sat} is determined DC magnetization data. Numbers in parentheses are standard uncertainties in the last given digit(s) from Rietveld refinement. χ^2 is equal to $(r_{\text{wp}}/r_{\text{exp}})$.

	T	mom. per mag ion (μ_B)		total moment	M_{sat} ($H = 2$ T)	χ^2
	(K)	8c	12d	(μ_B/f.u.)	(μ_B/f.u.)	
$Co_8Zn_9Mn_3$	350					0.84
	100	1.00(6)	0.99(28)	11(1)	12.1	0.98
	14	0.82(8)	0.15(41)	7.0(1.4)	12.3	0.98
$Co_7Zn_7Mn_6$	300					0.80
	100	0.64(5)	0.75(16)	6.3(1.0)	6.7	0.85
	14	0.38(4)	0	3.0(3)	7.3	1.05

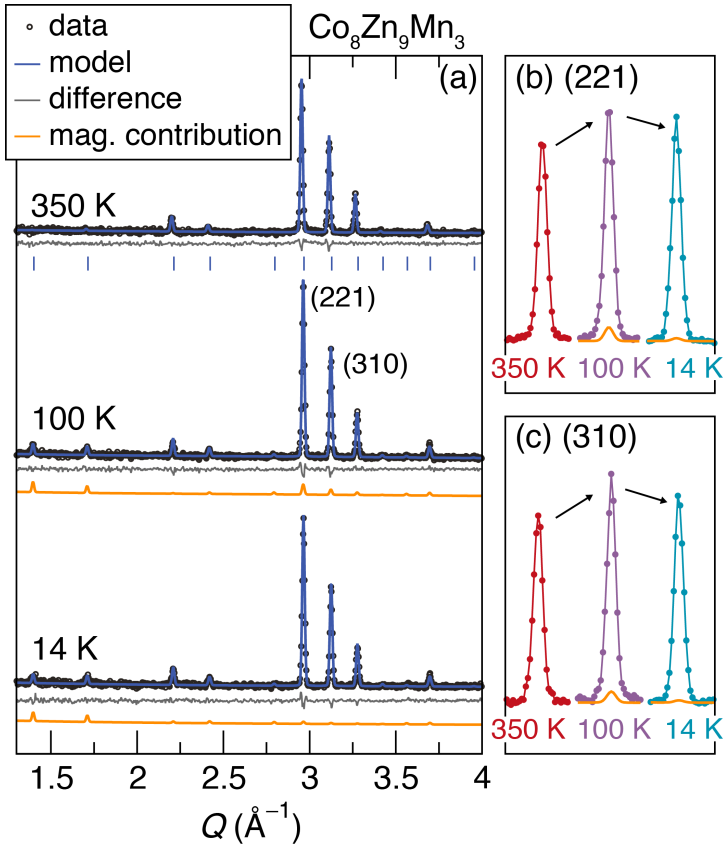

Figure 7.6: Magnetic neutron Rietveld refinements for the $Co_8Zn_9Mn_3$ sample at 100 K and 14 K. (a) shows how a magnetic contribution to the pattern grows in below the magnetic ordering temperature. Tick marks underneath the 350 K pattern indicate allowed nuclear peaks for the β-Mn structure; no magnetic intensity is seen at forbidden peak positions, however some magnetic peaks occur at allowed structural peak positions which have nearly zero intensity in the paramagnetic pattern. (b) and (c) shows a close view of the temperature evolution of the largest structural peaks, the (221) and (310). In both cases, the peak is seen to have a larger intensity at 100 K than 14 K, driven by the larger magnetic contribution (orange) at 100 K than 14 K.

In the $Co_7Zn_7Mn_6$ sample (Figure 7.7), the magnetic contribution to the 100 K pattern is even smaller than in the $Co_8Zn_9Mn_3$. A Rietveld refinement assuming collinear ferromagnetism gives a moment of 0.64(5) μ_B per magnetic ion on the 8c site and 0.75(16) μ_B per magnetic ion on the 12d site (Table 7.6). These small ordered moments suggest that, as seen in the magnetization data, the $Co_7Zn_7Mn_6$ sample shows more magnetic disorder than the $Co_8Zn_9Mn_3$ sample. Nevertheless, at this tempera-

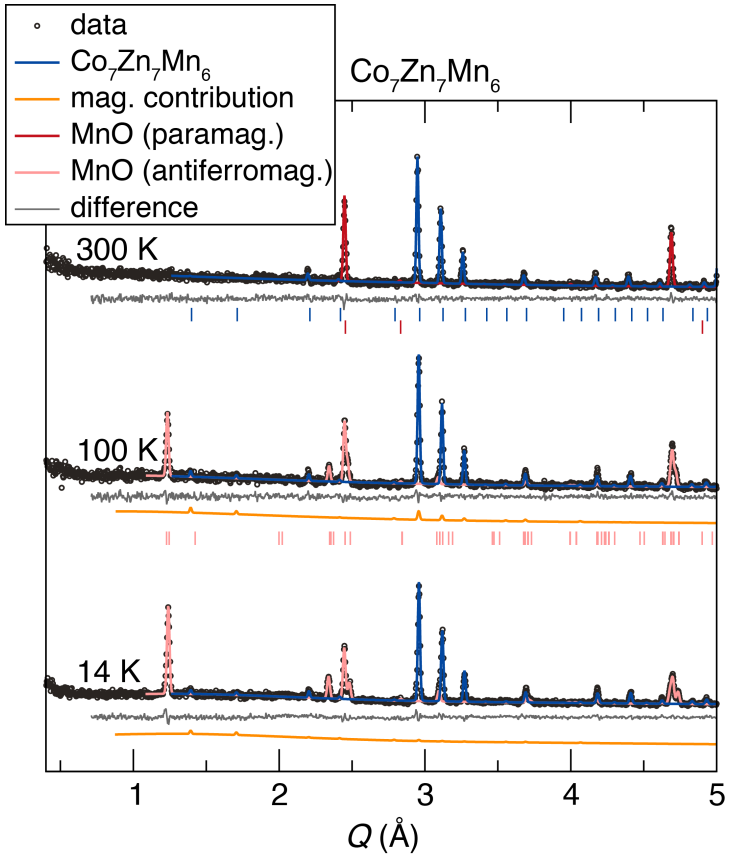

Figure 7.7: Magnetic neutron Rietveld refinements for the $Co_7Zn_7Mn_6$ sample at 100 K and 14 K. Below the observed magnetic ordering temperature (210 K), a small magnetic contribution is found to grow in to the β-Mn structure. The paramagnetic to antiferromagnetic transition of MnO at 118 K is also seen. This transition is accompanied by a rhombohedral structural distortion, which, along with the magnetic ordering, changes the space group from $Fm\bar{3}m$ to the monoclinic group C_c2/c' [361].

ture, both the Co spins and the Mn spins apparently have some tendency to order, as seen by the nonzero refined moment, which is consistent with the saturated magnetic moment at 100 K (6.3(1.0) μ_B *vs.* 6.7μ_B). Like in $Co_8Zn_9Mn_3$, the magnetic contribution to the pattern drops as the sample is cooled through the observed glass transition. At 14 K, the moment on the 12d site refined to zero, and so was fixed to zero while the 8c site was allowed to refine to 0.38(4) μ_B. This suggests that, as was the case in $Co_8Zn_9Mn_3$, the 12d site is completely magnetically disordered at low temperature while the Co-rich 8c site maintains some net order.

In a conventional spin glass, the spins transition directly from a fluctuating paramagnetic state to a frozen glass state as temperature is lowered. Here, we see that the Mn spins in $Co_xZn_yMn_z$ go through at least three regimes. At the observed Curie temperature of the material, the moments transition from a paramagnetic state at high temperature to a dynamically fluctuating, yet partially-ordered state, at intermediate temperatures. At lower temperature, the spins freeze into a fully disordered spin glass, with no net moment. Based on this behavior, we may characterize these materials as"reentrant" spin cluster glass, as has been observed in some other systems [362–365]. An interesting feature of such systems is that, because the system transitions from a spin glass state to a "ferromagnetic" state, upon warming, the "ferromagnetic" state must have higher entropy than the glass state, despite its being an ordered state. In this case, this apparent contradiction is resolved by the fact that the ferromagnetic state is in fact a dynamic, fluctuating state which is only partially ordered, and therefore has a higher entropy than the frozen spin glass.

7.3.5 Nature of the magnetic transitions in $Co_xZn_yMn_z$

In order to further understand the effect of the Mn moment disorder on the magnetic properties of $Co_xZn_yMn_z$ materials, we characterized the magnetocaloric properties of the samples using indirect isothermal entropy change measurements, which can be obtained from DC magnetization data. Isothermal magnetic entropy upon application of fields up to 5 T is shown in Figure 7.8 for the five samples studied. In each case, the dominant effect is negative, *i.e.* application of a magnetic field decreases the entropy of the system, as is typical for a ferromagnet, where an applied field suppresses spin fluctuations. As expected, the largest negative effect is observed near the observed Curie temperature, where the spins are most easily polarized by an external field.

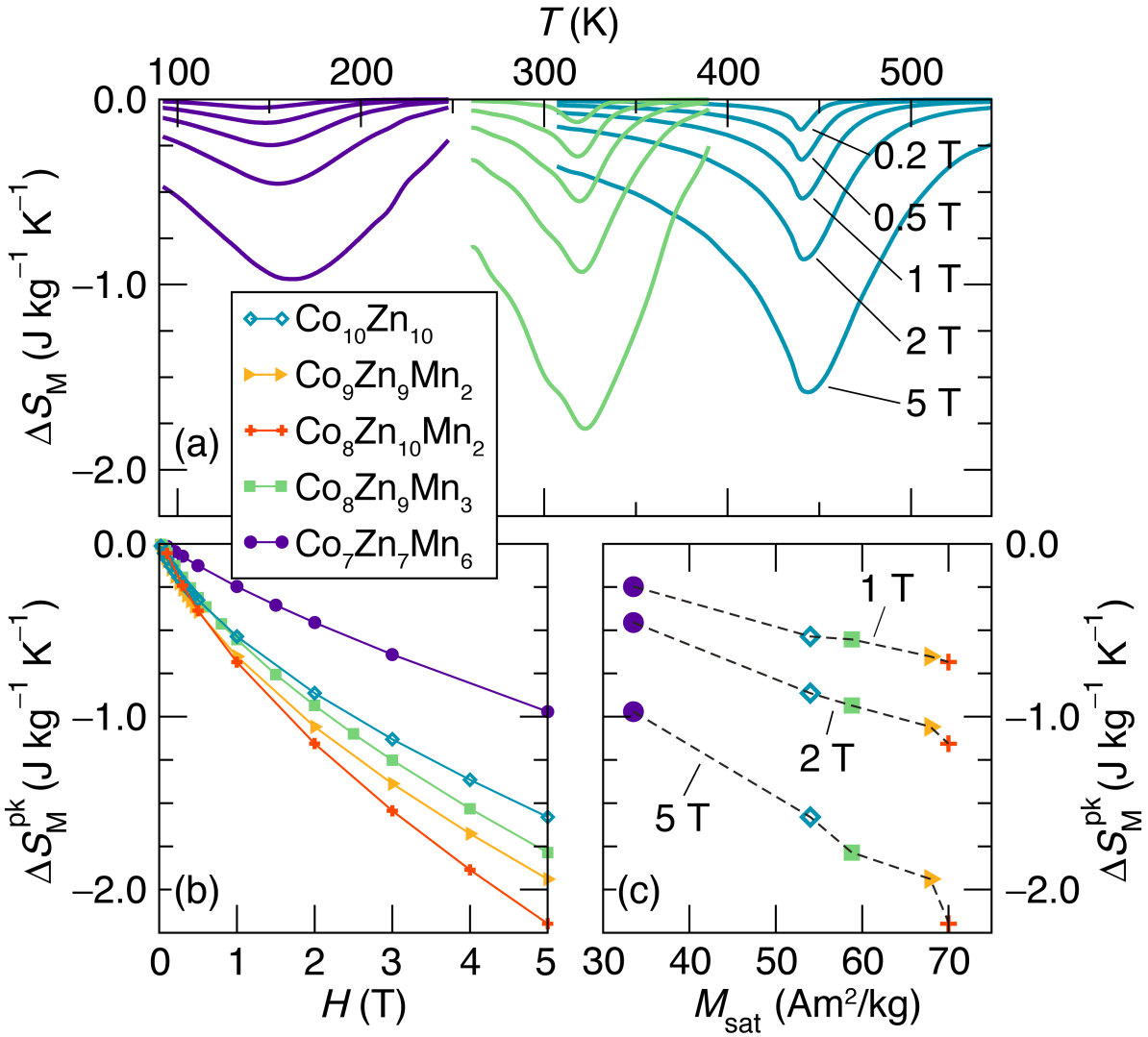

Figure 7.8: Magnetocaloric evaluation of $Co_xZn_yMn_z$. $\Delta S_M(T, H)$, the entropy change of the material upon isothermal magnetization to magnetic field H, is calculated from magnetization data using equation 7.2. Larger $|\Delta S_M|$ values indicate a larger magnetocaloric effect. (a) ΔS_M as a function of temperature for several applied field values for three $Co_xZn_yMn_z$ compositions. The largest effect is seen at the Curie temperature for each material. (b) Peak values of ΔS_M as a function of applied field for five $Co_xZn_yMn_z$ compositions. (c) Peak ΔS_M for different $Co_xZn_yMn_z$ compositions as a function of magnetic saturation of the composition. There is a clear relationship between magnetocaloric effect and magnetic moment in these samples.

As can be seen in Figure 7.8c, the peak magnetocaloric effect is observed to be directly related to the low-temperature saturation magnetization, which in turn is related

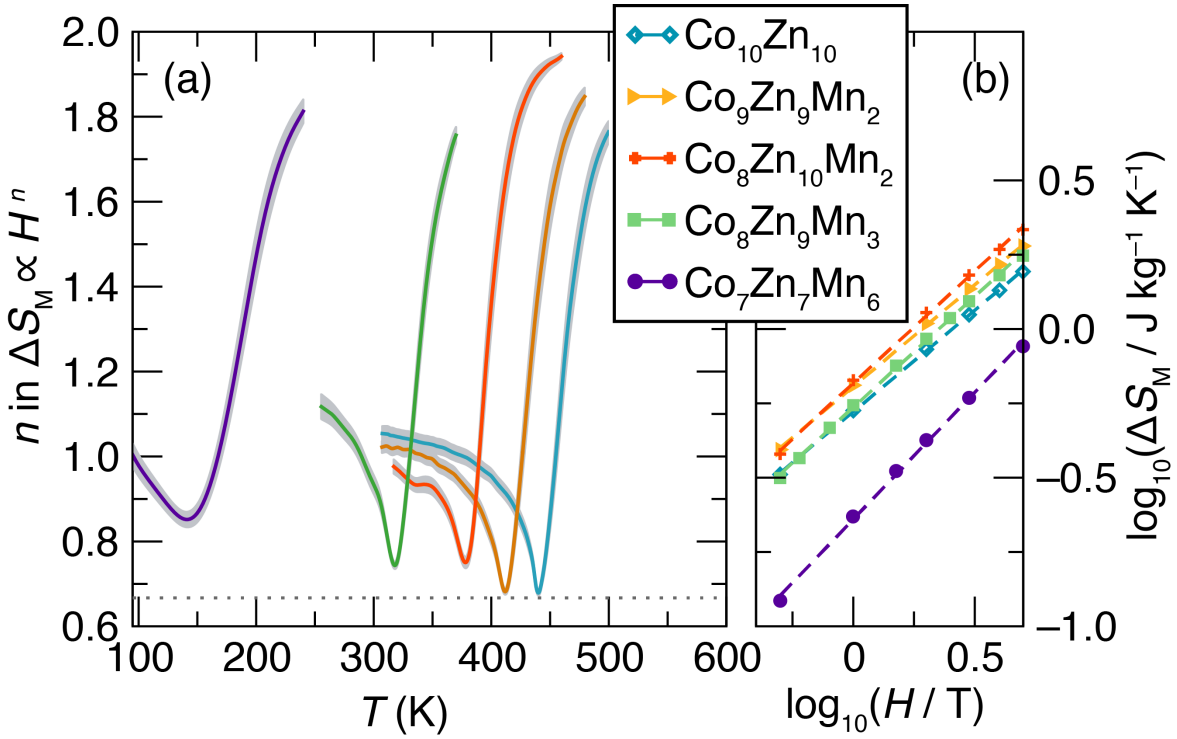

Figure 7.9: (a) Temperature dependence of the power law exponent, n, of the magnetocaloric effect ($\Delta S_M(H) \propto H^n$). This exponent is obtained from linear fits of log-log plots of ΔS_M *vs.* field for applied fields between 500 mT and 5T, as shown for the critical temperatures in (b). For all samples, the power law exponents are found to show a standard shape, characteristic of a continuous magnetic transition. The minimum n in each curve is the critical exponent n_c, which occurs at the critical temperature T_c. The dashed line shows the expected critical exponent for the mean field model, $n_c = 2/3$. As Mn content increases, n_c increases relative to the mean field model value, suggesting increasingly disordered magnetic interactions.

non-monotonically to the composition (Figure 7.3b). While saturation magnetization is not, in general, a good predictor of magneticaloric effect [18], it is often the case that ΔS_M^{pk} correlates with saturation magnetization within a specific family of materials [79, 83, 103, 216, 366], particularly in cases where there are no structural transitions concurrent with the magnetic transition.

Using this ΔS_M data, we have performed an analysis of power law exponents associated with this magnetic entropy change, $\Delta S_M(H) \propto H^n$. At the critical point

temperature T_c this exponent is a critical exponent ($\Delta S_M(H, T = T_c) \propto H^{n_c}$). For a continuous magnetic transition, this n_c can be related to the other magnetic critical exponents of the system by applying equation 7.2 to the Arrott-Noakes equation of state [217, 367], yielding:

$$n_c = 1 + \frac{1}{\delta}\left(1 - \frac{1}{\beta}\right) \tag{7.3}$$

δ and β are the standard critical exponents relating H to M and M to T, respectively, and are readily available for various of magnetic exchange models, giving $n_c = 2/3$ for the mean-field model, and lower values for Ising, Heisenberg, and XY models. Beyond the critical behavior, it has been found that the power law relation $\Delta S_M \propto H^n$ often holds across a broad temperature range, with n showing a distinctive temperature evolution, increasing from n_c to 1 as temperature is decreased and increasing from n_c to 2 at the temperature is increased.

As seen in Figure 7.9, this canonical shape of n_c is observed for all $Co_xZn_yMn_z$ samples when considering only the high field data ($H \geq$0.5 T). The minimum exponent (n_c), which is seen at the critical temperature T_c, however, evolves as Mn is added. For CoZn, the exponent is 0.68(1), which is comparable to the mean field theory value. As Mn is added, n_c rises monotonically reaching 0.85(2) for $Co_7Zn_7Mn_6$. Any values of n_c larger than 2/3 cannot be explained with the standard models of ferromagnetism (mean field, Heisenberg, XY, and Ising). However, elevated values are generally obtained for ferromagnetic bulk magnetic glasses [367–371], where magnetic interactions are disordered and multi-scale. Taken together, Figs. 7.8 and 7.9 show that the $Co_xZn_yMn_z$ samples behave, at fields above about 0.5 T, as ferromagnets with continuous transitions and reduced effective moments due to the fluctuating Mn spins. These Mn spins serve to progressively disorder the overall magnetic interactions, including those felt by the Co atoms.

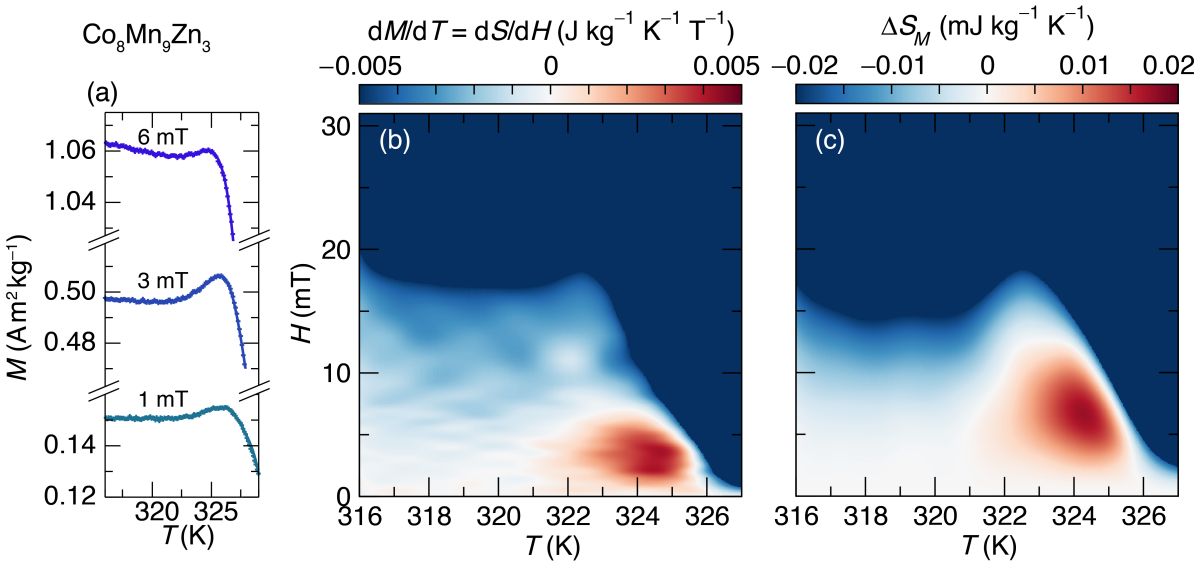

Figure 7.10: Magnetoentropic analysis of the low-field behavior of $Co_8Zn_9Mn_3$. (a) Representative M *vs.* T data under three different applied fields. The slope of many such curves, $\partial M/\partial T = \partial S/\partial H$ is shown as a heatmap in (b), with colorbar chosen symmetrically about zero to highlight the areas of conventional (negative, blue) and inverse (positive, red) magnetocaloric effect. (c) Heatmap of the isothermal entropy change upon application of a given magnetic field at a given temperature $\Delta S_M(T, H)$, which is obtained by integrating (b) in the field direction (equation 7.2). This analysis reveals three clear areas: (i) A blue region at high temperature and field representing the region in which the sample is behaving as a conventional field-polarized ferromagnet or paramagnet. In this regime, application of a magnetic field suppresses fluctuations and decreases entropy. (ii) A white region at low temperatures and fields, where the system shows a long-period helimagnetic or partially polarized conical magnetic phase. In this region, application of a magnetic field causes the planes of spins in the conical structure to progressively cant in the direction of the field, but has little effect on the entropy of the system. (iii) A red pocket just below the Curie temperature. This corresponds to the phase region where a hexagonal skyrmion lattice has been observed in this class of materials and other cubic skyrmion hosts. The increased entropy in this region is due to increased entropy in the skyrmion lattice relative to the helical or conical phases. However, due to the disorder in the sample, it is difficult to resolve this feature into clear phase boundaries, and differentiate it from a Brazovskii transition.

The lower-field magnetocaloric effect is expected to be more complex in skyrmion hosts materials as the various first order phase transitions between the skyrmion lattice phase and other chiral and non-chiral phases manifest themselves as anomalies in the magnetization and magnetocaloric effect [299]. Figure 7.10 shows a detailed

measurement of the low-field magnetocaloric effect in a 0.74 mg piece of $Co_8Zn_9Mn_3$. A region of positive (red) ΔS_M, indicating high entropy relative to the conical, helical, or ferromagnetic phases, can be seen in the field- temperature phase diagram just below the magnetic ordering temperature, where the equilibrium skyrmion lattice is expected. This is consistent with our understanding of the skyrmion lattice as a dynamic, fluctuation-stabilized phase. In the case of FeGe, this anomalous magnetocaloric behavior can be resolved into a phase diagram involving first-order transitions between the skyrmion lattice phase and the surrounding conical phase and a separate first-order Brazovskii transition [339, 341] between the ordered phases and a fluctuation-disordered phase at higher temperatures [299]. In the case of our $Co_xZn_yMn_z$ samples, these individual phase transition lines are difficult to resolve due to macroscopic disorder in the samples. Appendix Figure 7.14 shows a comparison of the $M(T)$ of a 66 mg piece and a 0.74 mg piece of the same $Co_8Zn_9Mn_3$ sample. The smaller piece shows a clear bump (precursor anomaly) in the magnetization just beneath the onset of magnetic ordering, while the larger sample shows no such anomaly. This bump, when processed through equation 7.2, becomes the anomalous magnetocaloric signal associated with the skyrmion lattice formation. Apparently, in larger samples, the subtle anomaly is completely smeared out by compositional variation across the sample, or by an inhomogenous demagnetizing field. Even in the 0.74 mg sample, some smearing of this feature occurs relative to the signal seen in small single crystals of well-ordered metal-metalloid compound like FeGe or MnSi.

7.4 Conclusions

The $Co_xZn_yMn_z$ system of high-temperature skyrmion hosts presents an interesting case of coexistence of several types of magnetic interactions. Like previously studied skyrmion host materials, $Co_xZn_yMn_z$ shows a low-field phase diagram made up of a variety of long-wavelength (λ between 100 nm and 200 nm) modulated magnetic structures, including several types of skyrmion lattices. Here, we have carefully characterized the atomic and magnetic disorder in $Co_xZn_yMn_z$ materials with various compositions, explaining the exotic local magnetic structure that those chiral modulations are built upon.

Through synchrotron and neutron diffraction, as well as DFT total energy calculations, we find that both the 8c and 12d site of $Co_xZn_yMn_z$ have atomic disorder. Neutron and synchrotron diffraction, as well as DFT calculations, show that the 8c atomic sublattice is mostly filled with Co atoms, while the larger 12d site is mostly filled with Mn and Zn. Mn's stability on the large 12d site is driven by its ability to develop a large local moment on that site.

DC and AC Magnetic measurements, and magnetic neutron diffraction refinements clarify the disordered magnetic behavior of these materials. $Co_xZn_yMn_z$ shows two-sublattice magnetic behavior, with coexistence of small, ferromagnetic Co moments behaving like a conventional ferromagnet, and large, dynamically disordered Mn moments which continue fluctuating below the ordering temperature of the Co spins, and ultimately freeze into a reentrant clustered spin glass at low temperature while the Co spins remain largely ordered. This behavior is observed in all of our samples containing Mn, with the magnetic signatures of disorder and glassiness increasing with increasing Mn concentration.

This unique magnetic structure allows for the dramatic and novel skyrmionic phase behavior recently observed in the $Co_xZn_yMn_z$ system. For example, in $Co_8Zn_8Mn_4$, a metastable skyrmion lattice is observed down to low temperatures, including below the magnetic glass transition temperature [348]. In $Co_7Zn_7Mn_6$, a new type of equilibrium disordered skyrmion lattice is found near the glass transition temperature [37]. In both cases, the observations are attributed to the influence of disorder. The two-sublattice magnetic structure allows for the coexistence of ordered magnetism (on the Co atoms) and disordered (on the Mn atoms) magnetism. This means that long-range ordered skyrmion lattice phases may coexist with, and be influenced by, a disordered magnetic glass system.

7.5 Appendix: Supplemental material

7.5.1 Additional diffraction patterns

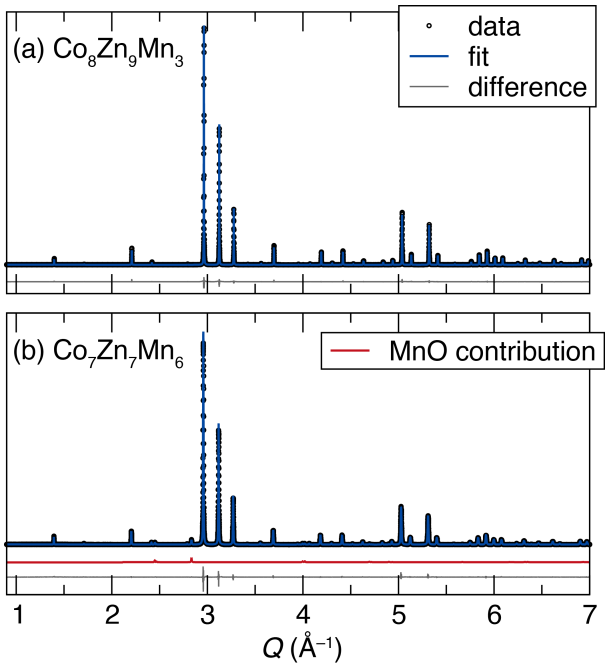

Figure 7.11: Synchrotron powder diffraction of $Co_8Zn_9Mn_3$ and $Co_7Zn_7Mn_6$ at 100K, displayed with fit from Rietveld co-refinement with neutron data shown in Figure 7.

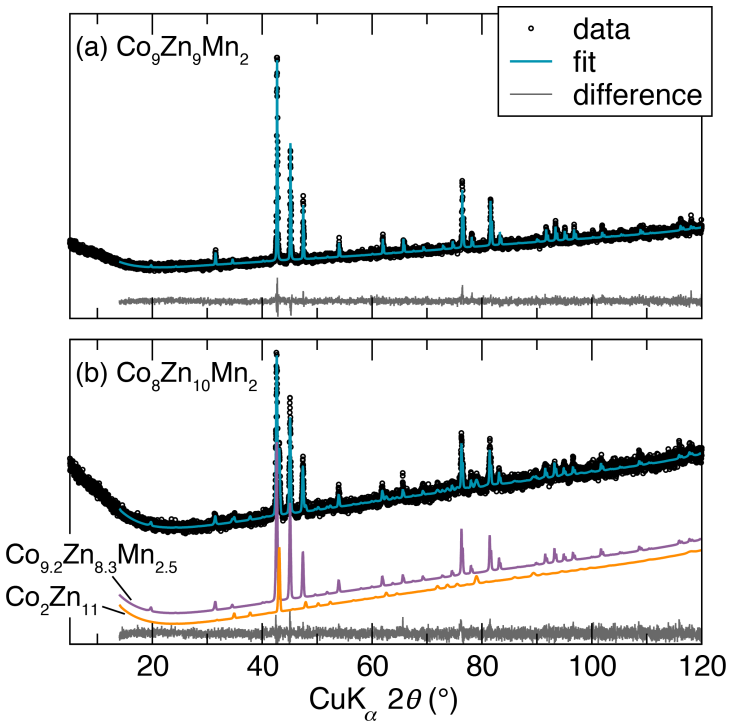

Figure 7.12: Laboratory X-ray diffraction of $Co_9Zn_9Mn_2$ (a) and $Co_8Zn_{10}Mn_2$ (b), displayed with Rietveld fit. The $Co_9Zn_9Mn_2$ sample shows no resolvable impurities, while the $Co_8Zn_{10}Mn_2$ samples contains 20.1(6) wt.% of the β-brass $Co_{9.2}Zn_{8.3}Mn_{2.5}$

7.5.2 Magnetization *vs.* temperature for $Co_xZn_yMn_z$ samples

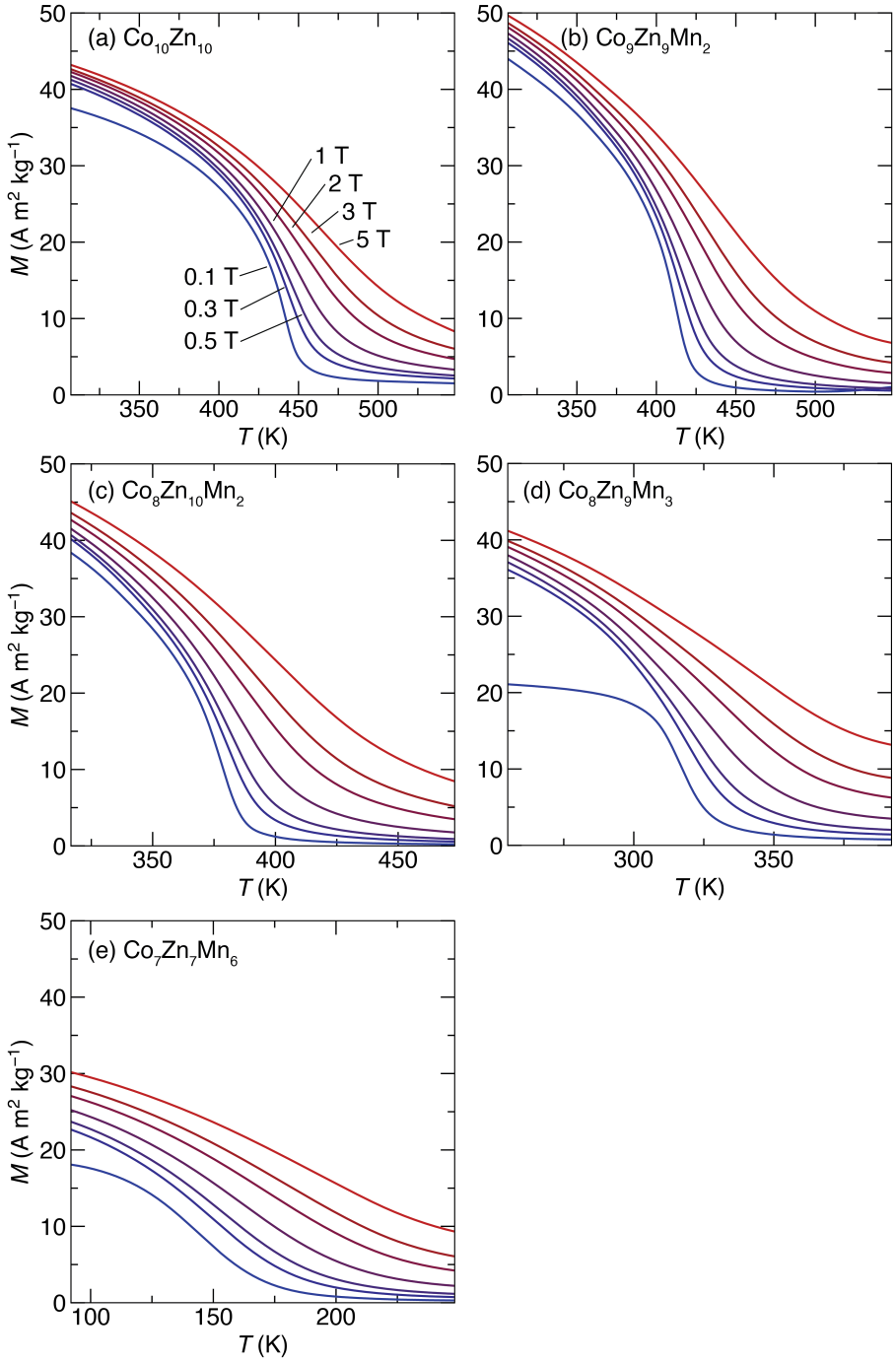

Figure 7.13: Magnetization as a function of temperature at different applied fields for each of the samples. This data is processed into the ΔS_M, and its power law exponent, as displayed in the main text Figs. 8-9.

7.5.3 Sample size dependence of precursor anomaly in $Co_8Zn_9Mn_3$

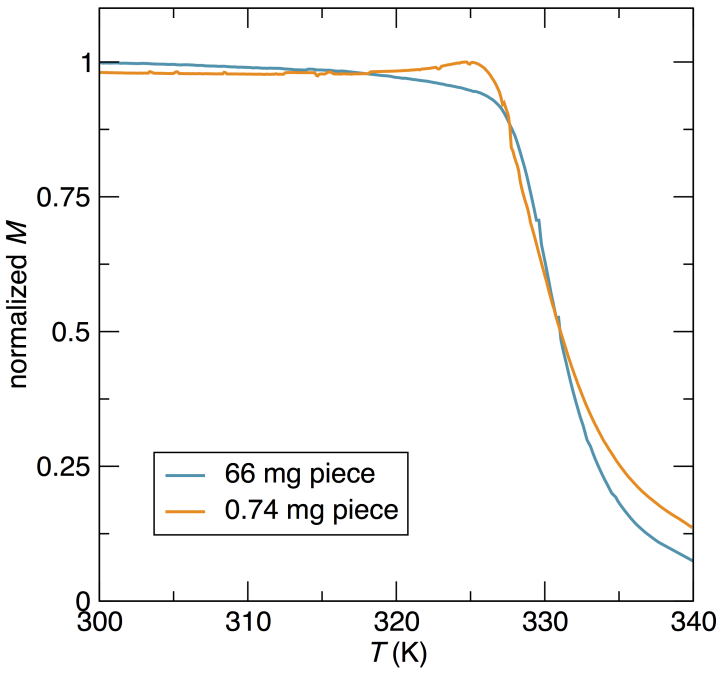

Figure 7.14: Comparison of magnetization *vs.* temperature under an applied field of 5 mT for two different pieces taken from a single sample of $Co_8Zn_9Mn_3$. The smaller piece shows a clear precursor anomaly- a small bump below the Curie temperature- while the larger piece does not. This may be caused by compositional disorder across the sample, or an inhomogeneous demagnetizing field. The larger sample contains a range of different magnetic transition temperatures, smearing out the subtle magnetic precursor anomalies. The smaller sample shows comparatively clearer behavior.

Chapter 8

Conclusions and future directions

In this dissertation I have presented several studies aimed at establishing a predictive understanding of the links between magnetism and crystal structure in intermetallics. In the case of magnetocalorics, it is demonstrated that the strength of magnetostructural coupling controls magnetocaloric performance. This is established in general on the basis of theory (Chapter 1, Section 1.2) and high-throughput computational studies (Chapters 2 and 3). Then, the specific behavior and origin of magnetostructural coupling is studied in detail for two specific magnetocalorics: MnAs (Chapter 4) and MnB (Chapter 5). These studies develop an understanding of *how* magnetostructural coupling arises: the key appears to be that pronounced competition between magnetism and bonding can lead to coupling of magnetic and structural degrees of freedom. Materials hosting this type of competition cannot simultaneously satisfy their magnetic interactions and chemical bonding at the same time: one always comes at the expense of the other. Therefore, a change in the magnetism can be compensated energetically by a structural distortion (and *vice-versa*), and so magnetism and structure couple. One consequence of this competition-driven coupling is that a small magnetic field can

greatly influence the carefully-balanced magnetostructural state and therefore cause large changes in entropy. Beyond magnetic refrigeration, these studies suggest other implications for the magnetostructural coupling. For example, good magnetocalorics should also be highly manipulatable by different types of strain stimulus in ways that will be predictable based on a microscropic understanding of the magnetism-bonding competition. Furthermore, in MnAs and other similar materials, our calculations suggest that the magnetism-bonding interplay becomes dynamic in the paramagnetic state, as spin fluctuations are expected to be accompanied by fluctuations in atomic positions and bonding. This exotic state is expected to have large implications for phonon and magnon transport, as well as for elastic behavior. Therefore, the studies I have presented in Chapters 2 through 5 motivate two lines of continuing investigation. Firstly, the ideas developed can be used for the rational design and control of new magnetocaloric materials. Secondly, these studies can be used to uncover new multifunctionalities that become possible when magnetism and structure are strongly coupled.

In Chapters 6 and 7, a different approach to the relation between crystal structure and magnetism is investigated. In skyrmion host materials, non-centrosymmetric crystal structures lead to long-range antisymmetric magnetic exchange interactions that compete with the standard symmetric exchange to yield a variety of long-wavelength magnetic structures, including topologically-protected skyrmions. Chapter 6 presents a method to study the complex magnetic phase diagrams arising from these competing magnetic interactions using magnetic entropy measurements very similar to those used earlier in the dissertation to characterize magnetocalorics. Chapter 7 uses this method, along with other computational and experimental techniques, to understand the structural and magnetic interactions that lead to the skyrmionic behavior in the $Co_xZn_yMn_z$ family of high-temperature skyrmion hosts. In this case, competition be-

tween magnetism and structure proves to be important in determining the crystalline site occupancies and, as a result, the low-temperature magnetic interactions. The result is that $Co_xZn_yMn_z$ shows an interesting two-sublattice magnetic structure where magnetic order and disorder can coexist, influencing the remarkable skyrmionic properties observed in this family of materials. Having understood the important role that the interplay between magnetism and crystal structure plays in controlling the behavior of skyrmion phases, one promising research direction is to control the skyrmion properties with strain *via* magnetostructural coupling.This research direction combines the lessons learned in both sections of this dissertation. One particularly interesting avenue is to search for strongly magnetostructurally-coupled materials that also have noncentrosymmetric crystal structures and can host skyrmions. In this way, exceptional control of skyrmions using strain, pressure, temperature, and magnetic field may be achievable.

Bibliography

[1] A. A. Mills. The lodestone: History, physics, and formation. *Ann. Sci.* **61** (2004) 273–319. doi:10.1080/00033790310001642812

[2] P. J. Wasilewski. Magnetic and microstructural properties of some lodestones. *Phys. Earth Planet. Inter.* **15** (1977) 349–362. doi:10.1016/0031-9201(77)90097-8

[3] P. Wasilewski and G. Kletetschka. Lodestone: Natures only permanent magnet-What it is and how it gets charged. *Geophys. Res. Lett.* **26** (1999) 2275–2278. doi:10.1029/1999GL900496

[4] F. Heusler. Über magnetische Manganlegierungen. *Verh. Dtsch. Phys. Ges.* **5** (1903) 219.

[5] F. Heusler. Über Manganbronze und über die Synthese magnetisierbarer Legierungen aus unmagnetischen Metallen. *Zeitschrift für Angew. Chemie* **17** (1904) 260–264. doi:10.1002/ange.19040170903

[6] F. Heusler and E. F. A. Haupt. *Über die ferromagnetischen Eigenschaften von Legierungen unmagnetischer Metalle*. Schriften der Gesellschaft zur beförderung der gesammten naturwissenschaften zu Marburg. N.G. Elwert (1904).

[7] S. Hilpert and T. Dieckmann. Über Arsenide. I. (Eisen- und Manganarsenide.). *Berichte der Dtsch. Chem. Gesellschaft* **44** (1911) 2378–2385. doi:10.1002/cber.19110440358

[8] F. Heusler and E. Take. The nature of the Heusler alloys. *Trans. Faraday Soc.* **8** (1912) 169. doi:10.1039/tf9120800169

[9] C. H. Desch. *Intermetallic compounds*. Monographs on inorganic and physical chemistry. Longmans, Green and Company (1914).

[10] J. F. Herbst. $R_2Fe_{14}B$ materials: Intrinsic properties and technological aspects. *Rev. Mod. Phys.* **63** (1991) 819–898. doi:10.1103/RevModPhys.63.819

[11] K. Ullakko. Magnetically controlled shape memory alloys: A new class of actuator materials. *J. Mater. Eng. Perform.* **5** (1996) 405–409. doi:10.1007/BF02649344

[12] V. Franco, J. Blázquez, J. Ipus, J. Law, L. Moreno-Ramírez, and A. Conde. Magnetocaloric effect: From materials research to refrigeration devices. *Prog. Mater. Sci.* **93** (2018) 112–232. doi:10.1016/j.pmatsci.2017.10.005

[13] A. Fert, V. Cros, and J. Sampaio. Skyrmions on the track. *Nat. Nanotechnol.* **8** (2013) 152–156. doi:10.1038/nnano.2013.29

[14] C. Broholm, R. J. Cava, S. A. Kivelson, D. G. Nocera, M. R. Norman, and T. Senthil. Quantum spin liquids. *Science* **367** (2020) eaay0668. doi:10.1126/science.aay0668

[15] B. Yan and C. Felser. Topological materials: Weyl semimetals. *Annu. Rev. Condens. Matter Phys.* **8** (2017) 337–354. doi:10.1146/annurev-conmatphys-031016-025458

[16] E. C. Stoner and E. P. Wohlfarth. A mechanism of magnetic hysteresis in heterogeneous alloys. *Philos. Trans. R. Soc. London. Ser. A, Math. Phys. Sci.* **240** (1948) 599–642. doi:10.1098/rsta.1948.0007

[17] T. Moriya and A. Kawabata. Effect of spin fluctuations on itinerant clectron ferromagnetism. *J. Phys. Soc. Japan* **34** (1973) 639–651. doi:10.1143/JPSJ.34.639

[18] J. D. Bocarsly, E. E. Levin, C. A. C. Garcia, K. Schwennicke, S. D. Wilson, and R. Seshadri. A simple computational proxy for screening magnetocaloric compounds. *Chem. Mater.* **29** (2017) 1613–1622. doi:10.1021/acs.chemmater.6b04729

[19] S. Plogmann, T. Schlathölter, J. Braun, M. Neumann, Y. M. Yarmoshenko, M. V. Yablonskikh, E. I. Shreder, E. Z. Kurmaev, A. Wrona, and A. Ślebarski. Local moments in Mn-based Heusler alloys and their electronic structures. *Phys. Rev. B* **60** (1999) 6428–6438. doi:10.1103/PhysRevB.60.6428

[20] J. Karel, F. Bernardi, C. Wang, R. Stinshoff, N.-O. Born, S. Ouardi, U. Burkhardt, G. H. Fecher, and C. Felser. Evidence for localized moment picture in Mn-based Heusler compounds. *Phys. Chem. Chem. Phys.* **17** (2015) 31707–31714. doi:10.1039/C5CP04944J

[21] K. Yosida. Magnetic properties of Cu-Mn alloys. *Phys. Rev.* **106** (1957) 893–898. doi:10.1103/PhysRev.106.893

[22] J. C. Slater. Cohesion in monovalent metals. *Phys. Rev.* **35** (1930) 509–529. doi:10.1103/PhysRev.35.509

[23] J. C. Slater. Atomic shielding constants. *Phys. Rev.* **36** (1930) 57–64. doi:10.1103/PhysRev.36.57

[24] A. Sommerfeld and H. Bethe. Elektronentheorie der Metalle. In *Aufbau Der Zusammenhängenden Mater.*, pages 333–622. Springer Berlin Heidelberg, Berlin, Heidelberg (1933) .

[25] P. Rhodes and E. P. Wohlfarth. The effective Curie-Weiss constant of ferromagnetic metals and alloys. *Proc. R. Soc. A Math. Phys. Eng. Sci.* **273** (1963) 247–258. doi:10.1098/rspa.1963.0086

[26] J. Hubbard. The magnetism of iron. *Phys. Rev. B* **19** (1979) 2626–2636. doi:10.1103/PhysRevB.19.2626

[27] M. L. Néel. Propriétés magnétiques des ferrites; ferrimagnétisme et antiferromagnétisme. *Ann. Phys. (Paris).* **12** (1948) 137–198. doi:10.1051/anphys/194812030137

[28] J. A. Cooley, J. D. Bocarsly, E. C. Schueller, E. E. Levin, E. E. Rodriguez, A. Huq, S. H. Lapidus, S. D. Wilson, and R. Seshadri. Evolution of noncollinear magnetism in magnetocaloric MnPtGa. *Phys. Rev. Mater.* **4** (2020) 044405. doi:10.1103/PhysRevMaterials.4.044405

[29] I. Dzyaloshinsky. A thermodynamic theory of "weak" ferromagnetism of antiferromagnetics. *J. Phys. Chem. Solids* **4** (1958) 241–255. doi:10.1016/0022-3697(58)90076-3

[30] T. Moriya. Anisotropic superexchange interaction and weak ferromagnetism. *Phys. Rev.* **120** (1960) 91–98. doi:10.1103/PhysRev.120.91

[31] Y. Ishikawa, K. Tajima, D. Bloch, and M. Roth. Helical spin structure in manganese silicide MnSi. *Solid State Commun.* **19** (1976) 525–528. doi:10.1016/0038-1098(76)90057-0

[32] B. Lebech, J. Bernhard, and T. Freltoft. Magnetic structures of cubic FeGe studied by small-angle neutron scattering. *J. Phys. Condens. Matter* **1** (1989) 6105–6122. doi:10.1088/0953-8984/1/35/010

[33] P. Bak and M. H. Jensen. Theory of helical magnetic structures and phase transitions in MnSi and FeGe. *J. Phys. C Solid State Phys.* **13** (1980) L881–L885. doi:10.1088/0022-3719/13/31/002

[34] A. N. Bogdanov and D. A. Yablonskii. Thermodynamically stable "vortices" in magnetically ordered crystals. The mixed state of magnets. *Zh. Eksp. Teor. Fiz* **95** (1989) 178–182.

[35] H. Wilhelm, M. Baenitz, M. Schmidt, U. K. Rößler, A. A. Leonov, and A. N. Bogdanov. Precursor phenomena at the magnetic ordering of the cubic helimagnet FeGe. *Phys. Rev. Lett.* **107** (2011) 127203. doi:10.1103/PhysRevLett.107.127203

[36] S. Muhlbauer, B. Binz, F. Jonietz, C. Pfleiderer, A. Rosch, A. Neubauer, R. Georgii, and P. Boni. Skyrmion lattice in a chiral magnet. *Science* **323** (2009) 915–919. doi:10.1126/science.1166767

[37] K. Karube, J. S. White, D. Morikawa, C. D. Dewhurst, R. Cubitt, A. Kikkawa, X. Yu, Y. Tokunaga, T.-h. Arima, H. M. Rønnow, Y. Tokura, and Y. Taguchi. Disordered skyrmion phase stabilized by magnetic frustration in a chiral magnet. *Sci. Adv.* **4** (2018) eaar7043. doi:10.1126/sciadv.aar7043

[38] I. Kézsmárki, S. Bordács, P. Milde, E. Neuber, L. M. Eng, J. S. White, H. M. Rønnow, C. D. Dewhurst, M. Mochizuki, K. Yanai, H. Nakamura, D. Ehlers, V. Tsurkan, and A. Loidl. Néel-type skyrmion lattice with confined orientation in the polar magnetic semiconductor GaV4S8. *Nat. Mater.* **14** (2015) 1116–1122. doi:10.1038/nmat4402

[39] A. K. Nayak, V. Kumar, T. Ma, P. Werner, E. Pippel, R. Sahoo, F. Damay, U. K. Rößler, C. Felser, and S. S. P. Parkin. Magnetic antiskyrmions above room temperature in tetragonal Heusler materials. *Nature* **548** (2017) 561–566. doi:10.1038/nature23466

[40] X. Z. Yu, W. Koshibae, Y. Tokunaga, K. Shibata, Y. Taguchi, N. Nagaosa, and Y. Tokura. Transformation between meron and skyrmion topological spin textures in a chiral magnet. *Nature* **564** (2018) 95–98. doi:10.1038/s41586-018-0745-3

[41] J. A. Cooley, M. K. Horton, E. E. Levin, S. H. Lapidus, K. A. Persson, and R. Seshadri. From waste-heat recovery to refrigeration: Compositional tuning of magnetocaloric $Mn_{1+x}Sb$. *Chem. Mater.* **32** (2020) 1243–1249. doi:10.1021/acs.chemmater.9b04643

[42] E. E. Levin, J. D. Bocarsly, J. H. Grebenkemper, R. Issa, S. D. Wilson, T. M. Pollock, and R. Seshadri. Structural coupling and magnetic tuning in $Mn_{2-x}Co_xP$ magnetocalorics for thermomagnetic power generation. *APL Mater.* **8** (2020) 041106. doi:10.1063/1.5142000

[43] Y. M. Oey, J. D. Bocarsly, E. E. Levin, M. Shatruk, and R. Seshadri. Structural changes upon magnetic ordering in magnetocaloric $AlFe_2B_2$. *in press at Appl. Pys. Lett.* (2020).

[44] L. Kautzsch, J. D. Bocarsly, C. Felser, S. D. Wilson, and R. Seshadri. Controlling Dzyaloshinskii-Moriya interactions in the skyrmion host candidates $FePd_{1-x}Pt_xMo_3N$. *Phys. Rev. Mater.* **4** (2020) 024412. doi:10.1103/PhysRevMaterials.4.024412

[45] E. C. Schueller, D. A. Kitchaev, J. L. Zuo, J. D. Bocarsly, J. A. Cooley, A. Van der Ven, S. D. Wilson, and R. Seshadri. Structural evolution and skyrmionic phase diagram of the lacunar spinel $GaMo_4Se_8$. *in press at Phys. Rev. Mater.* (2020).

[46] W. F. Giauque and D. P. MacDougall. Attainment of temperatures below 1° absolute by demagnetization of $Gd_2(SO_4)_3 \cdot 8\ H_2O$. *Phys. Rev.* **43** (1933) 768–768. doi:10.1103/PhysRev.43.768

[47] G. V. Brown. Magnetic heat pumping near room temperature. *J. Appl. Phys.* **47** (1976) 3673. doi:10.1063/1.323176

[48] C. Zimm, A. Jastrab, A. Sternberg, V. Pecharsky, K. Gschneidner, M. Osborne, and I. Anderson. Description and performance of a near-room temperature magnetic refrigerator. In *Adv. Cryog. Eng.*, pages 1759–1766. Springer US, Boston, MA (1998) .

[49] D. Arent, R. Tol, E. Faust, J. Hella, S. Kumar, K. Strzepek, F. Tóth, and D. Yan. Key economic sectors and services. In C. Field, V. Barros, D. Dokken, K. Mach, M. Mastrandrea, T. Bilir, M. Chatterjee, K. Ebi, Y. Estrada, R. Genova, B. Girma, E. Kissel, A. Levy, S. MacCracken, P. Mastrandrea, and L. White, eds., *Climate change 2014: Impacts, adaptations, vulnerability. Part A. Contribution of working group II to the fifth assessment report of the Intergovernmental Panel on Climate Change*, chapter 10, pages 659–708. Cambridge University Press, Cambridge, UK and New York, NY, USA (2014) .

[50] I. Takeuchi and K. Sandeman. Solid-state cooling with caloric materials. *Phys. Today* **68** (2015) 48–54. doi:10.1063/PT.3.3022

[51] V. K. Pecharsky and K. A. Gschneidner. Advanced magnetocaloric materials: What does the future hold? *Int. J. Refrig.* **29** (2006) 1239–1249. doi:10.1016/j.ijrefrig.2006.03.020

[52] A. Kitanovski. Energy applications of magnetocaloric materials. *Adv. Energy Mater.* **1903741** (2020) 1903741. doi:10.1002/aenm.201903741

[53] H. S. Gutowsky, ed. *Halocarbons: Effects on stratospheric ozone*. National Academies Press, Washington, D.C. (1976).

[54] Montreal protocol on substances that deplete the ozone layer. In *United Nations Treaty Ser.*, chapter XXVII.2a. Montreal, Canada (1989) .

[55] M. P. Chipperfield, S. Bekki, S. Dhomse, N. R. Harris, B. Hassler, R. Hossaini, W. Steinbrecht, R. Thiéblemont, and M. Weber. Detecting recovery of the stratospheric ozone layer. *Nature* **549** (2017) 211–218. doi:10.1038/nature23681

[56] G. J. M. Velders, A. R. Ravishankara, M. K. Miller, M. J. Molina, J. Alcamo, J. S. Daniel, D. W. Fahey, S. A. Montzka, and S. Reimann. Climate benefits by limiting HFCs. *Sci. Mag.* **335** (2012) 922–923.

[57] Amendment to the montreal protocol on substances that deplete the ozone layer. In *United Nations Treaty Ser.*, chapter XXVII.2.f. Kigali, Rwanda (2016) .

[58] P. Hawken, ed. *Drawdown: The most comprehensive plan ever proposed to reverse global warming*. Penguin Books, New York, NY (2017).

[59] V. W. Bhatkar, V. M. Kriplani, and G. K. Awari. Alternative refrigerants in vapour compression refrigeration cycle for sustainable environment: a review of recent research. *Int. J. Environ. Sci. Technol.* **10** (2013) 871–880. doi:10.1007/s13762-013-0202-7

[60] A. Kitanovski and P. W. Egolf. Application of magnetic refrigeration and its assessment. *J. Magn. Magn. Mater.* **321** (2009) 777–781. doi:10.1016/j.jmmm.2008.11.078

[61] B. Yu, M. Liu, P. W. Egolf, and A. Kitanovski. A review of magnetic refrigerator and heat pump prototypes built before the year 2010. *Int. J. Refrig.* **33** (2010) 1029–1060. doi:10.1016/j.ijrefrig.2010.04.002

[62] A. Greco, C. Aprea, A. Maiorino, and C. Masselli. A review of the state of the art of solid-state caloric cooling processes at room-temperature before 2019. *Int. J. Refrig.* **106** (2019) 66–88. doi:10.1016/j.ijrefrig.2019.06.034

[63] M. Annaorazov, K. Asatryan, G. Myalikgulyev, S. Nikitin, A. Tishin, and A. Tyurin. Alloys of the Fe–Rh system as a new class of working material for magnetic refrigerators. *Cryogenics* **32** (1992) 867–872. doi:10.1016/0011-2275(92)90352-B

[64] O. Tegus, E. Brück, K. H. J. Buschow, and F. R. de Boer. Transition-metal-based magnetic refrigerants for room-temperature applications. *Nature* **415** (2002) 150–152. doi:10.1038/415150a

[65] E. Brück, O. Tegus, L. Zhang, X. Li, F. de Boer, and K. Buschow. Magnetic refrigeration near room temperature with Fe_2P-based compounds. *J. Alloys Compd.* **383** (2004) 32–36. doi:10.1016/j.jallcom.2004.04.042

[66] D. T. Cam Thanh, E. Brück, N. T. Trung, J. C. P. Klaasse, K. H. J. Buschow, Z. Q. Ou, O. Tegus, and L. Caron. Structure, magnetism, and magnetocaloric properties of $MnFeP_{1-x}Si_x$ compounds. *J. Appl. Phys.* **103** (2008) 07B318. doi:10.1063/1.2836958

[67] J. H. Grebenkemper, J. D. Bocarsly, E. E. Levin, G. Seward, C. Heikes, C. Brown, S. Misra, F. Seeler, K. Schierle-Arndt, S. D. Wilson, and R. Seshadri. Rapid microwave preparation and composition tuning of the high-performance magnetocalorics $(Mn,Fe)_2(P,Si)$. *ACS Appl. Mater. Interfaces* **10** (2018) 7208–7213. doi:10.1021/acsami.7b16988

[68] S. Fujieda, A. Fujita, and K. Fukamichi. Large magnetocaloric effect in $La(Fe_xSi_{1-x})_{13}$ itinerant-electron metamagnetic compounds. *Appl. Phys. Lett.* **81** (2002) 1276–1278. doi:10.1063/1.1498148

[69] B. G. Shen, J. R. Sun, F. X. Hu, H. W. Zhang, and Z. H. Cheng. Recent progress in exploring magnetocaloric materials. *Adv. Mater.* **21** (2009) 4545–4564. doi:10.1002/adma.200901072

[70] H. Wada and Y. Tanabe. Giant magnetocaloric effect of $MnAs_{1-x}Sb_x$. *Appl. Phys. Lett.* **79** (2001) 3302–3304. doi:10.1063/1.1419048

[71] J. Mira, F. Rivadulla, J. Rivas, A. Fondado, T. Guidi, R. Caciuffo, F. Carsughi, P. G. Radaelli, and J. B. Goodenough. Structural transformation induced by magnetic field and "colossal-like" magnetoresistance response above 313 K in MnAs. *Phys. Rev. Lett.* **90** (2003) 097203. doi:10.1103/PhysRevLett.90.097203

[72] T. Krenke, E. Duman, M. Acet, E. F. Wassermann, X. Moya, L. Mañosa, and A. Planes. Inverse magnetocaloric effect in ferromagnetic Ni–Mn–Sn alloys. *Nat. Mater.* **4** (2005) 450–454. doi:10.1038/nmat1395

[73] J. Liu, T. Gottschall, K. P. Skokov, J. D. Moore, and O. Gutfleisch. Giant magnetocaloric effect driven by structural transitions. *Nat. Mater.* **11** (2012) 620–626. doi:10.1038/nmat3334

[74] F. Guillou, G. Porcari, H. Yibole, N. van Dijk, and E. Brück. Taming the first-order transition in giant magnetocaloric materials. *Adv. Mater.* **26** (2014) 2671–2675. doi:10.1002/adma.201304788

[75] O. Gutfleisch, T. Gottschall, M. Fries, D. Benke, I. Radulov, K. P. Skokov, H. Wende, M. Gruner, M. Acet, P. Entel, and M. Farle. Mastering hysteresis in magnetocaloric materials. *Philos. Trans. R. Soc. A Math. Phys. Eng. Sci.* **374** (2016) 20150308. doi:10.1098/rsta.2015.0308

[76] T. Gottschall, K. P. Skokov, B. Frincu, and O. Gutfleisch. Large reversible magnetocaloric effect in Ni-Mn-In-Co. *Appl. Phys. Lett.* **106** (2015) 021901. doi:10.1063/1.4905371

[77] T. Gottschall, A. Gràcia-Condal, M. Fries, A. Taubel, L. Pfeuffer, L. Mañosa, A. Planes, K. P. Skokov, and O. Gutfleisch. A multicaloric cooling cycle that exploits thermal hysteresis. *Nat. Mater.* **17** (2018) 929–934. doi:10.1038/s41563-018-0166-6

[78] X. Tan, P. Chai, C. M. Thompson, and M. Shatruk. Magnetocaloric effect in $AlFe_2B_2$: toward magnetic refrigerants from earth-abundant elements. *J. Am. Chem. Soc.* **135** (2013) 9553–9557. doi:10.1021/ja404107p

[79] S. Singh, L. Caron, S. W. D'Souza, T. Fichtner, G. Porcari, S. Fabbrici, C. Shekhar, S. Chadov, M. Solzi, and C. Felser. Large magnetization and reversible magnetocaloric effect at the second-order magnetic transition in Heusler materials. *Adv. Mater.* **28** (2016) 3321–3325. doi:10.1002/adma.201505571

[80] M. Fries, Z. Gercsi, S. Ener, K. P. Skokov, and O. Gutfleisch. Magnetic, magnetocaloric and structural properties of manganese based monoborides doped with iron and cobalt – A candidate for thermomagnetic generators. *Acta Mater.* **113** (2016) 213–220. doi:10.1016/j.actamat.2016.05.005

[81] J. D. Bocarsly, E. E. Levin, S. A. Humphrey, T. Faske, W. Donner, S. D. Wilson, and R. Seshadri. Magnetostructural coupling drives magnetocaloric behavior: The case of MnB versus FeB. *Chem. Mater.* **31** (2019) 4873–4881. doi:10.1021/acs.chemmater.9b01476

[82] V. K. Pecharsky and K. A. Gschneidner, Jr. Giant magnetocaloric effect in $Gd_5(Si,Ge)_2$. *Phys. Rev. Lett.* **78** (1997) 4494–4497. doi:10.1103/PhysRevLett.78.4494

[83] K. Mandal, A. Yan, P. Kerschl, A. Handstein, O. Gutfleisch, and K. H. Müller. The study of magnetocaloric effect in R_2Fe_{17} (R = Y, Pr) alloys. *J. Phys. D* **37** (2004) 2628–2631. doi:10.1088/0022-3727/37/19/002

[84] K. G. Sandeman. Magnetocaloric materials: The search for new systems. *Scr. Mater.* **67** (2012) 566–571. doi:10.1016/j.scriptamat.2012.02.045

[85] N. H. Dung, L. Zhang, Z. Q. Ou, and E. Brück. From first-order magneto-elastic to magneto-structural transition in $(Mn,Fe)_{1.95}P_{0.50}Si_{0.50}$ compounds. *Appl. Phys. Lett.* **99** (2011) 092511. doi:10.1063/1.3634016

[86] V. Franco, J. Y. Law, A. Conde, V. Brabander, D. Y. Karpenkov, I. Radulov, K. Skokov, and O. Gutfleisch. Predicting the tricritical point composition of a

series of LaFeSi magnetocaloric alloys via universal scaling. *J. Phys. D* **50** (2017) 414004. doi:10.1088/1361-6463/aa8792

[87] G. de la Flor, D. Orobengoa, E. Tasci, J. M. Perez-Mato, and M. I. Aroyo. Comparison of structures applying the tools available at the Bilbao Crystallographic Server. *J. Appl. Crystallogr.* **49** (2016) 653–664. doi:10.1107/S1600576716002569

[88] C. A. C. Garcia, J. D. Bocarsly, and R. Seshadri. Computational screening of magnetocaloric alloys. *Phys. Rev. Mater.* **4** (2020) 024402. doi:10.1103/PhysRevMaterials.4.024402

[89] C. P. Bean and D. S. Rodbell. Magnetic disorder as a first-order phase transformation. *Phys. Rev.* **126** (1962) 104–115. doi:10.1103/PhysRev.126.104

[90] D. S. Rodbell and C. P. Bean. Some magnetic first-order transitions. *J. Appl. Phys.* **33** (1962) 1037–1041. doi:10.1063/1.1728593

[91] D. Paudyal, V. K. Pecharsky, K. A. Gschneidner, and B. N. Harmon. Electron correlation effects on the magnetostructural transition and magnetocaloric effect in $Gd_5Si_2Ge_2$. *Phys. Rev. B* **73** (2006) 144406. doi:10.1103/PhysRevB.73.144406

[92] G. Wang, L. Song, Z. Ou, Z. Zhao, and O. Tegus. Calculation of the magnetization and magnetocaloric effect in the $MnFeP_{0.45}As_{0.55}$ compound. *Acta Metall. Sin.* **20** (2007) 265–269. doi:10.1016/S1006-7191(07)60037-4

[93] S. Yahyaoui, M. Khalfaoui, S. Kallel, N. Kallel, J. Amaral, and A. Ben Lamine. Modeling the magnetic properties and magnetocaloric effect of $La_{0.7}Sr_{0.3}Mn_{0.9}Ti_{0.1}O_3$. *J. Alloys Compd.* **685** (2016) 633–638. doi:10.1016/j.jallcom.2016.05.318

[94] C. Romero-Muñiz, V. Franco, and A. Conde. Two different critical regimes enclosed in the Bean–Rodbell model and their implications for the field dependence and universal scaling of the magnetocaloric effect. *Phys. Chem. Chem. Phys.* **19** (2017) 3582–3595. doi:10.1039/C6CP06291A

[95] R. W. De Blois and D. S. Rodbell. Magnetic first-order phase transition in single-crystal MnAs. *Phys. Rev.* **130** (1963).

[96] C. Li and P. Wu. Correlation of bulk modulus and the constituent element properties of binary intermetallic compounds. *Chem. Mater.* **13** (2001) 4642–4648. doi:10.1021/cm0104203

[97] P. S. Lyman and C. T. Prewitt. Room- and high-pressure crystal chemistry of CoAs and FeAs. *Acta Crystallogr. Sect. B Struct. Sci.* **40** (1984) 14–20. doi:10.1107/S0108768184001695

[98] M. Dörfler and K. Bärner. The elastic constants of MnAs. *Phys. Status Solidi* **17** (1973) 141–148. doi:10.1002/pssa.2210170113

[99] K. Bärner and H. Berg. Elastic anomalies at the second-order phase transition in MnAs. *Phys. Status Solidi* **49** (1978) 545–554. doi:10.1002/pssa.2210490215

[100] O. Palumbo, C. Castellano, A. Paolone, and R. Cantelli. Extended x-ray absorption fine structure study of the MnAs local structure at the phase transitions. *J. Phys. Condens. Matter* **17** (2005) 1537–1545. doi:10.1088/0953-8984/17/10/009

[101] V. Basso. The magnetocaloric effect at the first-order magneto-elastic phase transition. *J. Phys. Condens. Matter* **23** (2011) 226004. doi:10.1088/0953-8984/23/22/226004

[102] M. E. Gruner, W. Keune, B. Roldan Cuenya, C. Weis, J. Landers, S. I. Makarov, D. Klar, M. Y. Hu, E. E. Alp, J. Zhao, M. Krautz, O. Gutfleisch, and H. Wende. Element-resolved thermodynamics of magnetocaloric $LaFe_{13-x}Si_x$. *Phys. Rev. Lett.* **114** (2015) 057202. doi:10.1103/PhysRevLett.114.057202

[103] V. Franco, J. Blázquez, B. Ingale, and A. Conde. The magnetocaloric effect and magnetic refrigeration near room temperature: Materials and models. *Annu. Rev. Mater. Res.* **42** (2012) 305–342. doi:10.1146/annurev-matsci-062910-100356

[104] M. F. J. Boeije, P. Roy, F. Guillou, H. Yibole, X. F. Miao, L. Caron, D. Banerjee, N. H. van Dijk, R. A. de Groot, and E. Brück. Efficient room-temperature cooling with magnets. *Chem. Mater.* **28** (2016) 4901–4905. doi:10.1021/acs.chemmater.6b00518

[105] F.-x. Hu, B.-g. Shen, J.-r. Sun, Z.-h. Cheng, G.-h. Rao, and X.-x. Zhang. Influence of negative lattice expansion and metamagnetic transition on magnetic entropy change in the compound $LaFe_{11.4}Si_{1.6}$. *Appl. Phys. Lett.* **78** (2001) 3675–3677. doi:10.1063/1.1375836

[106] A. Kitanovski, U. Plaznik, U. Tomc, and A. Poredoš. Present and future caloric refrigeration and heat-pump technologies. *Int. J. Refrig.* **57** (2015) 288–298. doi:10.1016/j.ijrefrig.2015.06.008

[107] T. Christiaanse and E. Brück. Proof-of-concept static thermomagnetic generator experimental device. *Metall. Mater. Trans. E* **1** (2014) 36–40. doi:10.1007/s40553-014-0006-9

[108] J. F. Elliott, S. Legvold, and F. H. Spedding. Some magnetic properties of gadolinium metal. *Phys. Rev.* **91** (1953) 28–30. doi:10.1103/PhysRev.91.28

[109] S. Dan'kov, a. Tishin, V. Pecharsky, and K. Gschneidner. Magnetic phase transitions and the magnetothermal properties of gadolinium. *Phys. Rev. B* **57** (1998) 3478–3490. doi:10.1103/PhysRevB.57.3478

[110] V. Franco and A. Conde. Scaling laws for the magnetocaloric effect in second order phase transitions: From physics to applications for the characterization of materials. *Int. J. Refrig.* **33** (2010) 465–473. doi:10.1016/j.ijrefrig.2009.12.019

[111] J. H. Belo, J. S. Amaral, A. M. Pereira, V. S. Amaral, and J. P. Araújo. On the Curie temperature dependency of the magnetocaloric effect. *Appl. Phys. Lett.* **100** (2012) 242407. doi:10.1063/1.4726110

[112] C. Magen, Z. Arnold, L. Morellon, Y. Skorokhod, P. A. Algarabel, M. R. Ibarra, and J. Kamarad. Pressure-induced three-dimensional ferromagnetic correlations in the giant magnetocaloric compound Gd_5Ge_4. *Phys. Rev. Lett.* **91** (2003) 207202. doi:10.1103/PhysRevLett.91.207202

[113] W. Choe, G. J. Miller, J. Meyers, S. Chumbley, and A. O. Pecharsky. "Nanoscale zippers" in the crystalline Solid. Structural variations in the giant magnetocaloric material $Gd_5Si_{1.5}Ge_{2.5}$. *Chem. Mater.* **15** (2003) 1413–1419. doi:10.1021/cm020928l

[114] l. J. Łażewski, P. Piekarz, J. Toboła, B. Wiendlocha, P. T. Jochym, M. Sternik, and K. Parlinski. Phonon mechanism of the magnetostructural phase transition in MnAs. *Phys. Rev. Lett.* **104** (2010) 147205. doi:10.1103/PhysRevLett.104.147205

[115] A. Jain, S. P. Ong, G. Hautier, W. Chen, W. D. Richards, S. Dacek, S. Cholia, D. Gunter, D. Skinner, G. Ceder, and K. A. Persson. Commentary: The Materials Project: A materials genome approach to accelerating materials innovation. *APL Mater.* **1** (2013) 011002. doi:10.1063/1.4812323

[116] J. E. Saal, S. Kirklin, M. Aykol, B. Meredig, and C. Wolverton. Materials design and discovery with high-throughput density functional theory: The Open Quantum Materials Database (OQMD). *JOM* **65** (2013) 1501–1509. doi:10.1007/s11837-013-0755-4

[117] S. Curtarolo, W. Setyawan, S. Wang, J. Xue, K. Yang, R. H. Taylor, L. J. Nelson, G. L. Hart, S. Sanvito, M. Buongiorno-Nardelli, N. Mingo, and O. Levy. AFLOWLIB.ORG: A distributed materials properties repository from high-throughput *ab initio* calculations. *Comput. Mater. Sci.* **58** (2012) 227–235. doi:10.1016/j.commatsci.2012.02.002

[118] J. Yan, P. Gorai, B. Ortiz, S. Miller, S. A. Barnett, T. Mason, V. Stevanović, and E. S. Toberer. Material descriptors for predicting thermoelectric performance. *Energy Environ. Sci.* **8** (2015) 983–994. doi:10.1039/C4EE03157A

[119] J. Brgoch, S. P. DenBaars, and R. Seshadri. Proxies from *ab initio* calculations for screening efficient Ce^{3+} phosphor hosts. *J. Phys. Chem. C* **117** (2013) 17955–17959. doi:10.1021/jp405858e

[120] S. Adams and R. P. Rao. High power lithium ion battery materials by computational design. *Phys. status solidi* **208** (2011) 1746–1753. doi:10.1002/pssa.201001116

[121] B. C. Melot, D. O. Scanlon, M. Reynaud, G. Rousse, J.-N. Chotard, M. Henry, and J.-M. Tarascon. Chemical and structural indicators for large redox potentials in Fe-based positive electrode materials. *ACS Appl. Mater. & Interfaces* **6** (2014) 10832–10839. doi:10.1021/am405579h

[122] Z. Rong, R. Malik, P. Canepa, G. Sai Gautam, M. Liu, A. Jain, K. Persson, and G. Ceder. Materials design rules for multivalent ion mobility in intercalation structures. *Chem. Mater.* **27** (2015) 6016–6021. doi:10.1021/acs.chemmater.5b02342

[123] X. F. Miao, L. Caron, Z. Gercsi, A. Daoud-Aladine, N. H. van Dijk, and E. Brück. Thermal-history dependent magnetoelastic transition in $(Mn,Fe)_2(P,Si)$. *Appl. Phys. Lett.* **107** (2015) 042403. doi:10.1063/1.4927285

[124] J. E. Douglas, E. E. Levin, T. M. Pollock, J. C. Castillo, P. Adler, C. Felser, S. Krämer, K. L. Page, and R. Seshadri. Magnetic hardening and antiferromagnetic/ferromagnetic phase coexistence in $Mn_{1-x}Fe_xRu_2Sn$ Heusler solid solutions. *Phys. Rev. B* **94** (2016) 094412. doi:10.1103/PhysRevB.94.094412

[125] A. C. Larson and R. B. Von Dreele. General Structure Analysis System (GSAS). *Los Alamos Natl. Lab. Rep. LAUR 86-748* (2000) 86–748.

[126] B. H. Toby. EXPGUI, a graphical user interface for GSAS. *J. Appl. Crystallogr.* **34** (2001) 210–213. doi:10.1107/S0021889801002242

[127] K. Momma and F. Izumi. VESTA 3 for three-dimensional visualization of crystal, volumetric and morphology data. *J. Appl. Crystallogr.* **44** (2011) 1272–1276. doi:10.1107/S0021889811038970

[128] G. Kresse and J. Furthmüller. Efficient iterative schemes for *ab initio* total-energy calculations using a plane-wave basis set. *Phys. Rev. B* **54** (1996) 11169–11186. doi:10.1103/PhysRevB.54.11169

[129] P. E. Blöchl. Projector augmented-wave method. *Phys. Rev. B* **50** (1994) 17953–17979. doi:10.1103/PhysRevB.50.17953

[130] G. Kresse and D. Joubert. From ultrasoft pseudopotentials to the projector augmented-wave method. *Phys. Rev. B* **59** (1999) 1758–1775. doi:10.1103/PhysRevB.59.1758

[131] J. P. Perdew, K. Burke, and M. Ernzerhof. Generalized gradient approximation made simple. *Phys. Rev. Lett.* **77** (1996) 3865–3868. doi:10.1103/PhysRevLett.77.3865

[132] S. P. Ong, W. D. Richards, A. Jain, G. Hautier, M. Kocher, S. Cholia, D. Gunter, V. L. Chevrier, K. A. Persson, and G. Ceder. Python Materials Genomics (pymatgen): A robust, open-source python library for materials analysis. *Comput. Mater. Sci.* **68** (2013) 314–319. doi:10.1016/j.commatsci.2012.10.028

[133] M. Catti. Calculation of elastic constants by the method of crystal static deformation. *Acta Crystallogr., Sect. A Found. Crystallogr.* **41** (1985) 494–500. doi:10.1107/S0108767385001052

[134] H. Wada and Y. Tanabe. Giant magnetocaloric effect of $MnAs_{1-x}Sb_x$. *Appl. Phys. Lett.* **79** (2001) 3302. doi:10.1063/1.1419048

[135] K. Katagiri, K. Nakamura, and H. Wada. Magnetocaloric properties and magnetic refrigerant capacity of $MnFeP_{1-x}Si_x$. *J. Alloys Compd.* **553** (2013) 286–290. doi:10.1016/j.jallcom.2012.11.127

[136] D. T. C. Thanh, E. Brück, O. Tegus, K. J. C. P., T. J. Gortenmulder, and K. H. J. Buschow. Magnetocaloric effect in MnFe(P,Si,Ge) compounds. *J. Appl. Phys.* **99** (2006) 08Q107. doi:10.1063/1.2170589

[137] O. Tegus, E. Brück, L. Zhang, Dagula, K. H. J. Buschow, and F. R. de Boer. Magnetic-phase transitions and magnetocaloric effects. *Physica B: Condensed Matter* **319** (2002) 174–192. doi:10.1016/s0921-4526(02)01119-5

[138] X. Zhang, Y. Chen, L. Lü, and Z. Li. A potential oxide for magnetic refrigeration application: CrO_2 particles. *J. Phys.: Condensed Matter* **18** (2006) L559–L566. doi:10.1088/0953-8984/18/44/l01

[139] X. Tan, P. Chai, C. M. Thompson, and M. Shatruk. Magnetocaloric effect in $AlFe_2B_2$: toward Magnetic refrigerants from earth-abundant elements. *J. Am. Chem. Soc.* **135** (2013) 9553–9557. doi:10.1021/ja404107p

[140] Songlin, Dagula, O. Tegus, E. Brück, J. C. P. Klaasse, F. R. de Boer, and K. H. J. Buschow. Magnetic phase transition and magnetocaloric effect in $Mn_{5-x}Fe_xSi_3$. *J. Alloys Compd.* **334** (2002) 249–252. doi:10.1016/s0925-8388(01)01776-5

[141] B. Kaeswurm, K. Friemert, M. Gürsoy, K. P. Skokov, and O. Gutfleisch. Direct measurement of the magnetocaloric effect in cementite. *J. Magn. Magn. Mater.* **410** (2016) 105–108. doi:10.1016/j.jmmm.2016.02.080

[142] M.-H. Phan and S.-C. Yu. Review of the magnetocaloric effect in manganite materials. *J. Magn. Magn. Mater.* **308** (2007) 325–340. doi:10.1016/j.jmmm.2006.07.025

[143] S. Lin, O. Tegus, E. Brück, W. Dagula, T. Gortenmulder, and K. Buschow. Structural and magnetic properties of $MnFe_{1-x}Co_xGe$ Compounds. *IEEE Trans. Magn.* **42** (2006) 3776–3778. doi:10.1109/tmag.2006.884516

[144] Z. G. Xie, D. Y. Geng, and Z. D. Zhang. Reversible room-temperature magnetocaloric effect in Mn_5PB_2. *Appl. Phys. Lett.* **97** (2010) 202504. doi:10.1063/1.3518064

[145] J. S. Llamazares, P. Álvarez-Alonso, C. Sánchez-Valdés, P. J. Ibarra-Gaytán, J. A. Blanco, and P. Gorria. Investigating the magnetic entropy change in single-phase Y_2Fe_{17} melt-spun ribbons. *Curr. Appl. Phys.* **16** (2016) 963–968. doi:10.1016/j.cap.2016.05.013

[146] P. Tong, B.-S. Wang, and Y.-P. Sun. Mn-based antiperovskite functional materials: Review of research. *Chin. Phys. B.* **22** (2013) 067501. doi:10.1088/1674-1056/22/6/067501

[147] P. Arora, M. K. Chattopadhyay, and S. B. Roy. Magnetocaloric effect in MnSi. *Appl. Phys. Lett.* **91** (2007) 062508. doi:10.1063/1.2768005

[148] Q. Recour, T. Mazet, and B. Malaman. Magnetocaloric properties of Mn_3Sn_2 from heat capacity measurements. *J. Appl. Phys.* **105** (2009) 033905. doi:10.1063/1.3074093

[149] R. A. Booth and S. A. Majetich. Crystallographic orientation and the magnetocaloric effect in MnP. *J. Appl. Phys.* **105** (2009) 07A926. doi:10.1063/1.3072022

[150] P. Tong, B.-S. Wang, and Y.-P. Sun. Mn-based antiperovskite functional materials: Review of research. *Chin. Phys. B.* **22** (2013) 067501. doi:10.1088/1674-1056/22/6/067501

[151] O. Tegus, E. Brück, L. Zhang, Dagula, K. H. J. Buschow, and F. R. de Boer. Magnetic-phase transitions and magnetocaloric effects. *Physica B: Condensed Matter* **319** (2002) 174–192. doi:10.1016/s0921-4526(02)01119-5

[152] M. Balli, P. Fournier, S. Jandl, and M. M. Gospodinov. A study of the phase transition and magnetocaloric effect in multiferroic La_2MnNiO_6 single crystals. *J. Appl. Phys.* **115** (2014) 173904. doi:10.1063/1.4874943

[153] X.-Y. Zhang, Y. Chen, and Z.-Y. Li. Magnetocaloric effect in 4d itinerant ferromagnet $SrRuO_3$. *J. Alloys Compd.* **459** (2008) 51–54. doi:10.1016/j.jallcom.2007.05.022

[154] V. Y. Verchenko, A. A. Tsirlin, A. V. Sobolev, I. A. Presniakov, and A. V. Shevelkov. Ferromagnetic order, strong magnetocrystalline anisotropy, and magnetocaloric effect in the layered telluride $Fe_{3-\delta}GeTe_2$. *Inorg. Chem.* **54** (2015) 8598–8607. doi:10.1021/acs.inorgchem.5b01260

[155] M. Akram and F. M. Nazar. Magnetic properties of CrTe, $Cr_{23}Te_{24}$, Cr_7Te_8, Cr_5Te_6, and Cr_3Te_4 compounds. *J. Mater. Sci.* **18** (1983) 423–429. doi:10.1007/bf00560631

[156] M. A. Nylund, M. M. A. Roger, J. P. Sénateur, and R. Fruchart. Evolution structurale des phosphures, arséniures et arséniophosphures M_2P, M_2As et $M_2(P_{1-x}As_x)$. *J. Solid State Chem.* **4** (1972) 115–122. doi:10.1016/0022-4596(72)90139-9

[157] M. Yuzuri, T. Kanomata, and T. Kaneko. The pressure effect on the Curie temperature and exchange striction of Cr_2S_3 and Cr_2Te_3. *J. Magn. Magn. Mater.* **70** (1987) 223–224. doi:10.1016/0304-8853(87)90416-1

[158] K. H. J. Buschow and D. B. D. Mooij. Crystal structure and magnetic properties of PtMnGa and PtMnAl. *J. Less Common Met.* **99** (1984) 125–130. doi:10.1016/0022-5088(84)90341-2

[159] M. Bacmann, D. Fruchart, A. Koumina, and P. Wolfers. Low temperature magnetic structure of CrNiAs. *Mater. Sci. Forum* **443-444** (2004) 379–382. doi:10.4028/www.scientific.net/msf.443-444.379

[160] F. Hulliger and E. Pobitschka. On the magnetic behavior of new 2H-NbS_2-type derivatives. *J. Solid State Chem.* **1** (1970) 117–119. doi:10.1016/0022-4596(70)90001-0

[161] J. M. D. Coey. *Magnetism and Magnetic Materials*. Magnetism and Magnetic Materials. Cambridge University Press (2010). URL `https://books.google.com/books?id=Ie72CFd-eSEC`.

[162] W. R, T. Ericsson, L. Häggström, and Y. Andersson. Magnetic properties of Fe_5SiB_2 and related compounds. *J. Phys. Colloq.* **37** (1976) C6–591–C6–593. doi:10.1051/jphyscol:19766122

[163] J. Cui and R. D. James. Study of Fe_3Pd and related alloys for ferromagnetic shape memory. *IEEE Trans. Magn.* **37** (2001) 2675–2677. doi:10.1109/20.951271

[164] M. Seeger and H. Kronmüller. The magnetic phase transition in ordered and disordered ferromagnets. *J. Magn. Magn. Mater.* **78** (1989) 393–402. doi:10.1016/0304-8853(89)90212-6

[165] M. A. McGuire and D. S. Parker. Magnetic and structural properties of ferromagnetic Fe_5PB_2 and Fe_5SiB_2 and effects of Co and Mn substitutions. *J. Appl. Phys.* **118** (2015) 163903. doi:10.1063/1.4934496

[166] R. J. Gambino. Magnetic properties of the iron-group metal phosphides. *J. Appl. Phys.* **38** (1967) 1253. doi:10.1063/1.1709566

[167] W. Sakakibara, Y. Hayashi, and H. Takizawa. $MnGa_2Sb_2$, a new ferromagnetic compound synthesized under high pressure. *J. Ceram. Soc. Jpn.* **117** (2009) 72–75. doi:10.2109/jcersj2.117.72

[168] K. Guo, D. Rau, L. Toffoletti, C. Müller, U. Burkhardt, W. Schnelle, R. Niewa, and U. Schwarz. Ternary metastable nitrides ϵ-Fe_2TMN (TM = Co, Ni): High-pressure, high-temperature synthesis, crystal structure, thermal stability, and magnetic properties. *Chem. Mater.* **24** (2012) 4600–4606. doi:10.1021/cm3031297

[169] Y. Ōnuki, K. Ina, T. Hirai, and T. Komatsubara. Magnetic properties of intercalation compound: $Mn_{1/4}MX_2$. *J. Phys. Soc. Jpn.* **55** (1986) 347–356. doi:10.1143/jpsj.55.347

[170] S. Cho, S. Choi, G.-B. Cha, S. C. Hong, Y. Kim, A. J. Freeman, J. B. Ketterson, Y. Park, and H.-M. Park. Synthesis of new pure ferromagnetic semiconductors: $MnGeP_2$ and $MnGeAs_2$. *Solid State Commun.* **129** (2004) 609–613. doi:10.1016/j.ssc.2003.11.040

[171] K. H. J. Buschow. Hydrogen absorption and its effect on the magnetic properties of rare-earth iron intermetallics. *Solid State Commun.* **19** (1976) 421–423. doi:10.1016/0038-1098(76)91181-9

[172] J. W. Drijver, S. G. Sinnema, and F. van der Woude. Magnetic properties of hexagonal and cubic Fe_3Ge. *J. Phys. F.* **6** (1976) 2165–2177. doi:10.1088/0305-4608/6/11/015

[173] D. Serrate, J. M. D. Teresa, and M. R. Ibarra. Double perovskites with ferromagnetism above room temperature. *J. Phys.: Condensed Matter* **19** (2006) 023201. doi:10.1088/0953-8984/19/2/023201

[174] H. Takizawa, T. Sato, T. Endo, and M. Shimada. High pressure synthesis and electrical and magnetic properties of $MnGe_4$ and $CoGe_4$. *J. Solid State Chem.* **88** (1990) 384–390. doi:10.1016/0022-4596(90)90232-m

[175] G. Cao, S. McCall, and J. E. Crow. Observation of itinerant ferromagnetism in layered $Sr_3Ru_2O_7$ single crystals. *Phys. Rev. B.* **55** (1997) R672–R675. doi:10.1103/physrevb.55.r672

[176] A. Houben, P. Müller, J. von Appen, H. Lueken, R. Niewa, and R. Dronskowski. Synthesis, crystal structure, and magnetic properties of the semihard Itinerant Ferromagnet $RhFe_3N$. *Angew. Chem.* **44** (2005) 7212–7215. doi:10.1002/anie.200502579

[177] K. Endo. Magnetic studies of $C1_b$-Compounds CuMnSb, PdMnSb and Cu_{1-x}(Ni or Pd)$_x$MnSb. *J. Phys. Soc. Jpn.* **29** (1970) 643–649. doi:10.1143/jpsj.29.643

[178] T. Klemmer, D. Hoydick, H. Okumura, B. Zhang, and W. A. Soffa. Magnetic hardening and coercivity mechanisms in $L1_0$ ordered FePd ferromagnets. *Scripta Metal. Mater.* **33** (1995) 1793–1805. doi:10.1016/0956-716x(95)00413-p

[179] P. J. Webster. Heusler alloys. *Contemp. Phys.* **10** (1969) 559–577. doi:10.1080/00107516908204800

[180] F. Grandjean and A. Gerard. Study by Mossbauer spectroscopy of the series of perovskite carbides M_3M'C with M=Fe or Mn, and M'=Al, Ga, Ge, Zn, Sn. *J. Phys. F.* **6** (1976) 451–467. doi:10.1088/0305-4608/6/3/019

[181] K. Miyatani, Y. Wada, and F. Okamoto. Magnetic properties of single crystal chalcogenide spinels; $CuCr_2X_3Y$ (X = S, Se and Te, Y = Cl, Br and I) system. *J. Phys. Soc. Jpn.* **25** (1968) 369–372. doi:10.1143/jpsj.25.369

[182] A. Iga and Y. Tawara. Magnetic properties of molybdenum- and wolfram-Modified Mn_3B_4. *J. Phys. Soc. Jpn.* **24** (1968) 28–35. doi:10.1143/jpsj.24.28

[183] V. Y. Irkhin and M. I. Katsnel'son. Half-metallic ferromagnets. *Phys. Uspekhi* **37** (1994) 659–676. doi:10.1070/pu1994v037n07abeh000033

[184] I. Nakatani, H. Nosé, and K. Masumoto. Magnetic properties of $CuCr_2Se_4$ single crystals. *J. Phys. Chem. Solids* **39** (1978) 743–749. doi:10.1016/0022-3697(78)90008-2

[185] N. Menyuk. Ferromagnetism in $CdCr_2Se_4$ and $CdCr_2S_4$. *J. Appl. Phys.* **37** (1966) 1387. doi:10.1063/1.1708484

[186] R. D. Shull, H. Okamoto, and P. A. Beck. Transition from ferromagnetism to mictomagnetism in Fe-Al alloys. *Solid State Commun.* **20** (1976) 863–868. doi:10.1016/0038-1098(76)91292-8

[187] P. Wojtowicz. Semiconducting ferromagnetic spinels. *IEEE Trans. Magn.* **5** (1969) 840–848. doi:10.1109/tmag.1969.1066666

[188] A. Tsuzuki, S. Sago, S. I. Hirano, and S. Naka. High temperature and pressure preparation and properties of iron carbides Fe_7C_3 and Fe_3C. *J. Mater. Sci.* **19** (1984) 2513–2518. doi:10.1007/bf00550805

[189] N. Mattern, W. X. Zhang, S. Roth, H. Reuther, C. Baehtz, and M. Richter. Structural and magnetic properties of non-stoichiometric Fe_2Zr. *J. Phys.: Condensed Matter* **19** (2007) 376202. doi:10.1088/0953-8984/19/37/376202

[190] S. G. Sankar and W. E. Wallace. Magnetic properties of $ScFe_2$. In *AIP Conf. Proc.* AIP Publishing (1976) page 334.

[191] S. Chikazumi. *Physics of Ferromagnetism 2e*. Int. Ser. Monogr. Phys. OUP Oxford (2009). URL https://books.google.com/books?id=AZVfuxXF2GsC.

[192] Z.-D. Zhang, R. Kershaw, K. Dwight, and A. Wold. Preparation and characterization of nickel substituted Fe_5C_2. *Mater. Res. Bull.* **21** (1986) 979–983. doi:10.1016/0025-5408(86)90135-2

[193] K. H. J. Buschow and A. M. van Diepen. Effect of hydrogen absorption on the magnetic properties of YFe_2 and $GdFe_2$. *Solid State Commun.* **19** (1976) 79–81. doi:10.1016/0038-1098(76)91734-8

[194] T. Kanomata, T. Kaneko, and Y. Nakagawa. Magnetic properties of the intermetallic compound Mn_3InC. *J. Solid State Chem.* **96** (1992) 451–454. doi:10.1016/s0022-4596(05)80281-6

[195] S. A. Marei, R. S. Craig, W. E. Wallace, and T. Tsuchida. Magnetic characteristics of some Laves phase systems containing Fe and Mn. *J. Less Common Met.* **13** (1967) 391–398. doi:10.1016/0022-5088(67)90033-1

[196] B. Deka, A. Kundu, S. Ghosh, and A. Srinivasan. Experimental and *ab initio* studies on sub-lattice ordering and magnetism in $Co_2Fe(Ge_{1-x}Si_x)$ alloys. *J. Appl. Phys.* **118** (2015) 133906. doi:10.1063/1.4932526

[197] N. Hayashi, T. Yamamoto, H. Kageyama, M. Nishi, Y. Watanabe, T. Kawakami, Y. Matsushita, A. Fujimori, and M. Takano. $BaFeO_3$: A ferromagnetic iron oxide. *Angew. Chem.* **50** (2011) 12547–12550. doi:10.1002/anie.201105276

[198] T. Shinjo, Y. Nakamura, and N. Shikazono. Magnetic study of Fe_3Si and Fe_5Si_3 by Mössbauer effect. *J. Phys. Soc. Jpn.* **18** (1963) 797–801. doi:10.1143/jpsj.18.797

[199] M. C. Cadeville, C. E. Dahmani, and F. Kern. Magnetism and spatial order in Ni-Pt and Co-Pt alloys. *J. Magn. Magn. Mater.* **54-57** (1986) 1055–1056. doi:10.1016/0304-8853(86)90378-1

[200] E. A. Zhurakovskii, T. B. Shashkina, and V. I. Kotlyar. X-ray absorption spectra of cobalt in ferromagnetic borides. *Soviet Phys. J.* **13** (1970) 14–17. doi:10.1007/bf00817215

[201] A. J. Barón-González, C. Frontera, J. L. García-Muñoz, J. Blasco, and C. Ritter. Cation order and structural transition in La_2MnCoO_6. *J. Phys.: Conf. Ser.* **325** (2011) 012007. doi:10.1088/1742-6596/325/1/012007

[202] J. Kübler, G. H. Fecher, and C. Felser. Understanding the trend in the Curie temperatures of Co_2-based Heusler compounds: *Ab initio* calculations. *Phys. Rev. B* **76** (2007). doi:10.1103/physrevb.76.024414

[203] M. C. Cadeville. Proprietes magnetiques des diborures de manganese et de chrome: MnB_2 et CrB_2. *J. Phys. Chem. Solids* **27** (1966) 667–670. doi:10.1016/0022-3697(66)90217-4

[204] S. Miyahara. Magnetic properties of FeS_2 and CoS_2. *J. Appl. Phys.* **39** (1968) 896. doi:10.1063/1.1656326

[205] C. Q. Jin, J. S. Zhou, J. B. Goodenough, Q. Q. Liu, J. G. Zhao, L. X. Yang, Y. Yu, R. C. Yu, T. Katsura, A. Shatskiy, and E. Ito. High-pressure synthesis of the cubic perovskite $BaRuO_3$ and evolution of ferromagnetism in $ARuO_3$ (A = Ca, Sr, Ba) ruthenates. *Proc. Natl. Acad. Sci.* **105** (2008) 7115–7119. doi:10.1073/pnas.0710928105

[206] N. M. Wolcott and R. L. Falge. Ferromagnetism of $CrBe_{12}$. *Phys. Rev.* **171** (1968) 591–595. doi:10.1103/physrev.171.591

[207] L. Bainsla and K. G. Suresh. Spin polarization studies in half-metallic Co_2TiX (X = Ge and Sn) Heusler alloys. *Curr. Appl. Phys.* **16** (2016) 68–72. doi:10.1016/j.cap.2015.09.015

[208] P. G. van Engen, K. H. J. Buschow, and M. Erman. Magnetic properties and magneto-optical spectroscopy of Heusler alloys based on transition metals and Sn. *J. Magn. Magn. Mater.* **30** (1983) 374–382. doi:10.1016/0304-8853(83)90079-3

[209] M. Terada, K. Endo, Y. Fujita, and R. Kimura. Magnetic Properties of $C1_b$ Compounds; CoVSb, CoTiSb and NiTiSb. *J. Phys. Soc. Jpn.* **32** (1972) 91–94. doi:10.1143/jpsj.32.91

[210] M. A. Kouacou, J. Pierre, and R. V. Skolozdra. Semiconductor-metal transition and the onset of itinerant ferromagnetism in the Heusler phases TiCoSn-TiCoSb. *J. Phys.: Condensed Matter* **7** (1995) 7373–7385. doi:10.1088/0953-8984/7/37/010

[211] L. Pal, S. Gupta, and K. Suresh. Structural and magnetic properties of $Co_2Ti_{1-x}Fe_xAl$ ($0 \leq x \leq 0.5$) Alloys. In *AIP Conf. Proc.*, volume 1591 (2014) pages 1526–1528.

[212] Y. Takahashi. On the origin of the Curie-Weiss law of the magnetic susceptibility in itinerant electron ferromagnetism. *J. Phys. Soc. Jpn.* **55** (1986) 3553–3573. doi:10.1143/jpsj.55.3553

[213] W. J. Takei, D. E. Cox, and G. Shirane. Magnetic structures in the MnSb-CrSb system. *Phys. Rev.* **129** (1963) 2008–2018. doi:10.1103/physrev.129.2008

[214] W. A. J. J. Velge and K. H. J. Buschow. Magnetic and crystallographic properties of some rare earth cobalt compounds with $CaZn_5$ Structure. *J. Appl. Phys.* **39** (1968) 1717. doi:10.1063/1.1656420

[215] R. Fruchart, A. Roger, and R. A. Senateur. Crystallographic and magnetic properties of solid solutions of the phosphides M_2P, M = Cr, Mn, Fe, Co, and Ni. *J. Appl. Phys.* **40** (1969) 1250. doi:10.1063/1.1657617

[216] A. M. Tishin. Magnetocaloric effect in lanthanide materials. *J. Alloys Compd.* **250** (1997) 635–641. doi:10.1016/S0925-8388(96)02521-2

[217] A. Arrott and J. E. Noakes. Approximate equation of state for nickel near its critical temperature. *Phys. Rev. Lett.* **19** (1967) 786–789. doi:10.1103/PhysRevLett.19.786

[218] J. Hill, G. Mulholland, K. Persson, R. Seshadri, C. Wolverton, and B. Meredig. Materials science with large-scale data and informatics: Unlocking new opportunities. *MRS Bull.* **41** (2016) 399–409. doi:10.1557/mrs.2016.93

[219] L. Ward and C. Wolverton. Atomistic calculations and materials informatics: A review. *Curr. Opin. Solid State Mater. Sci.* **21** (2017) 167–176. doi:10.1016/j.cossms.2016.07.002

[220] A. Jain, G. Hautier, S. P. Ong, and K. Persson. New opportunities for materials informatics: Resources and data mining techniques for uncovering hidden relationships. *J. Mater. Res.* **31** (2016) 977–994. doi:10.1557/jmr.2016.80

[221] S. R. Kalidindi and M. De Graef. Materials data science: Current status and future Outlook. *Annu. Rev. Mater. Res.* **45** (2015) 171–193. doi:10.1146/annurev-matsci-070214-020844

[222] S. R. Kalidindi, D. B. Brough, S. Li, A. Cecen, A. L. Blekh, F. Y. P. Congo, and C. Campbell. Role of materials data science and informatics in accelerated materials innovation. *MRS Bull.* **41** (2016) 596–602. doi:10.1557/mrs.2016.164

[223] M. W. Gaultois, T. D. Sparks, C. K. H. Borg, R. Seshadri, W. D. Bonificio, and D. R. Clarke. Data-driven review of thermoelectric materials: performance and resource considerations. *Chem. Mater.* **25** (2013) 2911–2920. doi:10.1021/cm400893e

[224] Y. Xu, M. Yamazaki, and P. Villars. Inorganic materials database for exploring the nature of material. *Jpn. J. Appl. Phys.* **50** (2011) 11RH02. doi:10.1143/JJAP.50.11RH02

[225] C. S. Birkel, W. G. Zeier, J. E. Douglas, B. R. Lettiere, C. E. Mills, G. Seward, A. Birkel, M. L. Snedaker, Y. Zhang, G. J. Snyder, T. M. Pollock, R. Seshadri, and G. D. Stucky. Rapid microwave preparation of thermoelectric TiNiSn and TiCoSb half-Heusler compounds. *Chem. Mater.* **24** (2012) 2558–2565. doi:10.1021/cm3011343

[226] H. Nishihara, Y. Furutani, T. Wada, T. Kanomata, K. Kobayashi, R. Kainuma, K. Ishida, and T. Yamauchi. Magnetization process near the Curie temperature of a ferromagnetic Heusler Alloy Co_2VGa. *J. Supercond. Novel Magn.* **24** (2010) 679–681. doi:10.1007/s10948-010-0933-3

[227] G. Hautier, A. Jain, S. P. Ong, B. Kang, C. Moore, R. Doe, and G. Ceder. Phosphates as lithium-ion battery cathodes: An evaluation based on high-throughput ab Initio calculations. *Chem. Mater.* **23** (2011) 3495–3508. doi:10.1021/cm200949v

[228] J. J. de Pablo, N. E. Jackson, M. A. Webb, L.-Q. Chen, J. E. Moore, D. Morgan, R. Jacobs, T. Pollock, D. G. Schlom, E. S. Toberer, J. Analytis, I. Dabo, D. M. DeLongchamp, G. A. Fiete, G. M. Grason, G. Hautier, Y. Mo, K. Rajan, E. J. Reed, E. Rodriguez, V. Stevanovic, J. Suntivich, K. Thornton, and J.-C. Zhao. New frontiers for the materials genome initiative. *npj Comput. Mater.* **5** (2019) 41. doi:10.1038/s41524-019-0173-4

[229] G. H. Jóhannesson, T. Bligaard, A. V. Ruban, H. L. Skriver, K. W. Jacobsen, and J. K. Nørskov. Combined electronic structure and evolutionary search approach to materials design. *Phys. Rev. Lett.* **88** (2002) 255506. doi:10.1103/PhysRevLett.88.255506

[230] T. Bligaard, G. H. Jóhannesson, A. V. Ruban, H. L. Skriver, K. W. Jacobsen, and J. K. Nørskov. Pareto-optimal alloys. *Appl. Phys. Lett.* **83** (2003) 4527–4529. doi:10.1063/1.1631051

[231] S. Kirklin, J. E. Saal, V. I. Hegde, and C. Wolverton. High-throughput computational search for strengthening precipitates in alloys. *Acta Mater.* **102** (2016) 125–135. doi:10.1016/j.actamat.2015.09.016

[232] S. Kirklin, B. Meredig, and C. Wolverton. High-throughput computational screening of new Li-Ion battery anode materials. *Adv. Energy Mater.* **3** (2013) 252–262. doi:10.1002/aenm.201200593

[233] L. Yu and A. Zunger. Identification of potential photovoltaic absorbers based on first-principles spectroscopic screening of materials. *Phys. Rev. Lett.* **108** (2012) 068701. doi:10.1103/PhysRevLett.108.068701

[234] D. H. Fabini, M. Koerner, and R. Seshadri. Candidate inorganic photovoltaic materials from electronic structure-based optical absorption and charge transport proxies. *Chem. Mater.* **31** (2019) 1561–1574. doi:10.1021/acs.chemmater.8b04542

[235] J. M. Rondinelli, K. R. Poeppelmeier, and A. Zunger. Research update: Towards designed functionalities in oxide-based electronic materials. *APL Mater.* **3** (2015) 080702. doi:10.1063/1.4928289

[236] W. Choe, V. K. Pecharsky, A. O. Pecharsky, K. A. Gschneidner, V. G. Young, and G. J. Miller. Making and breaking covalent bonds across the magnetic transition in the giant magnetocaloric material $Gd_5(Si_2Ge_2)$. *Phys. Rev. Lett.* **84** (2000) 4617–4620. doi:10.1103/PhysRevLett.84.4617

[237] N. T. Trung, L. Zhang, L. Caron, K. H. J. Buschow, and E. Brück. Giant magnetocaloric effects by tailoring the phase transitions. *Appl. Phys. Lett.* **96** (2010) 172504. doi:10.1063/1.3399773

[238] C. Zhang, H. Shi, E. Ye, Y. Nie, Z. Han, and D. Wang. Magnetostructural transition and magnetocaloric effect in MnCoGe–NiCoGe system. *J. Alloys Compd.* **639** (2015) 36–39. doi:10.1016/j.jallcom.2015.03.118

[239] D. Zhang, Z. Nie, Z. Wang, L. Huang, Q. Zhang, and Y. D. Wang. Giant magnetocaloric effect in MnCoGe with minimal Ga substitution. *J. Magn. Magn. Mater.* **387** (2015) 107–110. doi:10.1016/j.jmmm.2015.03.095

[240] M. O. McLinden, J. S. Brown, R. Brignoli, A. F. Kazakov, and P. A. Domanski. Limited options for low-global-warming-potential refrigerants. *Nat. Commun.* **8** (2017) 14476. doi:10.1038/ncomms14476

[241] A. Davarpanah, J. H. Belo, V. S. Amaral, and J. S. Amaral. On the optimization of magneto-volume coupling for practical applied field magnetic refrigeration. *Phys. status solidi* **256** (2019) 1800419. doi:10.1002/pssb.201800419

[242] S. Lin, O. Tegus, E. Brück, W. Dagula, T. Gortenmulder, and K. Buschow. Structural and magnetic properties of $MnFe_{1-x}Co_xGe$ compounds. *IEEE Trans. Magn.* **42** (2006) 3776–3778. doi:10.1109/TMAG.2006.884516

[243] G. A. Landrum, R. Hoffmann, J. Evers, and H. Boysen. The TiNiSi family of compounds: Structure and bonding. *Inorg. Chem.* **37** (1998) 5754–5763. doi:10.1021/ic980223e

[244] A. Van der Ven, J. C. Thomas, Q. Xu, and J. Bhattacharya. Linking the electronic structure of solids to their thermodynamic and kinetic properties. *Math. Comput. Simul.* **80** (2010) 1393–1410. doi:10.1016/j.matcom.2009.08.008

[245] J. C. Thomas and A. Van der Ven. Finite-temperature properties of strongly anharmonic and mechanically unstable crystal phases from first principles. *Phys. Rev. B* **88** (2013) 214111. doi:10.1103/PhysRevB.88.214111

[246] B. Puchala and A. Van Der Ven. Thermodynamics of the Zr-O system from first-principles calculations. *Phys. Rev. B* **88** (2013) 094108. doi:10.1103/PhysRevB.88.094108

[247] A. Zunger, S.-H. Wei, L. G. Ferreira, and J. E. Bernard. Special quasirandom structures. *Phys. Rev. Lett.* **65** (1990) 353–356. doi:10.1103/PhysRevLett.65.353

[248] A. van de Walle, P. Tiwary, M. de Jong, D. Olmsted, M. Asta, A. Dick, D. Shin, Y. Wang, L.-Q. Chen, and Z.-K. Liu. Efficient stochastic generation of special quasirandom structures. *Calphad* **42** (2013) 13–18. doi:10.1016/j.calphad.2013.06.006

[249] C. Guillaud. Les points de transformation des composés définis MnAs, MnBi en relation avec un mécanisme probable d'antiferromagnétisme. *J. Phys. le Radium* **12** (1951) 223–227. doi:10.1051/jphysrad:01951001203022300

[250] B. T. M. Willis and H. P. Rooksby. Magnetic transitions and structural changes in hexagonal manganese compounds. *Proc. Phys. Soc. Sect. B* **67** (1954) 290–296. doi:10.1088/0370-1301/67/4/302

[251] G. E. Bacon and R. Street. Magnetic structure of manganese arsenide. *Nature* **175** (1955) 518–518. doi:10.1038/175518a0

[252] J. B. Goodenough and J. A. Kafalas. High-pressure study of the first-order phase transition in MnAs. *Phys. Rev.* **157** (1967) 389–395. doi:10.1103/PhysRev.157.389

[253] Z. B. Guo, Y. W. Du, J. S. Zhu, H. Huang, W. P. Ding, and D. Feng. Large magnetic entropy change in perovskite-type manganese oxides. *Phys. Rev. Lett.* **78** (1997) 1142–1145. doi:10.1103/PhysRevLett.78.1142

[254] N. Menyuk, J. A. Kafalas, K. Dwight, and J. B. Goodenough. Effects of pressure on the magnetic properties of MnAs. *Phys. Rev.* **177** (1969) 942–951. doi:10.1103/PhysRev.177.942

[255] R. H. Wilson and J. S. Kasper. The crystal structure of MnAs above 40°C. *Acta Crystallogr.* **17** (1964) 95–101. doi:10.1107/S0365110X64000330

[256] C. Kittel. Model of exchange-inversion magnetization. *Phys. Rev.* **120** (1960) 335–342. doi:10.1103/PhysRev.120.335

[257] M. Shimizu. On the conditions of ferromagnetism by the band model. *Proc. Phys. Soc.* **84** (1964) 397–408. doi:10.1088/0370-1328/84/3/309

[258] S. K. Asadov, É. A. Zavadskiĭ, V. I. Kamenev, E. P. Stefanovskiĭ, A. L. Sukstanskiĭ, and B. M. Todris. Relation of magnetic and structural factors in the course of phase transitions in MnAs-based alloys. *Phys. Solid State* **42** (2000) 1696–1704. doi:10.1134/1.1309454

[259] V. I. Val'kov and A. V. Golovchan. Electronic mechanism of structural phase transitions in manganese arsenide. *Low Temp. Phys.* **30** (2004) 711–720. doi:10.1063/1.1802956

[260] M. K. Niranjan, B. R. Sahu, and L. Kleinman. Density functional determination of the magnetic state of β-MnAs. *Phys. Rev. B* **70** (2004) 180406. doi:10.1103/PhysRevB.70.180406

[261] J. Łażewski, P. Piekarz, and K. Parlinski. Mechanism of the phase transitions in MnAs. *Phys. Rev. B* **83** (2011) 054108. doi:10.1103/PhysRevB.83.054108

[262] L. H. Schwartz, E. L. Hall, and G. P. Felcher. Magnetic structure of MnAs and $MnAs_{0.92}P_{0.08}$. *J. Appl. Phys.* **42** (1971) 1621–1622. doi:10.1063/1.1660367

[263] K. U. Neumann, K. R. Ziebeck, F. Jewiss, L. Däweritz, K. H. Ploog, and A. Murani. Magnetic correlations in the paramagnetic phases of MnAs. *Phys. B Condens. Matter* **335** (2003) 34–36. doi:10.1016/S0921-4526(03)00185-6

[264] K. Selte, A. Kjekshus, A. F. Andresen, and A. Zieba. On the magnetic properties of transition metal substituted MnAs. *J. Phys. Chem. Solids* **38** (1977) 719–725. doi:10.1016/0022-3697(77)90063-4

[265] G. A. Govor. Peculiarities of the first-order phase transition in MnAs. *Phys. status solidi* **90** (1985) K185–K188. doi:10.1002/pssa.2210900261

[266] S. Fujieda, Y. Hasegawa, A. Fujita, and K. Fukamichi. Thermal transport properties of magnetic refrigerants $La(Fe_xSi_{1-x})_{13}$ and their hydrides, and $Gd_5Si_2Ge_2$ and MnAs. *J. Appl. Phys.* **95** (2004) 2429–2431. doi:10.1063/1.1643774

[267] J. P. Perdew, A. Ruzsinszky, G. I. Csonka, O. A. Vydrov, G. E. Scuseria, L. A. Constantin, X. Zhou, and K. Burke. Restoring the density-gradient expansion for exchange in solids and surfaces. *Phys. Rev. Lett.* **100** (2008) 136406. doi:10.1103/PhysRevLett.100.136406

[268] A. Zieba, K. Selte, A. Kjekshus, A. F. Andresen, O. Smidsrød, C.-O. Pontchour, P. Phavanantha, S. Pramatus, B. N. Cyvin, and S. J. Cyvin. Phase transitions in MnAs. *Acta Chem. Scand.* **32a** (1978) 173–177. doi:10.3891/acta.chem.scand.32a-0173

[269] P. Haas, F. Tran, and P. Blaha. Calculation of the lattice constant of solids with semilocal functionals. *Phys. Rev. B* **79** (2009) 1–10. doi:10.1103/PhysRevB.79.085104

[270] I. Rungger and S. Sanvito. Ab initio study of the magnetostructural properties of MnAs. *Phys. Rev. B* **74** (2006) 024429. doi:10.1103/PhysRevB.74.024429

[271] S. Dudarev, G. Botton, S. Y. Savrasov, C. J. Humphreys, and A. P. Sutton. Electron-energy-loss spectra and the structural stability of nickel oxide: An LSDA+U study. *Phys. Rev. B* **57** (1998) 1505–1509. doi:10.1103/PhysRevB.57.1505

[272] V. I. Anisimov, J. Zaanen, and O. K. Andersen. Band theory and Mott insulators: Hubbard U instead of Stoner I. *Phys. Rev. B* **44** (1991) 943–954. doi:10.1103/PhysRevB.44.943

[273] V. P. Glazkov, D. P. Kozlenko, K. M. Podurets, B. N. Savenko, and V. A. Somenkov. Neutron diffraction investigation of the atomic and magnetic structures of MnAs at high pressures. *Crystallogr. Reports* **48** (2003) 54–57. doi:10.1134/1.1541743

[274] B. Alling, T. Marten, and I. A. Abrikosov. Effect of magnetic disorder and strong electron correlations on the thermodynamics of CrN. *Phys. Rev. B* **82** (2010) 184430. doi:10.1103/PhysRevB.82.184430

[275] G. Trimarchi, Z. Wang, and A. Zunger. Polymorphous band structure model of gapping in the antiferromagnetic and paramagnetic phases of the Mott insulators MnO, FeO, CoO, and NiO. *Phys. Rev. B* **97** (2018) 035107. doi:10.1103/PhysRevB.97.035107

[276] J. Varignon, M. Bibes, and A. Zunger. Origin of band gaps in 3d perovskite oxides. *Nat. Commun.* **10** (2019) 1658. doi:10.1038/s41467-019-09698-6

[277] D. J. Singh and M. H. Du. Density functional study of $LaFeAsO_{1-x}F_x$: A low carrier density superconductor near itinerant magnetism. *Phys. Rev. Lett.* **100** (2008) 2–5. doi:10.1103/PhysRevLett.100.237003

[278] D. A. Papaconstantopoulos, M. J. Mehl, and M. D. Johannes. Tight-binding Hamiltonian for LaOFeAs. *Phys. Rev. B* **82** (2010) 054503. doi:10.1103/PhysRevB.82.054503

[279] R. Dronskowski and P. E. Bloechl. Crystal orbital Hamilton populations (COHP): energy-resolved visualization of chemical bonding in solids based on density-functional calculations. *J. Phys. Chem.* **97** (1993) 8617–8624. doi:10.1021/j100135a014

[280] V. L. Deringer, A. L. Tchougréeff, and R. Dronskowski. Crystal Orbital Hamilton Population (COHP) analysis as projected from plane-wave basis sets. *J. Phys. Chem. A* **115** (2011) 5461–5466. doi:10.1021/jp202489s

[281] S. Maintz, V. L. Deringer, A. L. Tchougréeff, and R. Dronskowski. Analytic projection from plane-wave and PAW wavefunctions and application to chemical-bonding analysis in solids. *J. Comput. Chem.* **34** (2013) 2557–2567. doi:10.1002/jcc.23424

[282] S. Maintz, V. L. Deringer, A. L. Tchougréeff, and R. Dronskowski. LOBSTER: A tool to extract chemical bonding from plane-wave based DFT. *J. Comput. Chem.* **37** (2016) 1030–1035. doi:10.1002/jcc.24300

[283] S. Maintz, M. Esser, and R. Dronskowski. Efficient rotation of local basis functions using real spherical harmonics. *Acta Phys. Pol. B* **47** (2016) 1165. doi:10.5506/APhysPolB.47.1165

[284] G. J. Miller. Complex rare-earth tetrelides, $RE_5(Si_xGe_{1-x})_4$: New materials for magnetic refrigeration and a superb playground for solid state chemistry. *Chem. Soc. Rev.* **35** (2006) 799–813. doi:10.1039/B208133B

[285] J. Yao, P. Wang, and Y. Mozharivskyj. Tuning magnetic and structural transitions through valence electron concentration in the giant magnetocaloric $Gd_{5-x}Eu_xGe_4$ phases. *Chem. Mater.* **24** (2012) 552–556. doi:10.1021/cm203148e

[286] R. A. Kishore and S. Priya. A review on design and performance of thermomagnetic devices. *Renew. Sustain. Energy Rev.* **81** (2018) 33–44. doi:10.1016/j.rser.2017.07.035

[287] R. A. Kishore and S. Priya. Low-grade waste heat recovery using the reverse magnetocaloric effect. *Sustain. Energy Fuels* **00** (2017) 1–10. doi:10.1039/C7SE00182G

[288] M. F. J. Boeije, M. Maschek, X. F. Miao, N. V. Thang, N. H. van Dijk, and E. Brück. Mixed magnetism in magnetocaloric materials with first-order and second-order magnetoelastic transitions. *J. Phys. D* **50** (2017) 174002. doi:10.1088/1361-6463/aa5db9

[289] J. Y. Law, V. Franco, L. M. Moreno-Ramírez, A. Conde, D. Y. Karpenkov, I. Radulov, K. P. Skokov, and O. Gutfleisch. A quantitative criterion for determining the order of magnetic phase transitions using the magnetocaloric effect. *Nat. Commun.* **9** (2018) 2680. doi:10.1038/s41467-018-05111-w

[290] R. Barua, B. Lejeune, B. Jensen, L. Ke, R. McCallum, M. Kramer, and L. Lewis. Enhanced room-temperature magnetocaloric effect and tunable magnetic response in Ga-and Ge-substituted AlFe2B2. *J. Alloys Compd.* **777** (2019) 1030–1038. doi:10.1016/j.jallcom.2018.10.206

[291] Songlin, Dagula, O. Tegus, E. Brück, F. de Boer, and K. Buschow. Magnetic and magnetocaloric properties of $Mn_5Ge_{3-x}Sb_x$. *J. Alloys Compd.* **337** (2002) 269–271. doi:10.1016/S0925-8388(01)01935-1

[292] X. Zhang, Y. Chen, L. Lü, and Z. Li. A potential oxide for magnetic refrigeration application: CrO_2 particles. *J. Phys. Condens. Matter* **18** (2006) L559–L566. doi:10.1088/0953-8984/18/44/L01

[293] T. Shigematsu, T. Kanaizuka, K. Kosuge, M. Shiga, Y. Nakamura, and S. Kachi. Thermal expansion anomaly of MnB. *Phys. Lett. A* **53** (1975) 385–386. doi:10.1016/0375-9601(75)90041-9

[294] T. Kanaizuka. Invar like properties of transition metal monoborides $Mn_{1-x}Cr_xB$ and $Mn_{1-x}Fe_xB$. *Mater. Res. Bull.* **16** (1981) 1601–1608. doi:10.1016/0025-5408(81)90033-7

[295] J. Park, Y.-K. Hong, H.-K. Kim, W. Lee, C.-D. Yeo, S.-G. Kim, M.-H. Jung, C.-J. Choi, and O. N. Mryasov. Electronic structures of MnB soft magnet. *AIP Adv.* **6** (2016) 055911. doi:10.1063/1.4943240

[296] A. Gueddouh. The effects of magnetic moment collapse under high pressure, on physical properties in mono-borides TMB (TM = Mn, Fe): a first-principles. *Phase Transitions* **1594** (2017) 1–17. doi:10.1080/01411594.2017.1302088

[297] S. Ma, K. Bao, Q. Tao, P. Zhu, T. Ma, B. Liu, Y. Liu, and T. Cui. Manganese monoboride, an inexpensive room temperature ferromagnetic hard material. *Sci. Rep.* **7** (2017) 43759. doi:10.1038/srep43759

[298] J. J. Stickel. Data smoothing and numerical differentiation by a regularization method. *Comput. Chem. Eng.* **34** (2010) 467–475. doi:10.1016/j.compchemeng.2009.10.007

[299] J. D. Bocarsly, R. F. Need, R. Seshadri, and S. D. Wilson. Magnetoentropic signatures of skyrmionic phase behavior in FeGe. *Phys. Rev. B* **97** (2018) 100404. doi:10.1103/PhysRevB.97.100404

[300] G. W. Stinton and J. S. O. Evans. Parametric Rietveld refinement. *J. Appl. Crystallogr.* **40** (2007) 87–95. doi:10.1107/s0021889806043275

[301] T. Faske and W. Donner. X-ray diffractometer for the investigation of temperature- and magnetic field-induced structural phase transitions. *J. Appl. Crystallogr.* **51** (2018) 761–767. doi:10.1107/S1600576718004892

[302] T. Kanaizuka. Phase diagram of pseudobinary CrB-MnB and MnB-FeB systems: Crystal structure of the low-temperature modification of FeB. *J. Solid State Chem.* **41** (1982) 195–204. doi:10.1016/0022-4596(82)90202-X

[303] P. Mohn. The calculated electronic and magnetic properties of the tetragonal transition-metal monoborides. *J. Phys. C Solid State Phys.* **21** (1988) 2841–2851. doi:10.1088/0022-3719/21/15/016

[304] P. W. Stephens. Phenomenological model of anisotropic peak broadening in powder diffraction. *J. Appl. Crystallogr.* **32** (1999) 281–289. doi:10.1107/S0021889898006001

[305] T. Gottschall, D. Benke, M. Fries, A. Taubel, I. A. Radulov, K. P. Skokov, and O. Gutfleisch. A matter of size and stress: Understanding the first-order transition in materials for solid-state refrigeration. *Adv. Funct. Mater.* **27** (2017) 1606735. doi:10.1002/adfm.201606735

[306] E. Wohlfarth. Thermodynamic aspects of itinerant electron magnetism. *Phys. B+C* **91** (1977) 305–314. doi:10.1016/0378-4363(77)90199-1

[307] T. Moriya and K. Usami. Magneto-volume effect and invar phenomena in ferromagnetic metals. *Solid State Commun.* **34** (1980) 95–99. doi:10.1016/0038-1098(80)91241-7

[308] R. Huang, Y. Liu, W. Fan, J. Tan, F. Xiao, L. Qian, and L. Li. Giant negative thermal expansion in $NaZn_{13}$-type $La(Fe,Si,Co)_{13}$ compounds. *J. Am. Chem. Soc.* **135** (2013) 11469–11472. doi:10.1021/ja405161z

[309] F. Hu, F. Shen, J. Hao, Y. Liu, J. Wang, J. Sun, and B. Shen. Negative thermal expansion in the materials with giant magnetocaloric effect. *Front. Chem.* **6** (2018) 1–14. doi:10.3389/fchem.2018.00438

[310] L. Ludgren, O. Beckman, V. Attia, S. P. Bhattacheriee, and M. Richardson. Helical Spin Arrangement in Cubic FeGe. *Phys. Scr.* **1** (1970) 69–72. doi:10.1088/0031-8949/1/1/012

[311] S. Haraldson, L. Björn, O. Beckman, and U. Smith. Magnetic resonance in cubic FeGe. *J. Magn. Reson.* **8** (1972) 271–273. doi:10.1016/0022-2364(72)90009-1

[312] Y. Ishikawa and M. Arai. Magnetic phase diagram of MnSi near critical temperature studied by neutron small angle scattering. *J. Phys. Soc. Japan* **53** (1984) 2726–2733. doi:10.1143/JPSJ.53.2726

[313] A. Bogdanov and A. Hubert. Thermodynamically stable magnetic vortex states in magnetic crystals. *J. Magn. Magn. Mater.* **138** (1994) 255–269. doi:10.1016/0304-8853(94)90046-9

[314] C. Pappas, E. Lelièvre-Berna, P. Falus, P. M. Bentley, E. Moskvin, S. Grigoriev, P. Fouquet, and B. Farago. Chiral paramagnetic skyrmion-like phase in MnSi. *Phys. Rev. Lett.* **102** (2009) 197202. doi:10.1103/PhysRevLett.102.197202

[315] X. Z. Yu, Y. Onose, N. Kanazawa, J. H. Park, J. H. Han, Y. Matsui, N. Nagaosa, and Y. Tokura. Real-space observation of a two-dimensional skyrmion crystal. *Nature* **465** (2010) 901–904. doi:10.1038/nature09124

[316] H. Wilhelm, M. Baenitz, M. Schmidt, C. Naylor, R. Lortz, U. K. Rößler, A. A. Leonov, and A. N. Bogdanov. Confinement of chiral magnetic modulations in the precursor region of FeGe. *J. Phys. Condens. Matter* **24** (2012) 294204. doi:10.1088/0953-8984/24/29/294204

[317] L. Cevey, H. Wilhelm, M. Schmidt, and R. Lortz. Thermodynamic investigations in the precursor region of FeGe. *Phys. status solidi* **250** (2013) 650–653. doi:10.1002/pssb.201200632

[318] E. Moskvin, S. Grigoriev, V. Dyadkin, H. Eckerlebe, M. Baenitz, M. Schmidt, and H. Wilhelm. Complex chiral modulations in FeGe close to magnetic ordering. *Phys. Rev. Lett.* **110** (2013) 077207. doi:10.1103/PhysRevLett.110.077207

[319] A. Bauer and C. Pfleiderer. Magnetic phase diagram of MnSi inferred from magnetization and ac susceptibility. *Phys. Rev. B* **85** (2012) 214418. doi:10.1103/PhysRevB.85.214418

[320] A. Bauer and C. Pfleiderer. Generic aspects of skyrmion lattices in chiral magnets. In J. Seidel, ed., *Topol. Struct. ferroic Mater.*, volume 228 of *Springer Series in Materials Science*, chapter 1, pages 1–28. Springer International Publishing, Cham (2016) .

[321] K. Kadowaki, K. Okuda, and M. Date. Magnetization and magnetoresistance of MnSi. *J. Phys. Soc. Japan* **51** (1982) 2433–2438. doi:10.1143/JPSJ.51.2433

[322] A. Bauer, M. Garst, and C. Pfleiderer. Specific heat of the skyrmion lattice phase and field-induced tricritical point in MnSi. *Phys. Rev. Lett.* **110** (2013) 1–5. doi:10.1103/PhysRevLett.110.177207

[323] W. Jiang, W. Zhang, G. Yu, M. B. Jungfleisch, P. Upadhyaya, H. Somaily, J. E. Pearson, Y. Tserkovnyak, K. L. Wang, O. Heinonen, S. G. E. te Velthuis, and A. Hoffmann. Mobile Néel skyrmions at room temperature: status and future. *AIP Adv.* **6** (2016) 055602. doi:10.1063/1.4943757

[324] N. Nagaosa and Y. Tokura. Topological properties and dynamics of magnetic skyrmions. *Nat. Nanotechnol.* **8** (2013) 899–911. doi:10.1038/nnano.2013.243

[325] Y. Tokunaga, X. Z. Yu, J. S. White, H. M. Rønnow, D. Morikawa, Y. Taguchi, and Y. Tokura. A new class of chiral materials hosting magnetic skyrmions beyond room temperature. *Nat. Commun.* **6** (2015) 7638. doi:10.1038/ncomms8638

[326] X. Z. Yu, N. Kanazawa, Y. Onose, K. Kimoto, W. Z. Zhang, S. Ishiwata, Y. Matsui, and Y. Tokura. Near room-temperature formation of a skyrmion crystal in thin-films of the helimagnet FeGe. *Nat. Mater.* **10** (2011) 106–109. doi:10.1038/nmat2916

[327] X. Yu, N. Kanazawa, W. Zhang, T. Nagai, T. Hara, K. Kimoto, Y. Matsui, Y. Onose, and Y. Tokura. Skyrmion flow near room temperature in an ultralow current density. *Nat. Commun.* **3** (2012) 988. doi:10.1038/ncomms1990

[328] S. Emori, U. Bauer, S.-M. Ahn, E. Martinez, and G. S. D. Beach. Current-driven dynamics of chiral ferromagnetic domain walls. *Nat. Mater.* **12** (2013) 611–616. doi:10.1038/nmat3675

[329] S. Woo, K. Litzius, B. Krüger, M.-Y. Im, L. Caretta, K. Richter, M. Mann, A. Krone, R. M. Reeve, M. Weigand, P. Agrawal, I. Lemesh, M.-A. Mawass, P. Fischer, M. Kläui, and G. S. D. Beach. Observation of room-temperature magnetic skyrmions and their current-driven dynamics in ultrathin metallic ferromagnets. *Nat. Mater.* **15** (2016) 501–506. doi:10.1038/nmat4593

[330] M. J. Stolt, Z.-A. Li, B. Phillips, D. Song, N. Mathur, R. E. Dunin-Borkowski, and S. Jin. Selective chemical vapor deposition growth of cubic FeGe nanowires that support stabilized magnetic skyrmions. *Nano Lett.* **17** (2017) 508–514. doi:10.1021/acs.nanolett.6b04548

[331] M. J. Stolt, X. Sigelko, N. Mathur, and S. Jin. Chemical pressure stabilization of the cubic B20 structure in skyrmion hosting $Fe_{1-x}Co_xGe$ Alloys. *Chem. Mater.* **30** (2018) 1146–1154. doi:10.1021/acs.chemmater.7b05261

[332] K. Karube, J. S. White, N. Reynolds, J. L. Gavilano, H. Oike, A. Kikkawa, F. Kagawa, Y. Tokunaga, H. M. Rønnow, Y. Tokura, and Y. Taguchi. Robust metastable skyrmions and their triangular–square lattice structural transition in a high-temperature chiral magnet. *Nat. Mater.* **15** (2016) 1237–1242. doi:10.1038/nmat4752

[333] C. Phatak, O. Heinonen, M. De Graef, and A. Petford-Long. Nanoscale skyrmions in a nonchiral metallic multiferroic: Ni_2MnGa. *Nano Lett.* **16** (2016) 4141–4148. doi:10.1021/acs.nanolett.6b01011

[334] Z. Hou, W. Ren, B. Ding, G. Xu, Y. Wang, B. Yang, Q. Zhang, Y. Zhang, E. Liu, F. Xu, W. Wang, G. Wu, X. Zhang, B. Shen, and Z. Zhang. Observation of various and spontaneous magnetic skyrmionic bubbles at room temperature in a frustrated kagome magnet with uniaxial magnetic anisotropy. *Adv. Mater.* **29** (2017) 1701144. doi:10.1002/adma.201701144

[335] L. Caron, Z. Ou, T. Nguyen, D. Cam Thanh, O. Tegus, and E. Brück. On the determination of the magnetic entropy change in materials with first-order transitions. *J. Magn. Magn. Mater.* **321** (2009) 3559–3566. doi:10.1016/j.jmmm.2009.06.086

[336] G. Porcari, F. Cugini, S. Fabbrici, C. Pernechele, F. Albertini, M. Buzzi, M. Mangia, and M. Solzi. Convergence of direct and indirect methods in the magnetocaloric study of first order transformations: The case of Ni-Co-Mn-Ga Heusler alloys. *Phys. Rev. B* **86** (2012) 104432. doi:10.1103/PhysRevB.86.104432

[337] M. Balli, D. Fruchart, D. Gignoux, and R. Zach. The "colossal" magnetocaloric effect in $Mn_{1-x}Fe_xAs$: What are we really measuring? *Appl. Phys. Lett.* **95** (2009) 072509. doi:10.1063/1.3194144

[338] L. Xu, J. Fan, W. Sun, Y. Zhu, D. Hu, J. Liu, Y. Ji, D. Shi, and H. Yang. Magnetic field-driven 3D-Heisenberg-like phase transition in single crystalline helimagnet FeGe. *Appl. Phys. Lett.* **111** (2017) 052406. doi:10.1063/1.4992107

[339] S. A. Brazovskiĭ. Phase transition of an isotropic system to a nonuniform state. *Sov. Phys.-JETP* **41** (1975) 85–89.

[340] S. A. Brazovskiĭ, I. E. Dzyaloshinskii, and B. G. Kukharenko. First-order magnetic phase transitions and fluctuations. *Sov. Physics-JETP* **43** (1976) 1178–1183.

[341] M. Janoschek, M. Garst, A. Bauer, P. Krautscheid, R. Georgii, P. Böni, and C. Pfleiderer. Fluctuation-induced first-order phase transition in Dzyaloshinskii-Moriya helimagnets. *Phys. Rev. B* **87** (2013) 134407. doi:10.1103/PhysRevB.87.134407

[342] J. D. Bocarsly, C. Heikes, C. M. Brown, S. D. Wilson, and R. Seshadri. Deciphering structural and magnetic disorder in the chiral skyrmion host materials $Co_xZn_yMn_z$ $(x + y + z = 20)$. *Phys. Rev. Mater.* **3** (2019) 014402. doi:10.1103/PhysRevMaterials.3.014402

[343] X. Z. Yu, Y. Tokunaga, Y. Kaneko, W. Z. Zhang, K. Kimoto, Y. Matsui, Y. Taguchi, and Y. Tokura. Biskyrmion states and their current-driven motion in a layered manganite. *Nat. Commun.* **5** (2014) 3198. doi:10.1038/ncomms4198

[344] W. Münzer, A. Neubauer, T. Adams, S. Mühlbauer, C. Franz, F. Jonietz, R. Georgii, P. Böni, B. Pedersen, M. Schmidt, A. Rosch, and C. Pfleiderer. Skyrmion lattice in the doped semiconductor $Fe_{1-x}Co_xSi$. *Phys. Rev. B* **81** (2010) 041203. doi:10.1103/PhysRevB.81.041203

[345] S. Buhrandt and L. Fritz. Skyrmion lattice phase in three-dimensional chiral magnets from Monte Carlo simulations. *Phys. Rev. B* **88** (2013) 195137. doi:10.1103/PhysRevB.88.195137

[346] H. Oike, A. Kikkawa, N. Kanazawa, Y. Taguchi, M. Kawasaki, Y. Tokura, and F. Kagawa. Interplay between topological and thermodynamic stability in a metastable magnetic skyrmion lattice. *Nat. Phys.* **12** (2015) 62–66. doi:10.1038/nphys3506

[347] R. Ritz, M. Halder, C. Franz, A. Bauer, M. Wagner, R. Bamler, A. Rosch, and C. Pfleiderer. Giant generic topological Hall resistivity of MnSi under pressure. *Phys. Rev. B* **87** (2013) 134424. doi:10.1103/PhysRevB.87.134424

[348] K. Karube, J. S. White, D. Morikawa, M. Bartkowiak, A. Kikkawa, Y. Tokunaga, T. Arima, H. M. Rønnow, Y. Tokura, and Y. Taguchi. Skyrmion formation in a bulk chiral magnet at zero magnetic field and above room temperature. *Phys. Rev. Mater.* **1** (2017) 074405. doi:10.1103/PhysRevMaterials.1.074405

[349] H. Nakamura, K. Yoshimoto, M. Shiga, M. Nishi, and K. Kakurai. Strong antiferromagnetic spin fluctuations and the quantum spin-liquid state in geometrically frustrated -Mn, and the transition to a spin-glass state caused by non-magnetic impurity. *J. Phys. Condens. Matter* **9** (1997) 4701–4728. doi:10.1088/0953-8984/9/22/022

[350] O. B. Karlsen, A. Kjekshus, H. Fjellvåg, P. Ravindran, R. Vidya, and B. C. Hauback. Structure and magnetism of the β-Mn-Co solid-solution phase. *J. Alloys Compd.* **476** (2009) 9–13. doi:10.1016/j.jallcom.2008.09.011

[351] C. P. Gräf, R. Birringer, and A. Michels. Synthesis and magnetic properties of cobalt nanocubes. *Phys. Rev. B* **73** (2006) 212401. doi:10.1103/PhysRevB.73.212401

[352] H. Q. Yuan, D. F. Agterberg, N. Hayashi, P. Badica, D. Vandervelde, K. Togano, M. Sigrist, and M. B. Salamon. S-wave spin-triplet order in superconductors without inversion symmetry: Li_2Pd_3B. *Phys. Rev. Lett.* **97** (2006) 017006. doi:10.1103/PhysRevLett.97.017006

[353] W. Wei, G. J. Zhao, D. R. Kim, C. Jin, J. L. Zhang, L. Ling, L. Zhang, H. Du, T. Y. Chen, J. Zang, M. Tian, C. L. Chien, and Y. Zhang. Rh_2Mo_3N: Non-centrosymmetric s-wave superconductor. *Phys. Rev. B* **94** (2016) 104503. doi:10.1103/PhysRevB.94.104503

[354] T. Hori, H. Shiraish, and Y. Ishii. Magnetic properties of β-MnCoZn alloys. *J. Magn. Magn. Mater.* **310** (2007) 1820–1822. doi:10.1016/j.jmmm.2006.10.582

[355] T. Hama, M. Matsumura, H. Kato, H. Yamagata, Y. Kohori, T. Kohara, and Y. Iwamoto. ^{55}Mn NQR study at Mn-II sites in β-Mn metal: A possible effect of geometrical frustration. *J. Phys. Soc. Japan* **73** (2004) 2305–2312.

[356] W. Xie, S. Thimmaiah, J. Lamsal, J. Liu, T. W. Heitmann, D. Quirinale, A. I. Goldman, V. Pecharsky, and G. J. Miller. β-Mn-type $Co_{8+x}Zn_{12-x}$ as a defect cubic laves phase: site preferences, magnetism, and electronic structure. *Inorg. Chem.* **52** (2013) 9399–9408. doi:10.1021/ic4009653

[357] J. Albertsson, S. C. Abrahams, and Å. . Kvick. Atomic displacement, anharmonic thermal vibration, expansivity and pyroelectric coefficient thermal dependences in ZnO. *Acta Crystallogr. Sect. B Struct. Sci.* **45** (1989) 34–40. doi:10.1107/S0108768188010109

[358] W. Xie and G. J. Miller. New Co–Pd–Zn γ-brasses with dilute ferrimagnetism and Co_2Zn_{11} revisited: Establishing the synergism between theory and experiment. *Chem. Mater.* **26** (2014) 2624–2634. doi:10.1021/cm500078w

[359] G. W. C. Kaye and T. H. Laby. *Tables of physical and chemical constants*. Longman, 16 edition (1995).

[360] J. A. Mydosh. Spin glasses: Redux: An updated experimental/materials survey. *Reports Prog. Phys.* **78** (2015). doi:10.1088/0034-4885/78/5/052501

[361] B. A. Frandsen and S. J. L. Billinge. Magnetic structure determination from the magnetic pair distribution function (mPDF): ground state of MnO. *Acta Crystallogr. Sect. A Found. Adv.* **71** (2015) 325–334. doi:10.1107/S205327331500306X

[362] W. Bao, S. Raymond, S. M. Shapiro, K. Motoya, B. Fåk, and R. W. Erwin. Unconventional ferromagnetic and spin-glass states of the reentrant spin glass $Fe_{0.7}Al_{0.3}$. *Phys. Rev. Lett.* **82** (1999) 4711–4714. doi:10.1103/PhysRevLett.82.4711

[363] T. Miyazaki, I. Okamoto, Y. Ando, and M. Takahashi. Classical and reentrant spin-glass behaviour in amorphous $(Fe_{1-x}M_x)_{77}Si_{10}B_{13}$ (M=V,Cr,Mn,Ni) alloys. *J. Phys. F Met. Phys.* **18** (1988) 1601–1610. doi:10.1088/0305-4608/18/7/026

[364] J. Dho, W. S. Kim, and N. H. Hur. Reentrant spin glass behavior in Cr-doped perovskite manganite. *Phys. Rev. Lett.* **89** (2002) 027202. doi:10.1103/PhysRevLett.89.027202

[365] S. Chatterjee, S. Giri, S. K. De, and S. Majumdar. Reentrant-spin-glass state in $Ni_2Mn_{1.36}Sn_{0.64}$ shape-memory alloy. *Phys. Rev. B* **79** (2009) 092410. doi:10.1103/PhysRevB.79.092410

[366] E. E. Levin, J. D. Bocarsly, K. E. Wyckoff, T. M. Pollock, and R. Seshadri. Tuning the magnetocaloric response in half-Heusler/Heusler $MnNi_{1+x}Sb$ solid solutions. *Phys. Rev. Mater.* **1** (2017) 075003. doi:10.1103/PhysRevMaterials.1.075003

[367] V. Franco, J. S. Blázquez, and A. Conde. Field dependence of the magnetocaloric effect in materials with a second order phase transition: A master curve for the magnetic entropy change. *Appl. Phys. Lett.* **89** (2006) 222512. doi:10.1063/1.2399361

[368] V. Franco, J. M. Borrego, C. F. Conde, A. Conde, M. Stoica, and S. Roth. Refrigerant capacity of FeCrMoCuGaPCB amorphous alloys. *J. Appl. Phys.* **100** (2006). doi:10.1063/1.2358311

[369] V. Franco, A. Conde, and L. F. Kiss. Magnetocaloric response of FeCrB amorphous alloys: Predicting the magnetic entropy change from the Arrott-Noakes equation of state. *J. Appl. Phys.* **104** (2008). doi:10.1063/1.2961310

[370] V. Franco, R. Caballero-Flores, A. Conde, K. E. Knipling, and M. A. Willard. Magnetocaloric effect and critical exponents of $Fe_{77}Co_{5.5}Ni_{5.5}Zr_7B_4Cu_1$: A detailed study. *J. Appl. Phys.* **109** (2011) 5–8. doi:10.1063/1.3535191

[371] S. Kaul. Static critical phenomena in ferromagnets with quenched disorder. *J. Magn. Magn. Mater.* **53** (1985) 5–53. doi:10.1016/0304-8853(85)90128-3